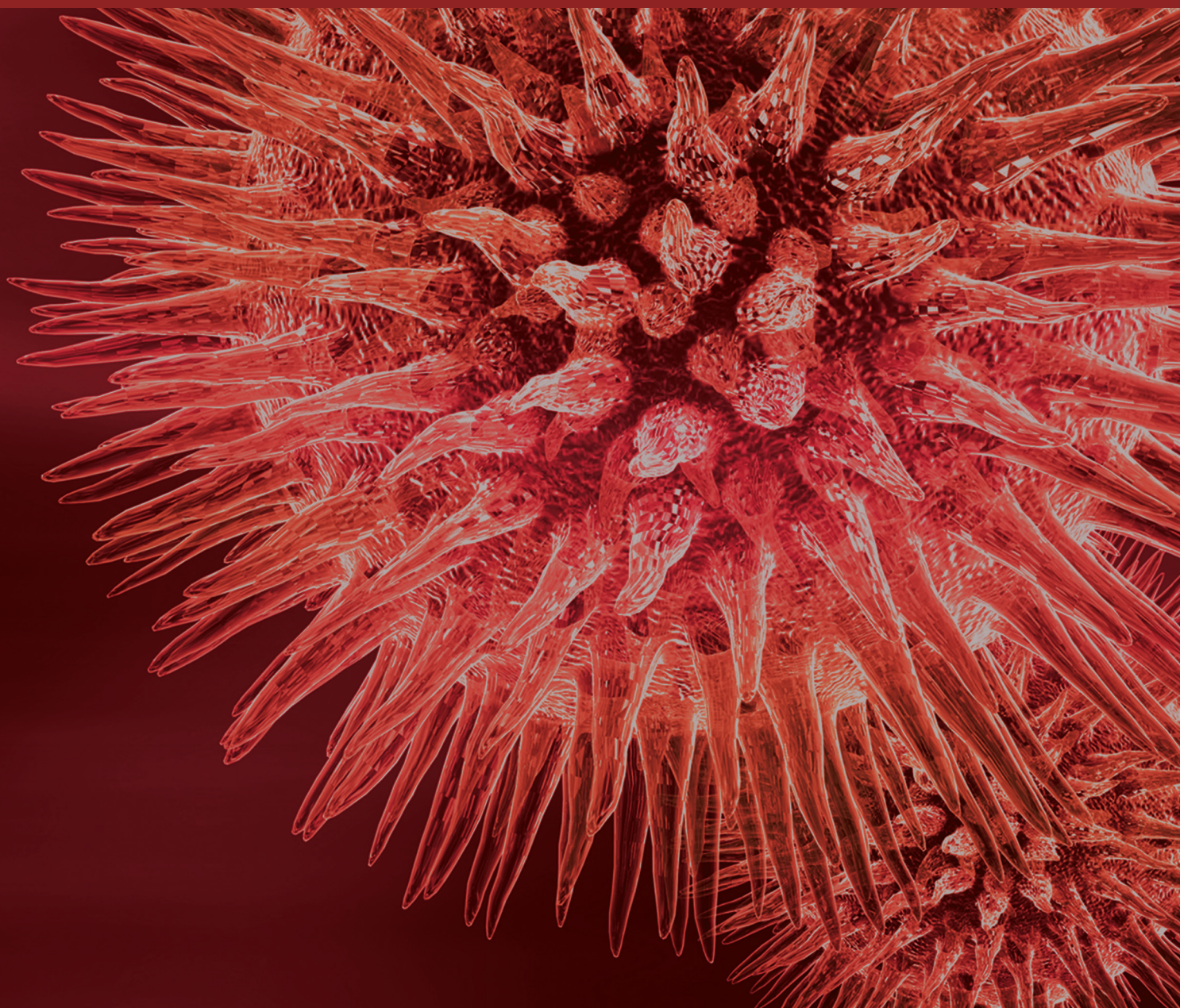


Quantitative Analysis of Musculoskeletal Ultrasound: Techniques and Clinical Applications

Guest Editors: Qing Wang, Qing-Hua Huang, John T. W. Yeow, Mark R. Pickering,
and Simo Saarakkala





Quantitative Analysis of Musculoskeletal Ultrasound: Techniques and Clinical Applications

BioMed Research International

Quantitative Analysis of Musculoskeletal Ultrasound: Techniques and Clinical Applications

Guest Editors: Qing Wang, Qing-Hua Huang, John T. W. Yeow,
Mark R. Pickering, and Simo Saarakkala



Copyright © 2017 Hindawi Publishing Corporation. All rights reserved.

This is a special issue published in “BioMed Research International.” All articles are open access articles distributed under the Creative Commons Attribution License, which permits unrestricted use, distribution, and reproduction in any medium, provided the original work is properly cited.

Contents

Quantitative Analysis of Musculoskeletal Ultrasound: Techniques and Clinical Applications

Qing Wang, Qing-Hua Huang, John T. W. Yeow, Mark R. Pickering, and Simo Saarakkala
Volume 2017, Article ID 9694316, 2 pages

A Novel Segmentation Approach Combining Region- and Edge-Based Information for Ultrasound Images

Yaoshong Luo, Longzhong Liu, Qinghua Huang, and Xuelong Li
Volume 2017, Article ID 9157341, 18 pages

Age and Sex Effects on the Active Stiffness of Vastus Intermedius under Isometric Contraction

Cong-Zhi Wang, Jing-Yi Guo, Tian-Jie Li, Yongjin Zhou, Wenxiu Shi, and Yong-Ping Zheng
Volume 2017, Article ID 9469548, 16 pages

Ultrasonography-Guided Lumbar Periradicular Injections for Unilateral Radicular Pain

Qing Wan, Shaoling Wu, Xiao Li, Caina Lin, Songjian Ke, Cuicui Liu, Wenjun Xin, and Chao Ma
Volume 2017, Article ID 8784149, 4 pages

A Review on Real-Time 3D Ultrasound Imaging Technology

Qinghua Huang and Zhaozheng Zeng
Volume 2017, Article ID 6027029, 20 pages

Semianalytical Solution for the Deformation of an Elastic Layer under an Axisymmetrically Distributed Power-Form Load: Application to Fluid-Jet-Induced Indentation of Biological Soft Tissues

Minhua Lu, Shuai Huang, Xianglong Yang, Lei Yang, and Rui Mao
Volume 2017, Article ID 9842037, 10 pages

Ultrasound-Guided versus Fluoroscopy-Guided Deep Cervical Plexus Block for the Treatment of Cervicogenic Headache

Qing Wan, Haiyun Yang, Xiao Li, Caina Lin, Songjian Ke, Shaoling Wu, and Chao Ma
Volume 2017, Article ID 4654803, 6 pages

Semiquantitative Evaluation of Extrasynovial Soft Tissue Inflammation in the Shoulders of Patients with Polymyalgia Rheumatica and Elderly-Onset Rheumatoid Arthritis by Power Doppler Ultrasound

Takeshi Suzuki, Ryochi Yoshida, Akiko Okamoto, and Yu Seri
Volume 2017, Article ID 4272560, 11 pages

Ultrasonographic Validation of Anatomical Landmarks for Localization of the Tendon of the Long Head of Biceps Brachii

Saiyun Hou, John Harrell, and Sheng Li
Volume 2017, Article ID 1925104, 5 pages

Ultrasonic Measurement of Dynamic Muscle Behavior for Poststroke Hemiparetic Gait

Xin Chen, Xudong Zhang, Wenxiu Shi, Jun Wang, Yun Xiang, Yongjin Zhou, and Wan-Zhang Yang
Volume 2017, Article ID 8208764, 8 pages

Early Detection of Tibial Cartilage Degradation and Cancellous Bone Loss in an Ovariectomized Rat Model

Yinong Wang, Zhiwei Liu, Qing Wang, Qianjin Feng, and Wufan Chen
Volume 2017, Article ID 9654056, 7 pages

Transverse and Oblique Long Bone Fracture Evaluation by Low Order Ultrasonic Guided Waves: A Simulation Study

Ying Li, Dan Liu, Kailiang Xu, Dean Ta, Lawrence H. Le, and Weiqi Wang
Volume 2017, Article ID 3083141, 10 pages

Combined Ultrasound Imaging and Biomechanical Modeling to Estimate Triceps Brachii Musculotendon Changes in Stroke Survivors

Le Li and Raymond Kai-yu Tong
Volume 2016, Article ID 5275768, 11 pages

Editorial

Quantitative Analysis of Musculoskeletal Ultrasound: Techniques and Clinical Applications

**Qing Wang,¹ Qing-Hua Huang,² John T. W. Yeow,³
Mark R. Pickering,⁴ and Simo Saarakkala⁵**

¹*Institute of Medical Information, School of Biomedical Engineering, Southern Medical University, Guangzhou, China*

²*South China University of Technology, Guangzhou, China*

³*University of Waterloo, Waterloo, ON, Canada*

⁴*The University of New South Wales, Canberra, ACT, Australia*

⁵*University of Oulu, Oulu, Finland*

Correspondence should be addressed to Qing Wang; wq8740@smu.edu.cn

Received 5 April 2017; Accepted 10 April 2017; Published 30 April 2017

Copyright © 2017 Qing Wang et al. This is an open access article distributed under the Creative Commons Attribution License, which permits unrestricted use, distribution, and reproduction in any medium, provided the original work is properly cited.

Musculoskeletal ultrasound is one of a number of musculoskeletal imaging modalities. It can be defined as an ultrasound imaging technique for the diagnosis and treatment of patients with musculoskeletal disorders. In comparison with advanced imaging modalities such as CT and MRI, advantages of ultrasound include the readily available bedside ultrasound equipment, the relatively low cost of the exam procedure, the capacity for dynamic evaluation of patients, and the use of nonionizing radiation. Therefore, musculoskeletal ultrasound has been widely adopted for many clinical applications. Recent advances in musculoskeletal ultrasound have provided physicians with valuable information in application areas such as sports medicine, osteoarthritis, osteoporosis, musculoskeletal pain, and rehabilitation. The new findings in these areas have also inspired novel signal and image processing techniques that are developed to facilitate many potential new clinical applications. Recently developed quantitative ultrasound techniques are able to provide quantitative assessment of the structure and function of musculoskeletal tissues. In addition, ultrasound biomicroscopy imaging with high-frequency probes is able to resolve finer imaging details of musculoskeletal tissues. In this issue readers will find 12 high-quality, peer-reviewed articles that provide researchers from diverse backgrounds such as biomedical engineering, medical ultrasound, rehabilitation, and computational sciences with the state-of-the-art knowledge of this emerging interdisciplinary research area.

In the review paper “A Review on Real-Time 3D Ultrasound Imaging Technology” by the special issue editor Q. Huang and Z. Zeng, a comprehensive review on traditionally designed 3D ultrasound techniques as well as the most advanced real-time 3D imaging using parallel computing hardware and methods is provided. It summarizes the pros and cons of different data acquisition protocols, discusses the algorithms of volume reconstruction, and introduces the clinical applications including musculoskeletal examinations.

Ultrasound images of the musculoskeletal system provide visible information of the structure of musculoskeletal tissues and organs such as muscles, tendons, ligaments, joints, and soft tissue. Ultrasonography is a useful tool to guide the treatment of patients with musculoskeletal disorders. Ultrasound-guided techniques help physicians accurately inject treatment drugs into the target tissues to satisfy the requirements of a successful and safe therapy. In this special issue, two papers introduce ultrasound-guided techniques that are applied in the treatment of musculoskeletal pain. The paper “Ultrasound-Guided versus Fluoroscopy-Guided Deep Cervical Plexus Block for the Treatment of Cervicogenic Headache” by Q. Wan et al. presents an ultrasound-guided approach to treating cervicogenic headache through injection in deep cervical plexus block. Q. Wan et al. also introduce an application of ultrasonography to guide the lumbar periradicular injection for patients with unilateral lower lumbar

radicular pain in their paper entitled “Ultrasonography-Guided Lumbar Periradicular Injections for Unilateral Radicular Pain.” The ultrasound-guided approach is shown to be a potentially promising method for the pain treatment due to its convenience and efficacy.

Rehabilitation for musculoskeletal disorders needs accurate diagnosis and follow-up evaluation of the outcomes during a relative long-term physical exercise therapy procedure. In this special issue, there are four papers that report the applications of musculoskeletal ultrasound in rehabilitation. In “Ultrasonographic Validation of Anatomical Landmarks for Localization of the Tendon of the Long Head of Biceps Brachii,” S. Hou et al. introduce two anatomical landmarks for localization of biceps tendon groove and validate the localization with ultrasonographic measurement. The reliable location of treatment and monitoring plays an important role in therapy and diagnosis for patients with musculoskeletal disorders. L. Li and R. K. Tong introduce a combined method of ultrasound imaging and biomechanical modeling for post-stroke muscular evaluation in their paper entitled “Combined Ultrasound Imaging and Biomechanical Modeling to Estimate Triceps Brachii Musculotendon Changes in Stroke Survivors.” Based on the ultrasonic parameters, the subject-specific biomechanical model could predict the changes of musculotendon properties for patients after stroke. In the paper “Ultrasonic Measurement of Dynamic Muscle Behavior for Poststroke Hemiparetic Gait” by X. Chen et al., the authors developed a synchronized system for simultaneously collecting ultrasonography signals, EMG, and joint angle to dynamically analyze the functional and morphological changes during muscle contraction. Ultrasonography can be deemed as an alternative method for examination of the morphological changes for stroke patients. C.-Z. Wang et al. describe a novel ultrasound technique called “vibroultrasound” that achieves the active stiffness of the muscles under isometric contraction. Their paper entitled “Age and Sex Effects on the Active Stiffness of Vastus Intermedius under Isometric Contraction” investigates the relationship between muscle stiffness and the contraction intensity and provides insight into the age and sex bias in musculoskeletal studies.

Quantitative ultrasound, a recently developed promising method, has been applied to quantitatively assess the structure and function of musculoskeletal tissues. This special issue presents three quantitative ultrasound studies for evaluation of the tissues in musculoskeletal diseases. The paper “Early Detection of Tibial Cartilage Degradation and Cancellous Bone Loss in an Ovariectomized Rat Model” by Y. Wang et al. proposes a quantitative high-frequency ultrasound approach for the early detection of rat tibial cartilage degradation. This is a promising method to detect the early degradation of articular cartilage induced by estrogen reduction in female osteoarthritis. T. Suzuki et al. present a semiquantitative evaluation of polymyalgia rheumatica and elderly-onset rheumatoid arthritis by power Doppler ultrasound in their paper entitled “Semiquantitative Evaluation of Extrasynovial Soft Tissue Inflammation in the Shoulders of Patients with Polymyalgia Rheumatica and Elderly-Onset Rheumatoid Arthritis by Power Doppler Ultrasound.” It is indicated that power Doppler ultrasound can be a reliable

tool to semiquantitatively evaluate the inflammation of soft tissues. The paper “Transverse and Oblique Long Bone Fracture Evaluation by Low Order Ultrasonic Guided Waves: A Simulation Study” by Y. Li et al. focuses on using ultrasound-guided waves to evaluate bone fracture and monitor its healing. This simulated study shows that the ultrasound-guided waves have good potential for evaluation of bone fractures and their healing monitoring.

There are two papers that report novel techniques of signal and image processing to extract and analyze the target tissues in this special issue. The paper “A Novel Segmentation Approach Combining Region- and Edge-Based Information for Ultrasound Images” by Y. Luo et al. demonstrates a new segmentation algorithm based on an improved machine learning strategy for extracting lesions from ultrasound images, for example, the breast and musculoskeletal ultrasound images. With accurate extraction of the lesion region in ultrasound images, computer aided diagnosis, which is of great help in routine musculoskeletal examinations in a clinical setting, can be easily conducted. The paper “Semianalytical Solution for the Deformation of an Elastic Layer under an Axisymmetrically Distributed Power-Form Load: Application to Fluid-Jet-Induced Indentation of Biological Soft Tissues” by M. Lu et al. presents an ultrasound indentation method for analyzing the biomechanical property of biological soft tissues. The clearer analysis of the biomechanical properties provided by this technique would be of great help in better understanding the function of the musculoskeletal tissues.

In summary, the 12 papers in the special issue report not only new clinical studies of musculoskeletal ultrasound but also recently developed ultrasound techniques for musculoskeletal tissue characterizations. We hope that this special issue will help to promote further development of musculoskeletal ultrasound methodologies for various clinical applications. Improvement and advances in musculoskeletal ultrasound may lead to better performance outcomes in diagnosis and treatment of patients with musculoskeletal disorders. Musculoskeletal ultrasound provides quantitative evaluation and dynamic monitoring and thus reduces the cost, duration, and overall impact of musculoskeletal diseases.

Acknowledgments

We would like to express our deepest gratitude to many reviewers, whose professional comments guaranteed the high quality of the selected papers. In addition, we also would like to express our appreciation to the editorial board members for their help and support throughout the preparation of this special issue.

*Qing Wang
Qing-Hua Huang
John T. W. Yeow
Mark R. Pickering
Simo Saarakkala*

Research Article

A Novel Segmentation Approach Combining Region- and Edge-Based Information for Ultrasound Images

Yaozhong Luo,¹ Longzhong Liu,² Qinghua Huang,^{1,3} and Xuelong Li⁴

¹School of Electronic and Information Engineering, South China University of Technology, Guangzhou, China

²Department of Ultrasound, The Cancer Center of Sun Yat-sen University, State Key Laboratory of Oncology in South China, Collaborative Innovation Center for Cancer Medicine, Guangdong, China

³College of Information Engineering, Shenzhen University, Shenzhen 518060, China

⁴Center for OPTical IMagery Analysis and Learning (OPTIMAL), State Key Laboratory of Transient Optics and Photonics, Xi'an Institute of Optics and Precision Mechanics, Chinese Academy of Sciences, Xi'an, Shaanxi 710119, China

Correspondence should be addressed to Qinghua Huang; qhhuang@scut.edu.cn

Received 9 September 2016; Revised 21 January 2017; Accepted 14 March 2017; Published 27 April 2017

Academic Editor: Cristiana Corsi

Copyright © 2017 Yaozhong Luo et al. This is an open access article distributed under the Creative Commons Attribution License, which permits unrestricted use, distribution, and reproduction in any medium, provided the original work is properly cited.

Ultrasound imaging has become one of the most popular medical imaging modalities with numerous diagnostic applications. However, ultrasound (US) image segmentation, which is the essential process for further analysis, is a challenging task due to the poor image quality. In this paper, we propose a new segmentation scheme to combine both region- and edge-based information into the robust graph-based (RGB) segmentation method. The only interaction required is to select two diagonal points to determine a region of interest (ROI) on the original image. The ROI image is smoothed by a bilateral filter and then contrast-enhanced by histogram equalization. Then, the enhanced image is filtered by pyramid mean shift to improve homogeneity. With the optimization of particle swarm optimization (PSO) algorithm, the RGB segmentation method is performed to segment the filtered image. The segmentation results of our method have been compared with the corresponding results obtained by three existing approaches, and four metrics have been used to measure the segmentation performance. The experimental results show that the method achieves the best overall performance and gets the lowest ARE (10.77%), the second highest TPVF (85.34%), and the second lowest FPVF (4.48%).

1. Introduction

Ultrasound (US) imaging is one of the most popular medical imaging modalities with numerous diagnostic applications due to the following merits: no radiation, faster imaging, higher sensitivity and accuracy, and lower cost compared to other imaging modalities, such as computed tomography (CT) or magnetic resonance imaging (MRI) [1–6]. However, sonography is operator-dependent, and reading US images requires well-trained and experienced radiologists. To reduce the interobserver variation among different clinicians and help them generate more reliable and accurate diagnostic conclusions, computer-aided diagnosis (CAD) has been proposed [3, 7, 8]. Generally, the CAD system based on the US image involves the following four steps: preprocessing, segmentation, feature extraction and selection, and

classification [9, 10]. Among these four procedures, image segmentation which separates the lesion region from the background is the key to the subsequent processing and determines the quality of the final analysis. In the previous clinical practice, the segmentation task is generally performed by manual tracing, which is laborious, time-consuming, and skill- and experience-dependent. Consequently, reliable and automatic segmentation methods are preferred to segment the ROI from the US image, to improve the automation and robustness of the CAD system. However, accurate and automatic US image segmentation remains a challenging task [11–13] due to various US artifacts, including high speckle noise [14], low signal-to-noise ratio, and intensity inhomogeneity [15].

In the last decade, a large number of segmentation methods have been developed for US images, for example,

thresholding-based methods [16–18], clustering-based methods [19–23], watershed-based methods [24–27], graph-based methods [28–35], and active contour models [36–42]. Thresholding is one of the frequently used segmentation techniques for the monochrome image. Yap et al. [18] adopted the thresholding segmentation to separate the lesion region from the background before detecting the initial boundary via edge detection. Clustering is a classification technique and has been successfully applied to image segmentation based on similarity between image regions or pixels. Isa et al. [19] used the moving k -means clustering to automatically select the seed and proposed a modified seed based region growing algorithm to detect the edge. Shan et al. [20] used a novel neurosophic clustering approach to detect the lesion boundary. Moon et al. [22] used the fuzzy C-means (FCM) clustering to extract the tumor candidates in their CAD system. The watershed transformation which is frequently used in the segmentation of grey scale images considers the gradient magnitude of an image as a topographic surface. Chen et al. [24] employed the two-pass watershed transformations to generate the cells and proposed a region-based approach called cell-competition algorithm to simultaneously segment multiple objects in a sonogram. L. Zhang and M. Zhang [26] used an extended fuzzy watershed method to segment US images fully automatically. The experiments showed that the proposed method could get good results on blurry US images.

In the last few years, graph-based segmentation has become a research hotspot due to the simple structure and solid theories. In graph-based segmentation, the image is modeled as a weighted, undirected graph. Zhang et al. [28] applied the discriminative graph-cut approach to segmenting tumors after discrimination between tumors and the background via a trained classifier. In 2014, Zhou et al. [29] proposed a novel US image segmentation method based on mean shift and graph cuts (MSGC). It uses mean shift filter to improve the homogeneity and applies graph-cut method, whose energy function combines region- and edge-based information to segment US images. The result showed that the method is rapid and efficient. Huang et al. [30] designed a novel comparison criterion for pairwise subregions which takes local statistics into account to make their method more robust to noises, and hence it was named as robust graph-based (RGB) segmentation method. The experimental results showed that accurate segmentation results can be obtained by this method. However, two significant parameters determining the segmentation result should be set empirically, and for different images they need to be adjusted by repeated tests to obtain good segmentation results. In 2013, Huang et al. [31] proposed an improvement method for RGB by using PSO algorithm to optimize the two significant parameters automatically. The between-class variance, which denotes the difference between the reference region and its adjacent regions, was introduced as the objective function and the method was named as parameter-automatically optimized robust graph-based (PAORGB) segmentation.

The active contour model (ACM), more widely known as snake, is another very popular segmentation method for US images and has been massively used as an edge-based segmentation method. This approach attempts to minimize

the energy associated with the initial contour as the sum of the internal and external energies. During the deformation process, the force is calculated from the internal energy and external energy. The internal energy derived from the contour model is used to control the shape and regularity of the contour, and the external energy derived from the image feature is used to extract the contour of the desired object. A 3D snake technique was used by Chang et al. [36] to obtain the tumor contour for the pre- and postoperative malignant tumor excision. Jumaat et al. [37] applied the Balloon Snake to segment the mass in the US image taken from Malaysian population. To overcome the curvature and topology problems in the ACM, level set has been employed to improve the US image segmentation. Sarti et al. [38] used a level set formulation to search the minimal value of ACM, and the segmentation results showed that their model is efficient and flexible. Gao et al. [40] combined an edge stopping term and an improved gradient vector flow snake in the level set framework, to robustly cope with noise and to accurately extract the low contrast and/or concave ultrasonic tumor boundaries. Liu et al. [39] proposed a novel probability density difference-based active contour method for ultrasound image segmentation. In 2010, Li et al. [43] proposed the new level set evolution model Distance Regularized Level Set Evolution (DRLSE) in which it adds a distance regularization term over traditional level set evolution to eliminate the need for reinitialization in evolution process and improve the efficiency. Some researchers combined texture information with other methods for US images segmentation [44–47]. In 2016, Lang et al. [44] used a multiscale texture identifier integrated in a level set framework to capture the spiculated boundary and showed improved segmentation result.

However, most of the above methods are purely region-based or edge-based. For region-based methods, they use homogeneity statistics and low-level image features like intensity, texture, and histogram to assign pixels to objects. Two pixels would be assigned to the same object if they are similar in value and connected to each other in some sense. The problem of applying these approaches to US images is that, without considering any shape information, they would classify pixels within the acoustic shadow as belonging to the tumor, while posterior acoustic shadowing is a common artifact in US images [48, 49]. For edge-based methods (ACM), they are used to handle only the ROI, not the entire image. Although they can obtain the precise contour of the desired object, they are sensitive to noise and heavily rely on the suitable initial contour which is very difficult to generate properly. Also, the deformation procedure is very time-consuming. Therefore, segmentation approaches which integrate region-based techniques and edge-based techniques have been proposed to obtain accurate segmentation results for US images [50–55]. Chang et al. [50] introduced the concepts of 3D stick, 3D morphologic process, and 3D ACM. The 3D stick is used to reduce the speckle noise and enhance the edge information in 3D US images. Then, the 3D morphologic process is used to obtain the initial contour of the tumor for the 3D ACM. Huang and Chen [51, 52] utilized the watershed transform and ACM to overcome the natural properties of US images

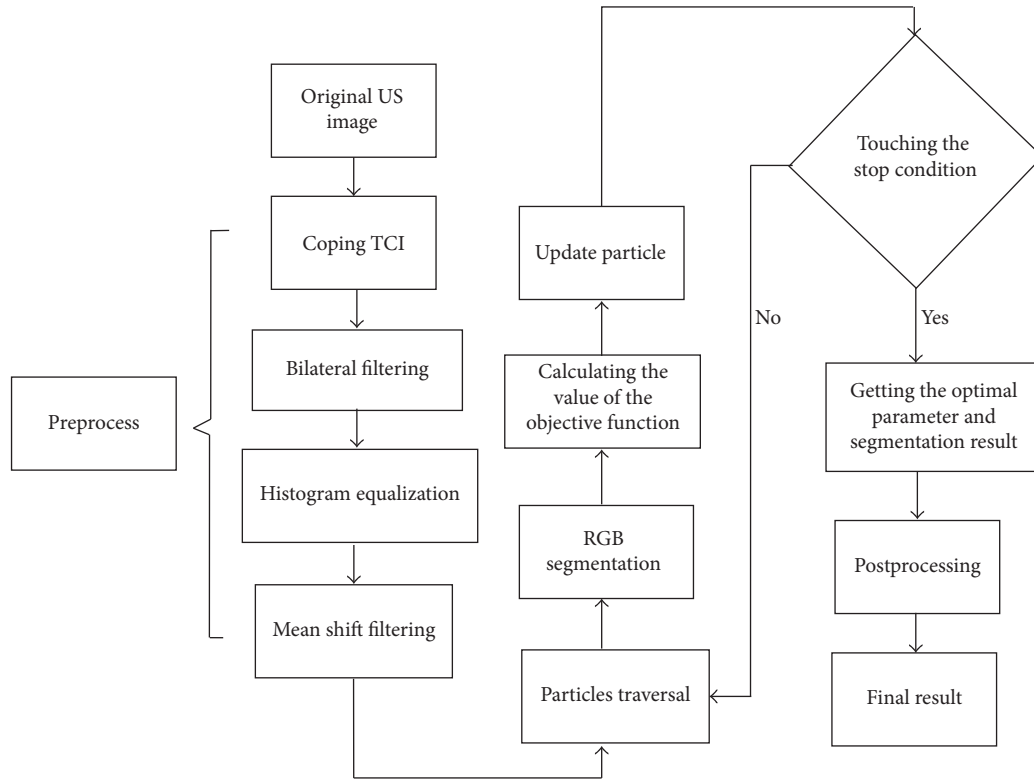


FIGURE 1: Flowchart of the proposed approach.

(i.e., speckle, noise, and tissue-related textures), to segment tumors precisely. In their methods, the watershed transform is performed as the automatic initial contouring procedure for the ACM. Then, the ACM automatically determines the exquisite contour of the tumor. Wang et al. [55] presented a multiscale framework for US image segmentation based on speckle reducing anisotropic diffusion and geodesic active contour. In general, the region-based technique is used to generate the initial contour for the edge-based technique. The experimental results of these approaches indicate that accurate segmentation results can be obtained by combining region-based and edge-based information of the US image.

In this paper, we propose a novel segmentation scheme for US images based on the RGB segmentation method [30] and particle swarm optimization (PSO) algorithm [56, 57]. In this scheme, the PSO is used to optimally set the two significant parameters determining the segmentation result automatically. To combine region-based and edge-based information, we consider the optimization as a multiobjective problem comparing with PAORGB. We use multiobjective optimization method (maximizing the difference between target and background, improving the uniformity within the target region, and considering the edge gradient) to improve the segmentation performance. We take the uniformity of the region and the information of the edge as the objective contents in the process of optimization. First, one rectangle is manually selected to determine the ROI on the original image. However, because of the low contrast and speckle

noises of US images, the ROI image is filtered by a bilateral filter and contrast-enhanced by histogram equalization. Next, pyramid mean shift is executed on the enhanced image to improve homogeneity. A novel objective function consisting of three parts corresponding to region-based and edge-based information is designed in the PSO. With the optimization of PSO, the RGB segmentation method is performed to segment the ROI image. Finally, the segmented image is processed by morphological opening and closing to refine the tumor contour.

This paper is organized as follows. Section 2 introduces the proposed method in detail. Next, the experimental results and comparisons among different methods are presented in Section 3. Finally, we provide some discussion and draw the conclusion in Section 4.

2. Methods

In this paper, our method is called multi-objectively optimized robust graph-based (MOORGB) segmentation method, which utilizes PSO algorithm to optimize the two key parameters of RGB segmentation method. In the MOORGB, a multiobjective optimization function which combines region-based and edge-based information is designed in the PSO to optimize the RGB. The flowchart of the proposed approach is shown in Figure 1. In the rest of this section, we introduce each step in the proposed approach in detail.

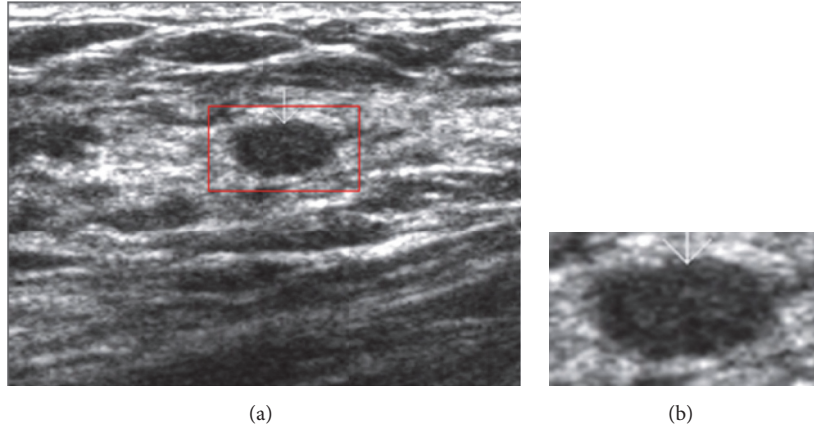


FIGURE 2: Example of extracting a TCI: (a) the original image and (b) the TCI image.

2.1. Preprocessing

2.1.1. Cropping Tumor Centered ROI. According to [11] a good segmentation method for clinical US images should have taken advantage of a priori knowledge to improve the segmentation result due to the relatively low quality. In addition, it is hard to describe the segmentation result quantitatively without any a priori knowledge; therefore, it is difficult to design objective function(s) without any a priori knowledge. Therefore, we employ the a priori knowledge used in [31], namely, asking the operator to roughly extract a relatively small rectangular ROI (in which the focus of interest is fully contained and located in the central part) from the US image. In this way, interferences from other unrelated regions can be reduced as much as possible, making the segmentation easier and more efficient. Besides, it gives useful a priori knowledge for design of objective function(s). Such a ROI is called tumor centered image (TCI) in this paper, and Figure 2 shows how a TCI is extracted from a US image.

2.1.2. Bilateral Filtering. Because of diverse interferences (e.g., attenuation, speckle, shadow, and signal dropout) in US images, speckle reduction is necessary to improving the quality of US images. Bilateral filter [58] which has proven to be an efficient and effective method for speckle reduction is adopted in the MOORGB.

2.1.3. Histogram Equalization. To improve the contrast of US images, histogram equalization is conducted to enhance the filtered TCI. Histogram equalization maps one distribution (the given histogram of intensity values in the filtered TCI) to another distribution (a wider and uniform distribution of intensity values). The classical histogram equalization method [59] is used in the MOORGB.

2.1.4. Mean Shift Filtering. After contrast enhancement, we improve the homogeneity by performing mean shift filtering. Mean shift filtering is based on mean shift clustering over grayscale and can well improve the homogeneity of US images and suppress the speckle noise and tissue-related

textures [60]. Figure 3 shows the preprocessing results of the image.

2.2. RGB Segmentation Method. Given an image which is initially regarded as a graph, the RGB method [30] aims to merge spatially neighboring pixels with similar intensities into a minimal spanning tree (MST), which corresponds to a subgraph (i.e., a subregion in the image). The image is therefore divided into several subregions (i.e., a forest of MSTs). Obviously, the step for merging pixels into a MST is the key, determining the final segmentation results. A novel pairwise region comparison predicate was proposed in the RGB to determine whether or not a boundary between two subgraphs should be eliminated. Given a graph $G = (V, E)$, the resulting predicate $D(C_1, C_2)$ which compares intersubgraph differences with within-subgraph differences is formulated as follows [30]:

$$D(C_1, C_2) = \begin{cases} \text{false,} & \text{if Dif}(C_1, C_2) > \text{MInt}(C_1, C_2) \\ \text{true,} & \text{other} \end{cases} \quad (1)$$

$$\text{Dif}(C_1, C_2) = |\mu(C_1) - \mu(C_2)| \quad (2)$$

$$\text{MInt}(C_1, C_2) = \min(\sigma(C_1) + \tau(C_1), \sigma(C_2) + \tau(C_2)) \quad (3)$$

$$\tau(C) = \frac{k}{|C|} \cdot \left(1 + \frac{1}{\alpha \cdot \beta}\right), \quad \beta = \frac{\mu(C)}{\sigma(C)}, \quad (4)$$

where $\text{Dif}(C_1, C_2)$ is the difference between two subgraphs, C_1 and $C_2 \in V$, $\text{MInt}(C_1, C_2)$ represents the smallest internal difference of C_1 and C_2 , $\mu(C)$ denotes the average intensity of C , $\sigma(C)$ is the standard deviation of C , and $\tau(C)$ is a threshold function of C while α and k are positive parameters. When k increases, τ increases as well and the regions merge more easily. On the contrary, when α increases, τ decreases and hence the regions are merged less easily.

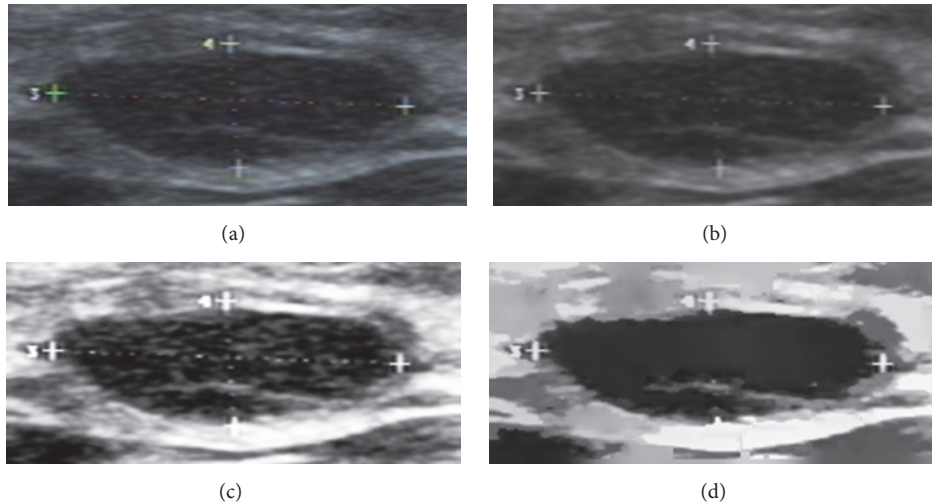


FIGURE 3: Example of preprocessing, (a) the TCI image, (b) the image after the bilateral filtering, (c) the image after histogram equalization, and (d) the image after mean shift filtering.

Based on the pairwise region comparison predicate, the general procedures of segmenting an image are as follows.

Step 1. Construct a graph $G = (V, E)$ for the US image to be segmented. In G , each pixel corresponds to a vertex and each edge connects two spatially neighboring vertices. The edge weight is defined by the absolute intensity difference between two adjacent pixels. Initially, each vertex is regarded as a subgraph and all edges constituting the edge set E are invalid.

Step 2. Sort the edges in E in nondescending order according to the edge weight, and set $q = 1$.

Step 3. Pick the q th edge in the sorted E . If the q th edge is an invalid edge (connecting two different subgraphs) and the boundary between these two subgraphs can be eliminated according to the pairwise region comparison predicate as mathematically expressed in (1)–(4); then merge these two subgraphs into a larger subgraph and set this edge valid. Let $q = q + 1$.

Step 4. Repeat Step 3 until all edges in E are traversed.

When all edges are traversed, a forest including a number of MSTs can be obtained. Each MST corresponds to a subregion in the image. However, the selection of α and k in (4) can significantly influence RGB's segmentation results [30]. As shown in Figure 4, it can be seen that inappropriate selections of α and k can lead to under- or oversegmentation. In [30], two significant parameters in RGB segmentation algorithm were empirically selected and usually manually assigned by testing repeatedly to achieve acceptable results. It cannot be fixed for real clinical application because good selections of α and k may be quite different for different images due to the diversity of US images.

Therefore, the PAORGB was proposed to optimize these two parameters and to achieve a good selection of them

automatically for each US image [31]. However, only region-based information and only one optimization goal (maximizing the difference between target and background) have been used. Although the PAORGB can obtain good segmentation results for some US images, its performance is not adequately stable. Therefore, we propose the MOORGB which uses multiobjective optimization method (maximizing the difference between target and background, improving the uniformity within the target region, considering the edge gradient) to improve the segmentation performance. The method makes comprehensive consideration of edge-based and region-based information.

2.3. PSO Optimization of Parameters. PSO algorithm is an evolutionary computation technique mimicking the behavior of flying birds and their means of information exchange [56, 57]. In PSO, each particle represents a potential solution, and the particle swarm is initialized with a population of random/uniform individuals in the search space. PSO searches the optimal solution by updating positions of particles in an evolutionary manner.

Suppose that there are n_p solutions, each of which corresponds to a particle, and the position (i.e., the solution) and velocity of the i th particle ($i = 1, \dots, n_p$) are represented by two m -dimensional ($m = 2$ in our study) vectors (i.e., $x_i = (x_{i1}, x_{i2}, \dots, x_{im})$ and $v_i = (v_{i1}, v_{i2}, \dots, v_{im})$, resp.). Position x is a vector and in our method, $x = (k, \alpha)$. Velocity v means the varied distance of the position at every iteration. c_1 , r_1 , c_2 , r_2 and w are scalars. According to specific issues, one or more objective functions are used to evaluate fitness of each particle, and then the comparison criterion is employed to obtain superior particles. Assume that $p_i = (p_{i1}, p_{i2}, \dots, p_{im})$ is the best position visited until the moment of the i th particle during the update process, and the global best position of the whole particle swarm obtained so far is indicated as $p_g = (p_{g1}, p_{g2}, \dots, p_{gm})$. At each generation, each particle updates its velocity and position according to

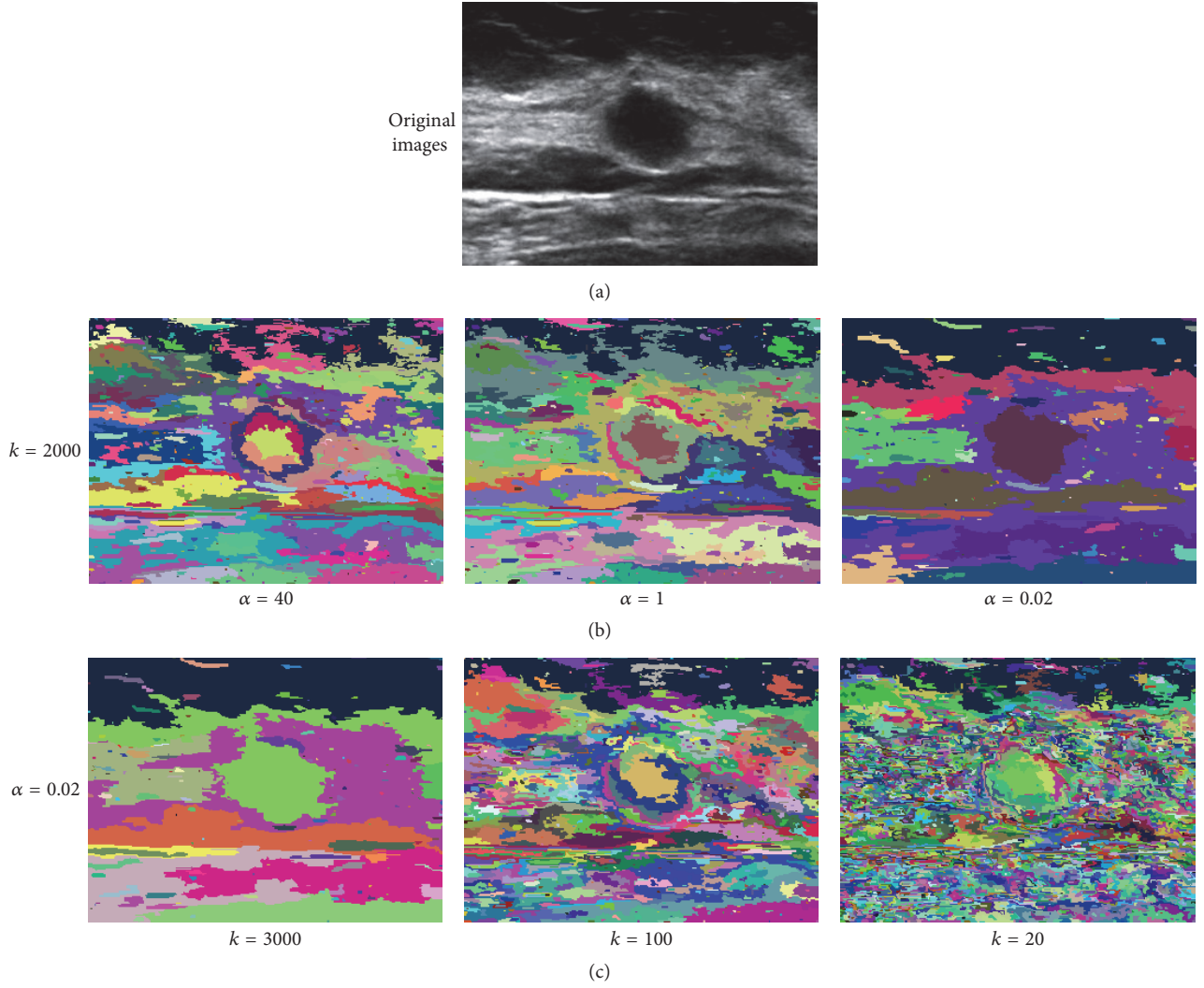


FIGURE 4: Influence of α and k : the image of (a) is the original image, the image of (b) shows the segmentation result with different α , and (c) shows the segmentation result with different k .

the following equations after p_i and p_g are acquired through fitness evaluation and the comparison criterion [56]:

$$v_i^{t+1} = wv_i^t + c_1r_1(p_i^t - x_i^t) + c_2r_2(p_g^t - x_i^t) \quad (5)$$

$$x_i^{t+1} = x_i^t + v_i^{t+1} \quad (6)$$

$$w^t = w_{\max} - \frac{(w_{\max} - w_{\min})}{T_{\max}} * t, \quad (7)$$

where t is the generation number, T_{\max} is the maximum iteration, w^t is the value of the t th iteration, w is the inertia weight, c_1 and c_2 are positive parameters known as acceleration coefficients, determining the relative influence of cognition and social components, and r_1 and r_2 are independently uniformly distributed random variables within the range of (0, 1). The value of w describes the influence of historical velocity. The method with higher w will have stronger global search ability and the method with smaller w will have stronger local search ability. At the beginning of the optimization

process, we initially set w to a large value in order to make better global exploration and gradually decrease it to find optimal or approximately optimal solutions and thus reduce the number of the iterations. Hence we let w decrease linearly from 1 towards 0.2, as shown in (7). We set $w_{\max} = 1$, $w_{\min} = 0.2$, and $T_{\max} = 200$. In (5), wv_i^t represents the influence of the previous velocity on the current one, and $c_1r_1(p_i^t - x_i^t)$ represents the personal experience while $c_2r_2(p_g^t - x_i^t)$ represents the collaborative effect of particles, which pulls particles to the global best solution the whole particle swarm has found so far. As suggested in [41], we set $c_1 = 0.5$ and $c_2 = 0.5$ and make personal experience and collaborative effect of particles play the same important role in optimization as shown in Figure 5.

To conclude, at each generation, the velocity and position of each particle are updated according to (5), and its position is updated by (6). At each time, any better position is stored for the next generation. Then, each particle adjusts its position based on its own “flying” experience and the experience of its companions, which means that if one particle arrives at a

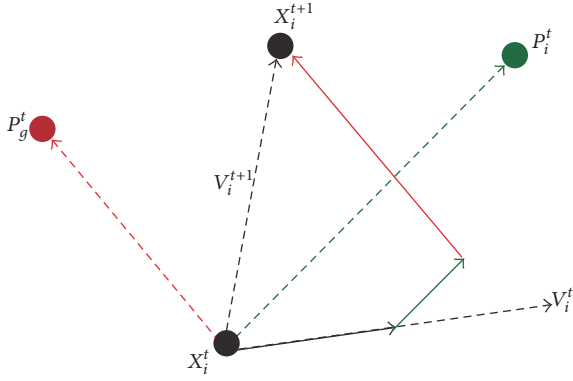


FIGURE 5: Update of the particle.

new promising position, all other particles then move closer to it. This process is repeated until a satisfactory solution is found or a predefined number of iterative generations is met.

The general procedure is summarized as follows.

Step 1. Properly set the size of particle swarm and randomly/uniformly initialize them according to the search space. In this study, the size of particle swarm is $n_p = 200$, and the particles are uniformly initialized. According to the work in [30], k varies from 100 to 4000 and α varies from 0.001 to 4.000, which form the search space.

Step 2. Traverse all particles: in each traversal (i.e., at each generation), each particle is evaluated through the objective function, and p_i and p_g are acquired according to the comparison criterion.

Step 3. Update the velocity and position of each particle according to (5) and (6). As suggested in [57], we set $c_1 = 0.5$ and $c_2 = 0.5$, and let w decrease linearly from 1 towards 0.2.

Step 4. Repeat Steps 2 and 3 until all particles converge to the predefined extent or the iterative number arrives at the predefined maximum. The predefined extent in this study is that p_g does not change for four iterations, and the maximum iteration is set to $N = 200$ empirically.

2.4. The Proposed Objective Function in the PSO. At each time, we use RGB to segment the TCI according to the information (i.e., α and k) of one particle. According to the a priori knowledge that the focus of interest is located in the central part of TCI, the central subregion with the central pixel of TCI is the possible tumor region. This central subregion is defined as the reference region, which varies with the setting of α and k , and the reference region is the expected tumor region when α and k are optimally set. Figure 6 gives an example of reference region (the original image is shown in Figure 2).

In MOORGB, a novel objective function consisting of three parts corresponding to region-based and edge-based information is adopted. Based on the above a priori knowledge, these three parts, that is, between-class variance, within-class variance, and average gradient, are defined as

follows. Compared with PAORGB, we add two objective functions, within-class variance and average gradient. It is not enough to optimize parameters just relying on edge information or region information for segmentation. We take the uniformity of the region and the information of the edge as the objective contents in the optimization process.

2.4.1. Between-Class Variance. Inspired by the idea of Otsu's method [61] which utilizes the difference between subregions to quantitatively describe the segmentation result to select an optimal threshold, the between-class variance (V_B) is defined as follows:

$$V_B = \sum_{i=1}^k P(C_i) (\mu(C_i) - \mu(C_{Ref}))^2, \quad (8)$$

where V_B denotes the sum of difference of mean intensity between subregion C and the reference region, k denotes the number of subregions adjacent to the reference region, and $\mu(C)$ denotes the mean intensity of subregion C while $P(C_i)$ denotes the proportion of the i th subregion in the whole TCI and is expressed as

$$P(C_i) = \frac{|C_i|}{|TCI|}, \quad (9)$$

where $|C_i|$ is the number of pixels in the i th subregion and $|TCI|$ is the number of pixels in the whole TCI.

From the definition, V_B denotes the difference between the reference region and its adjacent regions. Since the reference region corresponds to the interested tumor region in the US image, it is easy to understand that maximizing V_B can well overcome oversegmentation. By the way, this is the only part adopted in PAORGB [31].

2.4.2. Within-Class Variance. The aim of image segmentation is to segment a region with uniformity, which is always the target object, out of the background [62]. Therefore, considering the uniformity within the target region, we come up with another part called within-class variance (V_W) defined as follows:

$$V_W = \frac{\arctan\left(\frac{(1/|C_{Ref}|) \sum_{i=1}^{|C_{Ref}|} (I_i - \mu(C_{Ref}))^2}{P(C_{Ref})}\right)}{P(C_{Ref})}, \quad (10)$$

$$P(C_{Ref}) = \frac{|C_{Ref}|}{|TCI|},$$

where $|C_{Ref}|$ is the number of pixels in the reference region and I_i denotes the intensity of the i th pixel while $\mu(C_{Ref})$ denotes the mean intensity of the reference region, and $|TCI|$ is the number of pixels in the whole TCI. Since the minimizing of pure within-class variance $(1/|C_{Ref}|) \sum_{i=1}^{|C_{Ref}|} (I_i - \mu(C_{Ref}))^2$ will lead to oversegmentation, we add $P(C_{Ref})$ to suppress it. Since the value range of $(1/|C_{Ref}|) \sum_{i=1}^{|C_{Ref}|} (I_i - \mu(C_{Ref}))^2$ is much larger than the value range of $P(C_{Ref})$, we use arctan operation to make them comparable. From the definition, V_W denotes the difference within the reference region, and the undersegmentation problem can be well overcome by minimizing V_W .

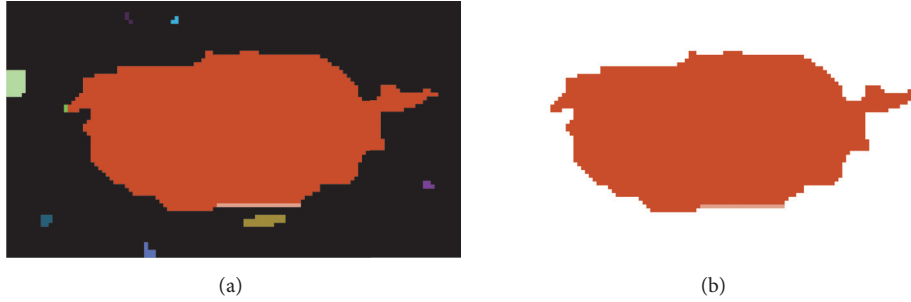


FIGURE 6: Example of reference region: (a) a segmented image by the RGB and (b) the reference region of (a).

2.4.3. Average Gradient. As mentioned above, the purpose of segmenting US images is to support the latter analysis and classification in the CAD system, and a wealth of useful and significant information for classification is contained in the contour of the focus. Accordingly, to achieve the objective of acquiring better tumor contours, another part called average gradient (G_A) is employed in our objective function. With the inspiration of the definition of energy in ACM, G_A is defined as follows:

$$G_A = \frac{1}{m} \sum_{i=1}^m |G_i|, \quad (11)$$

where m is the number of pixels included in the edge of the reference region and G_i denotes the gradient (calculated by the Sobel operator) of the i th pixel. Sobel operator is an edge detection operator based on 2D spatial gradient measurement. It can smooth the noise of the image and provide more accurate edge direction information than Prewitt and Roberts operators [59]. G_A denotes the average energy of the edge of the reference region.

Maximizing average gradient G_A obtains more accurate contour and avoids oversegmentation. If there were oversegmentation, the reference region would be included within the real target area; real target area would be a relatively homogeneous region within which every partitioned smaller region would have smaller G_A . Consequently, to increase G_A would force the contour of the reference region to move towards that of the real target area. Very often, the edges of the targets in the US image are not sufficiently clear and sharp such that we cannot use only G_A in the objective function. We take average gradient into account as one of the three objective functions in optimization process to improve the segmentation result. In ACM, the initial edge is forced to approach the real edge through maximizing the energy. Similar to ACM, maximizing G_A can force the contour of the reference region to approach the real contour of the tumor.

2.4.4. The Final Objective Function. Based on the above three parts, the objective function is defined as follows:

$$F_O = a * \frac{V_B}{f_B} - b * \frac{V_W}{f_W} + c * \frac{G_A}{f_A} \quad (12)$$

$$f_B = \frac{1}{n_p} \sum_{i=1}^{n_p} V_{Bi} \quad (13)$$

$$f_W = \frac{1}{n_p} \sum_{i=1}^{n_p} V_{Wi} \quad (14)$$

$$f_A = \frac{1}{n_p} \sum_{i=1}^{n_p} G_{Ai} \quad (15)$$

$$F_O = 0.3 * \frac{V_B}{f_B} - 0.3 * \frac{V_W}{f_W} + 0.4 * \frac{G_A}{f_A}, \quad (16)$$

where a , b , c are the weights of different objective parts ($a = 0.3$, $b = 0.3$, $c = 0.4$ in our experiment; they can be adjusted as needed). The final objective function in the experiment is defined as (16). V_B , V_W , and G_A are between-class variance, within-class variance, and average gradient, respectively. f_B , f_W , and f_A are normalized factors while $n_p = 200$ is the size of particle swarm. Because the value ranges of V_B , V_W , and G_A are quite different, they should be normalized to be comparable. For each US image, f_B , f_W , and f_A are calculated once after the uniform initialization of particle swarm but before the first iteration. We try to maximize F_O by the PSO.

2.5. Postprocessing. After the TCI is segmented by the RGB with the optimal α and k obtained by the PSO, we turn it into a binary image containing the object (tumor) and the background (tissue). Next, morphological opening and closing are conducted to refine the tumor contour, with opening to reduce the spicules and closing to fill the holes. A 5×5 elliptical kernel is used for both opening and closing.

2.6. The Proposed MOORGB Segmentation Method. Assuming that the position and velocity of the i th particle in our case are expressed as $x_i = (k_i, \alpha_i)$ and $v_i = (v_{ki}, v_{\alpha i})$, respectively, the general procedure of MOORGB is summarized as follows.

Step 1. Manually delineate TCI from the original US image.

Step 2. Use the bilateral filter to do the speckle reduction for TCI.

Step 3. Enhance the filtered TCI by histogram equalization to improve the contrast.

Step 4. Improve the homogeneity by performing pyramid mean shift filtering.

Step 5. Uniformly initialize the particle swarm within the search space, and let the iteration count $q = 0$ and so on.

Step 6. Let $q = q + 1$; traverse all n_p particles: in the q th traversal, RGB is performed with the position (i.e., $x_i = (k_i, \alpha_i)$) of each particle; then evaluate the segmentation result with the objective function F_O and obtain p_i and p_g by comparing values of F_O for updating each particle (including position and velocity) for next iteration.

Step 7. Iteratively repeat Step 6 until convergence (i.e., p_g remains stable for 4 generations) or $q = N$ ($N = 200$ in this paper).

Step 8. After finishing the iteration, the position of the globally best particle (i.e., p_g) is, namely, the optimal setting of α and k ; then get the final segmentation result by performing RGB with the optimal setting.

Step 9. Turn the segmentation result into a binary image; then get the final tumor contour by conducting morphological opening and closing.

2.7. Experimental Methods. We developed the proposed method with the C++ language using OpenCV 2.4.3 and VisualStudio 2010 and run it on a computer with 3.40 GHz CPU and 12.0 GB RAM. To validate our method, experiments have been conducted. Our work is approved by Human Subject Ethics Committee of South China University of Technology. In the dataset, 100 clinical breast US images and 18 clinical musculoskeletal US images with the subjects' consent forms were provided by the Cancer Center of Sun Yat-sen University and were taken from an HDI 5000 SonoCT System (Philips Medical Systems) with an L12-5 50 mm Broadband Linear Array at the imaging frequency of 7.1 MHz. The "true" tumor regions of these US images were manually delineated by an experienced radiologist who has worked on US imaging and diagnosis for more than ten years. The contour delineated by only one doctor is not absolutely accurate because different doctors may give different "real contours," which is indeed a problem in the research. Nevertheless, the rich diagnosis experience of the doctor has fitted the edge of every tumor as accurately as possible. This dataset consists of 50 breast US images with benign tumors, 50 breast US images with malignant tumors, and 18 musculoskeletal US images with cysts (including 10 ganglion cysts, 4 keratinizing cysts, and 4 popliteal cysts).

To demonstrate the advantages of the proposed method, besides PAORGB, we also compared the method with the other two well-known segmentation methods (i.e., DRLSE [43] and MSGC [29]). DRLSE method, an advanced level set evolution approach in recent years, is applied to an edge-based active contour model for image segmentation. It is an edge-based segmentation method that needs to set initial contour manually. The initial contour profoundly affects the final segmentation result. MSGC is a novel graph-cut method whose energy function combines region- and edge-based information to segment US images. It also needs to crop tumor centered ROI. Among the three comparative

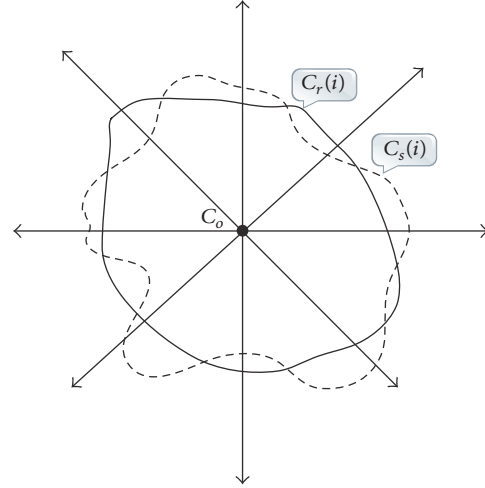


FIGURE 7: An illustration of computation principle for ARE.

methods, DRLSE is an edge-based method, PAORGB is a region-based method, and MSGC is a compound method. To make a comparison of computational efficiency, the methods PAORGB and MOORGB were programmed in the same software system. As such, the four methods were run with the same hardware configuration. The ROI is all the same for the four segmentation methods.

To quantitatively measure the experiment results, four criteria (i.e., averaged radial error (ARE), true positive volume fraction (TPVF), false positive volume fraction (FPVF), and false negative volume fraction (FNVF)) were adopted in this study. The ARE is used for the evaluation of segmentation performance by measuring the average radial error of a segmented contour with respect to the real contour which is delineated by an expert radiologist. As shown in Figure 7, it is defined as

$$\text{ARE}(n) = \frac{1}{n} \sum_{i=0}^{n-1} \frac{|C_s(i) - C_r(i)|}{|C_r(i) - C_o|} \times 100\%, \quad (17)$$

where n is the number of radial rays and set to 180 in our experiments while C_o represents the center of the "true" tumor region which is delineated by the radiologist and $C_s(i)$ denotes the location where the contour of the segmented tumor region crosses the i th ray, while $C_r(i)$ is the location where the contour of the "true" tumor region crosses the i th ray.

In addition, TPVF, FPVF, and FNVF were also used in the evaluation of the performance of segmentation methods. TPVF means true positive volume fraction, indicating the total fraction of tissue in the "true" tumor region with which the segmented region overlaps. FPVF means false positive volume fraction, denoting the amount of tissue falsely identified by the segmentation method as a fraction of the total amount of tissue in the "true" tumor region. FNVF means false negative volume fraction, denoting the fraction of tissue defined in the "true" tumor region that is missed by the segmentation method. In our study, the "true" tumor region is delineated by the radiologist. Figure 8 shows the

TABLE 1: Quantitative segmentation results of 50 breast US images with benign tumors.

Methods	ARE (%)	TPVF (%)	FPVF (%)	FNVF (%)
Our method	11.09 ± 12.47	85.60 ± 13.71	4.51 ± 20.18	14.40 ± 13.71
PAORGB [26]	16.47 ± 21.41	81.64 ± 29.94	10.52 ± 29.40	18.36 ± 29.94
DRLSE [46]	11.37 ± 13.04	93.60 ± 16.87	14.42 ± 24.33	6.40 ± 16.87
MSGC [24]	15.76 ± 13.18	75.34 ± 16.25	2.51 ± 14.60	24.66 ± 16.24

TABLE 2: Quantitative segmentation results of 50 breast US images with malignant tumors.

Methods	ARE (%)	TPVF (%)	FPVF (%)	FNVF (%)
Our method	10.41 ± 13.62	84.91 ± 16.39	4.43 ± 19.01	15.09 ± 16.39
PAORGB	19.12 ± 27.63	74.98 ± 27.49	10.16 ± 37.09	25.02 ± 27.49
DRLSE	15.84 ± 15.34	95.31 ± 19.75	24.05 ± 20.68	4.69 ± 19.75
MSGC	15.52 ± 22.66	74.12 ± 15.12	2.93 ± 13.17	25.88 ± 15.12

areas corresponding to TPVF, FPVF, and FNVF. Accordingly, smaller ARE, FPVF, and FNVF and larger TPVF indicate better segmentation performance. TPVF, FPVF, and FNVF are defined by

$$\begin{aligned}
 \text{TPVF} &= \frac{A_m \cap A_n}{A_m} \\
 \text{FPVF} &= \frac{A_n - A_m \cap A_n}{A_m} \\
 \text{FNVF} &= \frac{A_m - A_m \cap A_n}{A_m},
 \end{aligned} \tag{18}$$

where A_m is the area of the “true” tumor region delineated by the radiologist and A_n is the area of the tumor region obtained by the segmentation algorithm.

3. Experimental Results and Discussion

3.1. Qualitative Analysis. In this paper, we present the segmentation results for five tumors. Five US images with the segmentation results are shown in Figures 9–13. The quantitative segmentation results on US images are shown in Tables 1, 2, 3, and 4. Figures 9(a), 10(a), 11(a), 12(a), and 13(a) show original B-mode US images for two benign tumors, two malignant tumors, and one musculoskeletal cyst, respectively. After preprocessing the original images, the segmentation results using the MOORGB are illustrated in Figures 9(b), 10(b), 11(b), 12(b), and 13(b), those using the PAORGB in Figures 9(d), 10(d), 11(d), 12(d), and 13(d), those using the DRLSE in Figures 9(e), 10(e), 11(e), 12(e), and 13(e), and those using the MSGC in Figures 9(f), 10(f), 11(f), 12(f), and 13(f).

In Figures 9–13, we can see that our method achieved the best segmentation results compared with the other three methods, and the contour generated by our method is quite close to the real contour delineated by the radiologist. Undersegmentation happens in Figures 9(d) and 10(d), but not in Figures 9(b) and 10(b); and oversegmentation happens in Figures 12(d) and 13(d), but not in Figures 12(b)

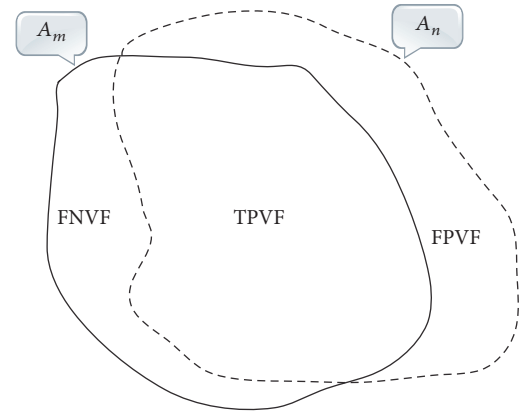


FIGURE 8: The areas corresponding to TPVF, FPVF, and FNVF, respectively. A_m indicates the “true” contour delineated by the radiologist and A_n denotes the contour obtained by the segmentation algorithm.

and 13(b). Comparing with the PAORGB, the MOORGB improves the segmentation results obviously, avoiding the undersegmentation and oversegmentation more effectively. Regional uniformity has been significantly improved, and the edge has been smoother. The reason is that the within-class variance and average gradient are introduced into the objective function of MOORGB by combining region- and edge-based information. The segmentation results of the MSGC are better than those of the PAORGB and DRLSE, since MSGC is also a compound method (region energy and boundary energy are both included in its energy function) and many preprocessing techniques are adopted. As shown in Figures 9(e), 10(e), 11(e), 12(e), and 13(e), the DRLSE can only roughly detect the tumor contour, and the detected contours are irregular. The reason is that it depends on edge-based information and is sensitive to speckle noise and sharp edge; hence it captures sharp edge easily and leads to boundary leakage and undersegmentation.

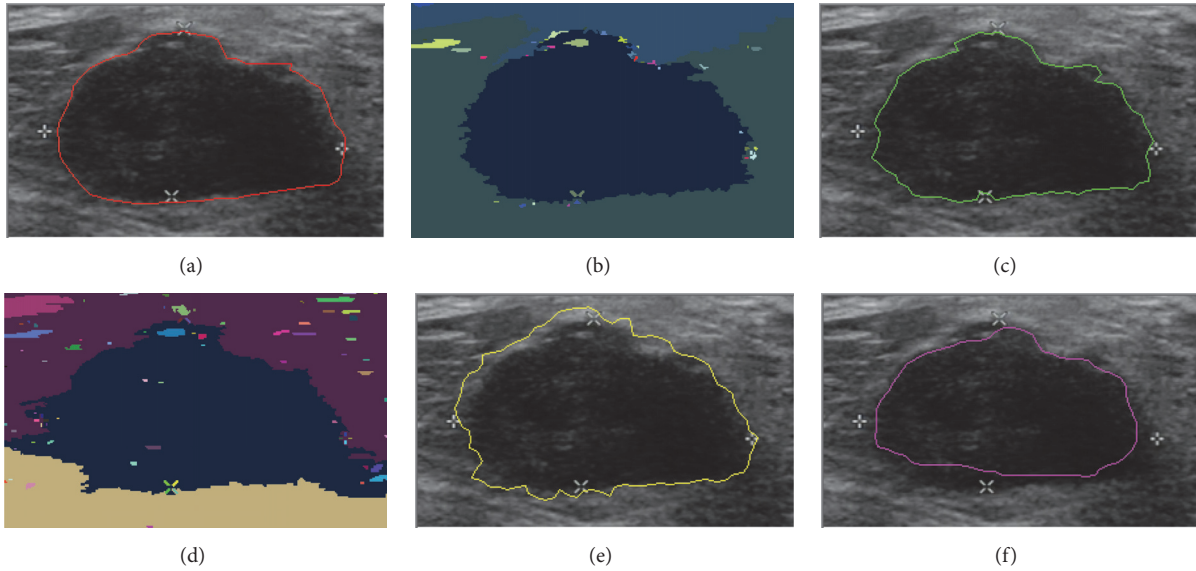


FIGURE 9: Segmentation results for the first benign breast tumor. (a) A breast US image with a benign tumor (the contour is delineated by the radiologist). (b) The result of MOORGB. (c) The final result of MOORGB. (d) The result of PAORGB. (e) The result of DRLSE. (f) The result of MSGC.

TABLE 3: Quantitative segmentation results of 18 musculoskeletal US images with cysts.

Methods	ARE (%)	TPVF (%)	FPVF (%)	FNVF (%)
Our method	10.85 ± 17.14	85.61 ± 7.75	4.52 ± 34.22	14.30 ± 7.80
PAORGB	20.90 ± 39.66	82.12 ± 29.33	18.00 ± 35.97	17.80 ± 29.40
DRLSE	8.60 ± 12.06	91.90 ± 21.61	10.90 ± 10.72	8.04 ± 21.66
MSGC	14.43 ± 27.30	80.50 ± 17.33	3.9 ± 43.41	19.35 ± 29.65

TABLE 4: Overall quantitative segmentation results of 118 US images.

Methods	ARE (%)	TPVF (%)	FPVF (%)	FNVF (%)	Averaged computing time (s)
Our method	10.77 ± 17.22	85.34 ± 16.69	4.48 ± 34.26	14.67 ± 16.67	50.54
PAORGB	18.27 ± 37.03	78.89 ± 30.24	10.51 ± 35.74	21.10 ± 30.23	719.78
DRLSE	12.84 ± 16.82	94.07 ± 18.51	17.97 ± 28.03	5.92 ± 23.78	5.93
MSGC	15.46 ± 26.27	75.61 ± 17.74	2.9 ± 42.41	24.37 ± 24.63	0.123

3.2. *Quantitative Analysis.* Table 4 shows the quantitative comparisons of different segmentation approaches on the whole dataset. Similarly, we show the quantitative segmentation results of the benign tumors, malignant tumors, and cysts in Tables 1, 2, and 3, respectively.

Comparing Tables 1 and 3 with Table 2, it is shown that all four segmentation methods perform better on benign tumors and musculoskeletal cysts than on malignant tumors on the whole, indicating that the boundaries of benign tumors and musculoskeletal cysts are more significant than those of malignant tumors. The shape of the benign tumor is more regular and similar to circle or ellipse. The shape of the malignant tumor is irregular and usually lobulated with burrs in the contour. The segmentation result of the malignant tumor is worse than benign tumors because the contour of

malignant tumor is less regular and less homogenous than that of benign tumor.

From Table 4, it is seen that our method achieved the lowest ARE (10.77%). Due to the undersegmentation, the DRLSE got the highest TPVF (94.07%) and FPVF (17.97%), indicating the high ratio of false segmentation. The MSGC got the lowest FPVF (2.9%), which indicates the low ratio of false segmentation, and is the fastest method (0.123 s) among the four methods. However it got the lowest TPVF (75.61%), showing oversegmentation in a way. Comparing with the original PAORGB (as shown in Table 4), our method improves the segmentation result obviously, achieving higher TPVF and lower ARE, FPVF, and FNVF. Although MOORGB could not achieve the best performance in all evaluation indices, it got the best overall performance. Comparing with DRLSE,

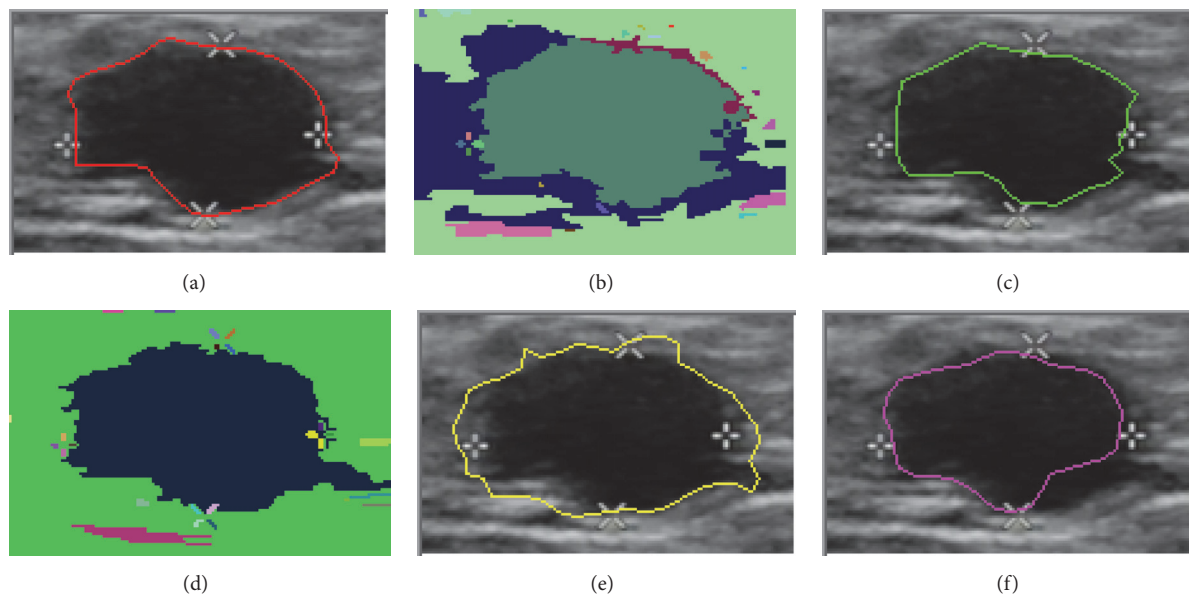


FIGURE 10: Segmentation results for the second benign breast tumor. (a) A breast US image with a benign tumor (the contour is delineated by the radiologist). (b) The result of MOORGB. (c) The final result of MOORGB. (d) The result of PAORGB. (e) The result of DRLSE. (f) The result of MSGC.

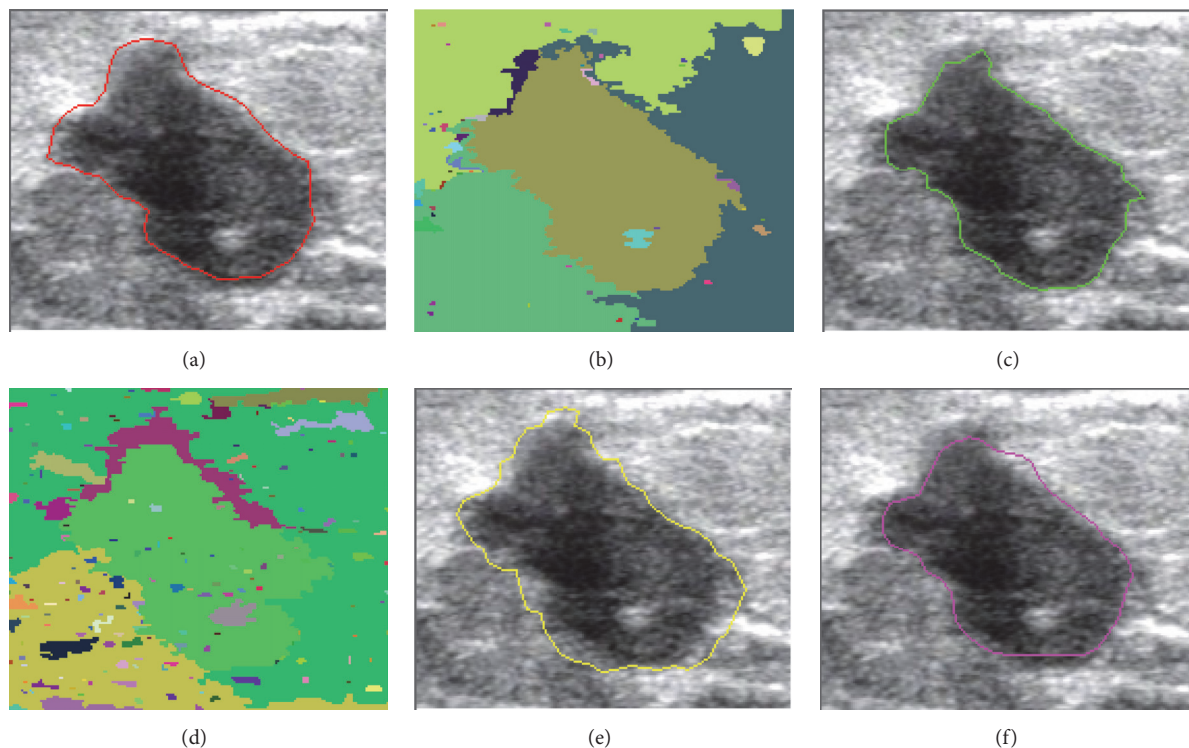


FIGURE 11: Segmentation results for the first malignant breast tumor. (a) A breast US image with a malignant tumor (the contour is delineated by the radiologist). (b) The result of MOORGB. (c) The final result of MOORGB. (d) The result of PAORGB. (e) The result of DRLSE. (f) The result of MSGC.

our method was 6.45% lower than it in TPVF but 8.75% better than it in FPVF, obtaining better overall performance. Comparing with MSGC, our method was 1.58% higher than it in FPVF but 9.93% better than it in TPVF, obtaining better

overall performance and avoiding oversegmentation in a way. As shown in Table 4, our method is faster than the PAORGB. It is because the convergence condition in our method is that “ p_g remains stable for 4 generations,” rather than that “the

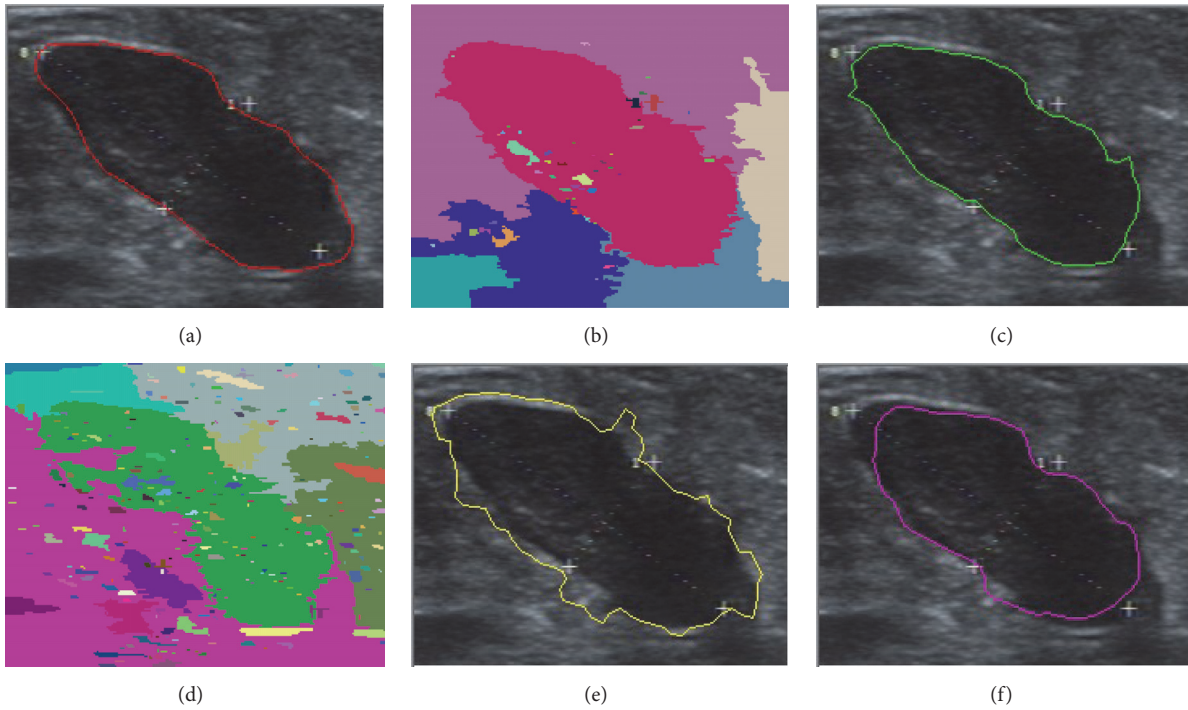


FIGURE 12: Segmentation results for the second malignant breast tumor. (a) A breast US image with a malignant tumor (the contour is delineated by the radiologist). (b) The result of MOORGB. (c) The final result of MOORGB. (d) The result of PAORGB. (e) The result of DRLSE. (f) The result of MSGC.

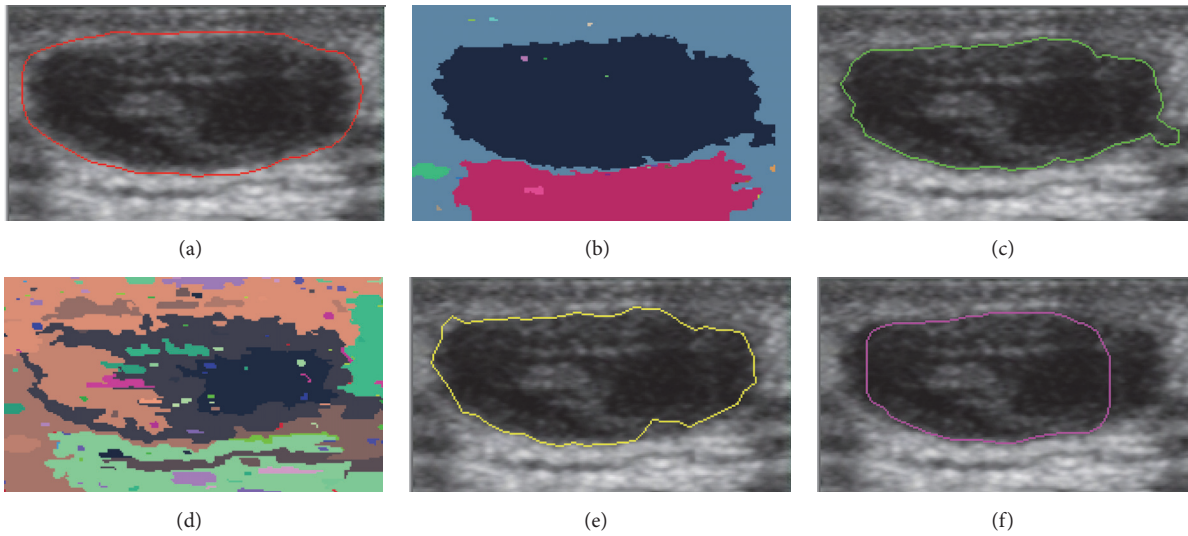


FIGURE 13: Segmentation results for the keratinizing cyst. (a) A musculoskeletal US image with a cyst (the contour is delineated by the radiologist). (b) The result of MOORGB. (c) The final result of MOORGB. (d) The result of PAORGB. (e) The result of DRLSE. (f) The result of MSGC.

updating of k is below 1 and that of α is below 0.00001 for all the particles in an experiment” in the PAORGB [31].

3.3. *The Influence of the Weight.* Our method synthesizes three optimization objective functions (between-class variance V_B , within-class variance V_W , and average gradient G_A). Thus the weight values of three objective parts (i.e., a ,

b , and c) are introduced. Figure 14 shows the comparison of experimental results with different weight values. From Figures 14(a), 14(b), and 14(c) and Table 5, we can see that when the weight values of the three objective functions are almost the same, three optimization objectives play nearly equal roles in the optimization process, making the algorithm not only region-based but also edge-based. When one of

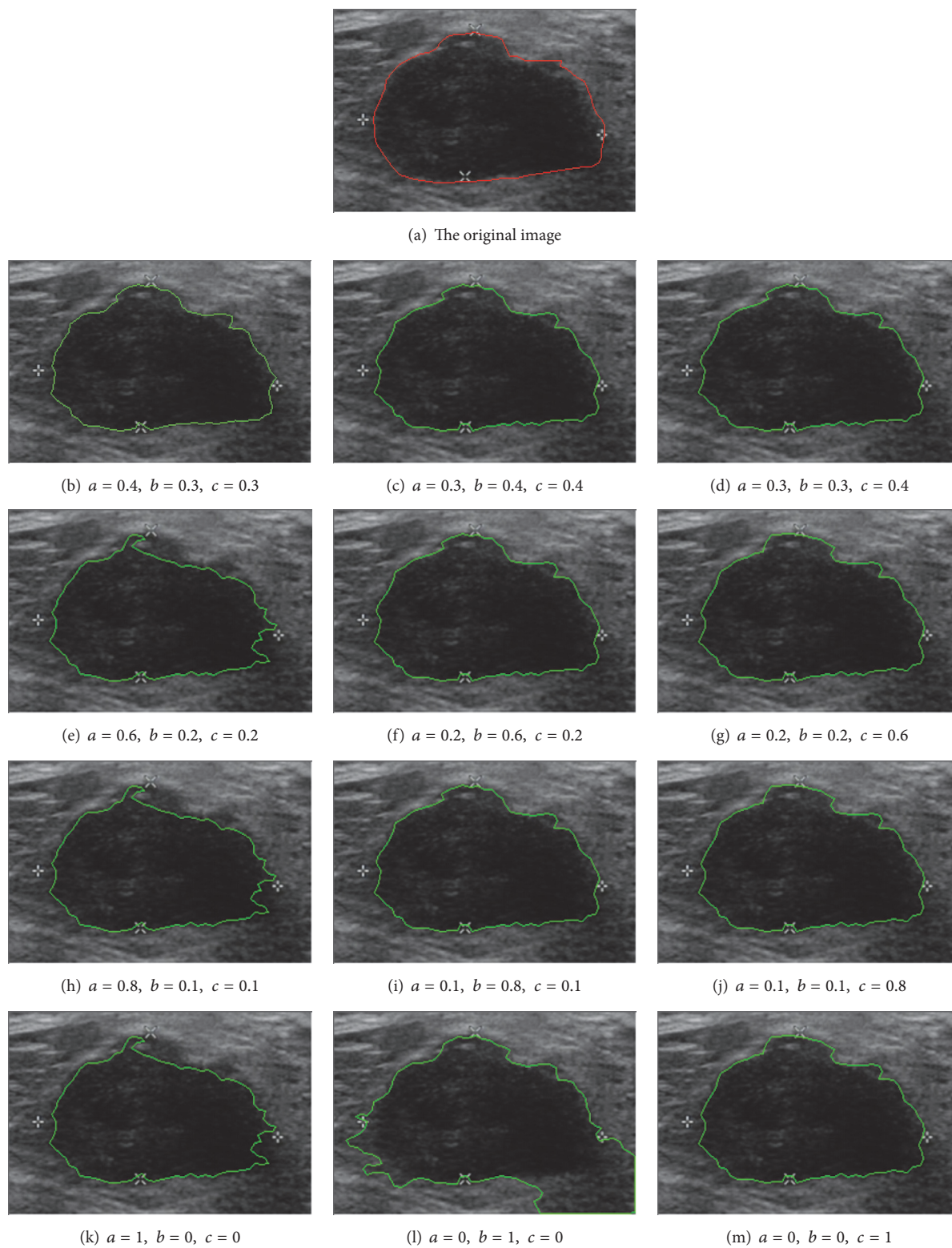
FIGURE 14: The segmentation results with different weights (a, b, c).

TABLE 5: Quantitative segmentation results of 15 US images with different weight values.

Methods	ARE (%)	TPVF (%)	FPVF (%)	FNVF (%)
$a = 0.4, b = 0.3, c = 0.3$	10.67	85.61	4.52	14.70
$a = 0.3, b = 0.4, c = 0.3$	10.71	85.60	4.51	14.69
$a = 0.3, b = 0.3, c = 0.4$	10.69	85.60	4.52	14.69
$a = 0.6, b = 0.2, c = 0.2$	10.47	85.51	4.49	14.91
$a = 0.2, b = 0.6, c = 0.2$	10.59	85.52	4.50	14.73
$a = 0.2, b = 0.2, c = 0.6$	10.74	85.64	4.80	14.75
$a = 0.8, b = 0.2, c = 0.2$	11.12	84.97	5.44	15.39
$a = 0.2, b = 0.8, c = 0.2$	11.25	85.03	5.78	15.41
$a = 0.2, b = 0.2, c = 0.8$	11.23	84.77	5.61	15.28
$a = 1, b = 0, c = 0$	12.92	83.39	6.78	16.07
$a = 0, b = 1, c = 0$	69.84	98.86	154.72	0.46
$a = 0, b = 0, c = 1$	8.97	87.79	10.49	17.93

the three weight values is overlarge, it would not be able to reflect the three optimization results evenly, hence leading to oversegmentation or undersegmentation. As shown in Figures 14(k), 14(l), and 14(m), if one of the three weight values equals one, the proposed method degenerated into a single objective optimization algorithm, and the optimization goal is only one role, which cannot avoid oversegmentation and undersegmentation effectively. Through analyzing the influence of different weight values of objective functions and our repeated experiments, we can set the system parameters as $a = b = 0.3, c = 0.4$. The final objective function is described as (16) which can make segmentation system work well.

4. Conclusions

In this paper, we propose a novel segmentation scheme for US images based on the RGB and PSO methods. In this scheme, the PSO is used to optimally set the two significant parameters in the RGB for determining the segmentation result automatically. To combine region-based and edge-based information, we consider the optimization as a multiobjective problem. First, because of the low contrast and speckle noises of US images, the ROI image is filtered by a bilateral filter and contrast-enhanced by histogram equalization and then pyramid mean shift is executed on the enhanced image to improve homogeneity. A novel objective function consisting of three parts corresponding to region-based and edge-based information is adopted by PSO. The between-class variance denotes the difference between the reference region and its adjacent regions. The within-class variance denotes the difference within the reference region, and the undersegmentation problem can be well overcome by minimizing it. Between-class variance and within-class variance reflect the regional information. The average gradient denotes the average energy of the edge of the reference region and maximizing it can force the contour of the reference region to approach the real contour of the tumor. Average gradient reflects the edge-based information of the image. Three optimization objectives play important roles in the optimization process, making the algorithm achieve

the corresponding segmentation effect, not only region-based but also edge-based. With the optimization of PSO, RGB is performed to segment the ROI image. Finally, the segmented image is processed by morphological opening and closing to refine the tumor contour. To validate our method, experiments have been conducted on 118 clinical US images, including breast US images and musculoskeletal US images. The segmentation results of our method have been compared with the corresponding results obtained by three existing approaches, and four metrics have been used to measure the segmentation performance. The experimental results show that our method could successfully segment US images and achieved the best segmentation results compared with the other three methods, MSGC, PAORGB, and DRLSE. The contour generated by our method was closer to the real contour delineated by the radiologist. The MOORGB obtained the lowest ARE and better overall performance in TPVF, FPVF, and FNVF, avoiding the undersegmentation and oversegmentation more effectively.

However, the step to obtain TCI (as shown in Figure 2) requires user's participation which may result in significant influence on the following segmentation. To obtain acceptable segmentation results, the operator should be well experienced in examining US images and identifying suspicious lesions in clinical practices. Moreover, the TCI should be carefully delineated to achieve the full lesion region with partial surrounding tissues, and the interested lesion region must be located in the central part. Consequently, how to automatically extract TCI from the BUS image is one of our future studies. In addition, the computation time is still far away from real-time applications. Accordingly, making efforts to reduce the computation time by adopting parallel processing techniques is also part of our future work. Besides, adopting our segmentation method in real CAD systems to validate the whole performance will be included in our future work.

Conflicts of Interest

The authors declare that they have no conflicts of interest.

Authors' Contributions

Yaozhong Luo and Longzhong Liu have contributed equally to this work.

Acknowledgments

This work was partially supported by National Natural Science Foundation of China (nos. 61372007 and 61571193), Guangzhou Key Lab of Body Data Science (no. 201605030011), and Guangdong Provincial Science and Technology Program-International Collaborative Projects (no. 2014A050503020).

References

- [1] B. Sahiner, H.-P. Chan, M. A. Roubidoux et al., "Malignant and benign breast masses on 3D US volumetric images: effect of computer-aided diagnosis on radiologist accuracy," *Radiology*, vol. 242, no. 3, pp. 716–724, 2007.
- [2] C.-M. Chen, Y.-H. Chou, K.-C. Han et al., "Breast lesions on sonograms: computer-aided diagnosis with nearly setting-independent features and artificial neural networks," *Radiology*, vol. 226, no. 2, pp. 504–514, 2003.
- [3] K. Drukker, M. L. Giger, K. Horsch, M. A. Kupinski, C. J. Vyborny, and E. B. Mendelson, "Computerized lesion detection on breast ultrasound," *Medical Physics*, vol. 29, no. 7, pp. 1438–1446, 2002.
- [4] Q. Li, W. Zhang, X. Guan, Y. Bai, and J. Jia, "An improved approach for accurate and efficient measurement of common carotid artery intima-media thickness in ultrasound images," *BioMed Research International*, vol. 2014, Article ID 740328, 8 pages, 2014.
- [5] B. O. Anderson, R. Shyyan, A. Eniu et al., "Breast cancer in limited-resource countries: an overview of the breast health global initiative 2005 guidelines," *Breast Journal*, vol. 12, no. 1, pp. S3–S15, 2006.
- [6] V. Naik, R. S. Gamad, and P. P. Bansod, "Carotid artery segmentation in ultrasound images and measurement of intima-media thickness," *BioMed Research International*, vol. 2013, Article ID 801962, 10 pages, 2013.
- [7] Y. L. Huang, D. R. Chen, and Y. K. Liu, "Breast cancer diagnosis using image retrieval for different ultrasonic systems," in *Proceedings of the International Conference on Image Processing, ICIP*, pp. 2957–2960, Institute of Electrical and Electronics Engineers, Singapore, 2004.
- [8] H. D. Cheng, J. Shan, W. Ju, Y. Guo, and L. Zhang, "Automated breast cancer detection and classification using ultrasound images: a survey," *Pattern Recognition*, vol. 43, no. 1, pp. 299–317, 2010.
- [9] Y. Li, W. Liu, X. Li, Q. Huang, and X. Li, "GA-SIFT: a new scale invariant feature transform for multispectral image using geometric algebra," *Information Sciences*, vol. 281, pp. 559–572, 2014.
- [10] J. Shi, S. Zhou, X. Liu, Q. Zhang, M. Lu, and T. Wang, "Stacked deep polynomial network based representation learning for tumor classification with small ultrasound image dataset," *Neurocomputing*, vol. 194, pp. 87–94, 2016.
- [11] J. A. Noble and D. Boukerroui, "Ultrasound image segmentation: a survey," *IEEE Transactions on Medical Imaging*, vol. 25, no. 8, pp. 987–1010, 2006.
- [12] J. Peng, J. Shen, and X. Li, "High-Order Energies for Stereo Segmentation," *IEEE Transactions on Cybernetics*, vol. 46, no. 7, pp. 1616–1627, 2016.
- [13] M. Xian, Y. Zhang, H.-D. Cheng, F. Xu, and J. Ding, "Neuro-connectedness cut," *IEEE Transactions on Image Processing*, vol. 25, no. 10, pp. 4691–4703, 2016.
- [14] P. N. T. Wells and M. Halliwell, "Speckle in ultrasonic imaging," *Ultrasonics*, vol. 19, no. 5, pp. 225–229, 1981.
- [15] G. Xiao, M. Brady, J. A. Noble, and Y. Zhang, "Segmentation of ultrasound B-mode images with intensity inhomogeneity correction," *IEEE Transactions on Medical Imaging*, vol. 21, no. 1, pp. 48–57, 2002.
- [16] S. Y. Joo, W. K. Moon, and H. C. Kim, "Computer-aided diagnosis of solid breast nodules on ultrasound with digital image processing and artificial neural network," in *Proceedings of the 26th Annual International Conference of*, vol. 2, pp. 1397–1400, San Francisco, CA, USA, 2004.
- [17] K. Horsch, M. L. Giger, C. J. Vyborny, and L. A. Venta, "Performance of Computer-Aided Diagnosis in the Interpretation of Lesions on Breast Sonography," *Academic Radiology*, vol. 11, no. 3, pp. 272–280, 2004.
- [18] M. H. Yap, E. A. Edirisinghe, and H. E. Bez, "Fully automatic lesion boundary detection in ultrasound breast images," in *Medical Imaging 2007: Image Processing*, vol. 6512 of *Proceedings of SPIE*, p. I5123, San Diego, Calif, USA, 2007.
- [19] N. A. M. Isa, S. Sabarudin, U. K. Ngah, and K. Z. Zamli, "Automatic detection of breast tumours from ultrasound images using the modified seed based region growing technique," in *Proceedings of the 9th International Conference on Knowledge-Based Intelligent Information and Engineering Systems*, vol. 3682, pp. 138–144, Springer, La Trobe University, Melbourne, Australia, 2005.
- [20] J. Shan, H. D. Cheng, and Y. Wang, "A novel segmentation method for breast ultrasound images based on neutrosophic l-means clustering," *Medical Physics*, vol. 39, no. 9, pp. 5669–5682, 2012.
- [21] H. B. Kekre and P. Shrinath, "Tumour delineation using statistical properties of the breast us images and vector quantization based clustering algorithms," *International Journal of Image, Graphics and Signal Processing*, vol. 5, no. 11, pp. 1–12, 2013.
- [22] W. K. Moon, C.-M. Lo, R.-T. Chen et al., "Tumor detection in automated breast ultrasound images using quantitative tissue clustering," *Medical Physics*, vol. 41, no. 4, Article ID 042901, 2014.
- [23] D. Boukerroui, O. Basset, N. Guérin, and A. Baskurt, "Multiresolution texture based adaptive clustering algorithm for breast lesion segmentation," *European Journal of Ultrasound*, vol. 8, no. 2, pp. 135–144, 1998.
- [24] C.-M. Chen, Y.-H. Chou, C. S. K. Chen et al., "Cell-competition algorithm: a new segmentation algorithm for multiple objects with irregular boundaries in ultrasound images," *Ultrasound in Medicine and Biology*, vol. 31, no. 12, pp. 1647–1664, 2005.
- [25] B. Deka and D. Ghosh, "Ultrasound image segmentation using watersheds and region merging," in *Proceedings of the IET Visual Information Engineering (VIE '06)*, p. 6, Bangalore, India, 2006.
- [26] L. Zhang and M. Zhang, "A fully automatic image segmentation using an extended fuzzy set," in *Proceedings of the International Workshop on Computer Science for Environmental Engineering and EcoInformatics*, vol. 159, pp. 412–417, Springer, Kunming, People's Republic of China, 2011.

- [27] W. Gomez, A. Rodriguez, W. C. A. Pereira, and A. F. C. Infantosi, "Feature selection and classifier performance in computer-aided diagnosis for breast ultrasound," in *Proceedings of the 10th International Conference and Expo on Emerging Technologies for a Smarter World, CEWIT*, IEEE, Melville, NY, USA, 2013.
- [28] J. Zhang, S. K. Zhou, S. Brunke, C. Lowery, and D. Comaniciu, "Database-guided breast tumor detection and segmentation in 2D ultrasound images," in *Medical Imaging 2010: Computer-Aided Diagnosis*, vol. 7624 of *Proceedings of SPIE*, p. 7, San Diego, Calif, USA, February 2010.
- [29] Z. Zhou, W. Wu, S. Wu et al., "Semi-automatic breast ultrasound image segmentation based on mean shift and graph cuts," *Ultrasonic Imaging*, vol. 36, no. 4, pp. 256–276, 2014.
- [30] Q.-H. Huang, S.-Y. Lee, L.-Z. Liu, M.-H. Lu, L.-W. Jin, and A.-H. Li, "A robust graph-based segmentation method for breast tumors in ultrasound images," *Ultrasonics*, vol. 52, no. 2, pp. 266–275, 2012.
- [31] Q. Huang, X. Bai, Y. Li, L. Jin, and X. Li, "Optimized graph-based segmentation for ultrasound images," *Neurocomputing*, vol. 129, pp. 216–224, 2014.
- [32] Q. Huang, F. Yang, L. Liu, and X. Li, "Automatic segmentation of breast lesions for interaction in ultrasonic computer-aided diagnosis," *Information Sciences*, vol. 314, pp. 293–310, 2015.
- [33] H. Chang, Z. Chen, Q. Huang, J. Shi, and X. Li, "Graph-based learning for segmentation of 3D ultrasound images," *Neurocomputing*, vol. 151, no. 2, pp. 632–644, 2015.
- [34] Q. Huang, B. Chen, J. Wang, and T. Mei, "Personalized video recommendation through graph propagation," in *Transactions on Multimedia Computing, Communications, and Applications*, vol. 10 of 4, pp. 1133–1136, ACM, 2012.
- [35] Y. Luo, S. Han, and Q. Huang, "A novel graph-based segmentation method for breast ultrasound images," in *Proceedings of the Digital Image Computing: Techniques and Applications (DICTA)*, pp. 1–6, IEEE, 2016.
- [36] R.-F. Chang, W.-J. Wu, C.-C. Tseng, D.-R. Chen, and W. K. Moon, "3-D Snake for US in Margin Evaluation for Malignant Breast Tumor Excision Using Mammotome," in *Proceedings of the IEEE Transactions on Information Technology in Biomedicine*, vol. 7 of 3, pp. 197–201, 2003.
- [37] A. K. Jumaat, W. E. Z. W. A. Rahman, A. Ibrahim, and R. Mahmud, "Segmentation of masses from breast ultrasound images using parametric active contour algorithm," in *Proceedings of the International Conference on Mathematics Education Research, ICMER*, pp. 640–647, Malacca, Malaysia, 2010.
- [38] A. Sarti, C. Corsi, E. Mazzini, and C. Lamberti, "Maximum likelihood segmentation of ultrasound images with rayleigh distribution," *IEEE Transactions on Ultrasonics, Ferroelectrics, and Frequency Control*, vol. 52, no. 6, pp. 947–960, 2005.
- [39] B. Liu, H. D. Cheng, J. Huang, J. Tian, X. Tang, and J. Liu, "Probability density difference-based active contour for ultrasound image segmentation," *Pattern Recognition*, vol. 43, no. 6, pp. 2028–2042, 2010.
- [40] L. Gao, X. Liu, and W. Chen, "Phase- and GVF-based level set segmentation of ultrasonic breast tumors," *Journal of Applied Mathematics*, vol. 2012, Article ID 810805, pp. 22–ID 810805, 2012.
- [41] B. Wang, X. Gao, J. Li, X. Li, and D. Tao, "A level set method with shape priors by using locality preserving projections," *Neurocomputing*, vol. 170, pp. 188–200, 2015.
- [42] B. N. Li, J. Qin, R. Wang, and M. Wang, "Selective level set segmentation using fuzzy region competition," *IEEE Access*, vol. 4, pp. 4777–4788, 2016.
- [43] C. Li, C. Xu, C. Gui, and M. D. Fox, "Distance regularized level set evolution and its application to image segmentation," *IEEE Transactions on Image Processing*, vol. 19, no. 12, pp. 3243–3254, 2010.
- [44] I. Lang, M. Sklair-Levy, and H. Spitzer, "Multi-scale texture-based level-set segmentation of breast B-mode images," *Computers in Biology & Medicine*, vol. 72C, pp. 30–42, 2016.
- [45] A. Madabhushi and D. N. Metaxas, "Combining low-, high-level and empirical domain knowledge for automated segmentation of ultrasonic breast lesions," *IEEE Transactions on Medical Imaging*, vol. 22, no. 2, pp. 155–169, 2003.
- [46] D. R. Chen, R. F. Chang, W. J. Kuo, M. C. Chen, and Y. L. Huang, "Diagnosis of breast tumors with sonographic texture analysis using wavelet transform and neural networks," *Ultrasound in Medicine and Biology*, vol. 28, no. 10, pp. 1301–1310, 2002.
- [47] Y. Guo, A. Şengür, and J. W. Tian, "A novel breast ultrasound image segmentation algorithm based on neutrosophic similarity score and level set," *Computer Methods and Programs in Biomedicine*, vol. 123, pp. 43–53, 2016.
- [48] A. T. Stavros, D. Thickman, C. L. Rapp, M. A. Dennis, S. H. Parker, and G. A. Sisney, "Solid breast nodules: use of sonography to distinguish between benign and malignant lesions," *Radiology*, vol. 196, no. 1, pp. 123–134, 1995.
- [49] W. Leucht and D. Leucht, "Teaching Atlas of Breast Ultrasound," pp. 24–38, Thieme Medical, Stuttgart, Germany, 2000.
- [50] R. F. Chang, W. J. Wu, W. K. Moon, W. M. Chen, W. Lee, and D. R. Chen, "Segmentation of breast tumor in three-dimensional ultrasound images using three-dimensional discrete active contour model," *Ultrasound in Medicine and Biology*, vol. 29, no. 11, pp. 1571–1581, 2003.
- [51] Y. L. Huang and D. R. Chen, "Watershed segmentation for breast tumor in 2-D sonography," *Ultrasound in Medicine and Biology*, vol. 30, no. 5, pp. 625–632, 2004.
- [52] Y. L. Huang and D. R. Chen, "Automatic contouring for breast tumors in 2-D sonography," in *Proceedings of the 27th Annual International Conference of the IEEE Engineering in Medicine and Biology Society (IEEE)*, pp. 3225–3228, IEEE, Shanghai, China, 2005.
- [53] Y. L. Huang, Y. R. Jiang, D. R. Chen, and W. K. Moon, "Level set contouring for breast tumor in sonography," *Journal of Digital Imaging*, vol. 20, no. 3, pp. 238–247, 2007.
- [54] M. Aleman-Flores, L. Alvarez, and V. Caselles, "Texture-oriented anisotropic filtering and geodesic active contours in breast tumor ultrasound segmentation," *Journal of Math Imaging Vision*, vol. 28, no. 1, pp. 81–97, 2007.
- [55] W. M. Wang, L. Zhu, J. Qin, Y. P. Chui, B. N. Li, and P. A. Heng, "Multiscale geodesic active contours for ultrasound image segmentation using speckle reducing anisotropic diffusion," *Optics and Lasers in Engineering*, vol. 54, pp. 105–116, 2014.
- [56] J. Kennedy and R. Eberhart, "Particle swarm optimization," in *Proceedings of the International Conference on Neural Networks, (ICNN '95)*, vol. 4, pp. 1942–1948, IEEE, Perth, Australia, 1995.
- [57] K. E. Parsopoulos and M. N. Vrahatis, "Particle swarm optimization method in multiobjective problems," pp. 603–607, Proceedings of the ACM symposium, Madrid, Spain, March 2002.
- [58] M. Elad, "On the origin of the bilateral filter and ways to improve it," *IEEE Transactions on Image Processing*, vol. 11, no. 10, pp. 1141–1151, 2002.
- [59] R. C. Gonzalez and R. E. Woods, *Digital Image Processing*, Prentice Hall, Upper Saddle River, NJ, USA, 2nd edition, 2001.

- [60] D. Comaniciu and P. Meer, "Mean shift analysis and applications," in *Proceedings of the 7th IEEE International Conference on Computer Vision*, vol. 2, pp. 1197–1203, Kerkyra, Greece, September 1999.
- [61] N. Otsu, "A threshold selection method from gray-level histograms," *Automatica*, vol. 11, pp. 23–27, 1975.
- [62] N. R. Pal and D. Bhandari, "Image thresholding: some new techniques," *Signal Processing*, vol. 33, no. 2, pp. 139–158, 1993.

Research Article

Age and Sex Effects on the Active Stiffness of Vastus Intermedius under Isometric Contraction

Cong-Zhi Wang,^{1,2} Jing-Yi Guo,² Tian-Jie Li,² Yongjin Zhou,³
Wenxiu Shi,³ and Yong-Ping Zheng²

¹Paul C. Lauterbur Research Center for Biomedical Imaging, Institute of Biomedical and Health Engineering, Shenzhen Institutes of Advanced Technology, Chinese Academy of Sciences, Shenzhen, China

²Interdisciplinary Division of Biomedical Engineering, the Hong Kong Polytechnic University, Hong Kong

³School of Biomedical Engineering, Shenzhen University, Shenzhen, China

Correspondence should be addressed to Yongjin Zhou; yjzhou@szu.edu.cn

Received 5 August 2016; Revised 30 October 2016; Accepted 16 March 2017; Published 3 April 2017

Academic Editor: Hiroshi Tanaka

Copyright © 2017 Cong-Zhi Wang et al. This is an open access article distributed under the Creative Commons Attribution License, which permits unrestricted use, distribution, and reproduction in any medium, provided the original work is properly cited.

Previously, a novel technique was proposed to quantify the relationship between the muscle stiffness and its nonfatigue contraction intensity. The method extended the measured range of isometric contraction to 100% maximum voluntary contraction (MVC) using an ultrasonic shear wave measurement setup. Yet, it has not been revealed how this relationship could be affected by factors like age or sex. To clarify these questions, vastus intermedius (VI) stiffness of 40 healthy subjects was assessed under 11 step levels of isometric contraction. The subjects were divided into four groups: young males, young females, elderly males, and elderly females ($n = 10$ for each). In a relaxed state, no significant difference was observed between the male and female subjects ($p = 0.156$) nor between the young and elderly subjects ($p = 0.221$). However, when performing isometric contraction, the VI stiffness of males was found to be significantly higher than that of females at the same level ($p < 0.001$), and that of the young was higher than the elderly ($p < 0.001$). Meanwhile, for two knee joint angles used, the stiffness measured at a 90° knee joint angle was always significantly larger than that measured at 60° ($p < 0.001$). Recognizing the active muscle stiffness of VI contributes to body stability, and these results may provide insight into the age and sex bias in musculoskeletal studies, such as those on fall risks.

1. Introduction

Skeletal muscle is the largest tissue within the fat-free human body mass. Its primary function, force generation, is based on its ability to contract voluntarily. The neuromuscular activity during muscle contraction has been studied in depth by means of electromyography (EMG) and mechanomyography (MMG) signals (e.g., [1, 2]). Similar studies have also been performed by morphological parameters, such as muscle thickness, pennation angle, fascicle length, and cross-sectional area (CSA), which can be estimated in vivo from medical images [3, 4]. In particular, the age and sex effects on these neuromuscular features and morphology characteristics have become the focus of research. The degenerative loss of skeletal muscle mass and strength in elderly humans have been confirmed and were found to be associated with the increased susceptibility to fall and a

decreasing mobility [5–8]. The higher risk of injury among females on their joints was also found to be related to the sex differences of the skeletal muscle characteristics [9–11]. Furthermore, for voluntary muscle contraction under different joint angles, EMG activity and some morphology characteristics have been proved to also change [12–15]. In addition to neuromuscular features and morphological characteristics, recently the mechanical properties of skeletal muscle have attracted more attention. Skeletal muscle is typically composed of contractile (myosin) and passive elastic (actin and connective tissues) components. Stiffness, which is observed in both active and passive muscle behaviours, has been shown to contribute significantly to muscle efficiency [16]. Passive stiffness of muscle is important for the control of movement because it determines the muscle resistance to external perturbations, while active muscle stiffness plays a key role in both force generation and body movements.

It is well-known from simple palpation that muscle stiffness increases during voluntary contraction, and quantifying muscle stiffness under different voluntary contraction levels can help us better understand the muscle recruitment strategies. Subsequently, a number of methods have been developed for noninvasive muscle stiffness assessment, such as the indentation assessment method [2], sonoelastography [17], transient elastography [18], supersonic shear imaging (SSI) [19, 20], shear wave dispersion ultrasound vibrometry (SDUV) [21], and magnetic resonance elastography (MRE) [22–24]. It has been reported that different muscles exhibited different stiffness in a relaxed state [23], and it has been also found that the stiffness of skeletal muscle is positively correlated to its nonfatigue contraction intensity within a small range of isometric contraction levels, that is, from 0% to 20–60% maximum voluntary contraction (MVC) levels [18, 20, 22, 24]. However, due to the limitation of the measurement range, this conclusion has rarely been verified over the entire range of isometric contraction, that is, from 0% to 100% MVC. In our previous study [25, 26], a vibroelastography setup has been reported to assess the shear modulus of skeletal muscle along the direction of muscle action. The positive correlation between the shear modulus of vastus intermedius (VI) and the relative isometric contraction level (% MVC) of the knee extensor has been verified over the entire range of isometric contraction on young and elderly healthy females subjects. However, the effects of different age ranges and sex on the relationship between muscle stiffness and isometric contraction levels have not been systematically studied, although some related studies have been performed separately [26–29], but none over the entire range of MVC. To clarify these questions, vastus intermedius, one of the quadriceps femoris muscles, was selected as the target of this study. Quadriceps femoris is a muscle group including four powerful extensors of knee joint on the front of the thigh. VI lies between vastus lateralis (VL) and vastus medialis (VM), right under the rectus femoris (RF) and above the femur. They are the strongest and leanest muscles of the human body and are crucial in walking, running, jumping, and squatting [30]. Previously, several studies have been performed to investigate the structure, function, and characteristics of quadriceps femoris muscles, including their mechanical properties [5, 22, 23, 31]. In addition, the sex difference between adult men and women [32] and the age difference between young and elderly adults [5] of the morphological parameters have also been compared. In the present study, VI stiffness was assessed on the subjects from four different subject groups: young males, young females, elderly males, and elderly females ($n = 10$ for each group), and the experiments were repeated at two different knee joint angles, 90° and 60° (0° corresponds to full extension for all joint angles in this paper). The age and sex effects on VI stiffness over the entire range of step isometric contraction were systematically analyzed and discussed. It is believed that these results could provide new information regarding the phenomenon, such as the higher risk of ACL (anterior cruciate ligament), cartilage injury, or fall among females than males, and facilitate investigations on the process of muscle ageing and the probability of its rehabilitation.

2. Materials and Methods

2.1. Ethics Statement. In this study, human subject ethical approval was obtained from the Human Ethics Committee of the Hong Kong Polytechnic University, and the experimental protocol was explained to all of the subjects and they were asked to sign the informed consent form prior to the experiment.

2.2. Subjects Selection. Forty healthy subjects volunteered to participate in the experiments and were divided into four groups: young males, young females, elderly males, and elderly females (Table 1). They were asked not to participate in any strength or flexibility training one day before the experiment.

The experimental setup was almost the same as that described in our previous study [26].

The vibroelastography system consists of a mechanical vibrator, a programmable ultrasound scanner, and a custom-made program for radiofrequency data acquisition. An electromagnetic vibrator (minishaker type 4810, Brüel & Kjær, Nærum, Denmark), which was driven by a power amplifier and controlled by a function generator, was used to induce transient low-frequency shear waves (monochromatic sinusoidal pulse). An ultrasound linear array probe was placed along the muscle action direction, so that the tissue movements in response to external mechanical vibration can be monitored by two separated ultrasound scan lines (to spatially sample the induced shear waves), as shown in Figures 1(a) and 1(b) [26]. The distance between these two lines was Δr (15 mm in this study) and the time delay between the two positions was Δt .

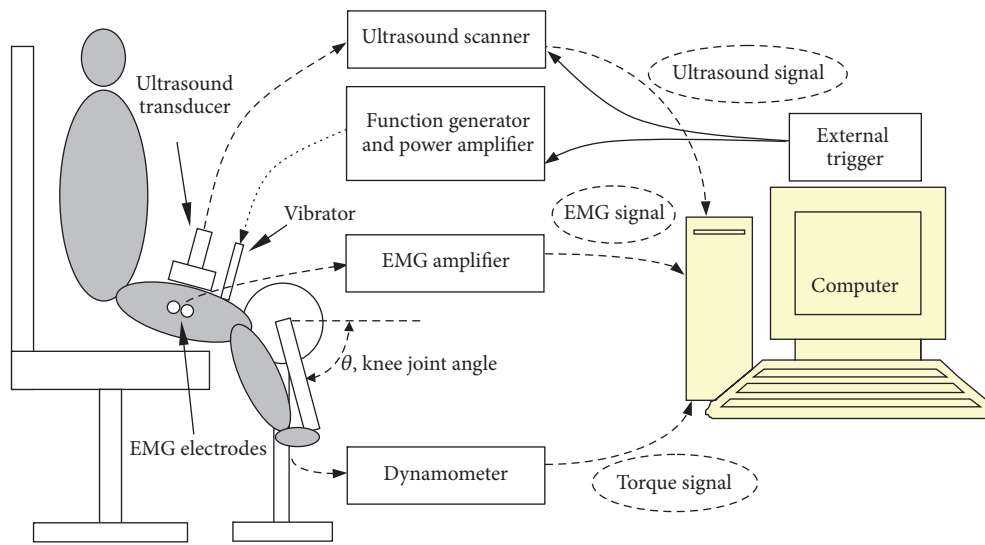
Then the shear wave velocity c_s could be calculated by

$$c_s = \frac{\Delta r}{\Delta t}. \quad (1)$$

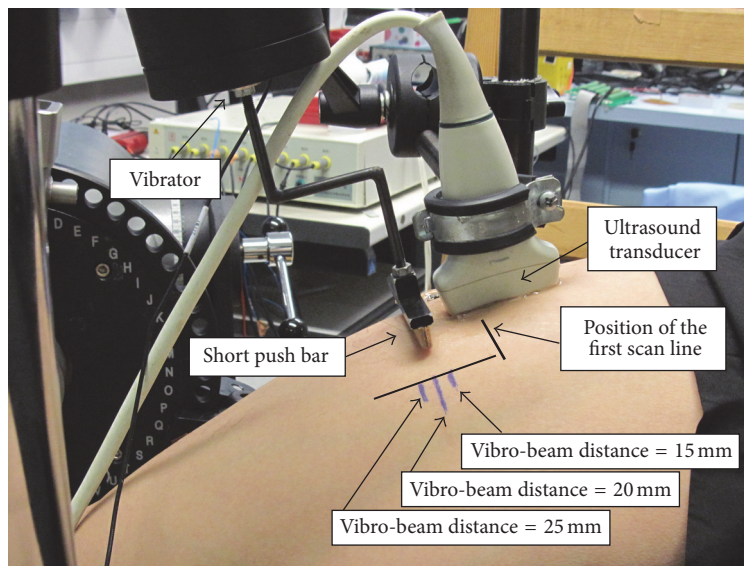
The shear modulus μ of the measured muscle can then be calculated via the following equation:

$$\mu = \rho c_s^2, \quad (2)$$

where ρ was the mass density of the muscle tissue, using a reported approximate value as 1000 kg/m^3 . The equation and the parameter value used have been proved to be promising for estimating the shear modulus of skeletal muscle in many previous studies [22–24, 26, 33]. The data acquisition part was developed based on a commercial ultrasound scanner SonixRP (Ultrasonix Medical Corp. Vancouver, Canada) with a 5–14 MHz linear array probe. B-mode images were first acquired using a predefined penetration depth (65 mm in this study) to help position the probe. When triggered by an external signal of starting vibration, B-mode imaging was stopped and two scan lines were repeated with a high frame rate (4.6 kHz in this study). The tissue movements were then estimated by an improved cross-correlation algorithm and the shear wave velocity and shear modulus were calculated. Isometric torque generated by the knee extensors was assessed using a HUMAC NORM rehabilitation system (Computer Sports Medicine, Inc., Stoughton, MA, USA).



(a)



(b)

FIGURE 1: Illustration (a) and photo (b) of the experiment setup for human subjects.

The machine was set to a knee joint isolated movement pattern and isometric resistance mode, under which the knee joint angle can be set and fixed. The EMG signals were also captured from the surface of VL muscle, but the results were not included in this paper. The whole experimental setup for human subjects is illustrated in Figure 1.

2.3. Experimental Protocol. At first, the ultrasound probe was placed on the middle part of the RF muscle belly right above the VI and femur with the guidance of B-mode images. The distance between the probe and vibrator was set to be approximately 10 mm (i.e., the distance between the short push bar and the proximal scan line was about 20 mm). The MVC torque was first assessed as the highest torque value of subjects produced from three successive isometric

contractions, when subjects were asked to put forth all of their strength to extend their knee joints. Next, the muscle stiffness was measured three times in a relaxed state. Then the subject was asked to maintain isometric contraction at different levels, from 10% to 100% MVC, with an increase of 10% MVC for each step. At each level, assessments were performed for three times with about a 1 min interval for a rest to avoid fatigue. For each trial, the subject was asked to maintain the isometric contraction for approximately 4 s. Experiments were performed at two different knee joint angles, 90° and 60°.

2.4. Data Analysis. Part of the data, measured on the young and elderly female subjects at a 60° knee joint angle, has been presented and analyzed in our previous study [26]. A more detailed comparison was performed in this paper

on the data of all four groups of subjects. A total of 2640 (4 [groups: young males, young females, elderly males, and elderly females] \times 10 [subjects per group] \times 11 [contraction levels: 0%–100% MVC] \times 2 [knee joint angles] \times 3 [measured three times]) shear modulus assessments were performed by the same investigator. To study the influences of the interested factors, including age and sex, on the muscle stiffness in a relaxed state and different isometric contraction levels, four-way repeated measure analyses of variance (ANOVA) (age [young and elderly] \times sex [male and female] \times knee joint angles [90° and 60°] \times % MVC [0%–100%, 11 levels]) were used to analyze the shear modulus of the VI. Specially, the comparison of the VI shear modulus measured in a relaxed state (0% MVC) was first performed separately using a three-way ANOVA method.

Two methods were used to exhibit the different contraction intensities; one was to use the relative muscle contraction level (% MVC), and the other one was to use the absolute torque of the knee joint extensors. These two methods focused on different aspects. Using the former aspect, muscle stiffness was studied at different relative levels of the maximal muscle contraction capability for each person, considering the individual muscle strength difference. On the other hand, using the later aspect, muscle stiffness was generally evaluated corresponding to the absolute torque and it is meaningful in a specific group of people. The results of both methods could help us to further understand the muscle function and recruitment strategies from different perspectives, that is, from the perspective of the changes of its mechanical properties over the entire range of step isometric contraction, besides the perspective of neuroelectric activity, which is conventionally measured by electromyography (EMG). In our study, to determine the relationship between the VI stiffness and relative isometric contraction level (% MVC), polynomial regression analyses by linear, quadratic, and cubic models were performed for each individual, and the coefficients of determination (R^2) values of these models were compared using one-way ANOVA to find the best model. The mean shear modulus values across the ten subjects in each group then were fitted with the relative isometric contraction level (% MVC) using a quadratic regression model. From another perspective, to study the relationship between the VI shear modulus and the corresponding absolute torque, quadratic regression was performed for each individual subject and the 10 sets of polynomial coefficients in each group were averaged to represent the trend of this relationship. The achieved quadratic curve was plotted in a range from 0 N·m to the mean MVC torque value in each group. All the data were analyzed using SPSS (SPSS Inc., Chicago, IL, USA). Statistical significance was set at the 5% probability level.

3. Results

3.1. Results of Multiway ANOVA Analysis. Firstly, the mean MVC torques of the knee extensors in each group, and for different knee joint angles, are listed in Table 2. The results of the three-way ANOVA showed that the main effects of age ($p = 0.01$), sex ($p < 0.001$), and knee joint angle ($p = 0.001$) factors were all significant for the mean MVC torque.

TABLE 1: Demographic information of the subjects presented with mean (SD).

	Age (yr)	Height (cm)	Mass (kg)
Young males ($n = 10$)	29.4 (4.8)	174.7 (8.1)	73.3 (13.0)
Young females ($n = 10$)	27.6 (5.0)	164.3 (4.4)	55.3 (4.0)
Elderly males ($n = 10$)	60.6 (7.6)	166.7 (5.8)	66.1 (11.9)
Elderly females ($n = 10$)	56.7 (4.9)	156.9 (5.6)	58.9 (8.4)

However, all of the two-way interaction effects were not significant (all $p > 0.1$). According to the estimated marginal mean values provided by the ANOVA method (the marginal means for one factor are the means for that factor averaged across all levels of the other factors), the conclusion was that the mean MVC torque for males was larger than that for females; the values from young subjects were larger than those from elderly subjects; the values measured at the 90° knee joint angle were larger than those measured at 60°.

Comparison of the VI shear modulus in a relaxed state (0% MVC) was performed first. The means of VI shear modulus from each group are shown in Table 3. Results of the multiway ANOVA showed that there was no significant main effect for sex ($p = 0.156$) and age ($p = 0.221$) factors, and an interactive effect between each of the two factors (all $p > 0.05$) on the VI shear modulus was measured in a relaxed state. However, there was a significant main effect for the knee joint angle factor ($p = 0.001$) on the VI shear modulus. The estimated marginal mean value of the VI shear modulus measured at 90° knee joint angle (16.2 ± 8.1 kPa) was larger than the mean value at 60° knee joint angle (11.1 ± 4.4 kPa) in this state.

For the VI shear modulus measured under different step isometric contraction levels, there were no significant four- or three-way interaction effects among the four factors (sex \times age \times % MVC \times knee joint angles, all $p > 0.05$). All of the main effects of the single factor on the VI shear modulus were significant. The estimated marginal mean value of males was larger than that of females ($p < 0.001$). The mean value of young subjects was larger than that of elderly participants ($p < 0.001$), and the mean value measured at a 90° knee joint angle was larger than that measured at 60° ($p < 0.001$). In addition, the results of the post hoc Bonferroni test for the VI shear modulus measured at different percentages of MVC levels are shown in Table 4, which shows the detailed effects of the relative isometric contraction level on VI stiffness. Furthermore, all of the two-way interactions, including the sex factor, were not significant (all $p > 0.1$) and all other two-way interaction effects, that is, age and % MVC, joint angles and % MVC, and age and joint angles, were significant (all $p < 0.001$). For age and % MVC interaction, with an increase in the % MVC, differences between the VI shear modulus of young subjects and that of elderly subjects also increased. A similar relationship was also found for joint angles and % MVC; with an increase in the % MVC, differences between the VI shear modulus measured at a 90° knee joint angle and that at 60° also increased. For age and joint angles, the differences of VI shear modulus between the young and elderly subjects were larger at a 90° knee joint angle than

TABLE 2: The mean MVC torque (N·m) of knee extensors in each group at 90° and 60° knee joint angles.

Knee joint angle	Young male	Young female	Elderly male
90°	166 ± 32.8	126 ± 34.0	102 ± 30.4
60°	136 ± 18.4	102 ± 32.0	84 ± 18.4

TABLE 3: The mean VI shear modulus (kPa) of each group in a relaxed state (0% MVC), shown separately for 90° and 60° knee joint angles.

Knee joint angle	Young male	Young female	Elderly male	Elderly female
90°	14.5 ± 6.3	19.0 ± 10.2	13.8 ± 7.4	17.2 ± 8.4
60°	11.6 ± 3.5	12.8 ± 5.4	10.3 ± 5.0	9.5 ± 3.3

TABLE 4: Multiway ANOVA showed significant main effects of percentage of MVC level on VI shear modulus. The post hoc Bonferroni comparisons results showed the details of the relationships among these levels.

Percentage of MVC	Post hoc comparisons results
0%	<30%–100%, $p < 0.05$
10%	<40%–100%, $p < 0.005$
20%	<50%–100%, $p < 0.001$
30%	>0%, $p < 0.05$; <50%–100%, $p < 0.05$
40%	>0%–10%, $p < 0.005$; <60%–100%, $p < 0.001$
50%	>0%–30%, $p < 0.05$; <70%–100%, $p < 0.001$
60%	>0%–40%, $p < 0.001$; <80%–100%, $p < 0.001$
70%	>0%–50%, $p < 0.001$; <80%–100%, $p < 0.05$
80%	>0%–70%, $p < 0.05$; <90%–100%, $p < 0.005$
90%	>0%–80%, $p < 0.005$; <100%, $p < 0.001$
100%	>0%–90%, $p < 0.001$

at 60°. The detailed relationships are shown in Figure 2 by plotting the estimated marginal means of the VI shear modulus together.

3.2. Analysis Based on Relative Isometric Contraction Level (% MVC). Polynomial regression analyses by linear, quadratic, and cubic models were performed on the relationship between VI shear modulus and relative isometric contraction level (% MVC) for each individual and the mean R^2 of three models were 0.937 ± 0.034 (linear), 0.992 ± 0.007 (quadratic), and 0.995 ± 0.004 (cubic), respectively. The results of the one-way ANOVA indicated that there was no significant difference between the R^2 of the quadratic model and cubic model ($p = 0.390$). However, significant differences were found between the R^2 of the linear model and the other two models (all $p < 0.001$). Thus, the quadratic model was selected to examine the relationship of the VI shear modulus and relative isometric contraction level. The mean shear modulus across the ten subjects in each group at the same knee joint angle was fitted using a quadratic regression model with the relative isometric contraction level, as shown in Figure 3. Pearson's correlation coefficients (CC) between VI shear modulus and % MVC level in each group and knee joint angle are listed in Table 5, which were all larger than 0.96. This indicated that the VI stiffness along the muscle action direction was positively correlated to the relative muscle

activity intensity level of the knee extensors over the entire range of step isometric contraction. The plots also indicated that the VI shear modulus measured at a 90° knee joint angle was larger than the corresponding value measured at a 60° knee joint angle at almost each % MVC level in each group of subjects, which was in agreement with the result of the multiway ANOVA analysis.

The results between young and elderly groups with the same sex at the same knee joint angle were compared, as shown in Figure 4. It was observed that, for both sexes and knee joint angles, the VI shear moduli of young subjects were larger than those of elderly participants, especially at the relatively higher % MVC level. The results were also compared between the two sexes with a similar age range at the same knee joint angle, as shown in Figure 5. The comparison showed that for both age ranges and knee joint angles, the VI shear moduli of males were larger than those of females, especially at the relatively higher % MVC level. However, at the corresponding relative muscle contraction level, the sex difference seemed to be smaller than the age difference. These results were both in agreement with those obtained using multiway ANOVA that the main effects of age and sex factors were significant.

3.3. Analysis Based on Absolute Isometric Contraction Torque. Since, for each individual subject, the R^2 value did not change when only the scale of the x -axis changed from the relative % MVC level to the absolute contraction torque, the quadratic regression model could also be used for examining the trend of the relationship between the VI shear modulus and absolute torque. The quadratic curves of each group were plotted to investigate the different trends at 90° and 60° knee joint angles, respectively. It was observed that, with the increasing absolute torque, VI shear modulus increased faster at a 90° knee joint angle than at a 60° knee joint angle, as demonstrated in Figure 6. This result was similar to the relationship between the VI shear modulus and relative muscle contraction level. The relationships between the VI shear modulus and absolute torque with different age ranges and the same sex at the same knee joint angle were also plotted (Figure 7). The results indicated that the VI shear modulus of young subjects increased faster compared with that of elderly subjects. This relationship also coincided with that between the VI shear modulus and relative muscle contraction level. Furthermore, the relationships between the VI shear modulus and the absolute torque of different

TABLE 5: Pearson’s correlation coefficients between VI shear modulus and relative isometric contraction levels in each group and at different knee joint angles.

Knee joint angle	Young male	Young female	Elderly male	Elderly female
90°	0.977	0.974	0.980	0.975
60°	0.971	0.968	0.975	0.979

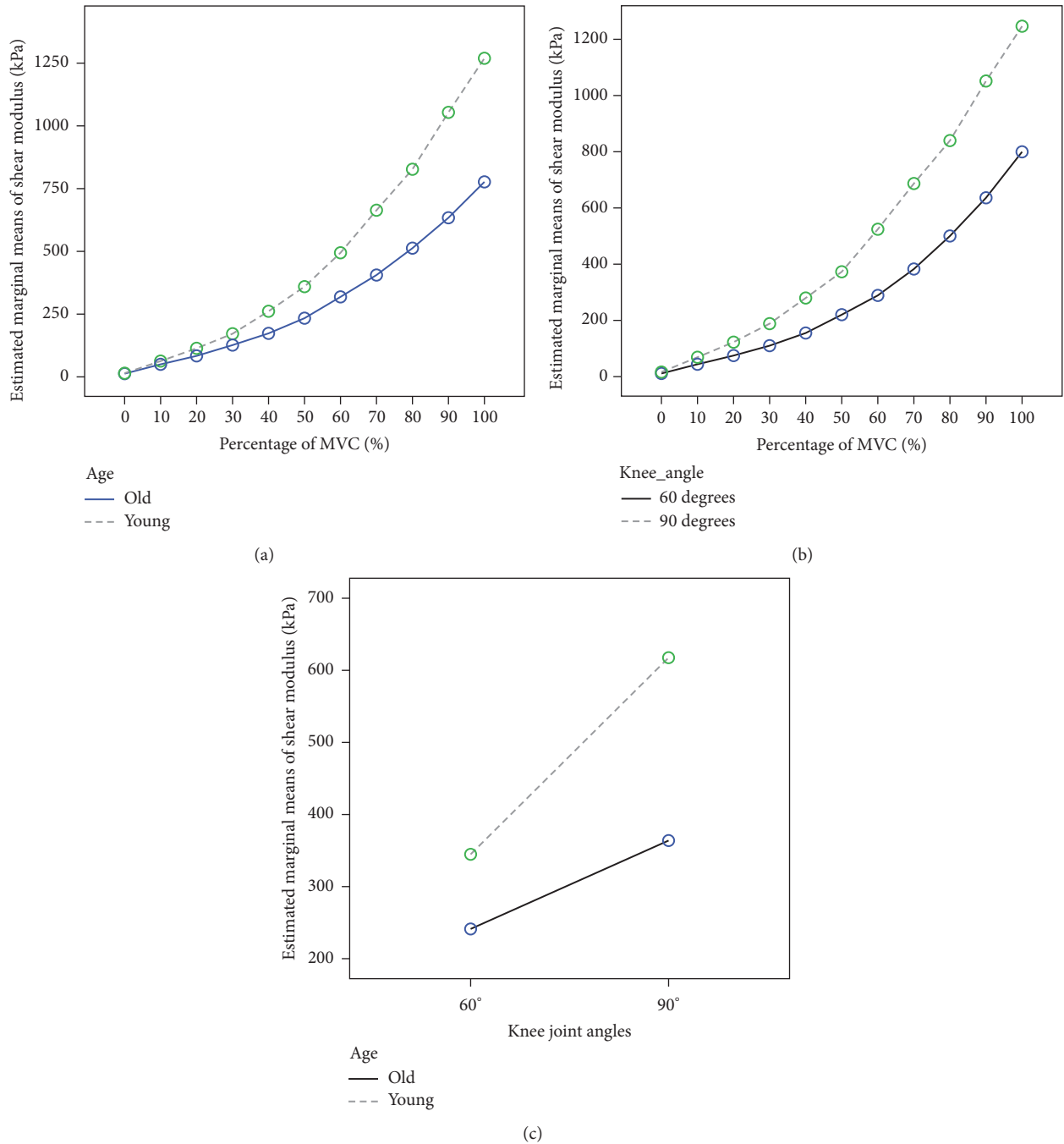


FIGURE 2: Estimated marginal means of VI shear modulus plotted for illustrating the significant two-way interaction effects for (a) age versus % MVC. (b) Angles versus % MVC. (c) Age versus joint angles.

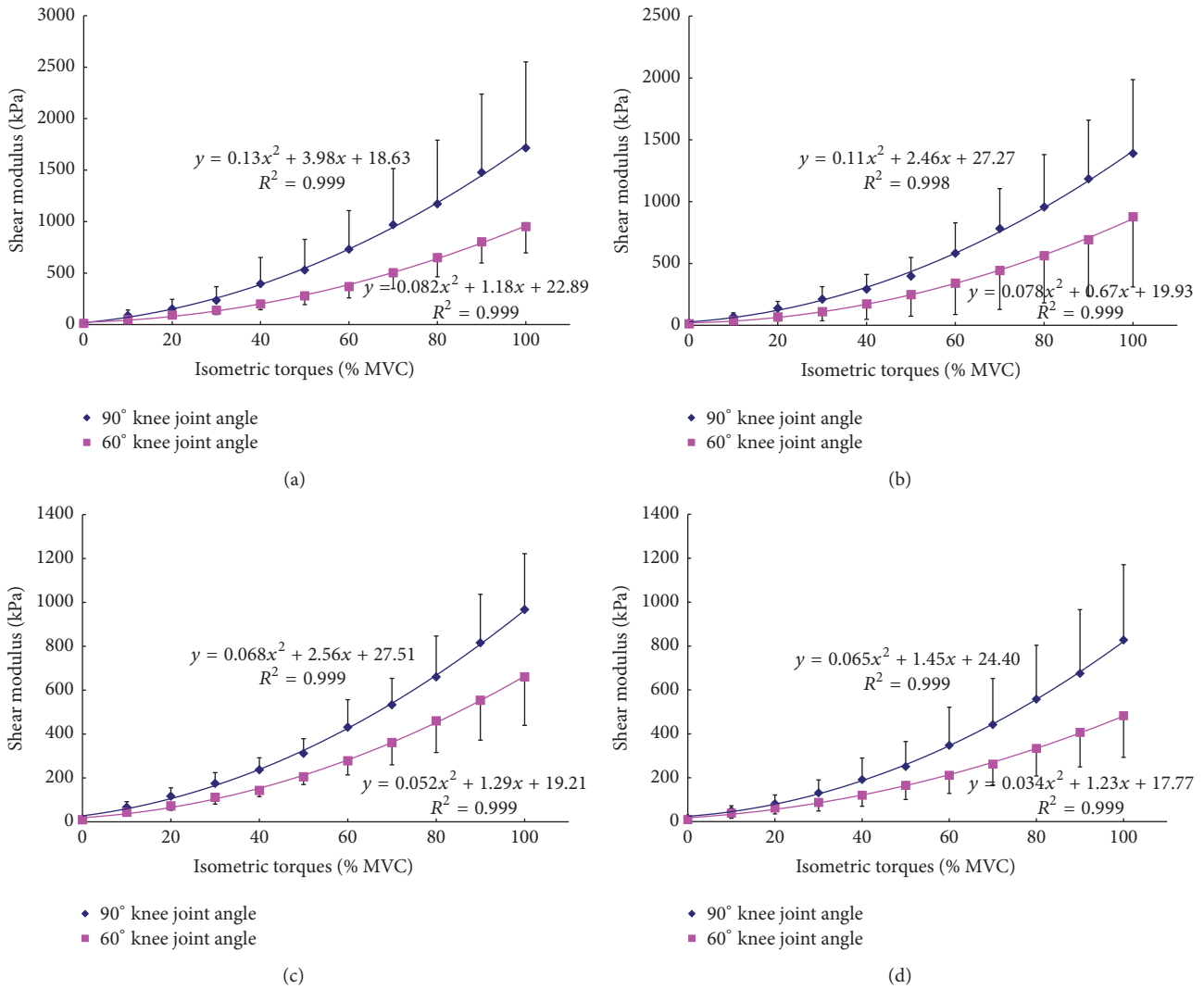


FIGURE 3: The mean VI shear modulus at different relative isometric contraction levels (% MVC) and different knee joint angles (90° and 60°) with the corresponding quadratic regression fitting curves for (a) young male subjects; (b) young female subjects; (c) elderly male subjects; and (d) elderly female subjects.

sexes and the same age range at the same knee joint angle were also compared, as shown in Figure 8. The results showed that the VI shear modulus of females increased faster than that of males. However, this result was opposite to the relationship between the VI shear modulus and relative muscle contraction level. The reason for this conflict might be due to the relatively smaller MVC torque of the female subjects and will be further discussed in the following section.

4. Discussion

The current study provided some quantitative information regarding the VI stiffness at various contraction levels, especially the difference related to different age, sex, and joint angle.

4.1. Stiffness of VI in a Relaxed State. It was found in our study that the mean shear moduli of VI in a relaxed state for all

subjects were 16.2 ± 8.1 kPa (at 90° knee joint angle) and 11.1 ± 4.4 kPa (at 60° knee joint angle). Although several methods based on shear wave velocity measurement have been used to estimate the shear modulus of muscle, few studies have been reported to assess the VI stiffness. The MRE method has been used on the quadriceps femoris muscles, but only on VL and VM. Bensamoun et al. [23] measured the shear modulus of VL and VM in a relaxed state on young healthy subjects. The mean values were 3.73 ± 0.85 kPa and 3.91 ± 1.15 kPa, respectively. The stiffness of VM was also assessed in another study [22], using both 2D MRE and 1D MRE methods, and the reported shear moduli were 4.36 ± 0.98 kPa and 3.69 ± 0.80 kPa, respectively. Although it was difficult to directly compare these results with ours since the target muscles were different, all of the measured shear modulus values fell into a similar range. It seemed that the VI muscle, which is a bipennate muscle, exhibited higher stiffness than VL and VM, in which the fiber orientation is unipennate. This difference

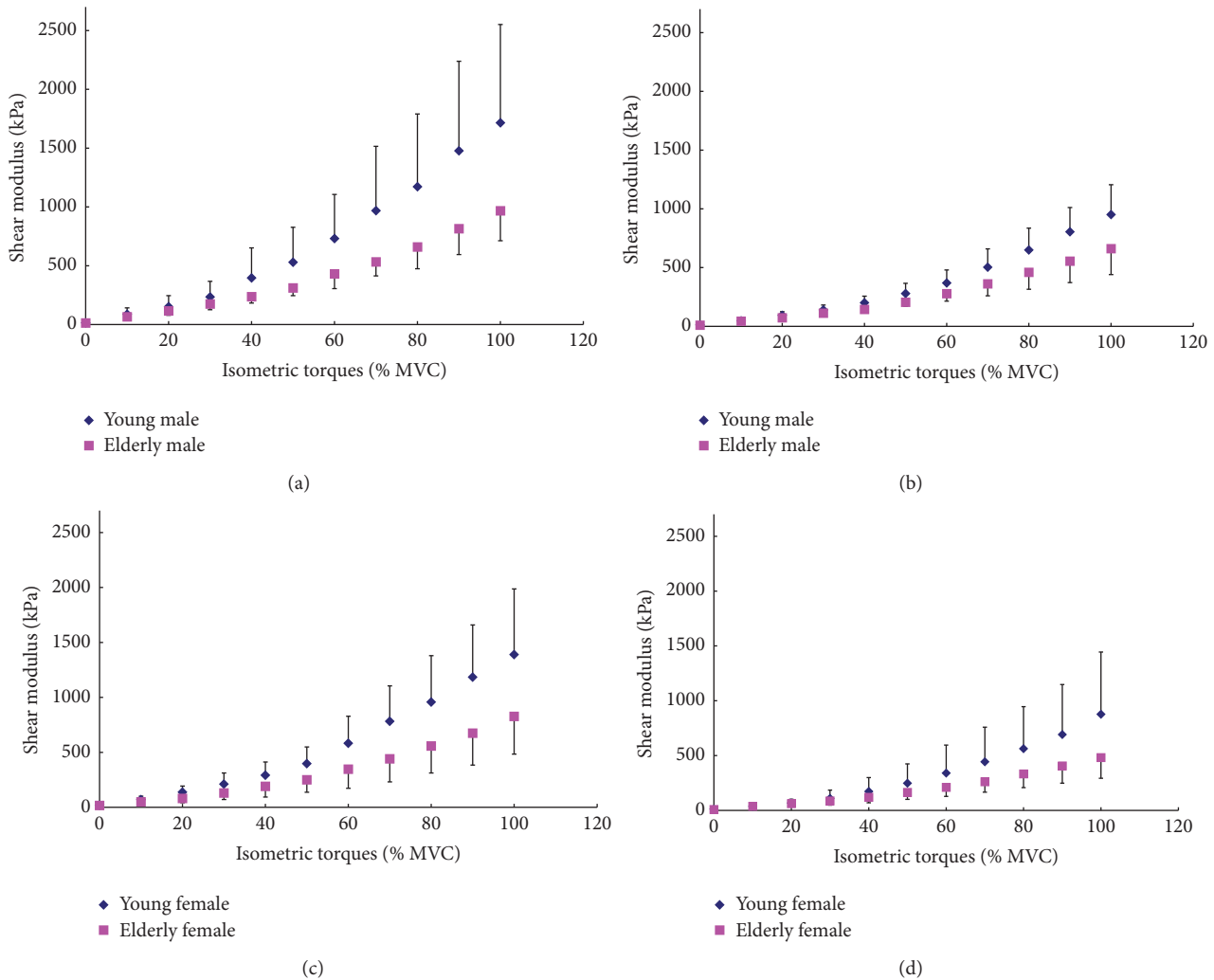


FIGURE 4: The age effects on the mean VI shear modulus at different relative isometric contraction levels (% MVC) between the subjects with same gender. Comparisons were made between young and elderly male subjects at (a) 90° and (b) 60° knee joint angles and between young and elderly female subjects at (c) 90° and (d) 60° knee joint angles.

may indicate that the propagation of shear waves is influenced by the muscle structure, such as muscle fiber orientation [23]. In addition, the different stiffness might be also related to muscle volume, muscle fiber type, muscle function, or other specific muscle characteristics. Furthermore, the results measured in a relaxed state might be also influenced by some other factors, such as the slight unconscious muscle tension during measurements and the momentary stiffness change due to the history of muscle use [29]. The effects of sports and exercises on muscle stiffness should be investigated in future studies. It was found that the mean value of VI shear modulus in a relaxed state measured at a 90° knee joint angle (16.2 ± 8.1 kPa) was significantly larger than that measured at a 60° knee joint angle (11.1 ± 4.4 kPa) ($p < 0.001$). Few studies have been performed to investigate the relationship between the VI shear modulus and knee joint angle. The shear moduli of relaxed tibialis anterior (TA) and lateral gastrocnemius (LG), which are muscles in distal leg, were studied using

MRE at different ankle joint angles [34]. Shear modulus of LG increased to 35.1 ± 0.4 kPa at 20° of dorsiflexion from 22.1 ± 0.2 kPa at neutral but decreased to 18.4 ± 0.1 kPa at 45° of plantar-flexion. The shear modulus of TA increased from 12.3 ± 0.5 kPa at neutral to 32.5 ± 0.2 kPa at 45° of plantar-flexion and was almost unchanged at 20° of dorsiflexion (13.5 ± 0.4 kPa). These results indicated that muscle stiffness increased with the larger passive stretching. This was in agreement with our results. At a 90° knee joint angle, the VI was more stretched than at a 60° knee joint angle; thus it was reasonable that the shear modulus measured at 90° was larger. In addition to passive stretching, the difference of VI shear modulus might also be related to the morphology change with the different knee joint angles, such as fascicle length and pennation angle. When the knee was extended, the fascicle length of quadriceps femoris was reported to be shortened, and the pennation angle was reported to increase in step with the changes of knee joint angle [14, 15]. However, the

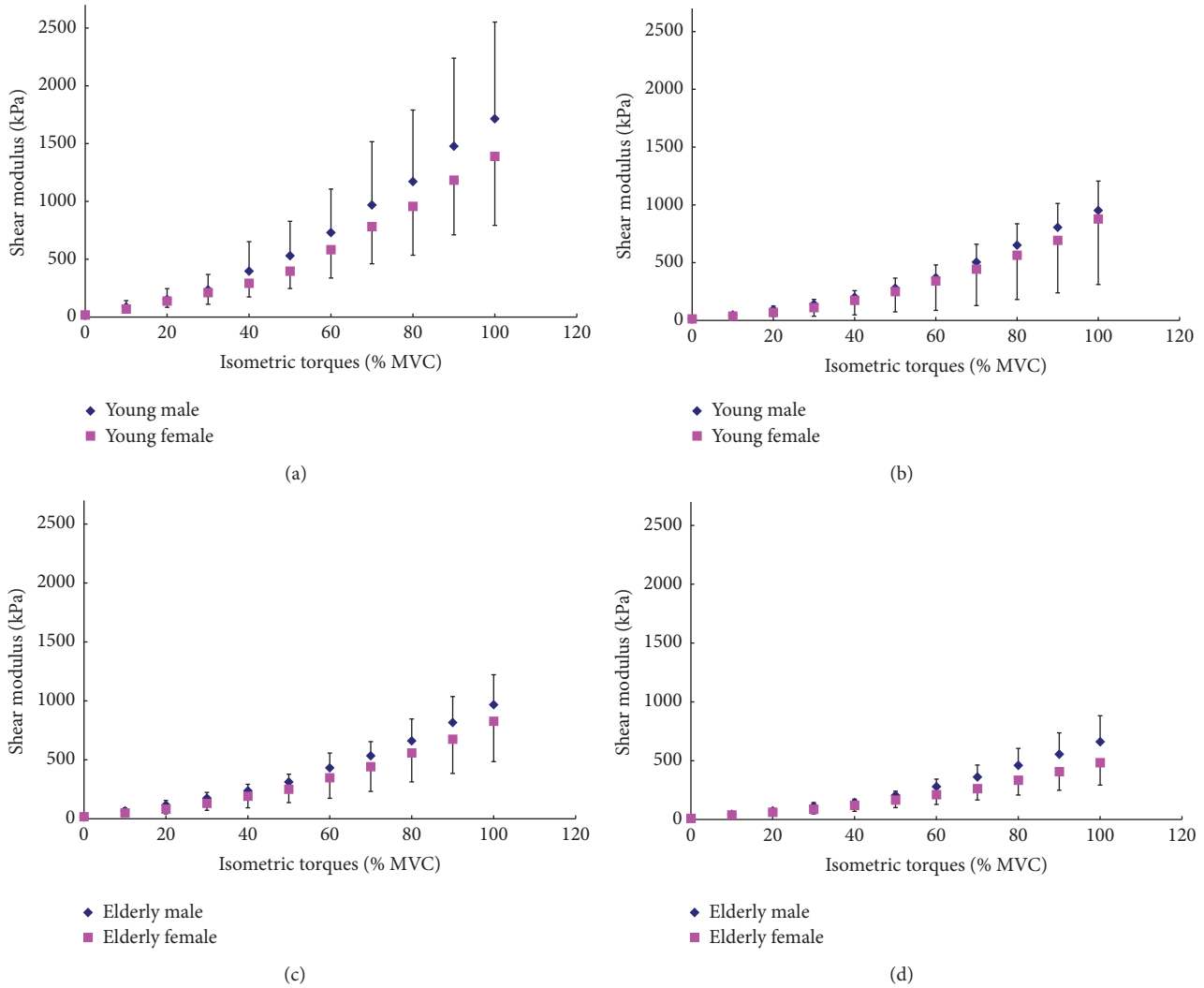


FIGURE 5: The gender effects on the mean VI shear modulus at different relative isometric contraction levels (% MVC) between subjects with similar age range. Comparisons were made between young male and female subjects at (a) 90° and (b) 60° knee joint angles, and between elderly male and female subjects at (c) 90° and (d) 60° knee joint angles.

detailed relationship between the changes of the VI stiffness and its morphology changes with the knee joint angle should be further studied.

4.2. Relationship between Muscle Stiffness and Step Isometric Contraction. As mentioned above, two methods have been used to exhibit the different contraction intensities, one is to use the relative muscle contraction level (% MVC), and the other one is to use the absolute torque of the knee joint extensor. In addition to these two methods, some previous studies also used different weight loads to represent the different muscle contraction levels, such as on the knee extensor [17] and on the elbow flexor [24]. However, the method using the weight load as an indicator was not accurate enough, since the length of limbs was different among the subjects and the lever of force was not counted.

4.2.1. Comparison with Previous Studies Based on Relative Isometric Contraction Levels. Our results demonstrated that the VI stiffness along the muscle action direction was positively correlated to the relative muscle contraction level (% MVC) at two different knee joint angles and over the entire range of isometric contraction. Some previous studies have been reported about the positive correlation between the muscle stiffness and the nonfatigue muscle contraction level on different muscles. In the study of Bensamoun et al. [23], the reported shear moduli of VL and VM were 6.11 ± 1.15 kPa and 4.83 ± 1.68 kPa at 10% MVC isometric contraction level measured using the MRE method, and when at 20% MVC contraction, the shear moduli of VL and VM were reported to be 8.49 ± 4.02 kPa and 6.40 ± 1.79 kPa, respectively. They also reported that the shear moduli of VL and VM in a relaxed state were 3.73 ± 0.85 kPa and 3.91 ± 1.15 kPa. Their results

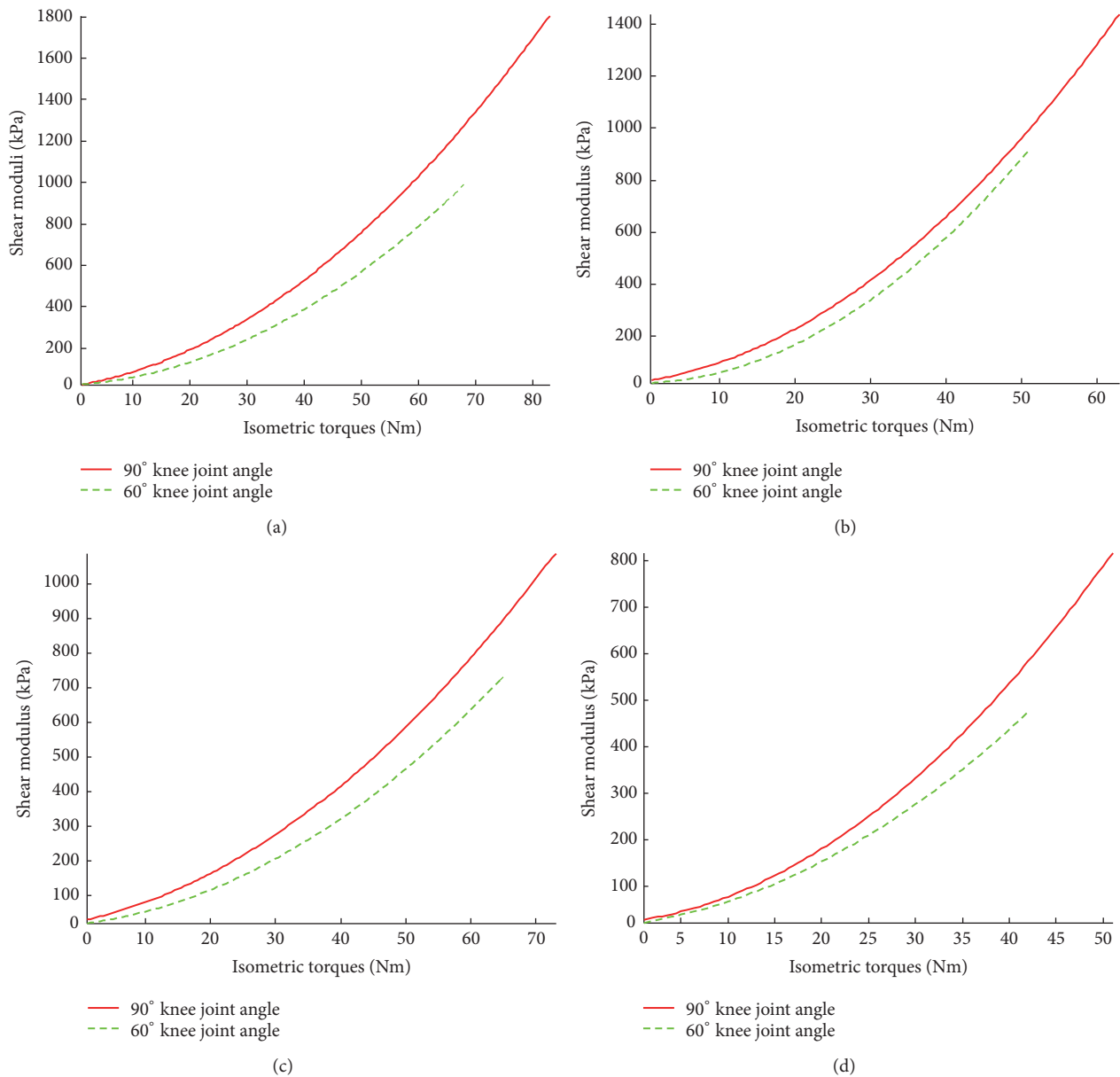


FIGURE 6: Comparison of the relationships between VI shear modulus and absolute torque at 90° and 60° knee joint angles for (a) young male subjects; (b) young female subjects; (c) elderly male subjects; and (d) elderly female subjects.

showed a significant increase ($p < 0.05$) in the shear modulus of VL and VM with the increase in the muscle contraction level. Since the subjects in this study were young males and young females, but were not distinguished by sex, the different structure of VI from VL and VM, as we mentioned above, and the different posture and knee joint angle they used were difficult to use to directly compare the stiffness values they measured with ours. However, our conclusion that there was a significant increase in the VI shear modulus with the increase in the isometric contraction level from 10% to 20% MVC was in good agreement with their finding.

4.2.2. Comparison with Previous Studies Based on Absolute Torques. In this study, it was demonstrated that the VI

shear modulus along the direction of muscle action was also positively correlated to the absolute torque. Some previous studies have reported the shear modulus measured under different absolute torques of joint extensors or flexors, but the investigation was rarely focused on the quadriceps femoris muscles. Several studies have been reported to assess the stiffness of distal leg muscles, such as TA, LG, medial gastrocnemius muscle (MG), and soleus muscle (SL), as groups of agonist and antagonist muscles. Muscle shear modulus was measured under isometric contraction when the subject resisted ankle plantar-flexing and dorsiflexing moments, of which the directions of applied moments were opposite. In the study of Heers et al. [35] using the MRE method, the shear modulus of TA increased significantly ($p < 0.0001$)

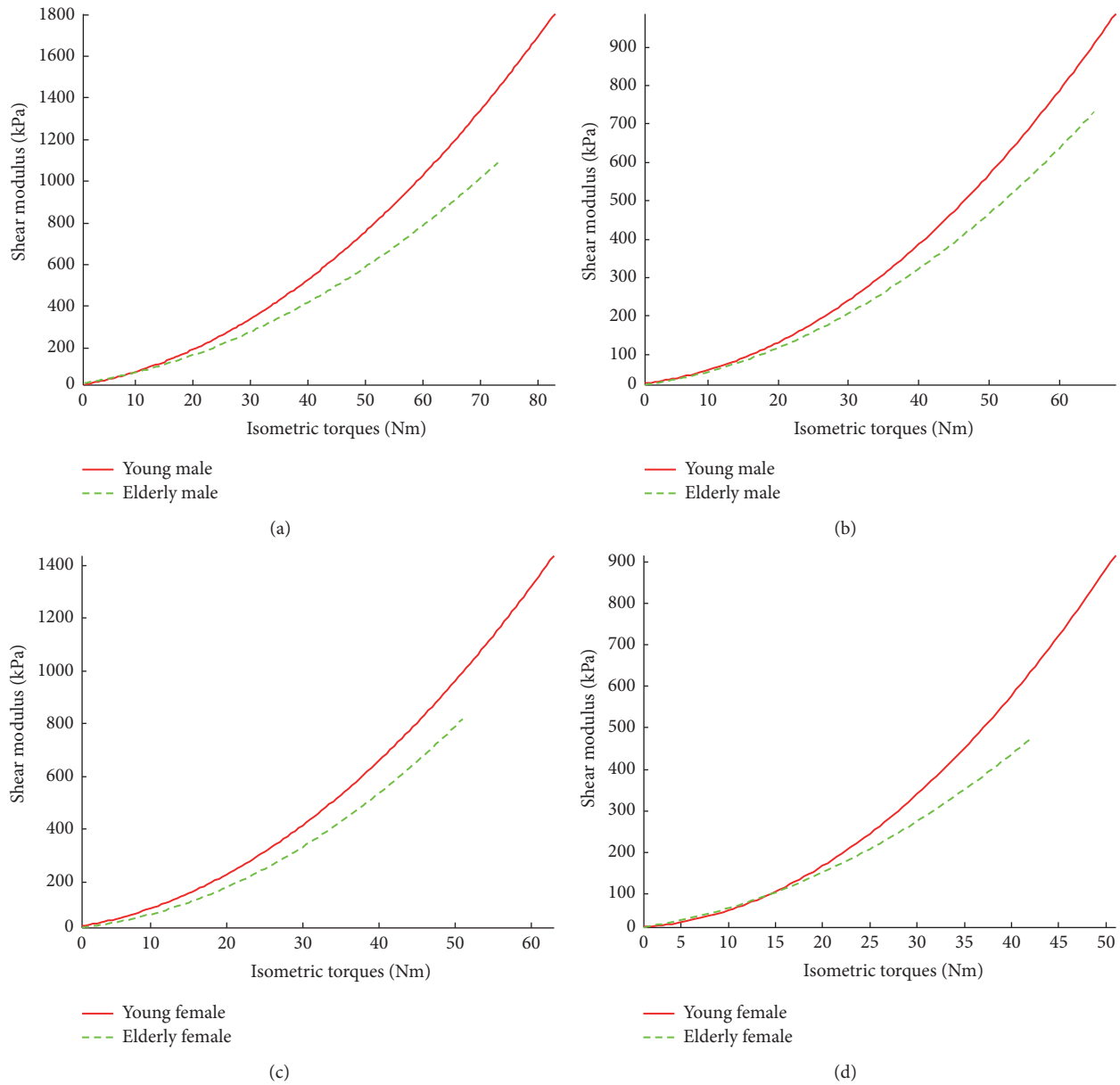


FIGURE 7: Age dependencies of the relationships between VI shear modulus and absolute torque. Comparisons were made between young and elderly male subjects at (a) 90° and (b) 60° knee joint angles and between young and elderly female subjects at (c) 90° and (d) 60° knee joint angles.

from 70.6 ± 1.8 kPa to 126.6 ± 5.1 kPa as the plantar-flexing moment increased from 8.2 N·m to 16.4 N·m. On the other hand, the shear modulus measured in the posterior muscles, that is, MG, LG, and SL, did not show significant changes ($p > 0.05$). Furthermore, when muscles resisted the dorsiflexing moments, as loads increased from 20.2 N·m to 40.4 N·m, the shear modulus increased significantly from 41.6 ± 5.1 kPa to 63.2 ± 5.1 kPa for MG ($p < 0.01$), from 27.6 ± 1.1 kPa to 73.1 ± 7.3 kPa for LG ($p < 0.003$), and from 36.0 ± 0.4 kPa to 65.6 ± 1.8 kPa for SL ($p < 0.001$). However, the shear modulus measured from TA did not change significantly with

load ($p > 0.05$), and a similar study was performed by Jenkyn et al. [34] on the distal leg muscles. The shear moduli of relaxed TA and LG with the foot in a neutral position were 12.4 ± 0.5 kPa and 22.1 ± 0.2 kPa, respectively. Shear modulus of TA increased to 133.7 ± 2.1 kPa during a 16 N·m dorsiflexing effort but was relatively unchanged during a 48 N·m plantar-flexing effort (30.1 ± 0.5 kPa). Shear modulus of LG decreased slightly during a 16 N·m dorsiflexing effort (15.0 ± 0.3 kPa) but significantly increased with a 48 N·m plantar-flexing effort (140.4 ± 0.3 kPa). Since the muscles they studied were different from ours, their results could not be directly compared with

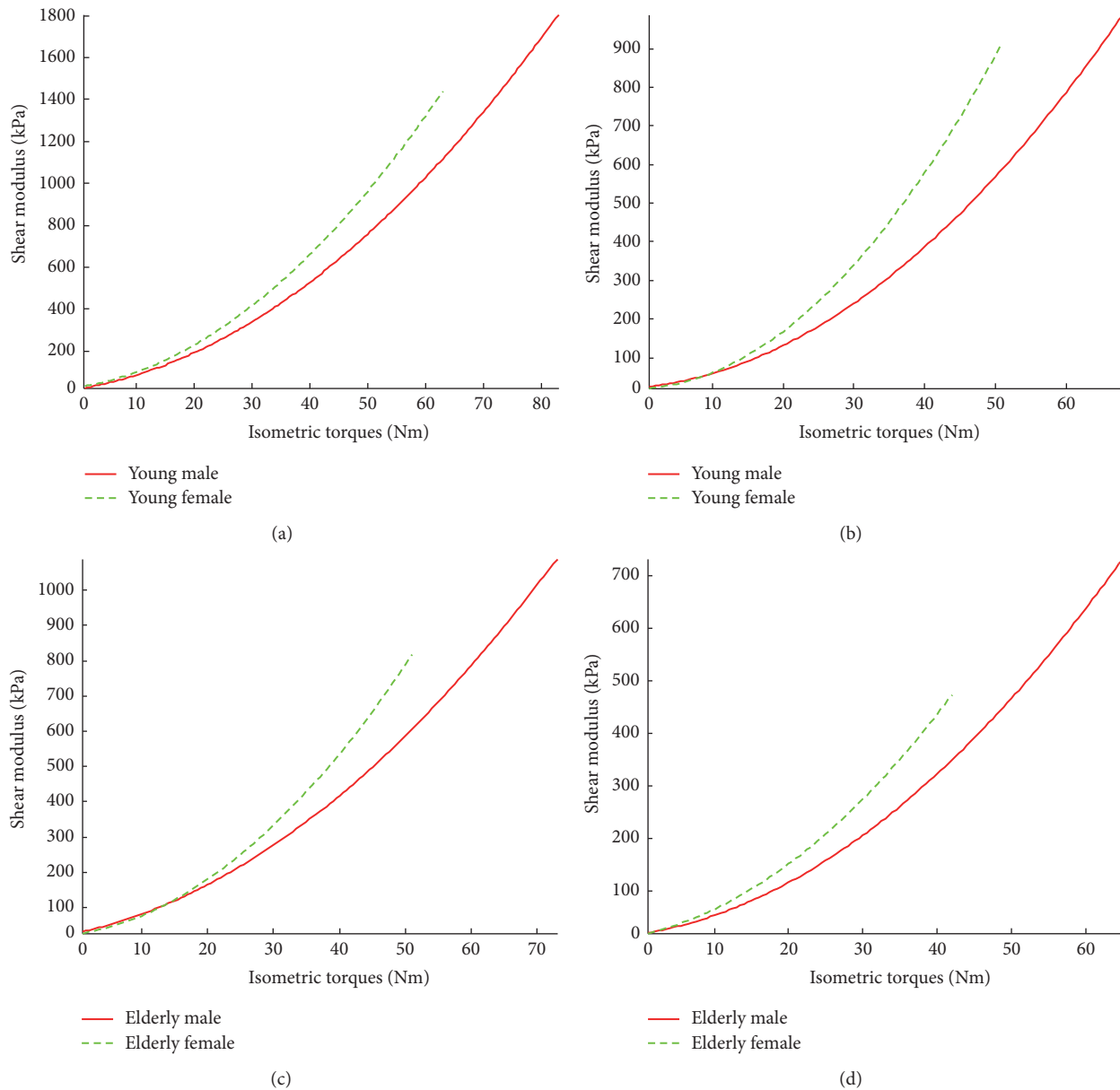


FIGURE 8: Gender dependencies of the relationships between VI shear modulus and absolute torque. Comparisons were made between young male and female subjects at (a) 90° and (b) 60° knee joint angles and between elderly male and female subjects at (c) 90° and (d) 60° knee joint angles.

ours [28]. However, our conclusion about the relationship between the increasing muscle stiffness and the increasing absolute torque was in good agreement with theirs.

4.2.3. Regression Analysis of the Relationship between Muscle Stiffness and Activity. Our results showed that, over the entire range of isometric contraction, the stiffness of VI along the direction of muscle action was positively correlated to both the relative contraction level (% MVC) and the absolute torques (N·m). These two relationships were both close to a quadratic curve. In previous studies, the results of regression analysis were mostly reported as linear relationship [17, 24]. However, in these studies, the muscle shear modulus was

only measured at 3–5 isometric contraction levels within a relatively smaller measurement range limited by the methods they used. In addition, it was a widely known approximation that a small range on the quadratic curve could be treated as being linear. That might be the reason of the difference between their conclusions and ours. Furthermore, from the results reported by Nordez and Hug [20], which measured the shear modulus of biceps brachii in a relatively larger muscle contraction range, the relationship between biceps brachii stiffness and isometric contraction torque seemed to be similar to a quadratic curve. However, they did not perform a quantitative regression analysis on their results in that paper.

4.2.4. Comparison with Previous Studies Based on Different Joint Angles. In our study, the results of the mean MVC torque measured at different knee joint angles showed that the MVC torque measured at a 90° knee joint angle was larger than that measured at 60° ($p = 0.001$). This result was in agreement with previous studies [12, 13, 36, 37]. We also found that the shear modulus of VI measured at a 90° knee joint angle was larger than that measured at 60° during step isometric contraction ($p < 0.001$). Furthermore, for the two factors, interaction of joint angles and % MVC, with the increase of % MVC, and differences between the VI shear modulus measured at a 90° knee joint angle and those measured at a 60° also increased. Few studies have been reported to investigate the relationship between VI shear modulus and knee joint angle, especially under different step isometric contraction levels. Sasaki et al. [28] reported that, with the increase in the ankle joint angle, the shear modulus of TA measured by SSI also increases when performing submaximal voluntary contractions. This result is in agreement with ours. Additionally, EMG activity of VL muscle has been studied with different knee joint angles and the results can be used as a reference. Suter and Herzog [38] studied the EMG activity of the VL muscle at 15°, 30°, 45°, 60°, and 90° knee joint angles. They reported that, at a 90° knee joint angle, the EMG activity in MVC state was significantly higher than those at the other knee joint angles. It has also been indicated that, at a joint angle where the EMG activity was relatively larger, the corresponding MVC torque was also larger [12, 13]. Considering the highly positive correlation between muscle stiffness and isometric contraction torque observed in this study, our results about the VI stiffness at different knee joint angles were considered to be reasonable. Furthermore, similar to what was discussed in a relaxed state, the larger muscle stiffness at a 90° knee joint angle might also be related to the relatively larger passive stretching on VI, and the morphological differences at different knee joint angles might also contribute to the different VI stiffness. However, all of these hypotheses should be further investigated in future studies.

4.3. Age Effect on the Relationship between Muscle Stiffness and Step Isometric Contraction. When performing step isometric contraction, the effect of age factor became significant. The VI shear modulus of young subjects was larger than that of elderly. The results regarding age differences have been also reported by several previous studies [5, 39]. However, our results further showed that, in a relaxed state with either 60° or 90° knee joint angles, there was no significant effect of age found. The mechanism behind this remains unclear.

On the other hand, by comparing the trends of VI shear modulus and absolute torque with different age ranges and the same sex, it was shown that the VI shear modulus of young subjects increased faster than that of elderly subjects at the same knee joint angle. This was coincident with the age effect on the relationship between VI shear modulus and relative muscle contraction level (% MVC).

Previous studies on the age differences of muscle shear modulus in a relaxed state and under step isometric contraction conditions were even rarer than those on the sex

differences. Domire et al. [27] measured the stiffness of TA using MRE in a relaxed state on 20 female subjects with an age range of 50–70 years. They found that there was no significant effect of age on muscle stiffness. This is in agreement with our results. Musculotendinous and musculoarticular stiffness have been also widely studied for the age difference. In the study of Ochala et al. [39], the stiffness of plantar flexor muscles was measured at 20%, 40%, 60%, and 80% MVC levels on young and elderly subjects. From the figures they published, it was clearly shown that the musculotendinous stiffness of elderly subjects was smaller than that of young subjects when measured at the same contraction level. This result of reduced musculotendinous stiffness due to muscle ageing is a valuable reference for our study. The age differences of morphology factors are related to the sarcopenia caused by the muscle ageing process and have been studied by many previous studies [6–8, 40]. However, few studies had been performed to evaluate the relationship between these morphology changes with muscle ageing and the muscle stiffness. Larsson et al. [41] found that the relative percentage of type I fibers increased with ageing and the fiber atrophy was most pronounced for type II fibers. As mentioned above, type I fibers were stiffer than type II fibers when generating equal active force. Therefore, the increasing percentage of type I fibers in elderly subjects should make the muscle stiffer in comparison with the young people when performing the same absolute contraction torque. However, this was opposite to the results observed in our study. One possible reason may be related to the increasing muscle coactivation level for the elderly [39, 40]. In our experiments, elderly subjects were also observed to be more strenuous when generating and keeping the isometric contraction levels. They noticeably tried to inspire the muscles in their whole body to accomplish the tasks. These coactivated muscles might share the original responsibility of VI and make the force generated by VI reduced comparing to the younger people. It is believed that the relative percentage of fiber types might not be the only or dominant factor for VI stiffness.

4.4. Sex Effect on the Relationship between Muscle Stiffness and Step Isometric Contraction. The mean MVC torque of knee extensors obtained from different sexes showed that the MVC torque of males were larger than that of females ($p < 0.001$). This result was in agreement with many previous studies [11, 29]. It was found that at both knee joint angles there was no significant main effect of sex ($p > 0.5$) on the VI shear modulus in a relaxed state. However, when performing step isometric contraction, the effect of sex factor was significant. The VI shear modulus of males was larger than that of females ($p < 0.001$). On the other hand, by comparing the trends of the relationship between VI shear modulus and absolute torque of the two sexes, it was found that the VI shear modulus of females increased faster than that of males under the same knee joint angle. This was opposite to the sex effect on the relationship between the VI shear modulus and relative contraction level (% MVC).

The sex effect on the shear modulus of skeletal muscles in a relaxed state and under step isometric contraction conditions has been rarely studied using methods based

on shear wave velocity measurement, such as MRE or SSI. Van De Steeg et al. [29] measured the stiffness of four different muscles (biceps brachii, flexor digitorum profundus, soleus, and gastrocnemius) in a relaxed state in eight young male and four female subjects using MRE. They reported that the comparisons between females and males did not reveal statistically significant differences for any muscles. Our results agreed well with theirs. Although few previous studies which were related to the sex difference of muscle shear modulus during isometric contraction could be found, some results using quick-release movement and sinusoidal perturbations methods to evaluate the musculotendinous stiffness and musculoarticular stiffness may be used as references. Ochala et al. [39] found that the musculotendinous and musculoarticular stiffness were both higher in elderly females than those in elderly males at the same absolute contraction torque. This result was coincident with ours. Granata et al. [42] found that, at 0% and 20% MVC levels, the musculoarticular stiffness of quadriceps femoris muscles and hamstring muscle in young males was larger than that in young females. This result also echoed with our findings. Sex differences on morphology parameters may be another reason for the different muscle stiffness between males and females when performing isometric contraction [9–11]. However, these geometric factors would result in a complex relationship with muscle stiffness and the detailed influence of morphology parameters is still unclear. Another possible reason may be the sex difference of fiber type distribution, as we know that the slow-twitch (type I) and fast-twitch (type II) fibers have different stiffness characteristics. For instance, in rats, type I fibers had been observed to be stiffer than type II fibers when generating the same active contraction force [36, 37]. Therefore, the relatively greater area occupied by type I fibers in females and the greater area occupied by type II fibers in males [11, 43] can at least partially explain the higher muscle stiffness in females than in males at the same absolute contraction torque. Interestingly, it has been reported that the incident rate of fall is higher among females than males and more in elderly than young population. Though muscle stiffness is not currently regarded as a fall risk indication, it will be our future research topic following the study.

5. Conclusions

In this study, the relationship between VI stiffness and relative isometric contraction level or absolute torque generated by the knee extensor were studied over the entire muscle contraction range, that is, from 0% to 100% MVC. Meanwhile, the age and sex effects on the relationships were also systematically investigated. When performing isometric contraction, the VI stiffness of males was found to be significantly higher than that of females, and that of the young was higher than the elderly. Additionally, the stiffness measured at a 90° knee joint angle was always significantly larger than that measured at 60°. These results extended our knowledge on how age and sex can affect the muscle stiffness especially when the contractions are approximating the higher MVC and, therefore, may provide new insights into the age and sex bias in musculoskeletal studies, such as those on fall risks.

Disclosure

The funders had no role in study design, data collection and analysis, decision to publish, or preparation of the manuscript.

Conflicts of Interest

The authors declare that they have no conflicts of interest.

Acknowledgments

This study was supported by the National Natural Science Found of China (nos. 61571431 and 61640018), the Science and Technology Planning Project of Guangdong Province (nos. 2015A020214022, 2015B020214007), the National Key Research and Development Project (2016YFC0105003), the Research Grant Council of Hong Kong (PolyU5331/06E), Hong Kong Innovation and Technology Fund (UI213), and the Guangdong Province Sci & Tech Projects (2013B010136006). The authors would like to thank the volunteers who participated in the study and Sally Ding for her help in editing the manuscript.

References

- [1] C.-Z. Wang, T.-J. Li, and Y.-P. Zheng, "Shear modulus estimation on Vastus Intermedius of elderly and young females over the entire range of isometric contraction," *PLoS ONE*, vol. 9, no. 7, Article ID e101769, 2014.
- [2] Y. Zheng, A. F. T. Mak, and B. Lue, "Objective assessment of limb tissue elasticity: development of a manual indentation procedure," *Journal of Rehabilitation Research and Development*, vol. 36, no. 2, pp. 71–85, 1999.
- [3] L. K. Kwah, R. Z. Pinto, J. Diong, and R. D. Herbert, "Reliability and validity of ultrasound measurements of muscle fascicle length and pennation in humans: a systematic review," *Journal of Applied Physiology*, vol. 114, no. 6, pp. 761–769, 2013.
- [4] J. Mula, J. D. Lee, F. Liu, L. Yang, and C. A. Peterson, "Automated image analysis of skeletal muscle fiber cross-sectional area," *Journal of Applied Physiology*, vol. 114, no. 1, pp. 148–155, 2013.
- [5] K. Karamanidis and A. Arampatzis, "Mechanical and morphological properties of human quadriceps femoris and triceps surae muscle-tendon unit in relation to aging and running," *Journal of Biomechanics*, vol. 39, no. 3, pp. 406–417, 2006.
- [6] C. I. Morse, J. M. Thom, K. M. Birch, and M. V. Narici, "Changes in triceps surae muscle architecture with sarcopenia," *Acta Physiologica Scandinavica*, vol. 183, no. 3, pp. 291–298, 2005.
- [7] M. V. Narici, N. Maffulli, and C. N. Maganaris, "Ageing of human muscles and tendons," *Disability and Rehabilitation*, vol. 30, no. 20–22, pp. 1548–1554, 2008.
- [8] M. V. Narici, C. N. Maganaris, N. D. Reeves, and P. Capodaglio, "Effect of aging on human muscle architecture," *Journal of Applied Physiology*, vol. 95, no. 6, pp. 2229–2234, 2003.
- [9] R. S. Chow, M. K. Medri, D. C. Martin, R. N. Leekam, A. M. Agur, and N. H. McKee, "Sonographic studies of human soleus and gastrocnemius muscle architecture: gender variability," *European Journal of Applied Physiology*, vol. 82, no. 3, pp. 236–244, 2000.

- [10] A. E. J. Miller, J. D. MacDougall, M. A. Tarnopolsky, and D. G. Sale, "Gender differences in strength and muscle fiber characteristics," *European Journal of Applied Physiology and Occupational Physiology*, vol. 66, no. 3, pp. 254–262, 1993.
- [11] R. S. Staron, F. C. Hagerman, R. S. Hikida et al., "Fiber type composition of the vastus lateralis muscle of young men and women," *Journal of Histochemistry and Cytochemistry*, vol. 48, no. 5, pp. 623–629, 2000.
- [12] T. M. Altenburg, A. De Haan, P. W. L. Verdijk, W. Van Mechelen, and C. J. De Ruijter, "Vastus lateralis single motor unit EMG at the same absolute torque production at different knee angles," *Journal of Applied Physiology*, vol. 107, no. 1, pp. 80–89, 2009.
- [13] C. J. De Ruijter, J. G. Hoddenbach, A. Huurnink, and A. De Haan, "Relative torque contribution of vastus medialis muscle at different knee angles," *Acta Physiologica*, vol. 194, no. 3, pp. 223–237, 2008.
- [14] T. Fukunaga, Y. Ichinose, M. Ito, Y. Kawakami, and S. Fukashiro, "Determination of fascicle length and pennation in a contracting human muscle in vivo," *Journal of Applied Physiology*, vol. 82, no. 1, pp. 354–358, 1997.
- [15] Y. Ichinose-Muraoka, Y. Kawakami, M. Ito, H. Kanehisa, and T. Fukunaga, "In vivo estimation of contraction velocity of human vastus lateralis muscle during 'isokinetic' action," *Journal of Applied Physiology*, vol. 88, no. 3, pp. 851–856, 2000.
- [16] Y. Yoshitake, M. Shinohara, H. Ue, and T. Moritani, "Characteristics of surface mechanomyogram are dependent on development of fusion of motor units in humans," *Journal of Applied Physiology*, vol. 93, no. 5, pp. 1744–1752, 2002.
- [17] S. F. Levinson, M. Shinagawa, and T. Sato, "Sonoelastic determination of human skeletal muscle elasticity," *Journal of Biomechanics*, vol. 28, no. 10, pp. 1145–1154, 1995.
- [18] A. Nordez, A. Guével, P. Casari, S. Catheline, and C. Cornu, "Assessment of muscle hardness changes induced by a submaximal fatiguing isometric contraction," *Journal of Electromyography and Kinesiology*, vol. 19, no. 3, pp. 484–491, 2009.
- [19] B. C. W. Kot, Z. J. Zhang, A. W. C. Lee, V. Y. F. Leung, and S. N. Fu, "Elastic modulus of muscle and tendon with shear wave ultrasound elastography: variations with different technical settings," *PLoS ONE*, vol. 7, no. 8, Article ID e44348, 2012.
- [20] A. Nordez and F. Hug, "Muscle shear elastic modulus measured using supersonic shear imaging is highly related to muscle activity level," *Journal of Applied Physiology*, vol. 108, no. 5, pp. 1389–1394, 2010.
- [21] S. G. Chen, M. W. Urban, C. Pislaru et al., "Shearwave dispersion ultrasound vibrometry (SDUV) for measuring tissue elasticity and viscosity," *IEEE Transactions on Ultrasonics, Ferroelectrics, and Frequency Control*, vol. 56, no. 1, pp. 55–62, 2009.
- [22] S. F. Bensamoun, K. J. Glaser, S. I. Ringleb, Q. Chen, R. L. Ehman, and K.-N. An, "Rapid magnetic resonance elastography of muscle using one-dimensional projection," *Journal of Magnetic Resonance Imaging*, vol. 27, no. 5, pp. 1083–1088, 2008.
- [23] S. F. Bensamoun, S. I. Ringleb, L. Littrell et al., "Determination of thigh muscle stiffness using magnetic resonance elastography," *Journal of Magnetic Resonance Imaging*, vol. 23, no. 2, pp. 242–247, 2006.
- [24] M. Alex Dresner, G. H. Rose, P. J. Rossman, R. Muthupillai, A. Manduca, and R. L. Ehman, "Magnetic resonance elastography of skeletal muscle," *Journal of Magnetic Resonance Imaging*, vol. 13, no. 2, pp. 269–276, 2001.
- [25] C. Z. Wang, Y. P. Zheng, Y. Xiao, W. Qiu, and H. Zheng, "Using vibro-ultrasound method to assess the vastus intermedius stiffness over the entire range of step isometric contraction of knee extensors," in *Proceedings of the IEEE International Ultrasonics Symposium (IUS '12)*, pp. 1351–1354, IEEE, Dresden, Germany, October 2012.
- [26] G. J. Wilson, A. J. Murphy, and J. F. Pryor, "Musculotendinous stiffness—its relationship to eccentric, isometric, and concentric performance," *Journal of Applied Physiology*, vol. 76, no. 6, pp. 2714–2719, 1994.
- [27] Z. J. Domire, M. B. McCullough, Q. Chen, and K.-N. An, "Feasibility of using magnetic resonance elastography to study the effect of aging on shear modulus of skeletal muscle," *Journal of Applied Biomechanics*, vol. 25, no. 1, pp. 93–97, 2009.
- [28] K. Sasaki, S. Toyama, and N. Ishii, "Length-force characteristics of in vivo human muscle reflected by supersonic shear imaging," *Journal of Applied Physiology*, vol. 117, no. 2, pp. 153–162, 2014.
- [29] C. Van De Steeg, A. Daffertshofer, D. F. Stegeman, and T. W. Boonstra, "High-density surface electromyography improves the identification of oscillatory synaptic inputs to motoneurons," *Journal of Applied Physiology*, vol. 116, no. 10, pp. 1263–1271, 2014.
- [30] B. Abernethy, S. Mackinnon, V. Kippers, S. Hanrahan, and M. Pandy, *The Biophysical Foundations of Human Movement*, Human Kinetics, Champaign, Ill, USA, 2nd edition, 2005.
- [31] K. Kubo, K. Ohgo, R. Takeishi et al., "Effects of isometric training at different knee angles on the muscle-tendon complex in vivo," *Scandinavian Journal of Medicine and Science in Sports*, vol. 16, no. 3, pp. 159–167, 2006.
- [32] A. J. Blazeovich, N. D. Gill, and S. Zhou, "Intra- and intermuscular variation in human quadriceps femoris architecture assessed in vivo," *Journal of Anatomy*, vol. 209, no. 3, pp. 289–310, 2006.
- [33] J. L. Gennisson, C. Cornu, S. Catheline, M. Fink, and P. Portero, "Human muscle hardness assessment during incremental isometric contraction using transient elastography," *Journal of Biomechanics*, vol. 38, no. 7, pp. 1543–1550, 2005.
- [34] T. R. Jenkyn, R. L. Ehman, and K.-N. An, "Noninvasive muscle tension measurement using the novel technique of magnetic resonance elastography (MRE)," *Journal of Biomechanics*, vol. 36, no. 12, pp. 1917–1921, 2003.
- [35] G. Heers, T. Jenkyn, M. Alex Dresner et al., "Measurement of muscle activity with magnetic resonance elastography," *Clinical Biomechanics*, vol. 18, no. 6, pp. 537–542, 2003.
- [36] T. Toursel, L. Stevens, and Y. Mounier, "Evolution of contractile and elastic properties of rat soleus muscle fibres under unloading conditions," *Experimental Physiology*, vol. 84, no. 1, pp. 93–107, 1999.
- [37] K. Uffmann, S. Maderwald, W. Ajaj et al., "In vivo elasticity measurements of extremity skeletal muscle with MR elastography," *NMR in Biomedicine*, vol. 17, no. 4, pp. 181–190, 2004.
- [38] E. Suter and W. Herzog, "Extent of muscle inhibition as a function of knee angle," *Journal of Electromyography and Kinesiology*, vol. 7, no. 2, pp. 123–130, 1997.
- [39] J. Ochala, D. Valour, M. Pousson, D. Lambertz, and J. Van Hoecke, "Gender differences in human muscle and joint mechanical properties during plantar flexion in old age," *Journals of Gerontology, Series A: Biological Sciences and Medical Sciences*, vol. 59, no. 5, pp. 441–448, 2004.
- [40] C. S. Klein, C. L. Rice, and G. D. Marsh, "Normalized force, activation, and coactivation in the arm muscles of young and old men," *Journal of Applied Physiology*, vol. 91, no. 3, pp. 1341–1349, 2001.

- [41] L. Larsson, B. Sjödin, and J. Karlsson, "Histochemical and biochemical changes in human skeletal muscle with age in sedentary males, age 22–65 years," *Acta Physiologica Scandinavica*, vol. 103, no. 1, pp. 31–39, 1978.
- [42] K. P. Granata, S. E. Wilson, and D. A. Padua, "Gender differences in active musculoskeletal stiffness. Part I. Quantification in controlled measurements of knee joint dynamics," *Journal of Electromyography and Kinesiology*, vol. 12, no. 2, pp. 119–126, 2002.
- [43] J.-A. Simoneau and C. Bouchard, "Human variation in skeletal muscle fiber-type proportion and enzyme activities," *American Journal of Physiology—Endocrinology and Metabolism*, vol. 257, no. 4, pp. E567–E572, 1989.

Clinical Study

Ultrasonography-Guided Lumbar Periradicular Injections for Unilateral Radicular Pain

Qing Wan,¹ Shaoling Wu,¹ Xiao Li,¹ Caina Lin,¹ Songjian Ke,¹
Cuicui Liu,¹ Wenjun Xin,² and Chao Ma¹

¹Pain Treatment Centre of Department of Rehabilitation Medicine, Sun Yat-sen Memorial Hospital, Sun Yat-sen University, Guangzhou, Guangdong Province, China

²Department of Physiology and Pain Research Center, Zhongshan Medical School, Sun Yat-sen University, Guangzhou, Guangdong Province, China

Correspondence should be addressed to Chao Ma; ma_chao99@126.com

Received 3 November 2016; Revised 9 February 2017; Accepted 22 February 2017; Published 30 March 2017

Academic Editor: Qing Wang

Copyright © 2017 Qing Wan et al. This is an open access article distributed under the Creative Commons Attribution License, which permits unrestricted use, distribution, and reproduction in any medium, provided the original work is properly cited.

Objective. The aim of this study was to compare the accuracy and efficacy of sonographically guided lumbar periradicular injections through in-plane or out-of-plane approach techniques for patients with unilateral lower lumbar radicular pain. The feasibility and accuracy of these techniques were studied by means of computed tomography (CT). **Methods.** A total of 46 patients with chronic unilateral lumbar radicular pain were recruited and randomly assigned to either the in-plane or out-of-plane injection group. A mixture of 3 mL 1% lidocaine and 7 mg betamethasone was injected. The visual analog scale (VAS) was used to assess pain before and after treatment. **Results.** The pain intensity, as measured by VAS, significantly decreased in both in-plane and out-of-plane injection groups. **Conclusions.** The sonographically guided periradicular injections are feasible and effective in treating lumbar unilateral radicular pain.

1. Introduction

Unilateral radicular pain is thought to be induced by inflammation or irritation of an exiting spinal nerve root originated from degeneration of intervertebral disc [1]. Nerve root blocking therapy is the most commonly performed minimally invasive management for low back pain. Steroids and local anesthetic are the most frequently used injectates [2, 3]. The underlying mechanism of steroid administration is to reduce inflammation by inhibiting release of proinflammatory mediators [4]. The nerve root blocking can be delivered by ultrasound-guided or fluoroscopy-controlled manner in clinical trials. Recently, the reliability and efficacy of ultrasound-guided injections in the lumbar spine have been broadly discussed and well accepted by patients and physicians because of the real-time guidance of injection and without radiation exposure [5–8].

With the real-time guidance of ultrasound, the spinous process and adjacent structures such as lamina, zygapophysial articulations, and transverse process can be clearly

identified. Several injection procedures have been introduced, including transforaminal injection through in-plane approach [9], medial branch block to the facet joint [10], and paravertebral injection through paramedian sagittal and paramedian sagittal oblique approaches [11]. The aim of our study is to compare the accuracy, safety, and the effect on pain relief of lumbar nerve root blocking through ultrasound guidance by in-plane and out-of-plane techniques.

2. Materials and Methods

2.1. Patient Characteristics. The study protocol was approved by the Institutional Review Board of Sun Yat-sen Memorial Hospital of Sun Yat-sen University, and written informed consent was obtained from all patients. There were 52 eligible patients with chronic unilateral lower lumbar radicular pain for more than 3 months and 46 patients participated in this randomized, single-blind study. The patients were recruited consecutively between January 2015 and September 2016. They were randomly assigned into two groups and received

TABLE 1: Demographic data for patients.

Characteristic	IP technique (<i>n</i> = 25)	OP technique (<i>n</i> = 21)
Age, years (SD)	56.23 (10.30)	58.17 (9.62)
Sex M/F, <i>n</i>	16/9	13/8
Weight, kilograms (SD)	58.76 (8.31)	59.82 (7.20)
Height, meters (SD)	1.64 (0.05)	1.67 (0.04)
Body mass index, kg/m ² (SD)	21.70 (2.78)	21.14 (2.34)
Left/right, <i>n</i>	15/10	14/7
Spinal level of injection		
L4, <i>n</i> (%)	14 (56.0)	12 (57.1)
L5, <i>n</i> (%)	11 (44.0)	9 (42.9)
VAS (SD) before injection	7.26 (1.00)	7.34 (1.08)

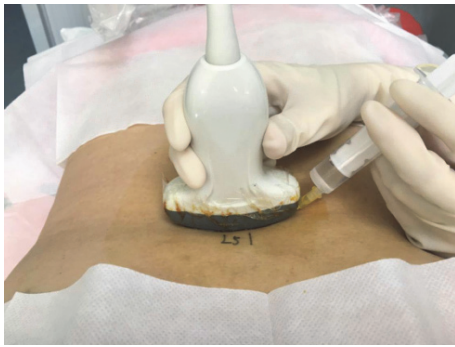


FIGURE 1: The position of the patient and the placement of transducer of in-plane approach.

one sonographically periradicular injection through either in-plane approach (IP, *n* = 25) or out-of-plane approach (OP, *n* = 21) techniques, respectively. A mixture of 3 mL 1% lidocaine and 7 mg betamethasone was injected.

All patients were diagnosed for low back pain with unilateral radicular pain through clinical presentations, medical examinations, computed tomography (CT), or magnetic resonance imaging (MRI). The excluded criteria were systemic inflammatory disease, uncontrolled diabetes, infections, previous injections within 3 months, taking oral anti-inflammatory medication, receiving physical therapy or other injection therapy during this study, and having underwent surgery. The demographic data for patients were demonstrated in Table 1.

2.2. Ultrasound-Guided Periradicular Injections In-Plane Approach. Ultrasound-guided selective nerve root block was conducted for 25 patients in 25 nerve roots. The patients were lying in the prone position with a pillow under the abdomen. The areas of injection treatment were disinfected and a sterile cover was placed on a curved array transducer. One experienced physician performed the ultrasound-guided injections using an Q9 (Xiang Sheng Company, Wuxi) device (Figure 1). The spinous processes were identified through a middle scan.

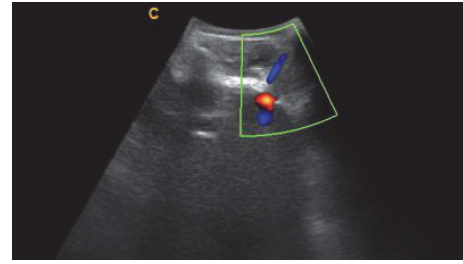


FIGURE 2: Transverse ultrasound image of the in-plane injection approach, the needle was inserted aiming to the Z-joint gap.



FIGURE 3: The position of the patient and the placement of transducer of out-of-plane approach.

First, the sacrum and the fifth lumbar spinous process were identified, and the target spinal level for the injection was confirmed by cephalad counting of the spinous process. At the target spinal level, a transverse axial plane was obtained by rotating the probe 90 degrees. The axial ultrasound image reflected the spinous process, lamina, facet joint, and transverse process. A needle (22 G) was inserted approximately 45 degrees into the skin using the in-plane technique, which enabled visualization of the path of the needle. When the needle tip reached the lateral side of the lamina or medial to the superior articular process (Figure 2), an inhalation test was performed to observe the presence of blood and cerebrospinal fluid. After confirming no inhalation, a mixture of 3 mL of 1% lidocaine and 7 mg betamethasone was injected.

2.3. Ultrasound-Guided Periradicular Injections Out-of-Plane Approach. The patients' position and sterilization were described previously. The transducer was placed longitudinally; the sacral spinous process and the fifth lumbar spinous process were identified. The lamina, facet joint, and transverse process were identified when moving the transducer from midline laterally. Then the transducer was moved back to visualize the edge of the zygapophyseal joints (Figure 3). After identification of the target injection level, a needle (22 G) was inserted approximately 70 degrees into the skin using the out-of-plane technique in the parasagittal view. The needle tip was located in the middle of the adjacent facet joints (Figure 4). The injection procedure and the medicine were described in the in-plane approach technique part.

TABLE 2: Procedure characteristics.

Characteristic	IP technique (n = 25)	OP technique (n = 21)	P
Patient treated, n (%)	23 (96.0)	20 (95.2)	0.567
Patient failed, n (%)	2 (4.0)	1 (4.8)	
Correct spinal segment identification, n (%)	24 (100)	20 (100)	
Accuracy of US- guided injection confirmed by CT, n (%)	22 (95.7)	19 (95.0)	0.720
VAS (SD) after injection	3.62 (0.81)	3.21 (0.90)	0.485

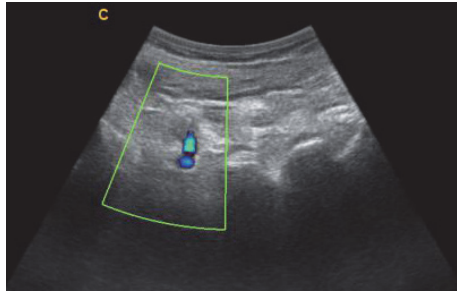


FIGURE 4: Longitudinal facet view was obtained and the needle was inserted approaching L4 nerve root.

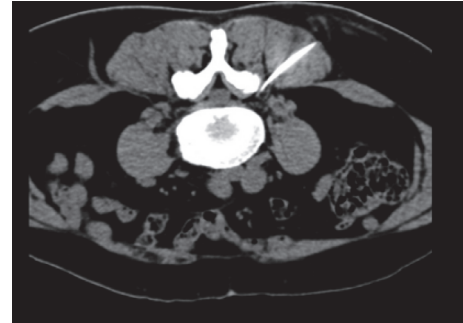


FIGURE 5: A representative image for confirmation of the needle pathway.

2.4. Confirmation of Nerve Root Blocking by CT. Patients were prepared as specified above for the US procedure. A radiopaque marker was placed at the indicated level. A low-dose topogram through the area of interest was obtained at 3 mm increments for a precise definition of the needle pathway by ultrasound guidance. A representative image for confirmation of the needle pathway is demonstrated in Figure 5.

2.5. Statistics. The data were analyzed using SPSS version 11.0 software (SPSS Inc., Chicago, IL, USA). Analysis of variance was used to compare the demographic characteristics of the patients, and a *t*-test was used for measurement data. $P < 0.05$ was considered statistically significant.

3. Results

3.1. Patient Characteristics. A total of 46 patients completed this study. The patients had comparable pain intensity assessed by VAS between IP (7.26 ± 1.00) and OP (7.34 ± 1.08) technique groups before injections. The spinal level of injections was located at L4 or L5. The demographic data of patients are present in Table 1.

3.2. Treatment Effects between the Approaches. The blocking procedures were tolerable for all the patients. None of the patients had any treatment-related complications. Table 2 illustrates the procedure characteristics.

The pain was significantly reduced after injection in both IP and OP technique groups. There were no significant differences in the VAS before and after the injections between IP and OP technique groups (Table 2).

4. Discussion

Radicular low back pain is commonly caused by intervertebral disc herniation, spinal stenosis, and intervertebral disc degeneration. Selective nerve root blocking is one of the most frequently performed mini-invasive interventions. Ultrasonography has been used broadly in evaluation and treatment of musculoskeletal disorders. Ultrasound has proved to be reliable and accurate in the demonstration of paravertebral anatomy and sonographically guided lumbar injections for the treatment of unilateral lower lumbar radicular pain have been previously studied for feasibility and accuracy [12, 13]. The most challenging part in sonographically guided lumbar periradicular injections is in placing the needle in the exact position at the target nerve root. The advantage of parasagittal out-of-plane approach is deposition of medication close to the nerve root compared with in-plane approach aiming to the facet joint.

The success ratio of the lumbar nerve root blocking is over 95% in our study; this indicates that, in both approaches, the drug is able to be delivered at the periradicular space. Relief of symptoms has been the gold standard for evaluating the success of US-guided injection [14]. However, the symptoms could also be relieved by systemic drug effect even if the needle was not inserted at the precise position. The accuracy of ultrasound guidance, especially the needle tip, was evaluated by CT assessment.

In our study, there was no significant difference in VAS evaluation between IP and OP injection techniques. This indicates that, in both approaches, the medication is able to reach the periradicular space. The long-term pain relieving effect needs further investigation.

In comparison with CT, ultrasonography has several advantages. There is no radiation exposure for the physician. And the device is portable; it can be used in outpatient and at bedside. Despite the above advantages, it has limitations in showing good quality view of spinal structures and the quality depends on experiences of the physician. It has been demonstrated that the reproducibility among physicians is low [15].

This study had some limitations: first, the sample size was small and the long-term effects were not evaluated; second, the outcome of injections was only pain score and functional tests of lumbar spine should be conducted in further researches.

5. Conclusions

The sonographically guided periradicular injections are feasible and effective in treating lumbar unilateral radicular pain.

Conflicts of Interest

The authors have no conflicts of interest to declare.

Authors' Contributions

Qing Wan and Shaoling Wu contributed equally to this work.

Acknowledgments

This work was supported by major program of Natural Science Foundation of Guangdong Province, China (no. 2016A030311045), and Science and Technology Research Projects of Guangzhou, China (no. 201607010254).

References

- [1] W. A. Katz and R. Rothenberg, "The nature of pain: pathophysiology," *Journal of Clinical Rheumatology*, vol. 11, no. 2, pp. S11–S15, 2005.
- [2] L. Manchikanti, K. A. Cash, V. Pampati, and F. J. E. Falco, "Transforaminal epidural injections in chronic lumbar disc herniation: a randomized, double-blind, active-control trial," *Pain Physician*, vol. 17, no. 4, pp. E489–E501, 2014.
- [3] K. D. Candido, M. V. Rana, R. Sauer et al., "Concordant pressure paresthesia during interlaminar lumbar epidural steroid injections correlates with pain relief in patients with unilateral radicular pain," *Pain Physician*, vol. 16, no. 5, pp. 497–511, 2013.
- [4] A. Lundin, A. Magnuson, K. Axelsson, O. Nilsson, and L. Samuelsson, "Corticosteroids preoperatively diminishes damage to the C-fibers in microscopic lumbar disc surgery," *Spine*, vol. 30, no. 21, pp. 2362–2367, 2005.
- [5] G. Yang, J.-F. Liu, L.-J. Ma et al., "Ultrasound-guided versus fluoroscopy-controlled lumbar transforaminal epidural injections: a prospective randomized clinical trial," *Clinical Journal of Pain*, vol. 32, no. 2, pp. 103–108, 2016.
- [6] S. M. Hashemi, M. R. Aryani, S. Momenzadeh et al., "Comparison of transforaminal and parasagittal epidural steroid injections in patients with radicular low back pain," *Anesthesiology and Pain Medicine*, vol. 5, no. 5, Article ID e26652, 2015.
- [7] M. Gofeld, S. J. Bristow, and S. Chiu, "Ultrasound-guided injection of lumbar zygapophyseal joints: an anatomic study with fluoroscopy validation," *Regional Anesthesia and Pain Medicine*, vol. 37, no. 2, pp. 228–231, 2012.
- [8] C. Darrieutort-Laffite, O. Hamel, J. Glémarec, Y. Maugars, and B. Le Goff, "Ultrasonography of the lumbar spine: sonoanatomy and practical applications," *Joint Bone Spine*, vol. 81, no. 2, pp. 130–136, 2014.
- [9] M. Gofeld, S. J. Bristow, S. C. Chiu, C. K. McQueen, and L. Bollag, "Ultrasound-guided lumbar transforaminal injections: feasibility and validation study," *Spine*, vol. 37, no. 9, pp. 808–812, 2012.
- [10] D. Kim, D. Choi, C. Kim, J. Kim, and Y. Choi, "Transverse process and needles of medial branch block to facet joint as landmarks for ultrasound-guided selective nerve root block," *Clinics in Orthopedic Surgery*, vol. 5, no. 1, pp. 44–48, 2013.
- [11] Y. H. Kim, H. J. Park, and D. E. Moon, "Ultrasound-guided paravertebral injection in the lumbar spine: a Comparative Study of the Paramedian Sagittal and Paramedian Sagittal Oblique Approaches," *Pain Practice*, vol. 15, no. 8, pp. 693–700, 2015.
- [12] Y. Park, J.-H. Lee, K. D. Park, J. K. Ahn, J. Park, and H. Jee, "Ultrasound-guided vs. fluoroscopy-guided caudal epidural steroid injection for the treatment of unilateral lower lumbar radicular pain: a prospective, randomized, single-blind clinical study," *American Journal of Physical Medicine and Rehabilitation*, vol. 92, no. 7, pp. 575–586, 2013.
- [13] A. Loizides, H. Gruber, S. Peer, K. Galiano, R. Bale, and J. Obernauer, "Ultrasound guided versus CT-controlled paravertebral injections in the lumbar spine: a prospective randomized clinical trial," *American Journal of Neuroradiology*, vol. 34, no. 2, pp. 466–470, 2013.
- [14] K. D. Riew, Y. Yin, L. Gilula et al., "The effect of nerve-root injections on the need for operative treatment of lumbar radicular pain. A prospective, randomized, controlled, double-blind study," *The Journal of Bone & Joint Surgery—American Volume*, vol. 82, no. 11, pp. 1589–1593, 2000.
- [15] B. E. Hashimoto, D. J. Kramer, and L. Wiitala, "Applications of musculoskeletal sonography," *Journal of Clinical Ultrasound*, vol. 27, no. 6, pp. 293–318, 1999.

Review Article

A Review on Real-Time 3D Ultrasound Imaging Technology

Qinghua Huang^{1,2} and Zhaozheng Zeng¹

¹*School of Electronic and Information Engineering, South China University of Technology, Guangzhou, China*

²*College of Information Engineering, Shenzhen University, Shenzhen 518060, China*

Correspondence should be addressed to Qinghua Huang; qhhuang@scut.edu.cn

Received 9 September 2016; Accepted 7 March 2017; Published 26 March 2017

Academic Editor: Kevin M. Coombs

Copyright © 2017 Qinghua Huang and Zhaozheng Zeng. This is an open access article distributed under the Creative Commons Attribution License, which permits unrestricted use, distribution, and reproduction in any medium, provided the original work is properly cited.

Real-time three-dimensional (3D) ultrasound (US) has attracted much more attention in medical researches because it provides interactive feedback to help clinicians acquire high-quality images as well as timely spatial information of the scanned area and hence is necessary in intraoperative ultrasound examinations. Plenty of publications have been declared to complete the real-time or near real-time visualization of 3D ultrasound using volumetric probes or the routinely used two-dimensional (2D) probes. So far, a review on how to design an interactive system with appropriate processing algorithms remains missing, resulting in the lack of systematic understanding of the relevant technology. In this article, previous and the latest work on designing a real-time or near real-time 3D ultrasound imaging system are reviewed. Specifically, the data acquisition techniques, reconstruction algorithms, volume rendering methods, and clinical applications are presented. Moreover, the advantages and disadvantages of state-of-the-art approaches are discussed in detail.

1. Introduction

Many imaging technologies have been applied to enhance clinicians' ability for diagnosis of the disease, for example, the X-ray, magnetic resonance (MR), computed tomography (CT), and ultrasound (US). Each imaging modality has its strengths and limitations in different applications [1]. Among these diagnosis-aid technologies, US gains more and more attention in recent years. Aside from low cost and no radiation, the interactive nature of US which is mostly needed in surgery facilitates its widespread use in clinical practices.

Conventional 2D US has been widely used because it can dynamically display 2D images of the region of interest (ROI) in real-time [2, 3]. However, due to the lack of the anatomy and orientation information, clinicians have to imagine the volume with the planar 2D images mentally when they need the view of 3D anatomic structures. The limitation of 2D US imaging makes the diagnostic accuracy much uncertain as it heavily depends on the experience and knowledge of clinicians. In order to address the foresaid problem, 3D US was proposed to help the diagnosticians acquire a full understanding of the spatial anatomic relationship. Physicians can

view arbitrary plane of the reconstructed 3D volume as well as panoramic view of the ROI which helps surgeons to ascertain whether a surgical instrument is placed correctly within the ROI or just locates peripherally during the surgery [4]. It is undeniable that 3D US enables clinicians to diagnose fast and accurately as it reduces the time spent on evaluating images and interacts with diagnosticians friendly to obtain a handle of the shape and location of the lesion.

Generally, 3D US imaging can be conducted with three main stages: that is, acquisition, reconstruction, and visualization. The acquisition refers to collecting the B-scans with relative position using conventional 2D probes or directly obtaining 3D images using dedicated 3D probes. The reconstruction aims to insert the collected 2D images into a predefined regular volume grid. The visualization is to render the built voxel array in a certain manner like any-plane slicing, surface rendering, or volume rendering. Traditional 3D US is temporally separated into the B-scan frame collection, volume reconstruction, and visualization stages individually, making it time-consuming and inefficient to obtain an accurate 3D image. Clinician has to wait for the data collection and volume reconstruction which often take several minutes

or even longer time before visualizing any part of the volume, rather than visualizing 3D anatomy simultaneously during the scanning of the ROI. Hence the clinician cannot select an optimal way to conduct the scanning process for subsequent diagnosis. Moreover, the separation has limited the applications in surgery where physicians require immediate feedback on intraoperative changes in the ROI [5]. It is no doubt that real-time 3D US will facilitate physicians' ability in diagnosis even better and help them work more efficiently during the surgery.

Many investigators have made their efforts to develop the real-time or near real-time US systems in recent decade. Several attempts with the dedicated 3D probe or traditional 2D probe to reconstruct and render a volume during data acquisition are now available. To provide systematic understanding of the relevant technology in real-time US, we review the state-of-the-art approaches for designing real-time or near real-time 3D US imaging system. Data acquisition techniques, reconstruction algorithms, rendering methods, and clinical applications are discussed in the following sections, including the advantage and disadvantages of each approach.

2. Data Acquisition

Obtaining 3D real-time US image without distortions is crucial for the subsequent clinical diagnosis. In any approach of data acquisition, the objectives are twofold: first to acquire relative locations and orientations of the tomographic images accurately, which ensures the 3D reconstruction without errors, and second to capture the ROI expeditiously, which is aimed at avoiding the artifacts caused by cardiac, respiratory, and involuntary motion, as well as enabling the 3D visualization of dynamic structures in real-time. Four representative real-time 3D US data acquisition techniques have been proposed, that is, 2D array transducers, mechanical 3D probes, mechanical localizers, and freehand scanners.

2.1. 2D Array Transducers. In conventional 1D array transducer, a subset of transducer elements or subaperture is sequentially selected to send an acoustic beam perpendicularly to the transducer surface, and one line is drawn at the same time. Through multiplexing or simply turning elements on and off, the entire aperture can be selected which forms a rectangular scan [6]. Analogously, 2D array transducers derive an acoustic beam steering in both azimuth and elevation dimensions, which enables obtaining a volumetric scan [7].

2D array transducers acquire 3D information by electronic scanning. As illustrated in Figure 1, the elements of 2D array transducer generate a diverging beam in a pyramidal shape and the received echoes are processed to integrate 3D US images in real-time. Since the beams can be steered and focused on the ROI by adjusting the phased array delays [8], the transducers can remain stationary while being used to scan.

A variety of 2D array patterns are proposed to fabricate 2D array transducers, such as sparse periodic array, Mills cross array [9], random array, and Vernier array. As 1D linear transducers, 2D array transducers can be sorted of concave

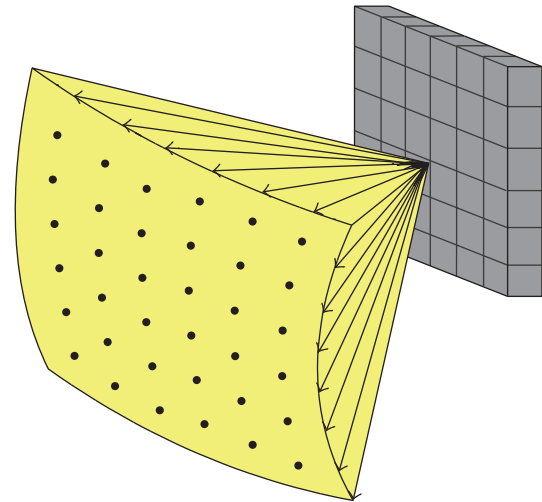


FIGURE 1: Principle of volumetric imaging with a 2D array transducer.

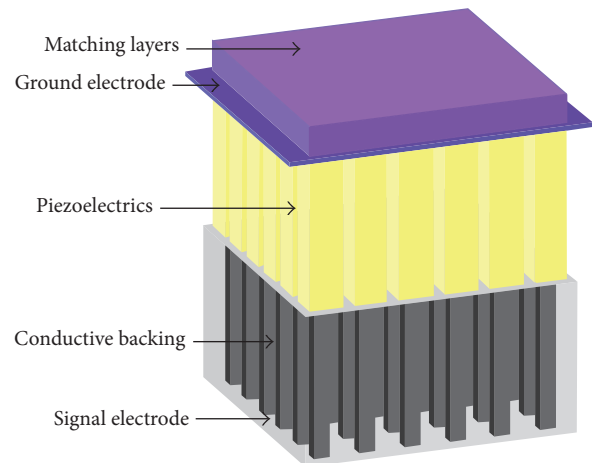


FIGURE 2: The consisting material of a single-unit type matrix transducer.

surface and flat surface. Concave transducers have an advantage of concentrating a higher energy to the focal areas. Flat transducers have a wider steerable area of acoustic field [10]. The elements of 2D array transducers can be arranged as either a rectangle or an annular array [11].

The substrates of 2D array transducers can be fabricated with various piezoelectric materials (Figure 2), such as lead zirconate titanate (PZT), lead magnesium niobate–lead titanate (PMN–PT), and piezocomposites [12]. Aside from piezoelectric transducers, capacitive micromachined US transducers (CMUTs) have also shown a potential performance as their counterparts [13].

Since the concept of 2D array transducers was proposed by Duke University in 1990s, various researchers and commercial companies are concentrated on the development of 2D array transducers. The real-time performance and fabrication parameters of several typical 2D array transducers are listed in Table 1.

TABLE 1: Performance and fabrication parameters of several typical real-time 2D array transducers.

Methods	Mill cross (17 × 17)	Mill cross (20 × 20)	T4 scanner (circular, d : 25 mm)	Receive multiplexing (256 × 256)	4Z1c matrix phased array	Imasonic SaS Voray (256 elements)
Transmitters	32	32	256	169	—	—
Receivers	32	32	256	1024	—	—
Frame rate	8 frames/s	8 frames/s	22 volumes/s	60 volumes/s	24 volumes/s	50 volumes/s
Scan view	65°	65°	64°	65°	—	90°
Frequency	1.7 MHz	1–2.3 MHz	2–3.5 MHz	5 MHz	2.8 MHz	4 MHz
Volume size	24 × 24	—	64 × 64 × 512	30 × 30 × 60	450 × 24 × 30	14 × 14 × 12
Resolution	4°	12 × 18	3 × 3 × 2 mm	—	2.5 mm	200 μm
Authors	von Ramm et al. [100] (1990)	von Ramm et al. [101] (1991)	Stetten et al. [102] (1998)	Yen and Smith [6] (2004)	Frey and Chiao [103] (2008)	Deán-Ben et al. [104] (2015)

Although 2D array transducers are capable of realizing the 3D visualization of dynamic structures in real-time directly and ideally, the electrical impedance of each element in 2D array transducers is much greater than that in 1D array transducers, which makes impedance matching of 2D array elements challenging [14]. Furthermore, to avoid the cross-talk between elements, a half-wavelength distance is needed for the neighbor elements, which results in a large number of elements and extremely small size of each element. To reduce the difficulties in fabrication of 2D array transducer, the size of the array cannot be large, which leads to a small field of view in imaging. Several problems should be resolved before 2D array transducer becoming widespread in clinical examinations.

2.2. Mechanical 3D Probes. Other 3D probes are developed for real-time 3D US imaging by assembling a linear array transducer inside a handheld instrument (Figure 3). In a mechanical 3D probe, a regular linear array transducer is motored to rotate, tilt, or translate within the probe under the computer control [15]. Multiple 2D images are acquired over the examined area when the motor is activated [16]. The axis of rotation, tilt, or translation can be used as reference frame for 3D images reconstruction. Three types of mechanical scanning are illustrated in Figure 4, that is, linear scanning, tilting scanning, and rotational scanning.

2.2.1. Linear Scanning. In this approach, the transducer is driven by a mechanism to translate across the ROI. The scanning route of the transducer is parallel to the surface of the skin and perpendicular to the image plane. The acquired images are parallel and equidistantly spaced and their spacing interval can be adjusted by changing the image frame rate. The resolution of 3D images produced by this approach is not isotropic. The resolutions in the directions parallel to acquired 2D image planes are the same as the original 2D images, and the resolution in the direction of scanning route depends on the elevational resolution of mechanical 3D probe.

2.2.2. Tilting Scanning. In the tilting scanning, the transducer is motored to tilt about an axis at the transduce surface. A

fan of planes is acquired and the angular separation between images is adjustable, which depends on the rotational speed of motors and the image frame rate. When acquiring images, the probe should be fixed on the skin of patients. The resolution of produced 3D images is not isotropic which degrades as the distance from the tilt axis increases. The time of obtaining 3D volume depends on image update rate and the quantity of the required images.

2.2.3. Rotational Scanning. In rotational scanning method, the transducer is driven to rotate with central axis of the probe. The axis should remain fixed when the ROI is being scanned. The rotational scanning probe is sensitive to the motion of transducer such that resulting 3D images will contain artifacts if any motion occurs during the scan. The resolution of the obtained 3D images is also not isotropic. The resolution will degrade as the distance from the axis increases. If a convex transducer is assembled in the probe, the corresponding resulting 3D images will be in a conical shape; otherwise, a cylinder will be obtained when a flat transducer is employed.

2.2.4. Summary. For various applications in clinical practice, a variety of mechanical 3D probes are developed in recent decades. For instance, Downey and Fenster [17] proposed a real-time 3D US imaging system which consists of rotating and linear mechanical 3D probes for different applications. The sequence of images can be acquired at 12.5 frames/s and reconstructed immediately. The system has been applied in breast, prostate, and vascular examination, and the acquisition resolution can be set as 0.3–1.0 mm depending on the ROI.

Mechanical 3D probes are made compactly and they are convenient to operate, though they are comparatively larger than conventional linear probes. The needed imaging and reconstruction time is short which enables viewing high-quality 3D images in real-time. However, clinicians are required to hold the mechanical 3D probes statically while acquiring images, which will lead to latent errors for data acquisition. Furthermore, a particular mechanical motor is needed for integrating with transducer, which is lack of universality.

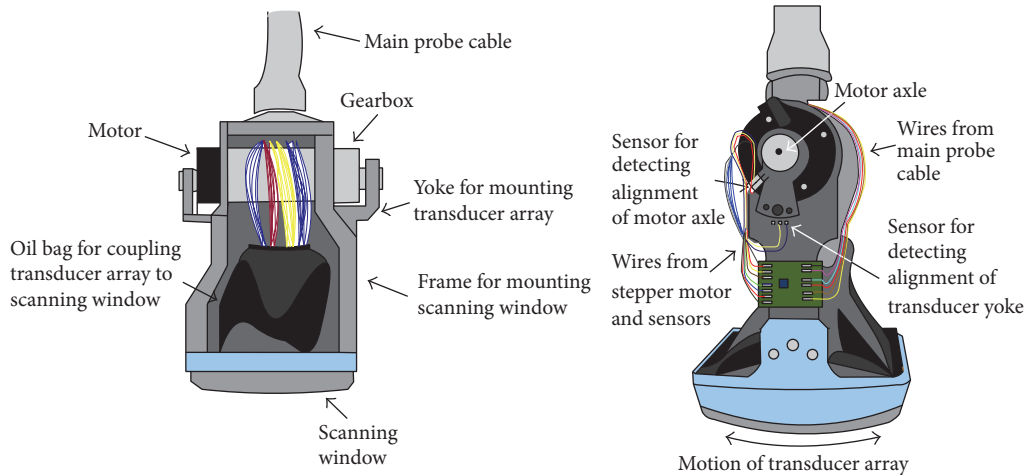


FIGURE 3: Schematic structure of a mechanical 3D probe.

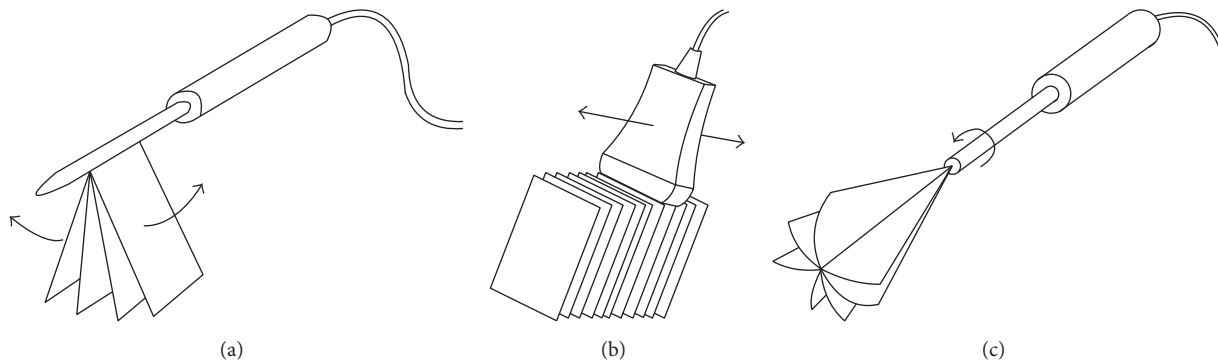


FIGURE 4: Schematic structure of three types of mechanical scanning: (a) tilting scanning; (b) linear scanning; (c) rotational scanning.

2.3. Mechanical Localizers. Similar to mechanical 3D probes, mechanical localizers are driven by motorized mechanisms. In a 3D mechanical probe, the scanning mechanism is integrated inside a handheld instrument together with a special 1D linear transducer. Nevertheless, a mechanical localizer consists of an external fixture which holds a conventional 1D transducer to acquire a series of sequential 2D images [18, 19].

Generally, the scanning route is predefined such that the relative positions and orientations of acquired 2D images can be precisely recorded in computers. With this location information, 3D US images can be reconstruction in real-time. The angular and spacing interval between each frame can be adjusted to obtain optimal resolution and minimize the scanning time. Similar to mechanical 3D probes, the patterns of mechanical localizers scanning can be grouped into 3 types: that is, linear, tilt, and rotation.

Several mechanical localizers systems have been proposed for real-time 3D US imaging, such as Life Imaging System L3Di 3D US acquisition system, which can drive probes in linear scanning for carotid arteries diagnosis [20]. The mechanical localizers have capacity of holding any conventional transducers such that they can undertake the developed US imaging probes without any update to themselves [21]. However, the mechanical localizers are always enormous and heavy, making them inconvenient in applications.

2.4. Freehand Scanners. Obviating the need for cumbersome mechanism, freehand scanners are flexible and convenient to operate. Using a freehand scanner, clinicians can scan the ROI in arbitrary directions and positions, enabling clinicians to choose optimal views and accommodate complexity of anatomy surface. Positions and orientations of 2D B-scans are needed for reconstructing 3D images. Four approaches with different positional sensors were proposed for tracking the US probe: that is, acoustic positioner, optical positioner, articulated arm positioner, and magnetic field sensor (Figure 5). In addition, image-based approaches without positional sensors were also developed, for example, speckle decorrelation.

2.4.1. Acoustic Positioner. In this approach, three sound emitting devices are mounted fixedly on the transducer, and an array of microphones is placed over the patient. The microphones receive acoustic wave continuously from sound emitters during the scanning. Positions and orientations can be calculated for reconstructing 3D images with knowledge of the speed of sound in air, the measured time-of-flight from each sound emitter to microphones, and the positions of microphones [22]. To guarantee a good signal-to-noise ratio (SNR), microphones should be placed closely to the patients and the space between emitters and microphones should be free of obstacles.

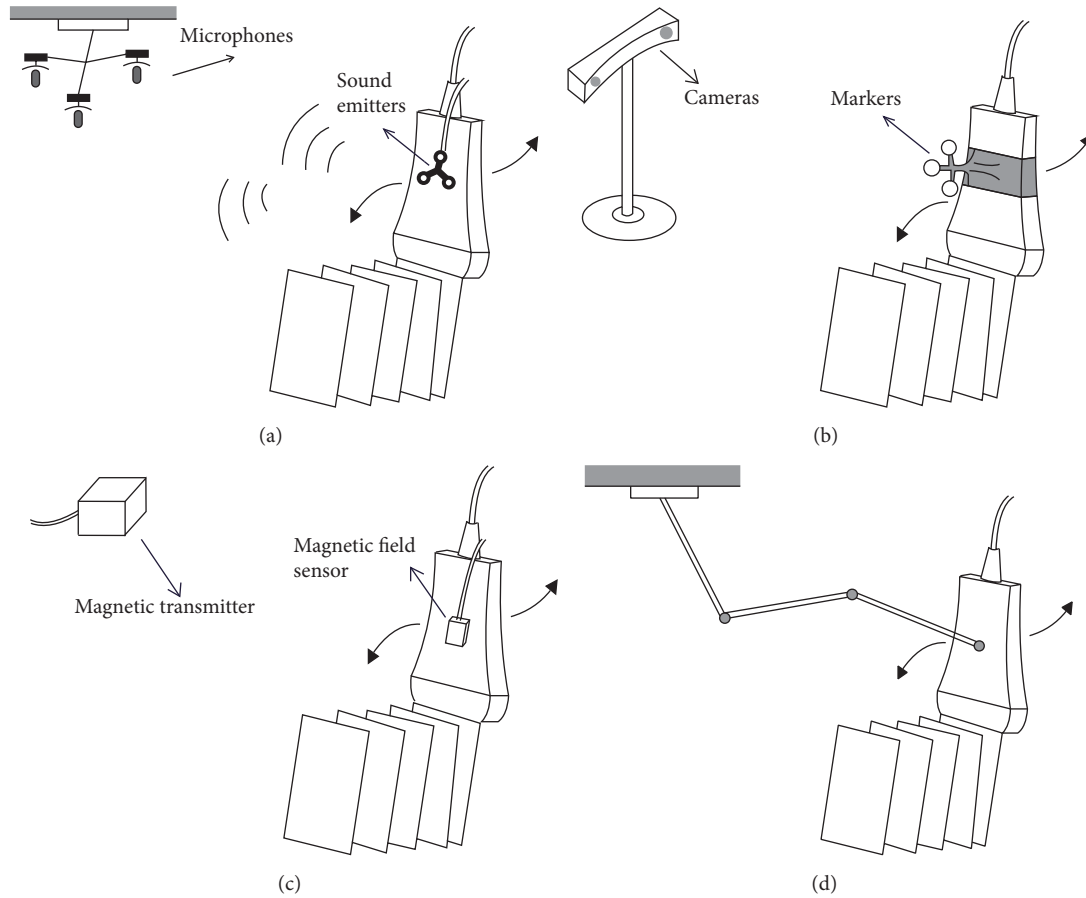


FIGURE 5: Schematic structure of three types of position sensor: (a) acoustic sensor; (b) optimal positioner; (c) magnetic field sensor; (d) articulated arm positioner.

2.4.2. Optical Positioner. A freehand transducer with optical positioner system consists of passive or active targets fixed on the transducer and at least two cameras used to track targets. By observing targets from 2D images, the position and orientation can be calculated with knowledge of relative positions of targets [23]. Optical positioners can be divided into passive stereovision system and active marker system. Passive stereovision systems make use of three or more matt objects as targets and active marker system utilizes several infrared diodes as markers, whose frequency is already known. A freehand transducer with optical positioner is stable and has high accuracy.

2.4.3. Articulated Arm Positioner. In this approach, a transducer is mounted on an articulated arm with multiple movable joints. Unlike mechanical localizer, clinicians can manipulate the transducer with an articulated arm positioner in arbitrary orientations to obtain optimal views. Potentiometers located on the joints can monitor the moving angulation and position of articulated arms continuously, which are effective for calculating the spacing information of transducer for 3D reconstruction. To improve the precision, the individual arms should be as short as possible, which will lead to a small range of view.

2.4.4. Magnetic Field Sensor. A transducer with magnetic field sensor consists of a time-varying magnetic transmitter placed near the patient and a receiver containing three orthogonal coils attached on the transducer. The receiver measures the strength of magnetic field in three orthogonal directions; then the position and orientation of the transducer can be calculated, which is needed for 3D reconstruction. Magnetic field sensors are relatively small and more flexible without a need for unobstructed sight. However, electromagnetic interference and existence of metallic objects may compromise the tracking accuracy and cause distortion. Furthermore, to avoid tracking errors, the magnetic field sampling rate should be increased.

2.4.5. Image-Based Sensing. Image-based sensing approach extracts the relative positions by analyzing the image feature, for example, speckles, instead of depending on position sensors [24]. According to the phenomenon of speckle decorrelation, the speckle pattern should be the same if two images are acquired at the same position, which results in nondecorrelation. However, the decorrelation is proportional to the distance between two images. To obtain the relative translation and rotation between two images, the acquired images are divided into small subregions. Calculated decorrelation

values can be used to analyze the relative position and orientation of adjacent 2D images. Using this scanning protocol, operators are supposed to move the transducer at a constant velocity in linear or rotational manners to guarantee appropriate intervals. However, this approach is lacking accuracy.

2.4.6. Summary. Welch et al. [23] proposed a real-time freehand 3D US system for image-guided surgery which utilized a 5 MHz linear transducer and an optical positioner to track the location and orientation. With the frame rate at 15 frames/s, the system was able to dynamically reconstruct, update, and render 3D volumes. Prager et al. [25] implemented volume measurement and visualization in real-time using a freehand US system with a magnetic field position sensor. With the help of optimized sequential algorithms, the 3D US volume could be resliced at 10 Hz. Dai et al. [26] developed a real-time freehand 3D US system which enabled us to semiautomatically determine the ROI using a 3.5 MHz concave probe and an electromagnetic position sensor. The system was capable of fast predetermining the reconstruction volume and assigning the optimal viewing direction, which achieved an accurate and fast reconstruction in real-time.

Without the predefined route, the freehand scanners should be moved over the skin surfaces in an appropriate speed to avoid significant gaps. Considering the variance of the environment and sensor positions, freehand scanner systems with position sensors should be calibrated every time before being used [27]. Usually, spatial calibration and time calibration are needed for calculating a spatial correction and time delay.

3. Reconstruction Algorithms

Aside from quality and rate of data acquisition, the speed and accuracy of volume reconstruction are significant for realizing real-time 3D US imaging. Various reconstruction algorithms were proposed for visualizing ROI simultaneously while scanning, most of which were based on the conventional 3D reconstruction algorithms and utilized parallel computing technique. Hence, reconstruction algorithms which have already completed or are potential for real-time visualization are introduced in this section. The real-time reconstruction algorithms of 3D voxel representation can be classified into 3 types based on implementation: that is, Voxel-Based Methods (VBMs), Pixel-Based Methods (PBMs), and Function-Based Methods (FBMs). The voxel value in the grid using methods mentioned above depends on the source pixels from the acquired 2D B-scan images. In the following illustrations, the 3D voxel grids are showed as 2D grids marking the centers of the voxels and the 2D input images are illustrated as lines where the points illustrate the centers of the pixels.

3.1. Voxel-Based Methods. In VBMs, every voxel in the predefined structured volume is traversed and assigned a value depending on one pixel or more from the acquired B-scans.

One Voxel with Support of One Pixel. The most popular one-pixel contribution is the Voxel Nearest Neighbor (VNN) [28] with a simple concept that each voxel is assigned the value of

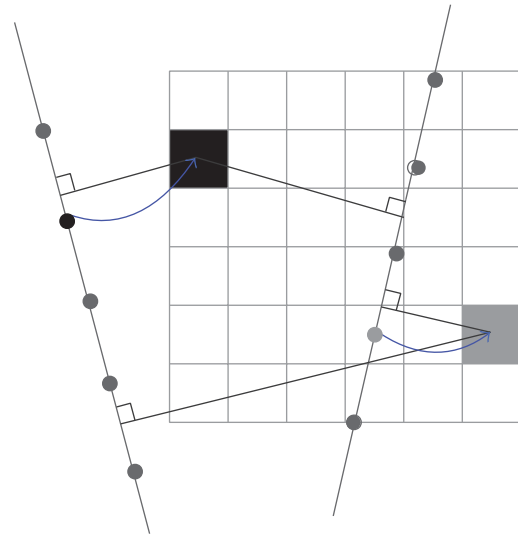


FIGURE 6: VNN. A normal from the voxel to two nearest frames is calculated and the nearest pixel is selected to be mapped into the voxel.

the nearest pixel from source 2D image (Figure 6). By taking into account the fact that the nearest pixel to the voxel lies on its normal to the nearest B-scan, the reconstruction can be speeded up rapidly [29]. Additionally, a volumeless method was proposed by Prager et al. [25] to produce arbitrary 2D slice through the origin data set. It traverses the pixels of the selected volume slice and maps the relative nearest pixels on the acquired frames to the slice by considering the fact that the US beam has a thickness to improve the quality of the slice (Figure 7). The system can generate planar and nonplanar slices quickly for it does not need to construct a volume grid.

Voxel-Based Methods with Interpolation (VBMI). The voxel value relies on the interpolation between several corresponding pixels of the captured frames. The interpolation methods that are popularly used refer to the distance weighted (DW) and its modified versions. The key concept of the DW is that the voxel value is assigned the weighted average of pixels in local neighborhood and the weight is often the inverse of the distance from the pixel to the voxel. Trobaugh et al. [30] proposed a method to traverse each voxel and search the closest two 2D B-scans on each side of the voxel. Then a normal to each surrounding B-scan was determined, passing through the voxel, to obtain the contact points on the two scans. The intensity value of the point was assigned by the bilinear interpolation of the four enclosing pixels on the scan. Afterwards, the target voxel had the value as a weighted average of the two contact points where the weight relied on the distance from the voxel to the scan plane (Figure 8). Another clever algorithm based on Trobaugh's was introduced by Coupé et al. [31] which estimated the probe trajectory between the two nearest B-scans to find intersecting points on the two planes corresponding to the current traversed voxel which was then assigned the weight sum of the two points. As what Trobaugh did, the value of the intersecting points came from the bilinear interpolation of the four closest pixels (Figure 9).

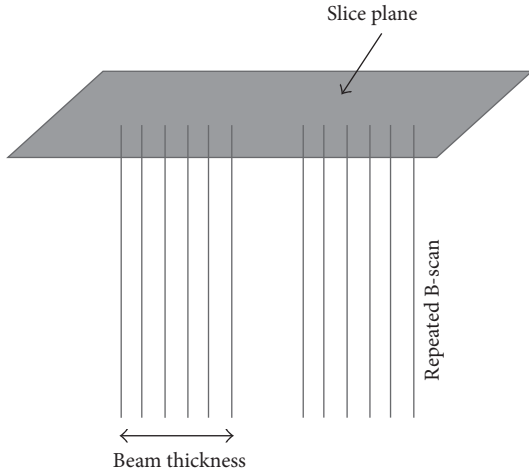


FIGURE 7: Consider the thickness of the US beam to improve inserted quality.

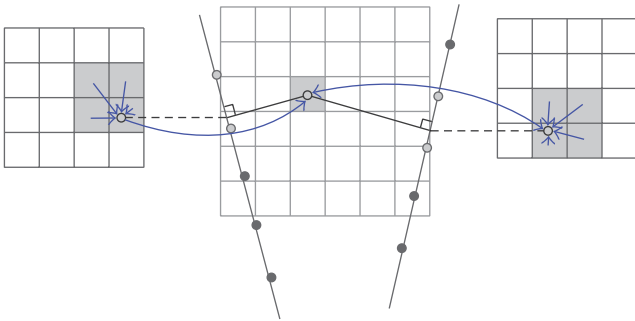


FIGURE 8: VBM with interpolation from the two nearest surrounding images where a normal to each image is calculated.

3.2. Pixel-Based Methods. PBMs are popular in most of the 3D US systems. They traverse the pixels of the acquired B-scans and attribute the pixel value to one or more voxels. There are some factors that result in gaps in the voxel array; for example, a sparse scanning or the voxel size is set small compared to the distance between the B-scans. Thus, a subsequent step is necessarily needed to fill the gaps. The basic algorithm mainly consists of two stages: a distribution stage (DS) and a gap-filling stage (GFS). In the DS, a current traversed pixel distributes pixel value to the nearest voxel or voxels in a definitive region with a weight value. After the DS step, gaps may occur in practice. Thus, the second stage, that is, GFS, has to fill the remaining gaps to get a desired result. We summarize algorithms for the two stages in the following.

3.2.1. DS. Pixel nearest neighbor interpolation (PNN) may be the earliest and simplest reconstruction algorithm as it just fills the pixel value to the nearest voxel in the volume. If more than one pixel runs through the voxel, then the voxel value can be the average (Nelson and Pretorius [32], Gobbi and Peters [33]), maximum value (Nelson and Pretorius [32]), the most recent value (Ohbuchi et al. [34]), or the first value (Trobaugh et al. [30]) of the pixels.

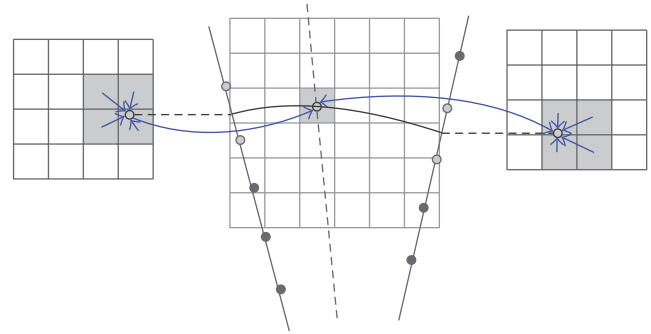


FIGURE 9: The probe trajectory used to find the two intersecting points on the two surrounding images is estimated.

Other investigators proposed some comparatively complex but improved interpolation algorithms for more accurate imaging [35–37]. These methods introduce a local neighborhood called kernel around the pixel to distribute the pixel value to the contained voxels. Every voxel accumulates the pixel values as well as the weight values which are then used to calculate the final voxel value. Thus, we can call these methods kernel-based algorithms, and some parameters, such as the weight function and the size and shape of the neighborhood, should be set prior to reconstruction.

The most commonly referred example of kernel-based algorithms is introduced by Barry et al. [38], who used a spherical kernel of radius R around the pixel with the weight, that is, the inverse distance. Any voxel lying in the neighborhood stores accumulated intensity contribution and relative weight from the central pixel. After traversing all the pixels, the final voxel value is computed by dividing its accumulated pixel intensity value by its accumulated weight value. It should be noted that the radius R influences mostly the DS result. Small R results in quantity of gaps, and large R leads to a highly smoothed volume.

Huang et al. [39] further improved the approach by introducing a positive parameter for the weight and the method is called the squared distance weighted (SDW) interpolation (Figure 10). The algorithm can be described as follows:

$$I(\vec{V}_C) = \frac{\sum_{k=0}^n W_k I(\vec{V}_P^k)}{\sum_{k=0}^n W_k}, \quad (1)$$

$$W_k = \frac{1}{(d_k + \alpha)^2},$$

where $I(\vec{V}_C)$ is the intensity value of the target central voxel, n refers to the number of pixels that fall within the predefined region, $I(\vec{V}_P^k)$ denotes the intensity of the k th pixel that transformed to locate on the volume C coordinate, while W_k is the relative weight for the k th pixel depends on the distance d_k from the k th pixel to the target voxel at C coordinate, and the positive parameter α is used to adjust the effect of the interpolation. The method can reduce the blurring effect in the 3D image since it offers the nonlinear assignment for the weights [39]. In addition, Huang and Zheng [40] proposed an adaptive strategy, namely, adaptive squared distance weighted

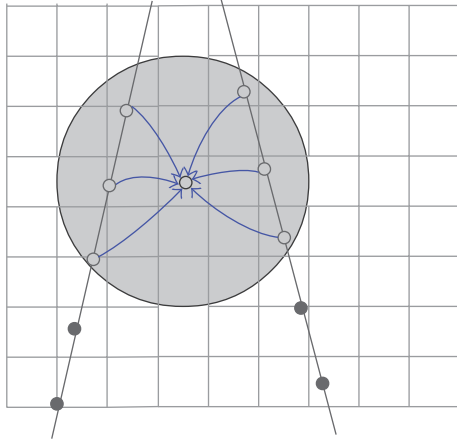


FIGURE 10: Squared distance weighted interpolation. Pixels that fall within the spherical region make value contribution to the central voxel.

(ASDW) method, to automatically adjust α by utilizing the local statistics of pixels in the spherical region around the target voxel with the goal to preserve tissue edges and reduce speckles in the 3D US image. Another adaptive method based on Gaussian convolution kernel, that is, adaptive Gaussian distance weighted (AGDW), is designed by Huang et al. [41], which performs well in speckle reduction and edges preservation as well. The simulation results show the adaptive process offers a good trade-off between the edges preservation and speckle suppression [42]. To reduce the interpolation errors, four median-filter-based methods are also proposed by Huang and Zheng [43] for calculating the voxel intensities.

Additionally, the kernel also can be cubic; for example, Gobbi and Peters [33] introduced the pixel trilinear interpolation (PTL) that made each pixel smeared into a $2 \times 2 \times 2$ kernel and then compounded or alpha-blended into the resulting volume at an appropriate location. The compounding approach used an accumulated buffer to accumulate the weights, indicating how much the voxel was impacted by the intersected pixels while the alpha-blending method put higher weight on the newly inserted pixel than the previous ones without using the accumulated buffer for efficient computation. The compounding method can be explained as the following formulas:

$$I_{k_{\text{voxel}}} = \frac{(b_k I_{\text{pixel}} + a_k I_{k_{\text{voxel}}})}{(b_k + a_k)}, \quad (2)$$

$$a_k = a_k + b_k,$$

where $I_{k_{\text{voxel}}}$ denotes the k th voxel in the volume, I_{pixel} means the pixel value on the B-scan, and the splat kernel coefficient b_k indicates how much the pixel impacts the voxel and the a_k accumulated weight for the corresponding voxel. The compounding method provides average of the new splat with the previous splat to reduce the noise [33].

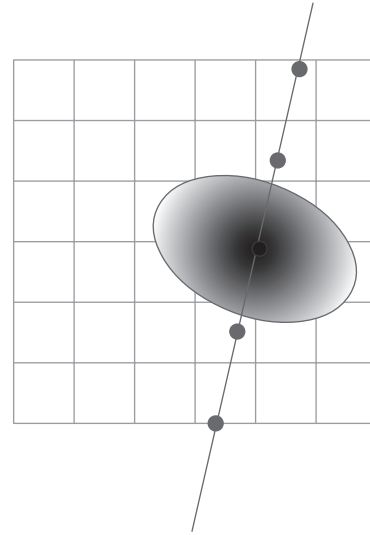


FIGURE 11: PBMs DS with a 3D ellipsoid Gaussian kernel around the pixel and the extent and weighting is determined by an ellipsoid Gaussian kernel.

The alpha-blending method uses the same equation that is used for image compositing via alpha blending as follows:

$$I_{k_{\text{voxel}}} = b_k I_{\text{pixel}} + (1 - b_k) I_{k_{\text{voxel}}}. \quad (3)$$

The additional initial condition requires that the initial voxel value $I_{k_{\text{voxel}}} = 0$. The voxel gets value unless it is hit by the splat and the first time would be $I_{k_{\text{voxel}}} = I_{\text{pixel}}$. In this method a new pixel obscures the contribution of the previous pixels and the scheme achieves faster reconstruction compared to the compounding one.

Some other kernel shapes have also been available proposed to reduce the reconstruction error and improve 3D images. By taking into account the asymmetric shape of the point spread function of the US beam, Ohbuchi et al. [34] applied an ellipsoid Gaussian convolution kernel to the neighboring pixels of each voxel (Figure 11). By assigning more weight to the most recent pixel, the change during sweeping can be taken into consideration.

3.2.2. *GFS*. After the DS, some gaps occur in the volume array if the size of the voxel or the local neighborhood is small compared to the distance between the acquired B-scans. Therefore a necessary processing, that is, GFS, is performed to fill the empty voxels to make the volume integrated and continuous. A variety of filled strategies have been proposed; for example, Hottier and Billon [44] traversed the volume voxels and applied bilinear interpolation between two closest nonempty voxels in the transverse direction to the B-scans to the empty voxel. Other investigators applied a kernel to the filled or empty voxel, and the kernel shape can be sphere or ellipsoid and so on. Some simple interpolation strategies include replacing the hole with a nearest nonempty voxel, an average (Nelson and Pretorius [32]) or a median (Estépar et al. [45]) of the filled voxels in a local neighborhood. Other hole-filling methods already existing with more reasonable filling are

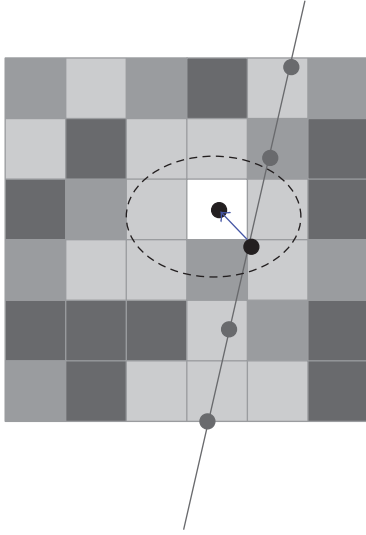


FIGURE 12: PBM GFS. Gap-filling with an ellipsoid kernel around a voxel, and the PSF of the US system is used to determine the kernel shape and weighting.

of great computational cost. Huang et al. [39] enlarged the spherical region of the empty voxels to include more voxels for calculating the weighted average value using SDW for the empty voxel and the voxel value is left zero if the region size exceeds a preset threshold [39]. Estépar et al. [45] applied a normalized convolution with an ellipsoid kernel whose shape and weighting depended on point spread function of the US system to the filled voxels instead of the empty ones to complete the hole-filling (Figure 12). In the kernel methods, it is an important issue to determine the kernel size. The size can be set arbitrarily great to fill all the empty voxels but brings a highly smooth volume. Otherwise, if the size is set small, there still exist gaps in the reconstructed volume after the hole-filling. However, it is reasonable to leave the holes unprocessed, indicating that the scanning sweep has missed those locations.

It should be noted that the GFS is not necessarily needed in some situations like scanning densely or taking into account the thickness of the US beam theoretically. However, it is safe to perform the additional gap-filling to acquire an integrated result since the physicians scan arbitrarily in practice without the guarantee of dense scans.

3.3. Function-Based Methods (FBM). The FBMs attempt to introduce functional interpolation for 3D US reconstruction. It chooses a particular function, for example, a polynomial, and utilizes the pixel values and relative positions to determine the function coefficients. Afterwards, the functions are evaluated at regular intervals to produce the voxel array (Figure 13). Rohling et al. [29] proposed the Radial Basis Function (RBF) that is an approximation with splines. The RBF should satisfy the smoothness requirement from an assumption that the input data is smooth at a scale of several B-scan pixels as well as the approximation requirement that comes from the existence of measurement errors. In order to efficiently

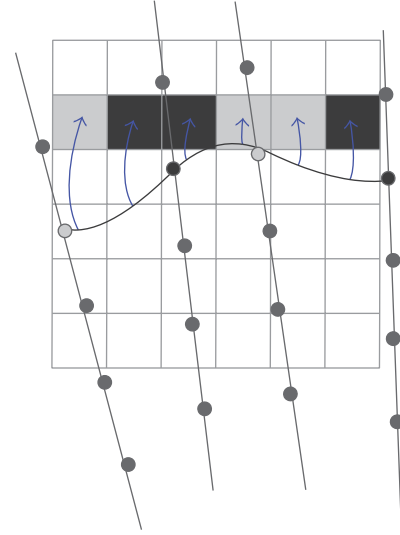


FIGURE 13: Functional interpolation. The function through the input points is estimated and evaluated at regular intervals to obtain the final voxel values.

increase the computed speed, the voxel array is divided into separated small, nonoverlapping rectangular segments where individual interpolating functions are calculated until all the voxel array is covered. An overlapping window that can be expanded sufficiently in all directions to encompass the pixels of the segment and the neighboring pixels is established to get smooth connections among the neighboring segments. All data inside the window is used to calculate the RBF for the enclosed segment and produce a continuous 3D result after all the segments have been traversed. Another popular algorithm called Rayleigh interpolation with a Bayesian framework estimates a function for the tissue by statistical methods where the Rayleigh distribution is to describe the US data. Sanches and Marques [46] further sped up the algorithm by running the first iterations on low resolution of the voxel volume.

Most recently, Huang et al. [47] have designed a fast interpolation method for 3D US with sparse scanning based on Bezier curve. They used a control window to cover 4 adjacent original frames and thus 4 pixel points at the same position on the 4 adjacent B-scans were set to be the control points to determine a 3rd-order Bezier curve. Then voxels located on the path in the reconstructed coordinate were interpolated. It can be described as the following formulas:

$$V(t) = P_0(1-t)^3 + 3P_1t(1-t)^2 + 3P_2t^2(1-t) + P_3t^3, \quad t \in [0, 1], \quad (4)$$

where $V(t)$ denotes the voxel value, P_0, P_1, P_2, P_3 are the 4 control points transformed from the corresponding 4 pixels, and t means the normalized distance from the voxel to P_0 .

After the voxels along the Bezier curves have been traversed, the control window moves to the next 4 adjacent B-scans along the scanning direction to repeat the voxel filling. In order to avoid gaps and make a continuous volume, the

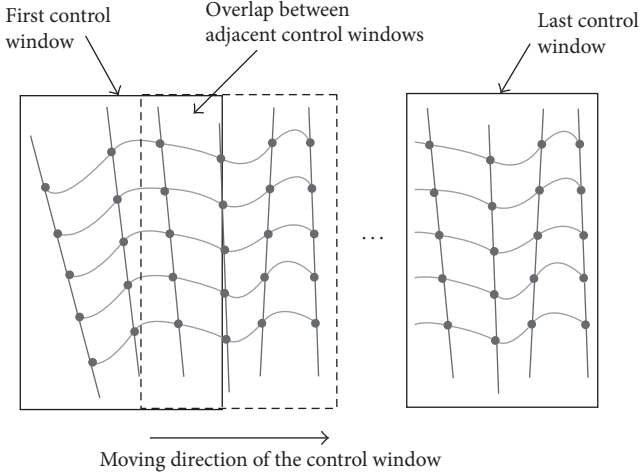


FIGURE 14: Bezier interpolation. Movement of the control window along with the sequences of B-scans for reconstruction of 3D volume.

adjacent control windows are overlapped by 50% and voxels falling into the overlapped region get values by a distance weighted averaging strategy as follows:

$$V = \frac{d_2}{d_1 + d_2} V_{\text{pre}} + \frac{d_1}{d_1 + d_2} V_{\text{cur}}, \quad (5)$$

where V_{pre} , V_{cur} denote the voxel values that are calculated from the previous and current control window, respectively, and d_1 , d_2 refer to the distance from the voxel to P_0 of the current Bezier curve and P_3 of the previous Bezier curve (Figure 14). The method can speed up the reconstruction mostly for a single 3rd-order Bezier curve using 4 control points is able to estimate more than 4 voxels whereas the estimation of a voxel value often requires a number of pixels in conventional techniques [47].

3.4. Computation Time. In terms of real-time 3D US system for practical clinic, like intraoperation, reconstruction and rendering speed are the most important aspects that should be taken into account. The reconstruction time of various algorithms is listed in Table 2. Since the raw B-scan data to be processed is different and the hardware differs in performance, the frame size, volume size, and hardware are included if possible to give a better comparison. From the table we can see that some of the algorithms reconstruct volume in real-time or near real-time (PTL, Bezier interpolation) while others need much long time (two adjacent frames' interpolation, RBF). It is obvious that the simple methods like VNN and PTL achieve a satisfying computation performance for they adopt plain process architecture. Those utilizing a neighborhood (i.e., 3D kernel) to achieve a more accurate reconstruction result increase the computation complexity, thus resulting in higher cost of computation time. For the kernel-based algorithms, computation cost can be reduced through minimizing the neighborhood size or selecting relative simple kernel and weighting (spherical kernel works

faster than ellipsoid kernel; linear weighting performs better than the nonlinear weighting with spherical kernel). Although the RBF is declared to achieve encouraging reconstruction accuracy, it cannot be acceptable in most practical application for its intolerable computation time. Another function-based algorithm, that is, Bezier interpolation, however, performs the reconstruction closely to real-time as it takes advantage of Bezier curves to use 4 control points to interpolate more voxels in the path. It is claimed to achieve fast and accurate reconstructed result compared to the VNN and DW methods in processing sparse raw data for it can better track the changing trend of the control points [47]. It should be noted that although the algorithms in the table cannot reach a fully real-time effect (B-scan image acquisition rate is typically 25 or 30 frames/s), the algorithms can be accelerated to reach real-time.

With the increasing computation power of hardware or the parallel computing technique, successful stories have been reported using Graphics Processing Unit (GPU) to make the reconstruction completed in real-time [48]. Dai et al. [49] accelerated the incremental reconstruction up to 90 frames/s with a common GPU. Chen and Huang [50] implemented two real-time visualized reconstruction methods based on SDW and Bezier interpolations with the help of a common GPU, which speed up the frame rate from 1.33 frames/s and 20 frames/s to 32 frames/s and 119 frames/s. Considering that a powerful processor is always expensive, GPU that can be found in most PCs may be a suitable choice to speed up the reconstruction for the real-time visualization. Algorithms work on GPU must be parallelized. Thus, parallel performance is one of the important aspects in choosing a reconstruction algorithm, and luckily, most of the algorithms in Table 2 meet the requirement.

3.5. Reconstruction Quality. The reconstruction accuracy and display quality are also needed in 3D real-time US imaging for effective diagnosis. Various factors impact the final reconstruction quality, including the probe resolution, the rationality of reconstruction algorithm, probe calibration, and position sensor accuracy. Among these factors, we are likely to analyze how the algorithms impact the reconstructed result. A commonly used quantitative analysis method for reconstruction quality is the leave-one-out test, where some pixels from the raw data are removed before the remaining data are used to reconstruct the voxel array, and the reconstruction error is defined to the average absolute difference between the missing pixels and the corresponding reconstructed voxels [47]; that is,

$$E = \frac{1}{N} \sum_{i=1}^N |p_i - r_i|. \quad (6)$$

Table 3 is extracted from [47] to show the averaged interpolation errors and the standard deviations for several reconstruction algorithms for reconstructing a fetus phantom and the data removing rate is 100%, that is, one frame. It may be a valuable comparison to detect the reconstruction quality of the three types of reconstruction algorithms.

TABLE 2: Reconstruction rate of different reconstruction algorithms.

Algorithm reconstruction	Computation time	Input image size	Volume size	Hardware used	Reference
VNN	0.96 sec per image	302×268	$200 \times 90 \times 330$	3.0 GHz CPU	Sherebrin et al. [28] (1996)
Stradx	0.1 sec per any-plane slice	—	—	Regular PC in 2002	Prager et al. [25, 105] (1999, 2002)
DW	0.067 sec per image	—	—	500 MHz Pentium III workstation	Welch et al. [23] (2000)
Probe trajectory	0.8–2.6 sec per image	510×441	—	3.2 GHz Pentium	Coupé et al. [31] (2005)
<i>PBMs</i>					
PNN	0.033 sec per image 0.05 sec per image (alpha blending)	Cropped from 320×240	—	2 CPU 933 MHz Pentium workstation	Gobbi and Peters [33] (2002)
PTL (kernel: $2 \times 2 \times 2$)	0.08 sec per image (compounding)	Cropped from 320×240	—	2 CPU 933 MHz Pentium workstation	Gobbi and Peters [33] (2002)
Spherical kernel ($9 \times 9 \times 9$) linear weighting SDW	0.62 sec per image	640×480	$205 \times 175 \times 273$	2.4 GHz Pentium IV	Barry et al. [38] (1997)
Spherical kernel ($9 \times 9 \times 9$) nonlinear weighting SDW	0.75 sec per image	640×480	$205 \times 175 \times 273$	2.4 GHz Pentium IV	Huang et al. [39] (2005)
Spherical kernel ($9 \times 9 \times 9$) nonlinear weighting	0.031 sec per image	302×268	$90 \times 81 \times 192$	3.4 GHz CPU 823 MHz GPU	Chen and Huang [50] (2016)
Ellipsoid kernel Gaussian weighting	1.5 sec per image	128×128	$128 \times 128 \times 128$	IBM RS6000 model 560 workstation	Ohbuchi et al. [34] (1992)
Ellipsoid kernel, off-plane: Gaussian in-plane: linear	2.6 sec per image	512×480	$128 \times 128 \times 128$	HP 9000/700 workstation	Ohbuchi et al. [34] (1992)
3D kernel	0.033 sec per image	480×413	$256 \times 256 \times 256$	1.86 GHz CPU 600 MHz GPU	Dai et al. [49] (2010)
<i>FBMs</i>					
Bezier interpolation	0.008 sec per image	302×268	$90 \times 81 \times 192$	3.4 GHz CPU 823 MHz GPU	Chen and Huang [50] (2016)

TABLE 3: The interpolation error of different reconstruction algorithms, and the scanned data is sparse.

VNN		DW		Bezier	
Mean	SD	Mean	SD	Mean	SD
13.32	1.69	11.29	1.26	10.58	1.38

VNN traverses the voxels in the grid and hence avoids the hole-filling stage, making it one of the fastest reconstruction algorithms. However, it seems to be the most inaccurate method compared to others in many published papers (Rohling et al. [29], Huang et al. [51]) for its inevitable drawback of introducing the most artifacts into the volume. The PNN outperforms the VNN as it allocates the pixel to the nearest voxel and a subsequent step is taken to fill the holes by combining pixel values in a neighborhood, making the volume continuous. Unfortunately, artifacts can be generated by this two-stage process, for example, the boundary between the highly detailed “nearest mapping” and the smoothed “hole-filling” voxels [29]. The VBMs and PBMs that apply a 3D kernel to the pixel (i.e., kernel-based algorithms) allow several pixels making contributions to the voxels in the neighborhood further and can improve the reconstruction accuracy [52]. Several parameters, for example, the shape of the kernel (spherical or ellipsoid), the size of the kernel, and the weighting type (linear and nonlinear inverse distance, Gaussian), influence the kernel-based methods’ computation cost and reconstruction accuracy. It is shown that the ellipsoid Gaussian kernel outperforms the spherical kernel for it takes the asymmetric shape of point spread function of the US beam [29]. Nevertheless, it requires expensive computation compared to the spherical one for it introduces more complex neighborhood shape and weight function. It should be noted that the kernel-based methods can reduce the computation time through minimizing the neighborhood size but bring in more holes that need to be filled in the hole-filling stage. Moreover, if the size is set to be large, smaller gaps but excessive smoothing will occur. The most recent function-based algorithm called Bezier interpolation deserves our full attention for its best performance in processing sparse raw scan data. In intraoperation, the physician may scan fast to get an immediate feedback of the scanning region; thus, the acquired B-scan data is usually sparse [45, 53]. With the advantage of fast reconstruction with better reconstruction accuracy, the Bezier interpolation method will make a big count in clinical practices.

3.6. Real-Time versus High-Quality Reconstruction. Generally speaking, a high-quality reconstruction algorithm introducing more complex processing architecture that requires expensive computation may not be implemented in real-time with current common processors. In order to achieve the real-time goal, the simple methods designed to minimize the time and the memory required for reconstruction become a suitable choice. Nevertheless, with the increases in the computational power of PCs and the rapid development in parallel computing technique, it is full of possibility of completing the high-quality algorithms in real-time. By taking advantage

of the large number of parallel executing cores in modern GPU [54], many researchers have used GPU as accelerators across a range of application domains [55], including the 3D US. Dai et al. [49] processed the PTL interpolation with compounding on the GPU in parallel and achieved a real-time reconstruction of up to 90 frames/s. Chen and Huang [50] performed the SDW interpolation on a common GPU and achieved a faster speed of 32 frames/s. Moreover, Chen and Huang [50] utilized the parallel computing on Bezier interpolation, which extremely accelerates the reconstruction speed at 119 frames/s. Hence, it is no doubt that GPU could be an ideal solution to settle the computational requirement in 3D US for a real-time goal.

4. Volume Rendering

4.1. Rendering Algorithms. The reconstruction speed and quality have a serious influence on the implementation of real-time visualization and the accuracy of practical diagnosis. However, the rendering technique also plays a significant and, at times, dominant role in transmitting the 3D information to the physicians timely. There exist three basic approaches for 3D visualization of US images: that is, slice projection, surface rendering, and volume rendering [56].

The slice projection allows users to view arbitrary slices from any angle of the scanned object. It can be real-time but still has the drawback that the physicians have to mentally reconstruct the 2D slices in 3D space [5]. Surface rendering based on visualization of tissue surfaces just simplifies the data set to rapidly describe the shapes of 3D objects such that the topography and 3D geometry are more easily comprehended [57]. In this approach, a segmentation or classification step is performed before rendering, losing some features of the data set, and making the method particularly sensitive to noise. Volume rendering displays the anatomy in a translucent manner. It allows physicians freely to choose the opacity values to selectively highlight particular features of the volume objects, which improves the diagnostic accuracy. Nevertheless, since every acquired data element influences every rendered view, this method requires expensive computation.

Both the slice projection and surface rendering only display a small part of the whole 3D information acquired at any one time. Due to the less computational requirement, many systems acquired the interactive rendering through slice projection in the past; for example, Prager et al. [25] rendered any slice of the scanned object using the Gouraud technique.

Volume rendering, however, preserves all the 3D information, making it the most common technique for 3D display [32]. Among volume rendering, the opacity-based ray-casting method is popularly used in 3D US display [58]. Thanks to the rapid development in computer technology, the method can be completed quickly, even in real-time. Therefore, we just give an outline of the opacity-based ray-casting volume rendering algorithms and put an emphasis on the rendering arrangement during volume reconstruction.

One early approach for ray-casting volume rendering is based on intensity projection techniques [59]. It casts rays through the 3D image and every ray intersects the image with a series of voxels and then the voxel values are weighted or just

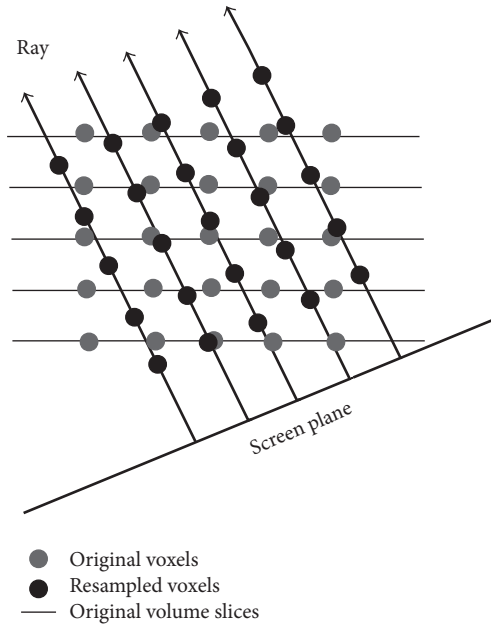


FIGURE 15: Volume rendering using direct ray casting. Voxels along each ray are resampled via a trilinear interpolation of eight neighboring original voxels.

picked the maximum value for each ray to show the anatomy in a translucent manner. A more realistic, opacity-based volume rendering technique based on optical models had been first proposed by Levoy [57] to delineate surfaces and convey depth information better (Figure 15). The rendering algorithm includes two main operations, that is, volume classification and shading. Volume classification assigns opacities to voxels in a volume dataset. Through a rational design of optimum opacity transfer functions, users can achieve high-quality rendering that makes structures of interest more prominent and the background structures less visible. Shading detects the surface orientation and assigns color to each voxel, depending on an illumination model and the surface orientation. After these two operations, a projection operation named as compositing casts rays from the pixels of the final present image plane into the volume to resample the voxels at equidistant intervals. The sampled voxels get opacities and colors through trilinear interpolation using the eight nearest voxels in the original volume grid and then the resampled opacities and colors are merged with each other and with the background by compositing to yield the final colors for the rays and since only one ray is cast per image pixel, for the corresponding pixels of the image plane.

The conventional direct-ray-cast volume rendering has an inevitable drawback of incoherent data access, thus resulting in an inefficient computation since memory architectures suffer from long latencies in case of random accesses. Some efforts were made to overcome the high computational cost. One of the fastest classic algorithms that are designed to overcome the expensive computation in direct-ray-cast method is the shear-warp algorithm which breaks down ray casting into two stages [60], that is, the shear component and the warp

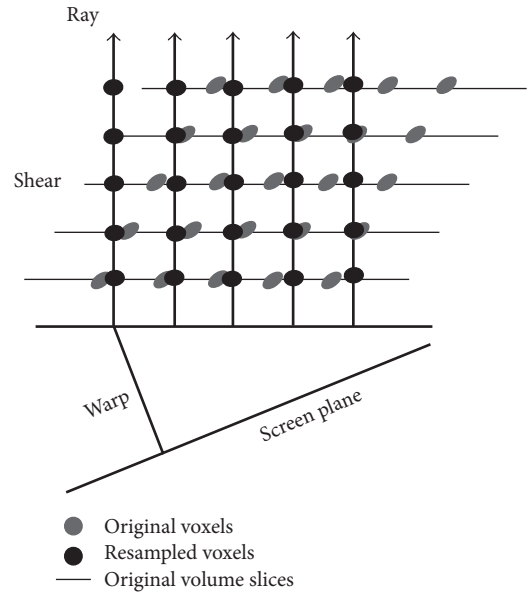


FIGURE 16: Fast volume rendering using shear-warp. Bilinear interpolation is used within each slice to resample each voxel along a ray from the four neighboring original voxels.

component (Figure 16). It processes the 3D data slice by slice on the original volume grid to reduce the computationally expensive trilinear interpolation to bilinear interpolation and at the same time makes the data access coherent by confining the resampled voxels to one slice at a time. However, the confinement of voxel sampling locations to discrete slice locations results in aliasing in compositing and loss of sharp details occurs because of multiple stages of resampling.

Another limitation is the Venetian-blinds artifact on some viewing angles due to the volume shear that is difficult to remove completely [61]. Wu et al. [62] proposed the shear-image-order algorithm (Figure 17) mainly to overcome the problems associated with shear-warp. It eliminates the need for the final affine warp in the shear-warp algorithm through resampling each slice to make the interpolated voxels aligned with the pixels in the final image, preserving the sharp details better. Also, the shear-image-order algorithm makes each slice undergo a 2D shear to correct for the distortion resulting from restricting the sampling locations to original slice locations, which remains the shear-warp's data-access efficiency [61].

4.2. Rendering Arrangement. There are mainly two arrangements for rendering during data acquisition and insertion: one is to render the volume as each newly acquired image arrived and has been inserted into the voxel grid (i.e., slice-by-slice incremental volume rendering); the other is to wait for a fixed number of frames to be mapped onto the volume before the rendering.

4.2.1. Multiple Scans per Rendering (MSPR). Due to the heavy computation in rendering and limited computational capacities of common processors, it is reasonable to render the partial volume after several scans have been inserted into

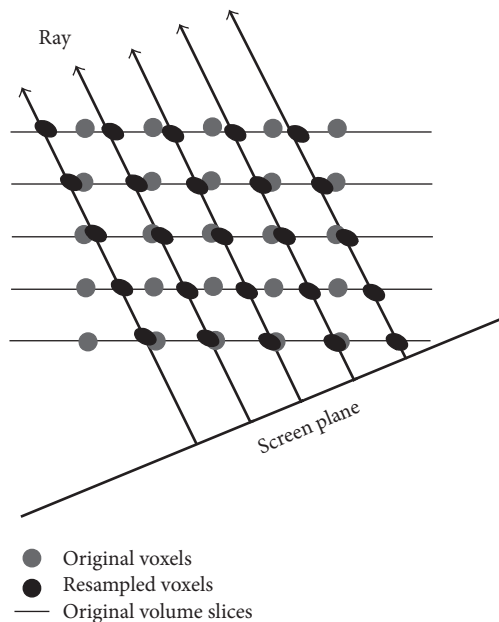


FIGURE 17: Fast volume rendering using shear-image-order. Bilinear interpolation is used within each slice to resample each voxel along a ray from the four neighboring original voxels.

the grid array to obtain a near real-time visualized feedback. Several researchers have attempted this arrangement to achieve a near real-time result. Welch et al. [23] developed a system that updates the scanned volume with the capacity to simultaneously view cross-sections through the volume and a volume-rendered perspective view. The system waits for a fixed number of frames to form a data scan block which is then mapped onto the volume where the voxel value comes from the average of pixels at that position. The gaps are filled using the distance weighted average of the two nearest scanned voxel values in the scan direction. Then a rendering engine provided by CBYON, Inc., is applied to render the partial volume. The render rate reached roughly 15 frames/s as well as the reconstruction rate and thus, the system achieved a near real-time result. In addition to the qualitative feedback, that is, views of the partial volume, Dai et al. [26, 49] designed a system that provides real-time quantitative feedback on reconstruction, allowing the physicians to get hold of the process rate of reconstruction and determine when to terminate the scanning. In the system, pixels of every newly acquired B-scan are assigned into the predefined volume with the PNN method presented by Rohling et al. [29], and after insertion of the latest captured image, the reconstruction ratio (RR) and increased ratio (IR) are calculated. The RR is updated immediately to users to provide the quantitative feedback while IR is used to drive the volume rendering as the IR exceeds a predefined threshold. The researchers used a module provided by Medical Imaging Toolkit (MITK) for the rendering. The reconstruction and visualization are all performed on a personal computer. They set the IR threshold to 5% and achieved a visualization rate of 12.5 frames/s when the size of the reconstructed volume was $200 \times 200 \times 200$ and the B-scan size was 552×274 .

To implement the real-time visualization during the data acquisition and improve reconstruction accuracy, Chen and Huang [50] proposed a real-time freehand 3D US imaging system based on Bezier interpolation. Their method computes the incremental volume reconstruction, hole-filling, and volume rendering on a common GPU. As for the volume reconstruction, every five newly acquired B-scans are calculated by 4th-order Bezier interpolation kernel in their corresponding allocated device memory and interpolated into voxels. A C-function which executes the Bezier interpolation kernel for M times in parallel by different CUDA threads is called. To speed up the reconstruction, the block size was set to 32×32 , while each thread processed 4×4 pixels of the image sequentially to reduce the insertion error. After the incremental reconstruction, some empty holes may exist. The hole-filling could be performed on the GPU, with the block grid set the same as the B-scan image number. In the volume rendering stage, a ray-casting volume rendering is used to render the 3D volume. Since the computation for composition is independent, each thread can deal with a subimage rendering in parallel. With the appropriate arrangement of reconstruction and rendering, utilizing the parallel computing of GPU can extremely accelerate the speed of visualization to 191 frames/s when the B-scan size was 302×268 and the volume size was $90 \times 81 \times 192$.

4.2.2. One Scan per Rendering (OSPR). The OSPR means the arrangement of rendering the partial volume immediately after a newly captured B-scan has been inserted into the volume grid. Its feasibility has been demonstrated.

Ohbuchi et al. [34] developed a system to perform the rendering immediately after every newly acquired B-scan was reconstructed into the volume. They selected a finite 3D Gaussian kernel for incremental reconstruction and the rendering algorithm is an improved image-order, ray-casting version based on Levoy's [57]. The rendering method takes advantage of the incremental nature of the input and only the voxels in the proximity of the new 2D slice are sampled. It keeps the result of each incremental ray-sampling in a 3D array. Also, they reduced the compositing cost by introducing the idea of tree-structured Hierarchical Ray-Cache (HRC). The HRC stores the ray samples in its leaves and partially composites the results in its nonleaf nodes which can be reused in the compositing procedure. Due to the limited computational capacity of the workstation, the incremental reconstruction and rendering algorithm yielded a disappointing speed of no more than 1 frame/s.

Gobbi and Peters [33] used the Visualization Toolkits (VTK) to perform the 3D rendering. There were totally 5 threads in a 2 CPU 933 MHz Pentium III workstation to perform the data acquisition, reconstruction, and visualization. One thread waited for the tracking information of the scanner while the second thread moved each acquired B-scan onto a stack along with a time stamp. Two threads parallelized the interpolation of the most recent acquired frame; one performed the splats for the top half of the video frame and the other for the bottom half of the frame, and the reconstruction rate was 20 frames/s for PTL via alpha blending and 12 frames/s for PTL via compounding when the frame size

was 320×240 and the volume size was $256 \times 193 \times 256$. The main application thread rendered the partially reconstructed volume. Due to the high computational load on the computer and the limited process or speed, however, the rendering refresh rate was just 5 Hz.

In order to complete a fully interactive 3D US imaging system, Dai et al. [49] took advantage of the large number of parallel executing cores in a modern GPU to accelerate the incremental volume reconstruction and rendering. In the reconstruction, each captured B-scan was inserted into the volume using pixel 3D kernel interpolation in which the kernel was a $2 \times 2 \times 2$ cube. Numerous threads in the GPU executed the incremental reconstruction kernel. A C-function defined in accordance with the NVIDIA Compute Unified Device Architecture (CUDA) inserted the image in parallel. Additionally, to avoid parallel insertion errors, each thread just processed 4×4 pixels of the image in order. In the volume rendering, they used ray casting to render the volume. Instead of performing ray casting for the entire display image every time a newly acquired B-scan was inserted into the volume. It just casted rays for pixels of the subimage that comes from the projection of the subvolume whose voxels were just updated from the most recent interpolation. There were two main steps to implement the incremental volume rendering. First, the position and size of the subimage in the projection image were figured out on the host and then sent to the device memory, that is, the GPU memory. Second, on the device, ray-casting kernel was called to update the subimage where each pixel was processed by a thread. Thanks to the rational arrangement of reconstruction and rendering and the powerful parallel computational capacities of the GPU, the system could provide real-time visualization feedback (over 25 frames/s) during data harvesting.

The foresaid real-time freehand 3D US imaging system proposed by Chen and Huang [50] could also take advantage of SDW interpolation, in which the incremental volume reconstruction, hole-filling, and volume rendering are calculated on a common GPU, similar to the Bezier interpolation method. However, the incremental kernel was called when every newly acquired scan arrives to perform insertion in parallel on the GPU. The block size was 32×32 to obtain a high speed while each thread managed 4×4 pixels of the acquired images. To avoid the insertion error, each thread processed all the pixels in the preset spherical neighborhood. Thanks to the parallel computing of GPU, the 3D volume could be reconstructed and displayed at 32 frames/s when the acquired B-scan size was 302×268 and the volume size was $90 \times 81 \times 192$.

4.2.3. OSPR versus MSPR. Since volume rendering needs a heavy load of computation, it is hard to achieve a real-time rendering in a common PC. Thus, an interactive 3D US system is hard to accomplish. However, it is possible to gain a near real-time effect if we choose a rational rendering arrangement during data acquisition. The OSPR arrangement can achieve a more smooth interaction with a higher time cost in rendering [33, 34]. The alternative method, that is, MSPR, yielding a better trade-off between computational cost and interactivity, can provide a better feedback [23, 26]. Nowadays, with a rapid development in the computer technology,

the powerful computational capacity and even the mature parallel computing technique can help in speeding up the reconstruction and rendering processing. As we can see, some systems have utilized the parallel technique to achieve an interactive result. For instance, Dai et al. [49] have made use of the large amounts of parallel executing cores of GPU to perform the incremental reconstruction and rendering in real-time. Therefore it would be better to choose the OSPR rather than the MSPR arrangement for a fully interactive effect since GPU is more and more common in standard PCs and many of the reconstruction and rendering algorithms can be easily parallelized.

5. Applications

With the improvements in acquisition techniques, reconstruction algorithms, rendering methods, and computer GPU acceleration approaches, nowadays real-time 3D US imaging has been inundated in everyday clinical use. The advantages of simultaneous visualization and flexible operations contribute the expansion in areas of clinical application. Hereon, several promising clinical applications of real-time 3D US imaging are discussed.

5.1. Obstetrics. Fetuses remain challenging and difficult to evaluate due to their random motions, rapid heart rates, and maternal respiratory. To minimize these artifacts, patients should hold their breath during the data acquisition of the fetus. Real-time 3D US imaging enables a quick view of expected results while scanning and permits setting up or adjusting the gain while acquiring images. As a result, clinicians can react immediately to dynamic changes in fetal position.

Using a convex transabdominal 3D mechanical probe (3.5 MHz) and surface rendering, a real-time 3D US imaging is available for fetuses surrounded by sufficient amniotic fluid in prenatal diagnosis. Abnormalities of fetal face, for example, micrognathia and cleft lip, can be detected in real-time 3D US imaging. In addition, real-time 3D US imaging can also be applied to assist the diagnosis in rib anomalies, fluid accumulation, and abnormal spine curvature [63]. Utilizing matrix array transducer allows multimodality, for example, live xPlane imaging and live 3D surface, to examine the fetal heart in real-time [64].

5.2. Cardiology. To avoid estimation errors in geometrical assumptions and illusory displacement of the true boundary caused by out-of-plane cardiac motion when using traditional 2D US images, real-time 3D echocardiography was proposed to entirely visualize the anatomy of the cardiac chambers.

With the integration of matrix transducers, real-time 3D echocardiography is increasingly used to quantitatively measure left ventricular volume and dynamic changes of chamber volume during the cardiac cycle. It provides functional information, for example, blood flow and ejection fractions, to diagnose ischemic and congenital heart disease [65]. In addition, using a full volume probe is able to reconstruct large-range pyramid-shaped 3D images in near real-time [66].

Transthoracic and transesophageal approaches are both feasible for real-time 3D echocardiography [67]. Tridimensional myocardial structures can be obtained to examine anatomic defects. By utilizing stress echocardiography method, coronary artery disease can also be detected [68].

5.3. Surgical Guidance. Conventional 2D US imaging has limitation in locating the precise position in an oblique plane. With the advent of real-time 3D US imaging technique, the full visualization of the entire tissue with multiple transverse scans has become available. Making use of matrix array transducers, the real-time 3D transrectal US can improve the accuracy of the prostate implant [69]. Other interventions, for example, cryoprobe, which assists in treating prostate cancer and prostatic hyperplasia, can also take advantage of precise guidance from real-time 3D US imaging with a mechanical 3D probe in rotational scanning [70].

With the guidance of real-time 3D US imaging, biopsy is able to definitively diagnose cancer and reduce the psychological trauma in surgery [71]. Real-time 3D US imaging acquired by a matrix array transducer or a mechanical 3D probe in rotational scanning and rendered by slice projection or volume rendering method can assist clinicians to manipulate the needle tip to targeted lesion within the breast or nerve [72].

With the merit of perceived safety, portability, and dynamic imaging, 3D real-time US is capable of minimizing the surgical invasion, which facilitates it to be a useful guidance for intraoperative resection of gliomas [72] and brain tumors [73]. It is also widely utilized for monitoring abdominal radiation therapy [74] as well as regional anesthesia of femoral nerve [75] and lumbar spine [76].

5.4. Musculoskeletal Tissues. Real-time 3D US imaging can easily demonstrate anatomical details of small joints which are undetectable using traditional 2D US imaging and dramatically reduce the examination time. These advantages make real-time 3D US imaging apparently more suitable for musculoskeletal examination. Due to the variety of size and location of musculoskeletal structures, the transducer for 3D musculoskeletal US imaging should be appropriately selected considering different frequency. Transducers with high frequency are able to obtain high-resolution images. However, their penetration is weaker, making them more suitable for superficial and small-size structures [77].

With the ability to image articular and periarticular structures, real-time 3D US imaging is increasingly applied into diagnosis of rheumatology. The detection of rheumatology includes bone erosions in small joints, enthesitis, and partial tear of tendons, which require the demonstrated images with high quality [78].

Making use of a mechanical localizer and parallel computing reconstruction, the forearm including bones, muscles, and connective tissues can be clearly visualized in near real-time [79]. Utilizing the mechanical 3D probes with PBMs, the 3D anatomy images of lumbar spine can be obtained and visualized in real-time as guidance in spinal needle injections. The epidural space and the facet joints are of significant interest among anatomical features. Using matrix

array transducer can increase the processing speed and improve the image quality at the same time [80].

5.5. Vascular Imaging. Accurate assessment of vascular characteristics, for example, vessel anatomy and blood flow distribution, requires imaging technique capable of producing 3D images in real-time [81]. Real-time 3D US has capacity of not only noninvasively providing the anatomic geometry for numerical simulation of hemodynamics, but also demonstrating the dynamic 3D behavior of vessels [82], enhancing its wide applications in diagnosis of angiosis.

Taking advantage of a mechanical 3D probe or a freehand convex probe (1–5 MHz) combining with a magnetic position tracker, the measurement of aortic diameter, plaque volume, and stenosis degree can be implemented for predicting aortic aneurysm [83]. The aortic wall strains, which are indicators of biomechanical changes caused by aortic aneurysm, can also be detected by real-time echocardiography [84].

The arterial wall motion and hemodynamics are of great significance in early diagnosis of carotid atherosclerosis. With a linear mechanical 3D probe, the wall shear stress which is considered being related to development of atherosclerosis can be evaluated accurately [82]. As for blood flow velocity distribution, Doppler imaging [85] or matrix array transducers at a high volume rate (4000 volumes/s) [86] are generally utilized in clinics.

In addition, real-time 3D intravascular US imaging making use of an electromagnetic tracking sensor or an optical positioner enables the precise alignment of endovascular aortic stent grafting [87] and detection of peripheral blood vessels for cannula insertion guidance [88].

5.6. Urology. Real-time 3D US has been demonstrated as a noninvasive alternative to conventional voiding cystourethrography (VCUG), which is an invasive investigation for diagnosis and treatment monitoring of vesicoureteral reflux [89, 90]. Using the marker-based tracking methods, real-time 3D US is capable of navigation in urological surgery [91] and removing obstructions in urinary flow [92].

Prostate brachytherapy is considered as an effective treatment for early prostate cancer [93]. To confirm the success of the execution of punctures, the needle should be placed on the correct positions critically and rapidly [94]. Under the guidance of the 3D real-time transrectal US, which is mounted with a micro-magnetic sensor or an optical sensor [95], the preoperative oncological data as well as surrounding vital anatomies can be better understood and the precision of placing needles or catheters into the prostate gland has been well increased [96]. The same technique can also be applied to implement prostate biopsy [97] and quantify the prostate swelling [98].

Besides, real-time 3D US-based virtual cystoscopy imaging can be utilized to detect the bladder cancer recurrence [99]. Transurethral US (TUUS) imaging method is generally used in evaluation of the pelvic floor, urethra, detrusor, and levator ani. It provides useful information in diagnosis of stress urinary incontinence and etiology of pelvic floor dysfunction.

6. Conclusions

With the inherent nature of low cost [64] and no radiation, the capacity of dynamically visualizing the anatomy and geometry in real-time and user-friendly interaction with the operators expands the application of real-time 3D US imaging in clinical examinations increasingly. The main approaches to accomplishing a real-time US imaging system are systematically discussed in this review. The technical details of implementation and comparison among various approaches provide a guidance to design an appropriate system for practical use and improve the real-time 3D US imaging potentially with a higher quality and lower time cost. The usefulness of the real-time 3D US has been demonstrated by a large variety of clinical applications, further indicating its role and significance in the fields of medical imaging and diagnosis.

Conflicts of Interest

The authors declare that they have no conflicts of interest.

Acknowledgments

This work was partially supported by National Natural Science Foundation of China (nos. 61372007 and 61571193), Guangdong Provincial Science and Technology Program-International Collaborative Projects (no. 2014A050503020), and Guangzhou Key Lab of Body Data Science (no. 201605030011).

References

- [1] X. Feng, X. Guo, and Q. Huang, "Systematic evaluation on speckle suppression methods in examination of ultrasound breast images," *Applied Sciences*, vol. 7, no. 1, p. 37, 2017.
- [2] Q. Huang, Y. Luo, and Q. Zhang, "Breast ultrasound image segmentation: a survey," *International Journal of Computer Assisted Radiology and Surgery*, vol. 12, no. 3, pp. 493–507, 2017.
- [3] Q. Huang, F. Yang, L. Liu, and X. Li, "Automatic segmentation of breast lesions for interaction in ultrasonic computer-aided diagnosis," *Information Sciences*, vol. 314, pp. 293–310, 2015.
- [4] H. Chang, Z. Chen, Q. Huang, J. Shi, and X. Li, "Graph-based learning for segmentation of 3D ultrasound images," *Neurocomputing*, vol. 151, no. 2, pp. 632–644, 2015.
- [5] J. N. Welch, J. A. Johnson, M. R. Bax et al., "Real-time freehand 3D ultrasound system for clinical applications," in *Medical Imaging 2001: Visualization, Display, and Image-Guided Procedures*, Proceedings of SPIE, pp. 724–730, San Diego, Calif, USA, February 2001.
- [6] J. T. Yen and S. W. Smith, "Real-time rectilinear 3-D ultrasound using receive mode multiplexing," *IEEE Transactions on Ultrasonics, Ferroelectrics, and Frequency Control*, vol. 51, no. 2, pp. 216–226, 2004.
- [7] J. T. Yen, J. P. Steinberg, and S. W. Smith, "Sparse 2-D array design for real time rectilinear volumetric imaging," *IEEE Transactions on Ultrasonics, Ferroelectrics, and Frequency Control*, vol. 47, no. 1, pp. 93–110, 2000.
- [8] S. W. Smith, H. G. Pavy, and O. T. von Ramm, "High-speed ultrasound volumetric imaging system. I. Transducer design and beam steering," *IEEE Transactions on Ultrasonics, Ferroelectrics, and Frequency Control*, vol. 38, no. 2, pp. 100–108, 1991.
- [9] C. E. M. Démoré, A. W. Joyce, K. Wall, and G. R. Lockwood, "Real-time volume imaging using a crossed electrode array," *IEEE Transactions on Ultrasonics, Ferroelectrics, and Frequency Control*, vol. 56, no. 6, pp. 1252–1261, 2009.
- [10] N. Hosaka, R. Koda, S. Onogi, T. Mochizuki, and K. Masuda, "Production and validation of acoustic field to enhance trapping efficiency of microbubbles by using a matrix array transducer," *Japanese Journal of Applied Physics*, vol. 52, no. 7, Article ID 07HF14, 2013.
- [11] S. Tamano, M. Yamazaki, S. Sano, K. Hara, J. Sakano, and Y. Miwa, "3D ultrasound imaging system using fresnel ring array," in *Proceedings of the IEEE Ultrasonics Symposium*, pp. 1310–1313, October 2003.
- [12] J. Woo and Y. Roh, "Ultrasonic two-dimensional array transducer of the single-unit type with a conductive backing of the 1–3 piezocomposite structure," *Japanese Journal of Applied Physics*, vol. 53, no. 7, Article ID 07KD06, 2014.
- [13] Y. Roh, "Ultrasonic transducers for medical volumetric imaging," *Japanese Journal of Applied Physics*, vol. 53, no. 7, Article ID 07KA01, 2014.
- [14] D. H. Turnbull and F. S. Foster, "Fabrication and characterization of transducer elements in two-dimensional arrays for medical ultrasound imaging," *IEEE Transactions on Ultrasonics, Ferroelectrics, and Frequency Control*, vol. 39, no. 4, pp. 464–475, 1992.
- [15] R. W. Prager, U. Z. Ijaz, A. H. Gee, and G. M. Treece, "Three-dimensional ultrasound imaging," *Proceedings of the Institution of Mechanical Engineers, Part H: Journal of Engineering in Medicine*, vol. 224, no. 2, pp. 193–223, 2010.
- [16] A. Fenster and D. B. Downey, "3-D ultrasound imaging: a review," *IEEE Engineering in Medicine and Biology Magazine*, vol. 15, no. 6, pp. 41–51, 1996.
- [17] D. B. Downey and A. Fenster, "Vascular imaging with a three-dimensional power Doppler system," *American Journal of Roentgenology*, vol. 165, no. 3, pp. 665–668, 1995.
- [18] T. R. Nelson and D. H. Pretorius, "Three-dimensional ultrasound imaging," *Ultrasound in Medicine and Biology*, vol. 24, no. 9, pp. 1243–1270, 1998.
- [19] Q. Huang, B. Xie, P. Ye, and Z. Chen, "3-D ultrasonic strain imaging based on a linear scanning system," *IEEE Transactions on Ultrasonics, Ferroelectrics, and Frequency Control*, vol. 62, no. 2, pp. 392–400, 2015.
- [20] C. D. Ainsworth, C. C. Blake, A. Tamayo, V. Beletsky, A. Fenster, and J. D. Spence, "3D ultrasound measurement of change in carotid plaque volume: a tool for rapid evaluation of new therapies," *Stroke*, vol. 36, no. 9, pp. 1904–1909, 2005.
- [21] J. Du, X.-L. Mao, P.-F. Ye, and Q.-H. Huang, "Three-dimensional reconstruction and visualization of human enamel ex vivo using high-frequency ultrasound," *Journal of Medical and Biological Engineering*, vol. 37, no. 1, pp. 112–122, 2017.
- [22] A. Fenster and D. B. Downey, "Three-dimensional ultrasound imaging," in *Handbook of Medical Imaging*, vol. 1 of *Physics and Psychophysics*, pp. 463–510, 2000.
- [23] J. N. Welch, J. A. Johnson, M. R. Bax, R. Badr, and R. Shahidi, "A real-time freehand 3D ultrasound system for image-guided surgery," in *Proceedings of the IEEE Ultrasonics Symposium*, pp. 1601–1604, October 2000.

- [24] H. Gao, Q. Huang, X. Xu, and X. Li, "Wireless and sensorless 3D ultrasound imaging," *Neurocomputing*, vol. 195, pp. 159–171, 2016.
- [25] R. W. Prager, A. Gee, and L. Berman, "Stradx: real-time acquisition and visualization of freehand three-dimensional ultrasound," *Medical Image Analysis*, vol. 3, no. 2, pp. 129–140, 1999.
- [26] Y. Dai, J. Tian, J. Xue, and J. Liu, "A qualitative and quantitative interaction technique for freehand 3D ultrasound imaging," in *Proceedings of the 28th Annual International Conference of the IEEE Engineering in Medicine and Biology Society (EMBS '06)*, pp. 2750–2753, IEEE, New York, NY, USA, September 2006.
- [27] R. W. Prager, R. N. Rohling, A. H. Gee, and L. Berman, "Rapid calibration for 3-D freehand ultrasound," *Ultrasound in Medicine and Biology*, vol. 24, no. 6, pp. 855–869, 1998.
- [28] S. Sherebrin, A. Fenster, R. N. Rankin, and D. Spence, "Freehand three-dimensional ultrasound: implementation and applications," in *Medical Imaging 1996: Physics of Medical Imaging*, pp. 296–303, Newport Beach, Calif, USA, February 1996.
- [29] R. Rohling, A. Gee, and L. Berman, "A comparison of freehand three-dimensional ultrasound reconstruction techniques," *Medical Image Analysis*, vol. 3, no. 4, pp. 339–359, 1999.
- [30] J. W. Trobaugh, D. J. Trobaugh, and W. D. Richard, "Three-dimensional imaging with stereotactic ultrasonography," *Computerized Medical Imaging and Graphics*, vol. 18, no. 5, pp. 315–323, 1994.
- [31] P. Coupé, P. Hellier, N. Azzabou, and C. Barillot, "3D freehand ultrasound reconstruction based on probe trajectory," in *Proceedings of the International Conference on Medical Image Computing and Computer-Assisted Intervention*, pp. 597–604, Palm Springs, Calif, USA, October 2005.
- [32] T. R. Nelson and D. H. Pretorius, "Interactive acquisition, analysis, and visualization of sonographic volume data," *International Journal of Imaging Systems and Technology*, vol. 8, no. 1, pp. 26–37, 1997.
- [33] D. G. Gobbi and T. M. Peters, "Interactive intra-operative 3D ultrasound reconstruction and visualization," in *Proceedings of the International Conference on Medical Image Computing and Computer-Assisted Intervention*, pp. 156–163, 2002.
- [34] R. Ohbuchi, D. Chen, and H. Fuchs, "Incremental volume reconstruction and rendering for 3-D ultrasound imaging," in *Visualization in Biomedical Computing '92*, vol. 1808 of *Proceedings of SPIE*, pp. 312–323, September 1992.
- [35] T. Wen, F. Yang, J. Gu, and L. Wang, "A novel Bayesian-based nonlocal reconstruction method for freehand 3D ultrasound imaging," *Neurocomputing*, vol. 168, pp. 104–118, 2015.
- [36] X. Chen, T. Wen, X. Li et al., "Reconstruction of freehand 3D ultrasound based on kernel regression," *BioMedical Engineering Online*, vol. 13, no. 1, article 124, 2014.
- [37] T. Wen, Q. Zhu, W. Qin et al., "An accurate and effective FMM-based approach for freehand 3D ultrasound reconstruction," *Biomedical Signal Processing and Control*, vol. 8, no. 6, pp. 645–656, 2013.
- [38] C. D. Barry, C. P. Allott, N. W. John et al., "Three-dimensional freehand ultrasound: image reconstruction and volume analysis," *Ultrasound in Medicine and Biology*, vol. 23, no. 8, pp. 1209–1224, 1997.
- [39] Q.-H. Huang, Y.-P. Zheng, M.-H. Lu, and Z. R. Chi, "Development of a portable 3D ultrasound imaging system for musculoskeletal tissues," *Ultrasonics*, vol. 43, no. 3, pp. 153–163, 2005.
- [40] Q.-H. Huang and Y.-P. Zheng, "An adaptive squared-distance-weighted interpolation for volume reconstruction in 3D freehand ultrasound," *Ultrasonics*, vol. 44, pp. e73–e77, 2006.
- [41] Q. Huang, Y. Zheng, M. Lu, T. Wang, and S. Chen, "A new adaptive interpolation algorithm for 3D ultrasound imaging with speckle reduction and edge preservation," *Computerized Medical Imaging and Graphics*, vol. 33, no. 2, pp. 100–110, 2009.
- [42] Q. Huang, M. Lu, Y. Zheng, and Z. Chi, "Speckle suppression and contrast enhancement in reconstruction of freehand 3D ultrasound images using an adaptive distance-weighted method," *Applied Acoustics*, vol. 70, no. 1, pp. 21–30, 2009.
- [43] Q.-H. Huang and Y.-P. Zheng, "Volume reconstruction of freehand three-dimensional ultrasound using median filters," *Ultrasonics*, vol. 48, no. 3, pp. 182–192, 2008.
- [44] F. Hottier and A. C. Billon, "3D echography: status and perspective," in *3D Imaging in Medicine*, pp. 21–41, Springer, 1990.
- [45] R. S. J. Estépar, M. Martín-Fernández, C. Alberola-López, J. Ellsmere, R. Kikinis, and C.-F. Westin, "Freehand ultrasound reconstruction based on roi prior modeling and normalized convolution," in *Proceedings of the International Conference on Medical Image Computing and Computer-Assisted Intervention*, pp. 382–390, 2003.
- [46] J. M. Sanches and J. S. Marques, "A multiscale algorithm for three-dimensional free-hand ultrasound," *Ultrasound in Medicine and Biology*, vol. 28, no. 8, pp. 1029–1040, 2002.
- [47] Q. Huang, Y. Huang, W. Hu, and X. Li, "Bezier interpolation for 3-D freehand ultrasound," *IEEE Transactions on Human-Machine Systems*, vol. 45, no. 3, pp. 385–392, 2015.
- [48] T. Wang, J. Wu, and Q. Huang, "Enhanced extended-field-of-view ultrasound for musculoskeletal tissues using parallel computing," *Current Medical Imaging Reviews*, vol. 10, no. 4, pp. 237–245, 2014.
- [49] Y. Dai, J. Tian, D. Dong, G. Yan, and H. Zheng, "Real-time visualized freehand 3D ultrasound reconstruction based on GPU," *IEEE Transactions on Information Technology in Biomedicine*, vol. 14, no. 6, pp. 1338–1345, 2010.
- [50] Z. Chen and Q. Huang, "Real-time freehand 3D ultrasound imaging," *Computer Methods in Biomechanics and Biomedical Engineering: Imaging & Visualization*, pp. 1–10, 2016.
- [51] W. Huang, Y. Zheng, and J. A. Molloy, "3D ultrasound image reconstruction from non-uniform resolution freehand slices," in *Proceedings of the IEEE International Conference on Acoustics, Speech, and Signal Processing (ICASSP '05)*, vol. 2, pp. ii/125–ii/128, 2005.
- [52] O. V. Solberg, F. Lindseth, H. Torp, R. E. Blake, and T. A. N. Hernes, "Freehand 3D ultrasound reconstruction algorithms—a review," *Ultrasound in Medicine and Biology*, vol. 33, no. 7, pp. 991–1009, 2007.
- [53] R. San José-Estépar, M. Martín-Fernández, P. P. Caballero-Martínez, C. Alberola-López, and J. Ruiz-Alzola, "A theoretical framework to three-dimensional ultrasound reconstruction from irregularly sampled data," *Ultrasound in Medicine and Biology*, vol. 29, no. 2, pp. 255–269, 2003.
- [54] H. K.-H. So, J. Chen, B. Y. S. Yiu, and A. C. H. Yu, "Medical ultrasound imaging: to GPU or not to GPU?" *IEEE Micro*, vol. 31, no. 5, pp. 54–65, 2011.
- [55] V. Archirapatkave, H. Sumilo, S. C. W. See, and T. Achalakul, "GPGPU acceleration algorithm for medical image reconstruction," in *Proceedings of the 9th IEEE International Symposium on Parallel and Distributed Processing with Applications (ISPA '11)*, pp. 41–46, May 2011.

- [56] T. R. Nelson and T. T. Elvins, "Visualization of 3D Ultrasound Data," *IEEE Computer Graphics and Applications*, vol. 13, no. 6, pp. 50–57, 1993.
- [57] M. Levoy, "Display of surfaces from volume data," *IEEE Computer Graphics and Applications*, vol. 8, no. 3, pp. 29–37, 1988.
- [58] A. Kaufman and K. Mueller, "Overview of volume rendering," *The Visualization Handbook*, vol. 7, pp. 127–174, 2005.
- [59] C. Barillot, "Surface and volume rendering techniques to display 3-D data," *IEEE Engineering in Medicine and Biology Magazine*, vol. 12, no. 1, pp. 111–119, 1993.
- [60] P. Lacroute and M. Levoy, "Fast volume rendering using a shear-warp factorization of the viewing transformation," in *Proceedings of the 21st Annual Conference on Computer Graphics and Interactive Techniques*, pp. 451–458, 1994.
- [61] K. Karadayi, R. Managuli, and Y. Kim, "Three-dimensional ultrasound: from acquisition to visualization and from algorithms to systems," *IEEE Reviews in Biomedical Engineering*, vol. 2, pp. 23–39, 2009.
- [62] Y. Wu, V. Bhatia, H. Lauer, and L. Seiler, "Shear-image order ray casting volume rendering," in *Proceedings of the ACM SIGGRAPH Symposium on Interactive 3D Graphics*, pp. 153–161, April 2003.
- [63] K. Baba, T. Okai, S. Kozuma, and Y. Taketani, "Fetal abnormalities: evaluation with real-time-processible three-dimensional US—preliminary report," *Radiology*, vol. 211, no. 2, pp. 441–446, 1999.
- [64] P. Acar, L. Battle, Y. Dulac et al., "Real-time three-dimensional foetal echocardiography using a new transabdominal xMATRIX array transducer," *Archives of Cardiovascular Diseases*, vol. 107, no. 1, pp. 4–9, 2014.
- [65] J. Pedrosa, D. Barbosa, N. Almeida, O. Bernard, J. Bosch, and J. D'hooge, "Cardiac chamber volumetric assessment using 3D ultrasound—a review," *Current Pharmaceutical Design*, vol. 22, no. 1, pp. 105–121, 2016.
- [66] Y. Hirasaki, Y. Seino, Y. Tomita, and M. Nomura, "Cardiac axis-oriented full-volume data acquisition in real-time three-dimensional transesophageal echocardiography to facilitate on-cart analysis," *Anesthesia and Analgesia*, vol. 113, no. 4, pp. 717–721, 2011.
- [67] M. V. Burri, D. Gupta, R. E. Kerber, and R. M. Weiss, "Review of novel clinical applications of advanced, real-time, 3-dimensional echocardiography," *Translational Research*, vol. 159, no. 3, pp. 149–164, 2012.
- [68] E. Picano and P. A. Pellikka, "Stress echo applications beyond coronary artery disease," *European Heart Journal*, vol. 35, no. 16, pp. 1033–1040, 2014.
- [69] P. Yan, "SU-F-T-41: 3D MTP-TRUS for prostate implant," *Medical Physics*, vol. 43, no. 6, pp. 3470–3471, 2016.
- [70] M. Ding, H. N. Cardinal, and A. Fenster, "Automatic needle segmentation in three-dimensional ultrasound images using two orthogonal two-dimensional image projections," *Medical Physics*, vol. 30, pp. 222–234, 2003.
- [71] A. Fenster, K. Surry, W. Smith, and D. B. Downey, "The use of three-dimensional ultrasound imaging in breast biopsy and prostate therapy," *Measurement*, vol. 36, no. 3-4, pp. 245–256, 2004.
- [72] S. Mahboob, R. McPhillips, Z. Qiu et al., "Intraoperative ultrasound-guided resection of gliomas: a meta-analysis and review of the literature," *World Neurosurgery*, vol. 92, pp. 255–263, 2016.
- [73] A. V. Moiyadi and P. Shetty, "Direct navigated 3D ultrasound for resection of brain tumors: a useful tool for intraoperative image guidance," *Neurosurgical Focus*, vol. 40, no. 3, article E5, 2016.
- [74] L. Su, S. Kien Ng, Y. Zhang et al., "MO-FG-CAMPUS-JeP3-04: feasibility study of real-time ultrasound monitoring for abdominal stereotactic body radiation therapy," *Medical Physics*, vol. 43, no. 6, p. 3727, 2016.
- [75] E. Smistad and F. Lindseth, "Real-time automatic artery segmentation, reconstruction and registration for ultrasound-guided regional anaesthesia of the femoral nerve," *IEEE Transactions on Medical Imaging*, vol. 35, no. 3, pp. 752–761, 2016.
- [76] D. Behnami, A. Seitel, A. Rasoulia et al., "Joint registration of ultrasound, CT and a shape+pose statistical model of the lumbar spine for guiding anesthesia," *International Journal of Computer Assisted Radiology and Surgery*, vol. 11, no. 6, pp. 937–945, 2016.
- [77] D. Kane, P. V. Balint, R. Sturrock, and W. Grassi, "Musculoskeletal ultrasound—a state of the art review in rheumatology. Part 1: current controversies and issues in the development of musculoskeletal ultrasound in rheumatology," *Rheumatology*, vol. 43, no. 7, pp. 823–828, 2004.
- [78] T. A. Wallny, R. L. Schild, D. S. Bertelsbeck, M. E. Hansmann, and C. N. Kraft, "Three-dimensional ultrasonography in the diagnosis of rotator cuff lesions," *Ultrasound in Medicine and Biology*, vol. 27, no. 6, pp. 745–749, 2001.
- [79] Z. Chen, Y. Chen, and Q. Huang, "Development of a wireless and near real-time 3D ultrasound strain imaging system," *IEEE Transactions on Biomedical Circuits and Systems*, vol. 10, no. 2, pp. 394–403, 2016.
- [80] M. Brudfors, A. Seitel, A. Rasoulia et al., "Towards real-time, tracker-less 3D ultrasound guidance for spine anaesthesia," *International Journal of Computer Assisted Radiology and Surgery*, vol. 10, no. 6, pp. 855–865, 2015.
- [81] M. Shabanmotlagh, J. Janjic, S. Raghunathan, M. A. Pertijs, N. de Jong, and M. Verweij, "The role of sub-dicing in the acoustical design of an ultrasound matrix transducer for carotid arteries imaging," in *Proceedings of the IEEE International Ultrasonics Symposium (IUS '16)*, pp. 1–4, IEEE, Tours, France, September 2016.
- [82] C.-Z. Jin, K.-H. Nam, and D.-G. Paeng, "The spatio-temporal variation of rat carotid artery bifurcation by ultrasound imaging," in *Proceedings of the IEEE International Ultrasonics Symposium (IUS '14)*, pp. 1900–1903, September 2014.
- [83] K. Pfister, W. Schierling, E. M. Jung, H. Apfelbeck, C. Henersperger, and P. M. Kasprzak, "Standardized 2D ultrasound versus 3D/4D ultrasound and image fusion for measurement of aortic aneurysm diameter in follow-up after EVAR," *Clinical Hemorheology and Microcirculation*, vol. 62, no. 3, pp. 249–260, 2016.
- [84] K. Karatolios, A. Wittek, T. H. Nwe et al., "Method for aortic wall strain measurement with three-dimensional ultrasound speckle tracking and fitted finite element analysis," *Annals of Thoracic Surgery*, vol. 96, no. 5, pp. 1664–1671, 2013.
- [85] M. G. Perez, M. Ble, M. Cladellas et al., "Combined use of tissue Doppler imaging and natriuretic peptides as prognostic marker in asymptomatic aortic stenosis," *International Journal of Cardiology*, vol. 228, pp. 890–894, 2017.
- [86] M. Correia, J. Provost, M. Tanter, and M. Pernot, "4D ultrafast ultrasound flow imaging: in vivo quantification of arterial volumetric flow rate in a single heartbeat," *Physics in Medicine and Biology*, vol. 61, no. 23, pp. L48–L61, 2016.

- [87] C. Shi, C. Tercero, X. Wu et al., “Real-time in vitro intravascular reconstruction and navigation for endovascular aortic stent grafting,” *The International Journal of Medical Robotics and Computer Assisted Surgery*, vol. 12, no. 4, pp. 648–657, 2016.
- [88] A. I. Chen, M. L. Balter, T. J. Maguire, and M. L. Yarmush, “3D near infrared and ultrasound imaging of peripheral blood vessels for real-time localization and needle guidance,” in *Proceedings of the International Conference on Medical Image Computing and Computer-Assisted Intervention*, pp. 388–396, 2016.
- [89] M. M. Woźniak, A. P. Wiczorek, A. Pawelec et al., “Two-dimensional (2D), three-dimensional static (3D) and real-time (4D) contrast enhanced voiding urosonography (ceVUS) versus voiding cystourethrography (VCUG) in children with vesicoureteral reflux,” *European Journal of Radiology*, vol. 85, no. 6, pp. 1238–1245, 2016.
- [90] R. Pichler, A. Buttazzoni, J. Bektic et al., “Endoscopic treatment of vesicoureteral reflux using dextranomer/hyaluronic acid copolymer in children: results of postoperative follow-up with real-time 3D sonography,” *Urologia Internationalis*, vol. 87, no. 2, pp. 192–198, 2011.
- [91] T. Simpfendorfer, G. Hatiboglu, B. A. Hadaschik et al., “Navigation in urological surgery: possibilities and limits of current techniques,” *Der Urologe*, vol. 54, no. 5, pp. 709–715, 2015.
- [92] M. A. P. Castañeda and F. A. Cosío, “Deformable model of the prostate for TURP surgery simulation,” *Computers and Graphics*, vol. 28, no. 5, pp. 767–777, 2004.
- [93] P. Yan, J. C. Cheeseborough, and K. S. C. Chao, “Automatic shape-based level set segmentation for needle tracking in 3-D TRUS-guided prostate brachytherapy,” *Ultrasound in Medicine and Biology*, vol. 38, no. 9, pp. 1626–1636, 2012.
- [94] M. Ritter, M.-C. Rassweiler, J. J. Rassweiler, and M. S. Michel, “New puncture techniques in urology using 3D-assisted imaging,” *Urologe—Ausgabe A*, vol. 51, no. 12, pp. 1703–1707, 2012.
- [95] O. Ukimura and I. S. Gill, “Imaging-assisted endoscopic surgery: cleveland clinic experience,” *Journal of Endourology*, vol. 22, no. 4, pp. 803–810, 2008.
- [96] F. Vicini, C. Vargas, G. Gustafson, G. Edmundson, and A. Martinez, “High dose rate brachytherapy in the treatment of prostate cancer,” *World Journal of Urology*, vol. 21, no. 4, pp. 220–228, 2003.
- [97] V. Chalasani, D. W. Cool, S. Sherebrin, A. Fenster, J. Chin, and J. I. Izawa, “Development and validation of a virtual reality transrectal ultrasound guided prostatic biopsy simulator,” *Canadian Urological Association Journal*, vol. 5, no. 1, pp. 19–26, 2011.
- [98] S. Shoji, T. Uchida, M. Nakamoto et al., “Prostate swelling and shift during high intensity focused ultrasound: implication for targeted focal therapy,” *Journal of Urology*, vol. 190, no. 4, pp. 1224–1232, 2013.
- [99] F. Gulsen, S. Dikici, I. Mihmanli et al., “Detection of bladder cancer recurrence with real-time three-dimensional ultrasonography-based virtual cystoscopy,” *Journal of International Medical Research*, vol. 39, no. 6, pp. 2264–2272, 2011.
- [100] O. T. von Ramm, S. W. Smith, and R. H. Schneider, “Real-time volumetric ultrasound imaging system,” in *Medical Imaging IV: Image Formation*, vol. 1231 of *Proceedings of SPIE*, pp. 15–22, Newport Beach, Calif, USA, February 1990.
- [101] O. T. von Ramm, H. G. Pavy, and S. W. Smith, “High-speed ultrasound volumetric imaging system. II. Parallel processing and image display,” *IEEE Transactions on Ultrasonics, Ferroelectrics, and Frequency Control*, vol. 38, no. 2, pp. 109–115, 1991.
- [102] G. D. Stetten, T. Ota, C. J. Ohazama et al., “Real-time 3D ultrasound: a new look at the heart,” *Journal of Cardiovascular Diagnosis and Procedures*, vol. 15, no. 2, pp. 73–84, 1998.
- [103] G. Frey and R. Chiao, “4Z1c real-time volume imaging transducer,” White Paper, Siemens Healthcare Sector, 2008.
- [104] X. L. Deán-Ben, S. J. Ford, and D. Razansky, “High-frame rate four dimensional optoacoustic tomography enables visualization of cardiovascular dynamics and mouse heart perfusion,” *Scientific Reports*, vol. 5, Article ID 10133, 2015.
- [105] R. Prager, A. Gee, G. Treece, and L. Berman, “Freehand 3D ultrasound without voxels: volume measurement and visualisation using the Stradx system,” *Ultrasonics*, vol. 40, pp. 109–115, 2002.

Research Article

Semianalytical Solution for the Deformation of an Elastic Layer under an Axisymmetrically Distributed Power-Form Load: Application to Fluid-Jet-Induced Indentation of Biological Soft Tissues

Minhua Lu,¹ Shuai Huang,¹ Xianglong Yang,² Lei Yang,² and Rui Mao³

¹Guangdong Key Laboratory for Biomedical Measurements and Ultrasound Imaging, School of Biomedical Engineering, Shenzhen University, Shenzhen, China

²College of Civil Engineering, Shenzhen University, Shenzhen, China

³Guangdong Province Key Laboratory of Popular High Performance Computers, College of Computer Science and Software Engineering, Shenzhen University, Shenzhen, China

Correspondence should be addressed to Xianglong Yang; xlyang@szu.edu.cn

Received 30 August 2016; Accepted 15 January 2017; Published 8 March 2017

Academic Editor: Mark R. Pickering

Copyright © 2017 Minhua Lu et al. This is an open access article distributed under the Creative Commons Attribution License, which permits unrestricted use, distribution, and reproduction in any medium, provided the original work is properly cited.

Fluid-jet-based indentation is used as a noncontact excitation technique by systems measuring the mechanical properties of soft tissues. However, the application of these devices has been hindered by the lack of theoretical solutions. This study developed a mathematical model for testing the indentation induced by a fluid jet and determined a semianalytical solution. The soft tissue was modeled as an elastic layer bonded to a rigid base. The pressure of the fluid jet impinging on the soft tissue was assumed to have a power-form function. The semianalytical solution was verified in detail using finite-element modeling, with excellent agreement being achieved. The effects of several parameters on the solution behaviors are reported, and a method for applying the solution to determine the mechanical properties of soft tissues is suggested.

1. Introduction

Indentation is one of the most commonly used methods to measure the mechanical properties (e.g., Young's modulus and Poisson's ratio) of biological soft tissues in situ or in vivo, such as articular cartilage [1, 2], the liver, human skin [3], and residual limbs [4], as it does not require special preparation for the specimens. Rigid cylindrical flat-ended or spherical indenters are often employed in both conventional and ultrasound indentation-based measurement techniques [5–9]. Once the loading force has been measured with a force sensor and the tissue deformation together with tissue thickness is recorded with an ultrasound transducer (in ultrasound indentation), Young's modulus and Poisson's ratio of a soft-tissue sample can be calculated from the relationship reported by Hayes et al. and other investigators [10–12].

However, the direct contact associated with the use of a stiff mechanical indenter may cause tissue damage, especially when the tissue has been in the degenerative conditions, and/or those organs, such as cornea, are not suitable for direct touch. Therefore, the use of noncontact devices is desirable whenever possible.

Systems based on fluid-jet-induced indentation have been developed by many researchers for measuring the mechanical properties of soft tissues. The key idea of such systems is to use a fluid jet as an indenter that exerts a mechanical load on the soft tissues so as to avoid the shortcomings associated with direct contact between a rigid measurement instrument and soft tissues. Water and air are commonly used as the fluid mediums. Duda et al. [13] developed a device based on water-jet-induced indentation with optical modality to quantify the cartilage stiffness and

demonstrated a strong correlation with standard indentation measurements. However, it cannot provide the tissue thickness which is a critical parameter to calculate Young's modulus of soft tissue from the indentation load-deformation curve. Lu et al. [14, 15] developed a noncontact indentation system utilizing the compression induced by a water jet and high-frequency ultrasound to measure the properties of soft tissues. They utilized high-frequency ultrasound to measure the initial thickness and dynamic deformation of tissues under water-jet loading. Their tests on phantoms showed that the system was able to quantify the elastic properties of soft tissues and had the capability for elasticity mapping of the tissues in a C-scan test. The system has also been employed to assess degeneration of articular cartilage [1]. Huang and Zheng [16] further designed a miniaturized water-jet- and ultrasound-based indentation system. Their results showed that the indentation system produced results comparable to those obtained using the conventional one and that it was able to characterize the integrity of articular cartilage under arthroscopic control.

Prompted by the inconvenience of water spillage when using a water jet to induce indentation inside the body, Huang et al. [17] developed an air-jet-based indentation system based on optical coherence tomography for measuring the mechanical properties of soft tissues. They performed experiments both on silicone phantoms and on the human hand in vivo, with the results demonstrating the capacity of the system to detect biomechanical changes in soft tissues. The air-jet-based indentation system was subsequently used by Chao et al. to characterize the biomechanical properties of the forefoot plantar soft tissue of different ages [18] and to measure the stiffness of the healing wounds in rat skin [19]. However, they found that the stiffness measured by the air-jet system differed greatly from those mechanical properties measured by the tensile testing machine.

In most of the above-reviewed researches, a stiffness coefficient (SC) was defined to interpret the loading-deformation data of the soft tissues:

$$SC = \frac{F}{d} \cdot \frac{L_0}{A}, \quad (1)$$

where F is the total force applied on the specimen by the fluid jet, A is the area of the outlet of the fluid nozzle, and L_0 and d are the initial thickness and deformation of the specimen, respectively. The definition looks very similar to the compressive Young's modulus of soft tissue measured by unconfined axial compression. However, it should be noted that the total force in (1) was calculated from the fluid pressure in the pipe supplying the fluid because the distribution of the impacting pressure of the fluid jet upon the specimen is complicated and difficult to measure directly. Moreover, the deformation of the specimen induced by a fluid jet also varies spatially across the sample surface, and the sensitivity depends on the lateral resolution of the ultrasound beam. The values of d and A are both ambiguous to some extent, and hence the calculated stiffness coefficient is essentially only a nominal value. The relationship among SC, Young's modulus, and Poisson's ratio is also not obvious. In general, obtaining Young's modulus and Poisson's ratio from the indentation

induced by an impinging fluid jet would require a calibration to be performed based on the conventional contact indentation. This requirement would be highly inconvenient when a fluid jet is used to induce indentation in vivo. Therefore, quantifying the mechanism of soft-material deformation due to compression caused by an impinging fluid jet will benefit the application of fluid-jet-induced indentation to clinical diagnosis.

The classical problem of an elastic half-space indented by a rigid indenter was investigated using theoretical analysis and finite-element simulation. Exact solutions in the form of force-indentation relationships, contact pressure distributions, and stress and displacement fields exist for axisymmetric indenter geometries (e.g., cylinder, sphere, and cone) [12, 20, 21]. The effects of many other parameters, including friction between the indenter and the soft tissue, model geometry, substrate deformability, and curvature, on the calculation of Young's modulus from indentation response of soft tissue were also studied [10, 22–25].

From a mathematical point of view, the indentation induced by contact with a conventional stiff object (e.g., cylinder or sphere indenter) differs significantly from that induced by a fluid jet. In the former, the deformation where the specimen touches the cylindrical flat-ended or spherical punch can be easily measured and it is always treated as a known condition in a theoretical analysis. However, in the latter, even the deformation of the specimen can be measured by an ultrasound transducer; the distribution of the impacting load applied by the fluid jet is unknown. In fact, the wall pressure (i.e., the fluid pressure on the surface of specimen) induced by the fluid jet is greatly affected by the scale (i.e., Reynolds number) as well as the boundary conditions (e.g., the nozzle geometry and the distance from the nozzle outlet to the target surface) [26]. Generally, the wall pressure follows a Gaussian profile for a two-dimensional jet but not for a three-dimensional jet [27]. Boyer et al. [3] applied classical contact mechanics to model the wall pressure by a function with a power form and achieved excellent agreement between the theoretically calculated pressure and the experimentally measured pressure on a rigid plate. Their solutions were used to assess the effects of ageing on the mechanical properties of skin in vivo with their air-jet-based indentation system. However, the solutions they used are derived from elastic materials with infinite thickness, and hence they might not be valid in most clinical applications where the thickness of the soft tissues is finite (and sometimes very small). This means that it is important to determine the analytical solution for the deformation of elastic materials with finite thickness compressed by an impinging fluid jet.

This study employed a semianalytical method to solve the equation describing the indentation induced by a fluid jet. The soft tissue was assumed to be a homogeneous, isotropic elastic layer with finite scale in thickness and infinite size in extent. It was overlaid on a rigid foundation. The wall pressure was modeled by a power-form function as reported by Boyer et al. [3]. To validate the solutions, finite-element modeling (FEM) was performed using a static structural module in the ANSYS software. The results of the analytical solutions and FEM were compared in detail.

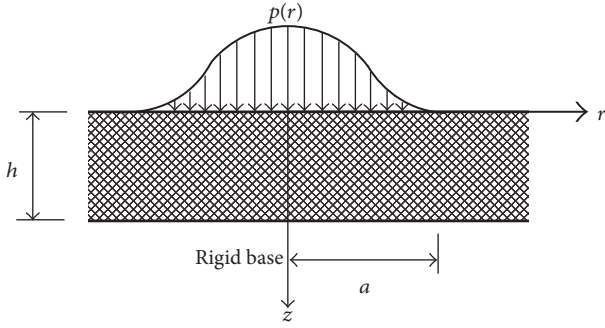


FIGURE 1: Schematic diagram of the deformation of an elastic layer under an axisymmetrically distributed load.

2. Mathematical Analysis

For homogeneous, isotropic materials, when the body forces and inertial effects are neglected and the deformation is small, the equilibrium equations of the linear theory of elasticity can be expressed in terms of the displacement vector as

$$(1 - 2\nu) \nabla^2 \mathbf{u} + \nabla (\nabla \cdot \mathbf{u}) = 0, \quad (2)$$

where \mathbf{u} is the displacement vector, ν is Poisson's ratio of soft tissue, and ∇ is the gradient operator.

Considering the equilibrium of an infinite elastic layer with thickness h adhering to an immovable rigid base, the layer deformation under an axisymmetrically distributed load from the impingement of a circular fluid jet is axisymmetric and so can be analyzed in a cylindrical coordinate system. A schematic diagram of this problem is shown in Figure 1.

The considered problem can be solved conveniently by using the Boussinesq-Papkovich potential functions for the components of the displacement vector; that is,

$$\begin{aligned} 2Gu_r &= -\frac{\partial}{\partial r} [\Phi_0 + z\Phi_1], \\ 2Gu_z &= -\frac{\partial \Phi_0}{\partial z} - z\frac{\partial \Phi_1}{\partial r} + (3 - 4\nu)\Phi_1, \end{aligned} \quad (3)$$

where $G = E/2(1 + \nu)$ is the elastic shear modulus, E is Young's modulus, (r, θ, z) are the radial, tangential, and axial coordinates in a cylindrical coordinate system, (u_r, θ, u_z) are the radial, tangential, and axial components of the displacement vector, respectively, and Φ_0 and Φ_1 are harmonic functions, which are written in the form

$$\begin{aligned} \Phi_0 &= \int_0^\infty [A(\lambda) sh\lambda (h - z) + B(\lambda) ch\lambda (h - z)] \\ &\quad \cdot J_0(\lambda r) d\lambda, \\ \Phi_1 &= \int_0^\infty [C(\lambda) sh\lambda (h - z) + D(\lambda) ch\lambda (h - z)] \\ &\quad \cdot J_0(\lambda r) d\lambda, \end{aligned} \quad (4)$$

where $A, B, C,$ and D are functions of λ to be determined, $J_0(\lambda r)$ is the Bessel function of the first kind of order zero, and

axial-direction coordinate z in the elastic layer ranges from 0 to h .

The normal and tangential stress components are given in terms of the potentials as

$$\begin{aligned} \sigma_{zz} &= 2(1 - \nu) \frac{\partial \Phi_1}{\partial z} - \frac{\partial^2 \Phi_0}{\partial z^2} - z \frac{\partial^2 \Phi_1}{\partial z^2}, \\ \sigma_{rz} &= \frac{\partial}{\partial r} \left[(1 - 2\nu)\Phi_1 - \frac{\partial \Phi_0}{\partial z} - z \frac{\partial \Phi_1}{\partial z} \right]. \end{aligned} \quad (5)$$

The elastic layer is indented on by a prescribed normally distributed load at the surface and the layer adheres to an immovable rigid base, and so the following boundary conditions apply:

(a) At the surface, $z = 0$:

$$\begin{aligned} \sigma_{zz} &= p(r), \\ \sigma_{rz} &= 0, \end{aligned} \quad (6)$$

$(0 \leq r \leq \infty),$

where $p(r)$ is a prescribed load function of radial coordinate, r .

(b) At the bottom, $z = h$:

$$u_r = u_z = 0, \quad (0 \leq r \leq \infty). \quad (7)$$

By using (3)–(5) and boundary conditions (6) and (7) and following the same procedures as described by Hayes et al. [12], the following integral equation can be obtained:

$$\int_0^\infty C'(\lambda) J_0(\lambda r) d\lambda = p(r), \quad (0 \leq r \leq \infty). \quad (8)$$

The axial component of the displacement at the layer surface ($z = 0$), which is a parameter of interest in many situations, can be given by

$$\frac{G}{1 - \nu} u_z(r, 0) = \int_0^\infty C'(\lambda) M(\lambda) J_0(\lambda r) d\lambda, \quad (9)$$

$(0 \leq r \leq \infty),$

where

$$M(\lambda) = \frac{1}{\lambda} \left[\frac{(3 - 4\nu)sh(\lambda h)ch(\lambda h) - \lambda h}{(\lambda h)^2 + 4(1 - \nu)^2 + (3 - 4\nu)sh^2(\lambda h)} \right]. \quad (10)$$

When $p(r)$ is known, (8) may be used to determine $C'(\lambda)$, and then displacement u_z at the layer surface ($z = 0$) can be obtained using (9).

In practical applications, it is convenient to introduce the dimensionless variables $\alpha = \lambda h$ and $r' = r/h$. After nondimensionalizing the load function by an appropriate constant P as $p'(r') = p(r)/P$, (8) and (9) become

$$\int_0^\infty Q(\alpha) J_0(\alpha r') d\alpha = p'(r'), \quad (0 \leq r' \leq \infty), \quad (11)$$

$$\frac{G}{1 - \nu} \frac{u_z(r', 0)}{hP} = \int_0^\infty \frac{1}{\alpha} Q(\alpha) M'(\alpha) J_0(\alpha r') d\alpha, \quad (12)$$

$(0 \leq r' \leq \infty),$

where

$$Q(\alpha) = \frac{C'(\lambda)}{hP}, \quad (13)$$

$$M'(\alpha) = \frac{(3-4\nu)sh\alpha c h\alpha - \alpha}{\alpha^2 + 4(1-\nu)^2 + (3-4\nu)sh^2\alpha}.$$

In the study of Boyer et al. [3], the pressure of an impinging circular fluid jet was modeled by a function of the power form

$$p(r) = \begin{cases} p_0 a^{-2(m-1/2)} (a^2 - r^2)^{m-1/2} & (0 \leq r < a), \\ 0 & (r \geq a), \end{cases} \quad (14a)$$

where a is the radius of the area over which jet is impinging, p_0 is the pressure at the center point of that area, and m is an integer. These three parameters depend on the nozzle geometry, the Reynolds number of the fluid jet, and the distance between the nozzle outlet and the tissue surface. There are two reasons why this form of pressure distribution was chosen: (i) this distribution fits the pressure of an impinging circular fluid jet with acceptable accuracy and (ii) according to Boussinesq theory there exist analytical solutions for the deformation of an elastic half-space under this form of load [28].

As mentioned above, function (14a) is convenient for deriving the analytical solution for the deformation of an elastic half-space (with infinite thickness), but it is not convenient for the deformation problem of an elastic layer with finite thickness. To derive the analytical solution for the deformation of an elastic layer, the pressure function is modified slightly as

$$p(r) = \begin{cases} p_0 a^{-2(m-1)} (a^2 - r^2)^{m-1} & (0 \leq r < a), \\ 0 & (r \geq a). \end{cases} \quad (14b)$$

Integer m may in general be sufficiently large (e.g., $m \geq 28$) [3] for the difference between (14a) and (14b) to be small. Figure 2 shows the fitted curves based on (14a) and (14b) and the experimental data that correspond to the case with a flow rate of 20 L_n/min and $a = 8$ mm [3]. The figure illustrates that the difference is acceptably small.

Introducing the dimensionless variable $r' = r/h$, (14b) becomes

$$p(r) = \begin{cases} p_0 \left(\frac{h}{a}\right)^{2(m-1)} \left[\left(\frac{a}{h}\right)^2 - r'^2\right]^{m-1} = Pp'(r'), & (0 \leq r' < \frac{a}{h}), \\ 0 & (r' \geq \frac{a}{h}), \end{cases} \quad (15)$$

where

$$P = p_0 \left(\frac{h}{a}\right)^{2(m-1)}, \quad (16)$$

$$p'(r') = \left[\left(\frac{a}{h}\right)^2 - r'^2\right]^{m-1}, \quad (0 \leq r' < \frac{a}{h}).$$

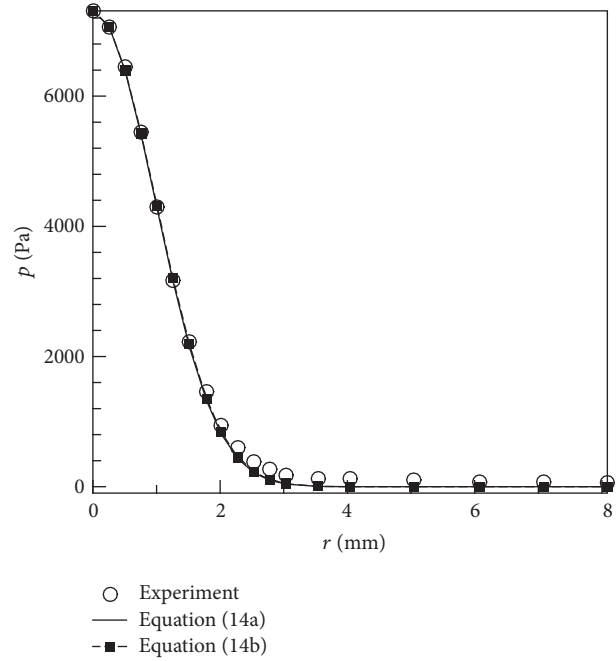


FIGURE 2: Comparison of the fitted curves and experimental data [3].

Using the Heaviside unit step function [29], namely,

$$H\left(\frac{a}{h} - r'\right) = \begin{cases} 1 & (0 \leq r' < \frac{a}{h}) \\ 0 & (r' \geq \frac{a}{h}), \end{cases} \quad (17)$$

and inserting (16) into (11) yield

$$\int_0^\infty Q(\alpha) J_0(\alpha r') d\alpha = \left[\left(\frac{a}{h}\right)^2 - r'^2\right]^{m-1} H\left(\frac{a}{h} - r'\right). \quad (18)$$

Letting $Q'(\alpha) = Q(\alpha)/\alpha$, (18) becomes

$$\int_0^\infty \alpha Q'(\alpha) J_0(\alpha r') d\alpha = \left[\left(\frac{a}{h}\right)^2 - r'^2\right]^{m-1} H\left(\frac{a}{h} - r'\right). \quad (19)$$

Using the Hankel integral transform [29], $Q'(\alpha)$ can be solved as

$$Q'(\alpha) = 2^{(m-1)} \Gamma(m) \left(\frac{a}{h}\right)^m \alpha^{-m} J_m\left(\frac{a}{h}\alpha\right), \quad (20)$$

and then

$$Q(\alpha) = \alpha Q'(\alpha) = \alpha 2^{(m-1)} \Gamma(m) \left(\frac{a}{h}\right)^m \alpha^{-m} J_m\left(\frac{a}{h}\alpha\right), \quad (21)$$

where $\Gamma(m) = (m-1)!$ is the factorial function and $J_m((a/h)\alpha)$ is the Bessel function of the first kind of order m .

Inserting (21) into (12) and rearranging it yield

$$u_z(r', 0) = \frac{p_0 h (1 - \nu^2)}{E} F\left(\nu, m, \frac{a}{h}, r'\right), \quad (22)$$

$$(0 \leq r' \leq \infty),$$

where

$$F\left(\nu, m, \frac{a}{h}, r'\right) = \left(\frac{a}{h}\right)^{2-m} 2^m \Gamma(m)$$

$$\cdot \int_0^\infty \frac{1}{\alpha^m} M'(\alpha) J_m\left(\frac{a}{h}\alpha\right) J_0(\alpha r') d\alpha. \quad (23)$$

This equation is a function of Poisson's ratio ν , fitted integer m , the ratio of the radius of the area over which the jet is impinging to the thickness of the elastic layer (a/h), and dimensionless radius r' . Equation (22) indicates that the axial displacement is proportional to the pressure at the center point of the fluid jet and inversely proportional to Young's modulus of the elastic layer, while it varies nonlinearly with other quantities. The infinite integral on the right-hand side of (23) includes the product of two Bessel functions of the first kind with different orders, and it can be integrated numerically using the adaptive Gaussian quadrature [30]. However, we found that if the Bessel functions are calculated sufficiently accurately, Gauss-Laguerre quadrature is also sufficiently accurate and efficient when m is not too small (e.g., $m > 3$) because the integrand in the infinite integral goes rapidly to zero as the argument increases.

The Bessel function can be calculated using its integral representation

$$J_m(x) = \frac{1}{\pi} \int_0^\pi \cos(m\theta - x \sin \theta) d\theta. \quad (24)$$

This integral can be calculated using Gauss-Legendre quadrature. However, the integral will be unstable when m is large (e.g., $m > 10$) for small x , leading to an incorrect value of the infinite integral on the right-hand side of (23), which is also calculated using Gauss-Laguerre quadrature. Alternatively, the Bessel function can be calculated using its infinite-power-series expansion form

$$J_m(x) = \frac{1}{\Gamma(m+1)} \left(\frac{x}{2}\right)^m$$

$$\cdot [1 - Z_1(1 - Z_2(1 - Z_3(1 - \dots)))]], \quad (25)$$

where

$$Z_k = \frac{1}{k(k+m)} \left(\frac{x}{2}\right)^2, \quad (k = 1, 2, 3, \dots). \quad (26)$$

The Bessel function calculated using (25) is stable when m is large and x is small, but it may be incorrect for large x because in practice only finite terms can be considered, so that the truncation error becomes nonnegligible with large x . Additionally, it is also limited by the machine precision when m and x are both large due to the presence of x^m term.

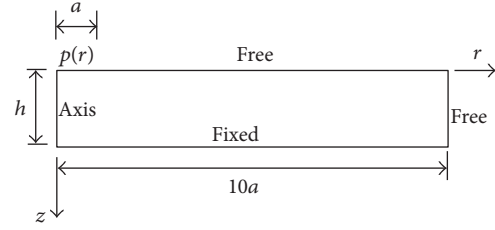


FIGURE 3: Geometry and boundary conditions for finite-element modeling (FEM).

We used a combination algorithm to calculate Bessel function $J_m(x)$; namely, (25) with 50 terms was used for $x \leq m/2$, while (24) with Gauss-Legendre quadrature was used for $x > m/2$. It was found that this combination algorithm works well over wide ranges of the values of m and x , and it was sufficiently accurate for our purposes.

In applications involving using a fluid jet to apply indentation on an elastic layer, the maximum axial displacement, which generally occurs at the center point on the layer surface ($r' = 0; z = 0$), is more useful and easier to obtain by various measurement techniques, such as ultrasound, optical coherence tomography, and other contact methods. Using the property of $J_0(0) = 1$, it can be derived that

$$u_{z\max} = u_z(0, 0) = \frac{p_0 h (1 - \nu^2)}{E} \kappa\left(\nu, m, \frac{a}{h}\right), \quad (27)$$

where

$$\kappa\left(\nu, m, \frac{a}{h}\right)$$

$$= \left(\frac{a}{h}\right)^{2-m} 2^m \Gamma(m) \int_0^\infty \frac{1}{\alpha^m} M'(\alpha) J_m\left(\frac{a}{h}\alpha\right) d\alpha \quad (28)$$

is a scaling factor that depends on Poisson's ratio of the elastic layer ν , fitted integer m , and aspect ratio a/h .

3. Finite-Element Modeling

To verify the validity of the analytical solutions obtained above, an axisymmetric finite-element model was established using a static structural module in ANSYS. The material was assumed to be linear, homogeneous, and isotropic (with constant Young's modulus and Poisson's ratio), and both the deformation and strain were assumed to be small. The model geometry and boundary conditions are shown in Figure 3. The computational domain is a rectangle with dimension $10a$ in the radial direction and h in the axial direction. The left side of the domain is an axis boundary, the bottom side has a fixed boundary, a normal pressure according to (14b) acts upon the top surface at $0 \leq r \leq a$, and the other boundaries are free. Since the stresses are much larger near a contact point [3], distance $10a$ is sufficiently far from the lateral boundary condition to ensure that its effects can be neglected.

Block-meshing technology was applied to ensure the accuracy of the FEM and reduce the computational costs. Uniformly distributed meshes with a grid size of $0.01a$ were

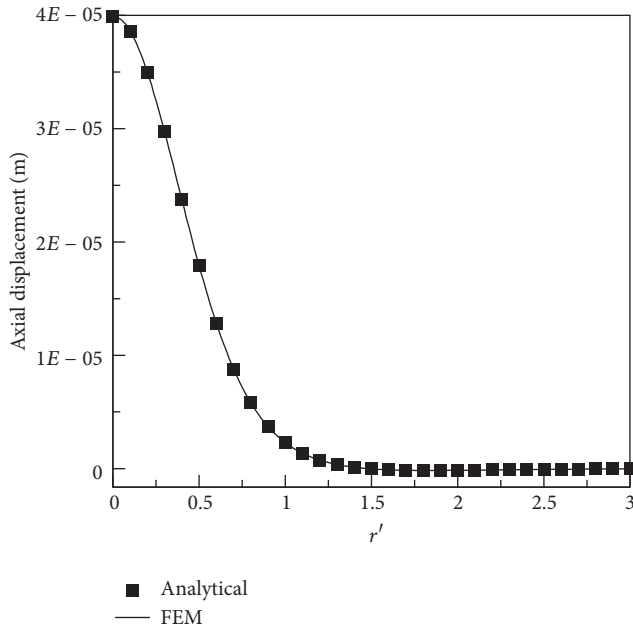


FIGURE 4: Axial displacements at the surface ($z = 0$) from the analytical solution and FEM, where $r' = r/h$.

applied in the radial direction at $0 \leq r \leq a$, and bias-type distributed meshes with a bias factor of 30 and a total number of 200 were used elsewhere. Uniform meshes with a grid size of $0.01a$ (the total number of meshes varied with the layer thickness, h) were used in the axial direction. It was verified that mesh-independent solutions were obtained when using this mesh density.

4. Results and Discussion

This section analyzes the solution of the model described above and discusses its applications in a fluid-jet-based indentation system. To facilitate our analyses, we decided to select one case as a base for further comparisons. The parameters for this case were as follows, which were comparable with those experimental values from the ultrasound water-jet indentation system [14]: thickness of the elastic layer (h), 0.004 m; radius of the area of the impinging fluid jet (a), 0.01 m; Young's modulus (E), 1.0×10^6 Pa; and Poisson's ratio (ν), 0.3. The pressure at the center point (p_0) was 2.0×10^4 Pa, and fitted integer m was 30.

The axial displacements at the surface ($z = 0$) obtained from the analytical solution using (22) and FEM are compared in Figure 4. It is obvious that excellent agreement was achieved.

To further verify the validity of the analytical solutions, more cases were calculated with a wide range of parameters. For simplicity, we report here only the maximum axial displacement, $u_{z\max}$. Equation (27) indicates that the relationships among $u_{z\max}$, p_0 , and E are very simple; namely, $u_{z\max}$ is proportional to p_0 and inversely proportional to E . However, the relationships among $u_{z\max}$, a , h , m , and ν are complex and need to be considered in more detail. Table 1 lists

the values of $u_{z\max}$ computed using (27) and simulated using FEM with constant $a = 0.01$ m and different h , m , and ν values. The table indicates that the analytical solutions agree very well with results from FEM over a wide range of parameters. Generally, the difference between analytical and simulated results increases with increasing fitted integer m and Poisson's ratio ν and decreasing h . The maximum difference was no more than 0.07%, which occurred for $h = 0.001$ m, $m = 40$, and $\nu = 0.5$.

To show how different parameter values affect the axial displacements, the nondimensional indentation, defined as the ratio of the nondimensional maximum axial displacement to nondimensional pressure ($u_{z\max}/h$)/(p_0/E) [12], is plotted against a/h for different m and ν values in Figure 5. It is obvious from the figure that when the aspect ratio (a/h) is small, the indentation varies markedly with this ratio, whereas Poisson's ratio has no significant effect. In contrast, when the aspect ratio is large, Poisson's ratio has a marked effect, while the aspect ratio has only a slight effect. It can be predicted that the indentation for each Poisson's ratio will tend to a limit as the aspect ratio increases, because this is similar to the problem of a thin layer being compressed by a large indenter, which means that the edge effects will be negligible. The indentations have similar features irrespective of the value of m . For small Poisson's ratios, the indentation increases with a/h , while for large Poisson's ratios the indentation first increases and then decreases as a/h increases further.

In fluid-jet-based indentation applications, (27) can be used to calculate Young's modulus. Rearranging that equation yields

$$E = \frac{p_0 h (1 - \nu^2)}{u_{z\max}} \kappa \left(\nu, m, \frac{a}{h} \right), \quad (29)$$

where parameters p_0 , a , and m only depend on characteristics of the fluid-jet instrument, namely, the nozzle geometry, the Reynolds number of the fluid jet, and the distance from the nozzle outlet to the target surface. These characteristics can be determined before the indentation tests are performed through mechanical measurements. Tissue thickness h can also be measured before indentation tests using ultrasound nondestructively or a needle punch which is a destructive method after indentation. Poisson's ratio of soft tissue is often considered to be constant in indentation tests or can be measured by ultrasound or mechanical methods [14]. The maximum axial displacement at the surface of the elastic layer, $u_{z\max}$, can be recorded during the tests by various approaches such as spatial sensors or ultrasonically. Knowledge of these parameters allows scaling factor κ to be calculated using (28), and then Young's modulus of the material can be calculated directly using (29).

Most soft tissues, such as articular cartilage, liver, and human skin, are viscoelastic materials, and so, in general, dynamic analysis should be used. However, as predicted by Hayes et al. [12], the theory based on elastic materials can be used in some limited cases, such as in creep tests, to predict the instantaneous elastic response under a step load. With the closed-form solution (e.g., the scaling factor) in the

TABLE 1: Maximum axial displacement ($u_{z_{\max}}, \times 10^{-5}$ m) values obtained from the analytical solution and FEM with different parameters.

ν	h (m)					
	0.001		0.01		0.02	
	Analytical	FEM	Analytical	FEM	Analytical	FEM
$m = 10$						
0.1	1.9303	1.9301	8.8642	8.8638	10.019	10.019
0.2	1.7795	1.7794	8.5055	8.5052	9.6679	9.6677
0.3	1.5035	1.5034	7.9206	7.9202	9.0892	9.0890
0.4	1.0574	1.0573	7.0899	7.0895	8.2731	8.2730
0.5	0.3691	0.3690	5.9795	5.9791	7.2017	7.2016
$m = 20$						
0.1	1.8959	1.8955	6.6904	6.6899	7.2850	7.2847
0.2	1.7529	1.7525	6.4408	6.4403	7.0400	7.0398
0.3	1.5021	1.5017	6.0317	6.0313	6.6354	6.6351
0.4	1.1104	1.1102	5.4532	5.4527	6.0660	6.0657
0.5	0.5261	0.5259	4.6875	4.6871	5.3227	5.3225
$m = 30$						
0.1	1.8602	1.8597	5.6252	5.6247	6.0257	6.0255
0.2	1.7247	1.7242	5.4230	5.4425	5.8269	5.8267
0.3	1.4924	1.4920	5.0909	5.0904	5.4981	5.4978
0.4	1.1366	1.1362	4.6219	4.6214	5.0357	5.0354
0.5	0.6153	0.6149	4.0043	4.0038	4.4338	4.4334
$m = 40$						
0.1	1.8250	1.8244	4.9577	4.9572	5.2598	5.2595
0.2	1.6963	1.6957	4.7835	4.7830	5.0882	5.0879
0.3	1.4788	1.4783	4.4969	4.4963	4.8041	4.8038
0.4	1.1498	1.1493	4.0926	4.0920	4.4050	4.4046
0.5	0.6732	0.6727	3.5617	3.5611	3.8861	3.8857

present analysis, a parametric analysis of the tests of fluid-jet-induced indentation can be easily carried out. Unfortunately, direct comparisons between the present theory and the experimental measurements reported in the literature [3, 13, 14, 17] are not possible, since the effects of applying a distributed pressure to the specimen surface using a fluid jet have not been measured. Future studies should investigate the behaviors of fluid jets and their effects on soft tissues.

5. Conclusions

To measure or image the mechanical properties of tissues has been attracting increasing research efforts during the recent decades. The stiffness of soft tissues may change under different pathologic situations, such as sclerosus cancer, edema, degeneration, fibrosis [31]. Normal tissues may also have different stiffness, which is important information for tissue characterization. The mechanical properties of tissues can have different values depending on whether they are measured in vivo or in vitro and in situ or as an excised specimen [32, 33]. During recent decades, ultrasound techniques together with compression, vibration, or indentation have been successfully used for the measurement or imaging of the mechanical properties of soft tissues, especially for the musculoskeletal tissues [34–39].

Our group previously developed a noncontact ultrasound indentation system for quantitative measurement of tissue stiffness [14]. The advantage of this technique is that it utilized water jet as a “soft indenter” instead of a rigid indenter to compress the soft tissue so as to avoid potential damage caused by a rigid indenter which may result in stress concentration at the edge of the indenter [10]. However, the loading during the water-jet indentation is not easy to measure directly; therefore the intrinsic Young’s modulus of soft tissue cannot be derived during the water-jet ultrasound indentation, which hinders the application of this technique.

In this study, a mathematical model for testing fluid-jet-induced indentation has been developed, and its semianalytical solution was determined. After detailed verification with FEM was carried out, the effects of altering the values of several parameters on the solution behavior were further analyzed. The following conclusions can be drawn from the results obtained:

- (1) The axial displacement of the elastic layer, u_z , is proportional to the pressure at the center point of the fluid jet, p_0 , and inversely proportional to Young’s modulus of the elastic layer, E , while it varies nonlinearly with other quantities.
- (2) When a/h is small, Poisson’s ratio has only a slight effect on the nondimensional indentation; however,

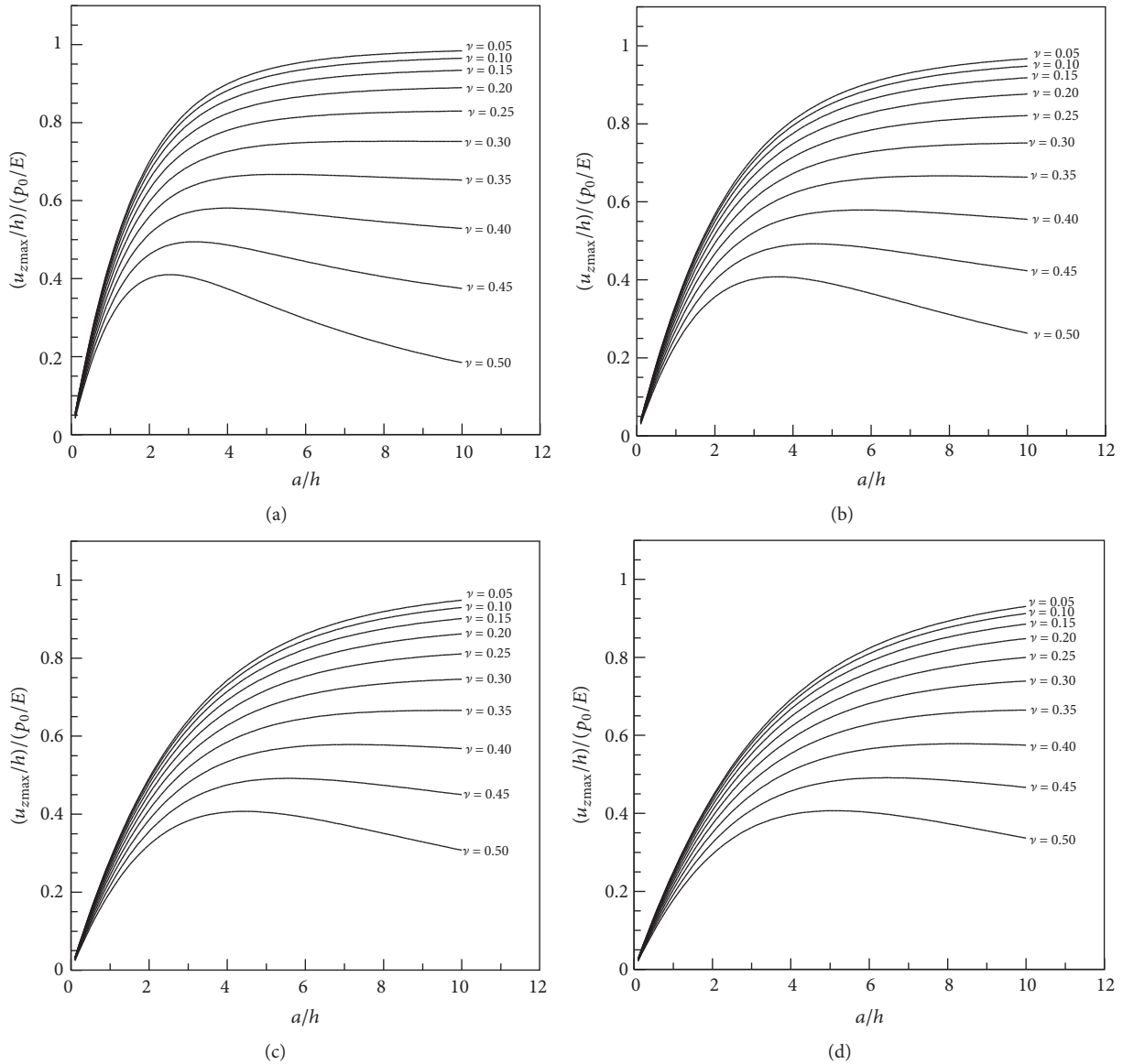


FIGURE 5: Nondimensional indentation versus aspect ratio for different Poisson's ratios with m values of (a) 10, (b) 20, (c) 30, and (d) 40.

when a/h is large, Poisson's ratio has a significant effect.

- (3) Parameters p_0 , a , m , h , and ν , can be determined before performing tests of fluid-jet-induced indentation. Combining with $u_{z\max}$ recorded during the indentation tests, Young's modulus of materials can be calculated directly by the analytical solution. It should be noted that the pressurized area a would need to be determined beforehand for various injection velocities and separation distance. In this study, it is assumed to be the same as the radius of the fluid-jet nozzle, ranging from 1.5 mm to 2 mm, based on our previous experimental experiences. We usually keep the distance between the fluid-jet nozzle and the tissue surface at around 5 mm, and the injection velocity changes from 0 to 15 m/s within 1 second

for an indentation test on soft tissue. However, the pressurized area a would be largely different from the nozzle radius when the nozzle is far from the tissue surface, especially when the injection velocity is low.

It would be of interest to comment on the tissue model used in our analysis. The soft tissue in this study was modeled as a thin layer of linear elastic, homogeneous, and isotropic material bonded to a rigid fixed substrate to simulate the boundary conditions of articular cartilage. However, the nonlinear and viscoelastic properties of soft tissues have not been addressed. Furthermore, instead of single-phase model to describe the soft tissue, the nonlinearity and viscoelasticity of soft tissues have been investigated using biphasic and triphasic models [40, 41]. In these models, the intrinsic fluid load support during indentation has been verified during the indentation by a rigid indenter. Whether the fluid-jet

indentation would have significant effect on the soft tissue when the soft tissue is modeled as multiphase material is a critical issue to be further analyzed.

Competing Interests

The authors declare that there is no conflict of interests regarding the publication of this paper.

Acknowledgments

Financial support from the NSF-China (Grants nos. 61471243, 61427806, and U1301252), China 863 (no. 2015AA015305), Guangdong Key Laboratory Project (no. 2012A061400024), and Shenzhen Projects (nos. JCYJ20150731160834611, SGLH20131010163759789, and JCYJ20140414170821323) for this project is gratefully acknowledged.

References

- [1] M.-H. Lu, Y. P. Zheng, Q.-H. Huang et al., "Noncontact evaluation of articular cartilage degeneration using a novel ultrasound water jet indentation system," *Annals of Biomedical Engineering*, vol. 37, no. 1, pp. 164–175, 2009.
- [2] X. Chen, B. K. Zimmerman, and X. L. Lu, "Determine the equilibrium mechanical properties of articular cartilage from the short-term indentation response," *Journal of Biomechanics*, vol. 48, no. 1, pp. 176–180, 2015.
- [3] G. Boyer, C. Paillet Mattei, J. Molimard, M. Pericoi, S. Laqueize, and H. Zahouani, "Non contact method for in vivo assessment of skin mechanical properties for assessing effect of ageing," *Medical Engineering and Physics*, vol. 34, no. 2, pp. 172–178, 2012.
- [4] A. F. T. Mak, M. Zhang, and E. W. C. Tam, "Biomechanics of pressure ulcer in body tissues interacting with external forces during locomotion," *Annual Review of Biomedical Engineering*, vol. 12, pp. 29–53, 2010.
- [5] Y. P. Zheng, Y. K. C. Choi, K. Wong, S. Chan, and A. F. T. Mak, "Biomechanical assessment of plantar foot tissue in diabetic patients using an ultrasound indentation system," *Ultrasound in Medicine and Biology*, vol. 26, no. 3, pp. 451–456, 2000.
- [6] V. C. Mow, M. C. Gibbs, W. M. Lai, W. B. Zhu, and K. A. Athanasiou, "Biphasic indentation of articular cartilage—II. A numerical algorithm and an experimental study," *Journal of Biomechanics*, vol. 22, no. 8-9, pp. 853–861, 1989.
- [7] J. P. A. Arokoski, M. M. Hyttinen, H. J. Helminen, and J. S. Jurvelin, "Biomechanical and structural characteristics of canine femoral and tibial cartilage," *Journal of Biomedical Materials Research*, vol. 48, no. 2, pp. 99–107, 1999.
- [8] K. A. Athanasiou, J. G. Fleischli, J. Bosma et al., "Effects of diabetes mellitus on the biomechanical properties of human ankle cartilage," *Clinical Orthopaedics and Related Research*, no. 368, pp. 182–189, 1999.
- [9] G. N. Kawchuk, O. R. Fauvel, and J. Dmowski, "Ultrasonic quantification of osseous displacements resulting from skin surface indentation loading of bovine para-spinal tissue," *Clinical Biomechanics*, vol. 15, no. 4, pp. 228–233, 2000.
- [10] M. Zhang, Y. P. Zheng, and A. F. T. Mak, "Estimating the effective Young's modulus of soft tissues from indentation tests—nonlinear finite element analysis of effects of friction and large deformation," *Medical Engineering and Physics*, vol. 19, no. 6, pp. 512–517, 1997.
- [11] J. Jurvelin, I. Kiviranta, A.-M. Säämänen, M. Tammi, and H. J. Helminen, "Indentation stiffness of young canine knee articular cartilage—influence of strenuous joint loading," *Journal of Biomechanics*, vol. 23, no. 12, pp. 1239–1246, 1990.
- [12] W. C. Hayes, L. M. Keer, G. Herrmann, and L. F. Mockros, "A mathematical analysis for indentation tests of articular cartilage," *Journal of Biomechanics*, vol. 5, no. 5, pp. 541–551, 1972.
- [13] G. N. Duda, R. U. Kleemann, U. Bluecher, and A. Weiler, "A new device to detect early cartilage degeneration," *American Journal of Sports Medicine*, vol. 32, no. 3, pp. 693–698, 2004.
- [14] M. H. Lu, Y. P. Zheng, and Q. H. Huang, "A novel noncontact ultrasound indentation system for measurement of tissue material properties using water jet compression," *Ultrasound in Medicine and Biology*, vol. 31, no. 6, pp. 817–826, 2005.
- [15] M.-H. Lu, Y.-P. Zheng, and Q.-H. Huang, "A novel method to obtain modulus image of soft tissues using ultrasound water jet indentation: A Phantom Study," *IEEE Transactions on Biomedical Engineering*, vol. 54, no. 1, article 16, pp. 114–121, 2007.
- [16] Y. P. Huang and Y. P. Zheng, "Development and phantom test of a minimized water-jet ultrasound indentation system for arthroscopic measurement of articular cartilage integrity," in *6th World Congress of Biomechanics (WCB 2010). August 1–6, 2010 Singapore*, pp. 903–906, Springer, Berlin, Germany, 2010.
- [17] Y.-P. Huang, Y.-P. Zheng, S.-Z. Wang, Z.-P. Chen, Q.-H. Huang, and Y.-H. He, "An optical coherence tomography (OCT)-based air jet indentation system for measuring the mechanical properties of soft tissues," *Measurement Science and Technology*, vol. 20, no. 1, Article ID 015805, 2009.
- [18] C. Y. L. Chao, Y.-P. Zheng, Y.-P. Huang, and G. L. Y. Cheing, "Biomechanical properties of the forefoot plantar soft tissue as measured by an optical coherence tomography-based air-jet indentation system and tissue ultrasound palpation system," *Clinical Biomechanics*, vol. 25, no. 6, pp. 594–600, 2010.
- [19] C. Y. L. Chao, G. Y. F. Ng, K.-K. Cheung, Y.-P. Zheng, L.-K. Wang, and G. L. Y. Cheing, "In vivo and ex vivo approaches to studying the biomechanical properties of healing wounds in rat skin," *Journal of Biomechanical Engineering*, vol. 135, no. 10, Article ID 101009, 2013.
- [20] M. Sakamoto, G. Li, T. Hara, and E. Y. S. Chao, "A new method for theoretical analysis of static indentation test," *Journal of Biomechanics*, vol. 29, no. 5, pp. 679–685, 1996.
- [21] K. D. Costa and F. C. P. Yin, "Analysis of indentation: implications for measuring mechanical properties with atomic force microscopy," *Journal of Biomechanical Engineering*, vol. 121, no. 5, pp. 462–471, 1999.
- [22] M. H. Lu and Y. P. Zheng, "Indentation test of soft tissues with curved substrates: a finite element study," *Medical and Biological Engineering and Computing*, vol. 42, no. 4, pp. 535–540, 2004.
- [23] P. C. Galbraith and J. T. Bryant, "Effects of grid dimensions on finite element models of an articular surface," *Journal of Biomechanics*, vol. 22, no. 4, pp. 385–393, 1989.
- [24] I. I. Argatov and F. J. Sabina, "Small-scale indentation of an elastic coated half-space: the effect of compliant substrate," *International Journal of Engineering Science*, vol. 104, pp. 87–96, 2016.
- [25] D. C. Lin, E. K. Dimitriadis, and F. Horkay, "Robust strategies for automated AFM force curve analysis—I. Non-adhesive indentation of soft, inhomogeneous materials," *Journal of Biomechanical Engineering*, vol. 129, no. 3, pp. 430–440, 2007.

- [26] Z. Xu and H. Hangan, "Scale, boundary and inlet condition effects on impinging jets," *Journal of Wind Engineering and Industrial Aerodynamics*, vol. 96, no. 12, pp. 2383–2402, 2008.
- [27] Y. Guo and D. H. Wood, "Measurements in the vicinity of a stagnation point," *Experimental Thermal and Fluid Science*, vol. 25, no. 8, pp. 605–614, 2002.
- [28] K. L. Johnson and K. L. Johnson, *Contact Mechanics*, Cambridge University Press, Cambridge, UK, 2001.
- [29] L. Debnath and D. Bhatta, *Integral Transforms and Their Applications*, Chapman and Hall/CRC Press, Boca Raton, Fla, USA, 2nd edition, 2007.
- [30] S. K. Lucas, "Evaluating infinite integrals involving products of Bessel functions of arbitrary order," *Journal of Computational and Applied Mathematics*, vol. 64, no. 3, pp. 269–282, 1995.
- [31] J. F. Greenleaf, M. Fatemi, and M. Insana, "Selected methods for imaging elastic properties of biological tissues," *Annual Review of Biomedical Engineering*, vol. 5, no. 1, pp. 57–78, 2003.
- [32] Y. C. Fung and R. Skalak, "Biomechanics: mechanical properties of living tissues," *Journal of Biomechanical Engineering*, vol. 103, no. 4, pp. 231–298, 1981.
- [33] V. C. Mow and W. C. Hayes, *Basic Orthopaedic Biomechanics*, Lippincott-Raven, New York, NY, USA, 2nd edition, 1997.
- [34] M. Fatemi and J. F. Greenleaf, "Ultrasound-stimulated vibro-acoustic spectrography," *Science*, vol. 280, no. 5360, pp. 82–85, 1998.
- [35] T. Defieux, J.-L. Gennisson, M. Tanter, and M. Fink, "Assessment of the mechanical properties of the musculoskeletal system using 2-D and 3-D very high frame rate ultrasound," *IEEE Transactions on Ultrasonics, Ferroelectrics, and Frequency Control*, vol. 55, no. 10, pp. 2177–2190, 2008.
- [36] Y.-P. Zheng and A. F. T. Mak, "An ultrasound indentation system for biomechanical properties assessment of soft tissues in-vivo," *IEEE Transactions on Biomedical Engineering*, vol. 43, no. 9, pp. 912–918, 1996.
- [37] J. Ophir, I. Céspedes, H. Ponnekanti, Y. Yazdi, and X. Li, "Elastography: a quantitative method for imaging the elasticity of biological tissues," *Ultrasonic Imaging*, vol. 13, no. 2, pp. 111–134, 1991.
- [38] J. L. Gennisson, C. Cornu, S. Catheline, M. Fink, and P. Portero, "Human muscle hardness assessment during incremental isometric contraction using transient elastography," *Journal of Biomechanics*, vol. 38, no. 7, pp. 1543–1550, 2005.
- [39] R. Mao, P. Zhang, X. Li, X. Liu, and M. Lu, "Pivot selection for metric-space indexing," *International Journal of Machine Learning and Cybernetics*, vol. 7, no. 2, pp. 311–323, 2016.
- [40] A. F. Mak, W. M. Lai, and V. C. Mow, "Biphasic indentation of articular cartilage-I. Theoretical analysis," *Journal of Biomechanics*, vol. 20, no. 7, pp. 703–714, 1987.
- [41] Q. Wang, Y. P. Zheng, H. J. Niu, and A. F. T. Mak, "Extraction of mechanical properties of articular cartilage from osmotic swelling behavior monitored using high frequency ultrasound," *Journal of Biomechanical Engineering*, vol. 129, no. 3, pp. 413–422, 2007.

Clinical Study

Ultrasound-Guided versus Fluoroscopy-Guided Deep Cervical Plexus Block for the Treatment of Cervicogenic Headache

Qing Wan,¹ Haiyun Yang,² Xiao Li,¹ Caina Lin,¹ Songjian Ke,¹ Shaoling Wu,¹ and Chao Ma¹

¹Pain Treatment Centre of Department of Rehabilitation Medicine, Sun Yat-sen Memorial Hospital, Sun Yat-sen University, Guangzhou, Guangdong Province, China

²Department of Medical Ultrasonics, Sun Yat-sen Memorial Hospital, Sun Yat-sen University, Guangzhou, Guangdong Province, China

Correspondence should be addressed to Shaoling Wu; wushaolinggz@126.com and Chao Ma; ma_chao99@126.com

Received 23 August 2016; Accepted 3 November 2016; Published 23 February 2017

Academic Editor: Qing Wang

Copyright © 2017 Qing Wan et al. This is an open access article distributed under the Creative Commons Attribution License, which permits unrestricted use, distribution, and reproduction in any medium, provided the original work is properly cited.

Objective. The aim of this study was to compare the efficacy of ultrasound-guided deep cervical plexus block with fluoroscopy-guided deep cervical plexus block for patients with cervicogenic headache (CeH). **Methods.** A total of 56 patients with CeH were recruited and randomly assigned to either the ultrasound-guided (US) or the fluoroscopy-guided (FL) injection group. A mixture of 2–4 mL 1% lidocaine and 7 mg betamethasone was injected along C₂ and/or C₃ transverse process. The measurement of pain was evaluated by patients' ratings of a 10-point numerical pain scale (NPS) before and 2 wks, 12 wks, and 24 wks after treatments. **Results.** The blocking procedures were well tolerated. The pain intensity, as measured by NPS, significantly decreased at 2 wks after injection treatment in both US and FL groups, respectively, compared with that of baseline ($P < 0.05$). The blocking procedures had continued, and comparable pain relieving effects appeared at 12 wks and 24 wks after treatment in both US and FL groups. There were no significant differences observed in the NPS before and 2 wks, 12 wks, and 24 wks after treatment between US and FL groups. **Conclusions.** The US-guided approach showed similar satisfactory effect as the FL-guided block. Ultrasonography can be an alternative method for its convenience and efficacy in deep cervical plexus block for CeH patients without radiation exposure.

1. Introduction

Cervicogenic headache (CeH) is a common diagnosis for patients with unilateral referred pain to the head from the upper cervical spine [1]. The prevalence of CeH has been estimated at up to 20% among patients with chronic headaches [2]. Treatment strategies for CeH are wide and varied, such as medication, physical therapy, acupuncture, manipulation, transcutaneous electrical nerve stimulation, pulsed radiofrequency, injections, and surgery [3, 4]. The majority of patients preferred to choose the noninvasive strategies, including physical and manual therapies, activity modification, and various medication trials before considering anesthetic blocks [1, 2, 5–7]. There is an ongoing need for evidences of long-term effect and high-quality randomized controlled trial investigations for these strategies.

The C₂-C₃ zygapophysial and atlantoaxial joints are believed to be primary causes for CeH and the C₂ nerve

may be more susceptible to injury by aseptic inflammation or compression than the other structures [3]. Thus, several local anesthetic techniques have been used in treating CeH, including occipital nerve blocks, cervical facet joint blocks, and cervical epidural injections [8–11]. Real time fluoroscopy imaging guidance is frequently required to ensure correct needle placement [12–14]. However, repeated exposure to radiation is a great threat to the health of physicians. Ultrasound-guided injections have been described recently in the literatures, and the absence of radiation exposure, equipment affordability, and bedside setting are advantages of ultrasonography compared with traditional radiological imaging [15–18].

The objective of this study was to evaluate the efficacy of ultrasound-guided deep cervical plexus block for patients with CeH in comparison with fluoroscopy-guided block through a prospective, randomized, single-blind clinical trial.



FIGURE 1: (a) The position of the patient. (b) Transverse ultrasound view of C_2 spinal process (SP), spinal canal (SC), and vertebral lamina (VL).

2. Materials and Methods

There were 84 eligible patients with CeH and 60 patients participated in this randomized, single-blind study. They were enrolled and then randomly assigned into two groups according to a random number table and underwent ultrasound-guided (US, $n = 30$) or fluoroscopy-guided (FL, $n = 30$) C_2 and/or C_3 transverse process injection, respectively, in the pain center of Sun Yat-sen Memorial Hospital from July 2011 to January 2014. The study was approved by our university and all patients gave informed consent before this study.

The patients had experienced screening that included medical history and physical examination followed by X-ray, CT scan, or MRI of the cervical spine. All patients were diagnosed with CeH according to the diagnostic criteria of Sjaastad et al. [19]: (1) unilateral or bilateral pain starting in the neck and radiating to the frontotemporal region, (2) pain aggravated by neck movement, (3) restricted cervical range of motion, (4) joint tenderness in at least one of the joints of the upper cervical spine (C_2 - C_3), and (5) headache frequency of at least 1 per week over a period greater than 3 months. In this study, we chose the patients with unilateral pain. Our exclusion criteria included (1) pathologic fracture, cancer, and other diseases of the cervical vertebra, (2) headache caused by nervous system diseases, or other factors.

2.1. US-Guided Blockade Procedures. The patients were placed in sitting position with the neck bending forward and the head was supported (Figure 1(a)). The selection of the site for injection was determined by first having the patient identify the more painful side [8, 11]. An Esaote MyLab60 (Esaote, Italy) ultrasound machine equipped with a multifrequency linear probe (4–13 MHz) was used. The skin was prepared with betadine and draped in the usual sterile fashion at the region of injection. The ultrasound probe was also sterilized with betadine. On the transverse section, the spinal process of C_2 or C_3 was identified on the ultrasound image (Figure 1(b)). Then, the probe was moved laterally from midline and the posterior elements, including layers

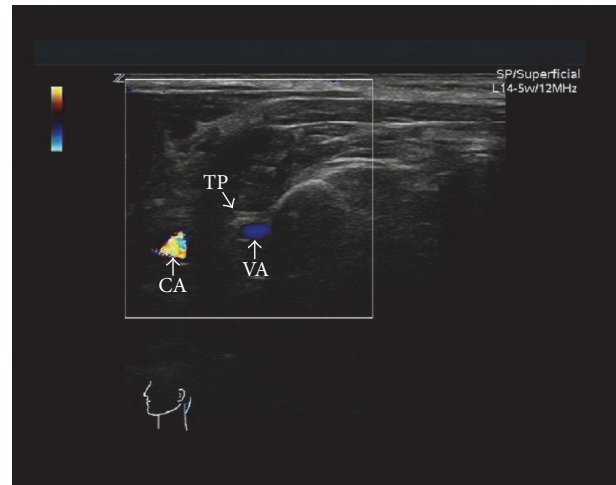


FIGURE 2: Transverse ultrasound view of C_2 transverse process (TP), vertebral artery (VA), and carotid artery (CA) (left side).

of muscle, lamina, interlaminar space, facet joint, C_2 or C_3 transverse process, and vertebral artery that were identified on the transverse sonograms at the same level (Figure 2). A 22-gauge 3.5-inch spinal needle was inserted to C_2 or C_3 transverse process (Figures 3(a) and 3(b)). When the needle reached the bone, after negative aspiration, total 2–4 mL of 1% lidocaine with 7 mg of betamethasone was injected in slow speed while maintaining communication and questioning of the patient to ensure that the needle was not intravascular or intrathecal. If the headache was unilateral in nature, the block was performed only on the affected side (C_2 and/or C_3). If necessary, the patients would receive the second injection in one-week interval after the first injection. All procedures were performed in the same fashion by C. M and HY. Y.

2.2. FL-Guided Blockade Procedures. The patients were placed in supine and, using external landmarks, the C_2 or C_3 spinal process was identified on the lateral view (Figure 4).



FIGURE 3: (a) Ultrasound-guided C₂ transverse process block (left side). (b) The needle is targeted just lateral to the transverse process (TP) (left side).



FIGURE 4: The C₂ or C₃ spinal process is identified on the lateral view under fluoroscopy guidance with external landmarks.



FIGURE 5: The position of needle is confirmed in the lateral projection.

After routine skin preparation and sterilization, a 22-gauge 3.5-inch spinal needle was inserted into the lateral recess of C₂-C₃ and its position was confirmed in the AP and lateral projections (Figure 5). All procedures were performed by the same physician Q. W. In one week at the return visit, the physician applied the second block treatment if necessary, depending on the symptom of patients.

2.3. Outcome Assessment. The measurement of pain was evaluated by patients' ratings of a 10-point numerical pain scale (NPS, from 0, no pain, to 10, the worst pain). Pain was assessed before the injection and the return visit was conducted in 2 weeks after treatment to exclude any major complications. All the patients were followed up at 12-week

and 24-week intervals with telephone consultation and visits to the pain clinic.

2.4. Data Analysis. The pain intensities were measured on a 0–10 NPS. The characteristics of the US and FL groups such as sex, age, and duration of pain were compared by the χ^2 test and Mann–Whitney *U* method. At each time point of injection, the NPS was compared by repeated-measures analysis of variance, and the Bonferroni correction was conducted for post hoc comparison. Statistical analysis was carried out using SPSS 16.0 (SPSS Inc., Chicago, IL, USA). Values are expressed as means \pm SD and a *P* value of less than 0.05 was considered to be statistically significant.

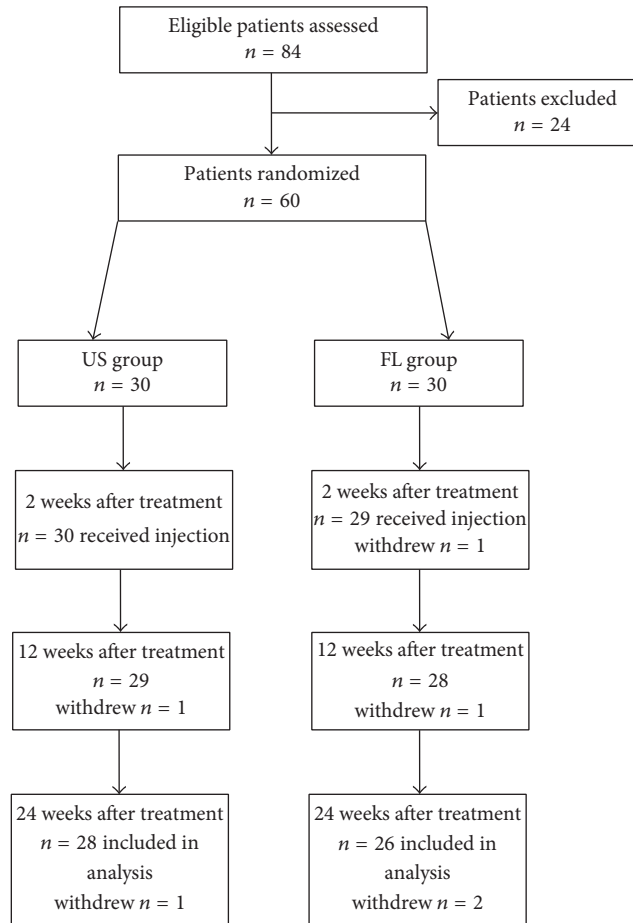


FIGURE 6: Schematic presentation of participant flow.

3. Results

3.1. Patient Characteristics. A total of 84 consecutive patients were assessed for eligibility during this study, with 60 of them being enrolled and 54 patients completing the study. A flow diagram with patient selection and follow-up is presented in Figure 6. In US group, two patients lost track in the follow-up and the other patients ($n = 28$, 7 males and 21 females) completed the injection and 12 patients received the second injection treatment. In FL group, one patient chose other noninvasive interventions and three patients were lost in the follow-up because of refusal to radiation exposure; a total of 26 patients (5 males and 21 females) completed this study and one-half of them received the second block. The patients had comparable pain duration for 10.06 ± 3.47 months as that of US group. The majority of location of the block was the C2 transverse process (71.43% in US group and 80.77% in FL group). The demographic data of patients are present in Table 1.

3.2. Treatment Effects between the Approaches. The blocking procedures were tolerable for all the patients during the treatment. However, 3 patients in US group felt dizzy immediately after injection; the symptom disappeared when they lay down

TABLE 1: General characteristics of the patients.

	US ($n = 28$)	FL ($n = 26$)	<i>P</i>
Age	49.2 ± 10.3	47.6 ± 9.7	0.419
Gender			0.747
Male	7	5	
Female	21	21	
Duration (mos)	9.35 ± 3.68	10.06 ± 3.47	0.725
Pain side			0.781
Left	10	11	
Right	18	15	
Number of injections			0.785
1	16	13	
2	12	13	
Injection position			0.530
C ₂	20	21	
C ₃	8	5	

on the bed for several minutes. A total of 4 patients (2 in US group and 2 in FL group) complained of neck and shoulder uncomfortableness. None of the patients in this study had any treatment-related severe complications. There were 25

TABLE 2: Comparison of the NRS before and after treatment.

	US	FL
Baseline	7.61 ± 1.12	7.50 ± 1.06
2 wks	3.45 ± 0.54 ^a	3.40 ± 0.58 ^a
12 wks	2.41 ± 0.62 ^{a,b}	2.39 ± 0.68 ^{a,b}
24 wks	2.36 ± 0.56 ^{a,b}	2.43 ± 0.59 ^{a,b}

^aSignificantly different from the baseline at $P < 0.05$.

^bSignificantly different from 2 wks after treatment at $P < 0.05$.

patients (12 in US group and 13 in FL group) who received the second injection according to their symptoms at the return visit.

There were no significant differences observed in the NPS before and 2 wks, 12 wks, and 24 wks after the injections between US and FL groups (Table 2). The pain intensity, as measured by NPS, significantly decreased at 2 wks after injection treatment in both US and FL groups, respectively, compared with that of baseline ($P < 0.05$). The blocking procedures had continued, and comparable pain relieving effects appeared at 12 wks and 24 wks after treatment in both US and FL groups (Table 2), the NPS score significantly decreased 12 wks and 24 wks after treatment compared with that at baseline ($P < 0.05$) and at 2 wks after injection ($P < 0.05$). It indicated that steroid injection guided by either ultrasound or fluoroscopy had sustained pain-relieving effect for CeH patients.

4. Discussion

Cervicogenic headache is a common clinical syndrome and few conservative managements lead to satisfactory clinical efficacy. There are multiple causes of CeH, including the C₂-C₃ and C₃-C₄ z-joints, A-A joint, C₂-C₃ intervertebral disk, A-O joint, and the greater or lesser occipital nerve [1]. Anatomically, the main dorsal ramus of C₂ becomes the greater occipital nerve after passing the posterior aspect of the C_{1/2} facet joint. The C₂ and C₃ ventral rami become the lesser occipital nerve, and the C₃ dorsal ramus becomes the third occipital nerve [1, 2, 8, 11]. The pain of CeH most commonly originates from the C_{2/3} facet joints [20]. In this study, US or FL-guided C₂ and/or C₃ transverse process steroid injections were applied to 54 patients with CeH and comparable pain relief effect was observed. It has been frequently demonstrated that blockade of the greater occipital nerve, the lesser occipital nerve, the stellate ganglion, and other various blocking treatments are effective strategies for CeH. Zhou et al. reported that, of the 28 CeH patients, 26 of them had abnormalities in the cervical spine below the C_{1/2} and C_{2/3} levels and C_{1/2}, C_{2/3} facet joint injections and C₂, C₃ spinal rami blocks were effective and well tolerated by the patients [8]. Anthony reported that injection of methylprednisolone into the greater and lesser occipital nerve region could relieve headache completely in 169 out of 180 patients for a duration of 10–77 days [21]. Our results also showed sustained pain relief effect of steroid injections for as long as 6 months; however, these results were inconsistent

with those of Goldberg et al. [11]. The authors applied FL-guided deep cervical plexus block to 39 patients with CeH; the mean pain scores were significantly lower than baseline at 3 months but by 6 months the pain had returned to pretreatment levels. One possible explanation could be the difference in inclusion criteria; the study of Goldberg et al. recruited patients suffering from atypical headaches for longer duration of 4–5 years, while it were typical CeH patients with the symptoms only for 5.7–13.5 months in our study. Another factor contributing to the varied results could be frequency of injection treatment for patients with longer and shorter history. Our patients with a history for 5.7–13.5 months received 1–2 blockade treatments, while the great majority of patients (87%) with a history for more than 4 years in their study only had a median treatment frequency for 2 injections. For patients with longer history of CeH, more treatment sessions might be considered for longer pain relief effect.

The C₂ and/or C₃ transverse process block technique is a modification of the deep cervical plexus block that has been utilized to provide anesthesia to the head and neck region [15]. This technique is relatively safe since the cervical foramen is not entered and vertebral artery (Figure 2) can easily be detected by ultrasonography. Although this block occurred more peripherally compared to z-joint and transforaminal block, our results demonstrated that the blocking strategy has efficient pain relief effect. The analgetic solution spreads within the cervical region to adjacent levels since the paravertebral space communicates freely [22], which allows local injection at one level that can achieve the same beneficial effect.

The FL-guided injection procedure is most commonly used in treating pain-associated diseases to ensure correct needle placement. However, radiation exposure was unavoidable, and there is a risk of vertebral artery injury. The US-guided method has several advantages in comparison with the FL-guided method. Gofeld et al. explored US-guided lumbar transforaminal and z-joint injection techniques for patients with spinal pain, and their studies demonstrated that US-guided injections are accurate and feasible [23, 24]. It has also been reported that US-guided selective nerve root block and caudal injection for low back pain are feasible, easy-to-perform, and effective procedures [15, 18]. Ultrasonography may be a viable alternative to fluoroscopy or computed tomography as a guidance method, because it overcomes the disadvantages of radiation exposure and poor vascular display. Furthermore, the device of ultrasonography is portable and convenient to be used at bedside for patients with severe pain.

The main limitations of the study are as follows: first, the sample size was small; thus, clinical findings still need to be confirmed with larger clinical trials. Second, this study was not a double-blind control study. It was difficult to conduct a double-blind control study with nontraditional modalities such as ultrasound and fluoroscopy. Additional investigations may be needed to improve the limitations.

In summary, deep cervical plexus block in C₂ or C₃ transverse process for treating patients with cervicogenic headache provided significant and prolonged pain relief (6

months' follow-up). The US-guided approach showed similar satisfactory effect as the FL-guided block. Ultrasonography can be an alternative method for its convenience and efficacy in deep cervical plexus block without radiation exposure.

Competing Interests

All named authors declare that they have no conflict of interests.

Authors' Contributions

Qing Wan and Haiyun Yang contributed equally to this work.

References

- [1] M. J. Mehnert and M. K. Freedman, "Update on the role of Z-joint injection and radiofrequency neurotomy for cervicogenic headache," *PM & R*, vol. 5, no. 3, pp. 221–227, 2013.
- [2] N. H. L. Chua, H. A. van Suijlekom, K. C. Vissers, L. Arendt-Nielsen, and O. H. Wilder-Smith, "Differences in sensory processing between chronic cervical zygapophysial joint pain patients with and without cervicogenic headache," *Cephalalgia*, vol. 31, no. 8, pp. 953–963, 2011.
- [3] J. Zhang, D.-S. Shi, and R. Wang, "Pulsed radiofrequency of the second cervical ganglion (C2) for the treatment of cervicogenic headache," *Journal of Headache and Pain*, vol. 12, no. 5, pp. 569–571, 2011.
- [4] M. B. Vincent, "Headache and neck," *Current Pain and Headache Reports*, vol. 15, no. 4, pp. 324–331, 2011.
- [5] M. K. McDonnell, S. A. Sahrman, and L. Van Dillen, "A specific exercise program and modification of postural alignment for treatment of cervicogenic headache: a case report," *Journal of Orthopaedic and Sports Physical Therapy*, vol. 35, no. 1, pp. 3–15, 2005.
- [6] S. B. Silverman, "Cervicogenic headache: interventional, anesthetic, and ablative treatment," *Current Pain and Headache Reports*, vol. 6, no. 4, pp. 308–314, 2002.
- [7] G. Jull, P. Trott, H. Potter et al., "A randomized controlled trial of exercise and manipulative therapy for cervicogenic headache," *Spine*, vol. 27, no. 17, pp. 1835–1842, 2002.
- [8] L. Zhou, Z. Hud-Shakoor, C. Hennessey, and A. Ashkenazi, "Upper cervical facet joint and spinal rami blocks for the treatment of cervicogenic headache," *Headache*, vol. 50, no. 4, pp. 657–663, 2010.
- [9] Z. M. Naja, M. El-Rajab, M. A. Al-Tannir, F. M. Ziade, and O. M. Tawfik, "Repetitive occipital nerve blockade for cervicogenic headache: expanded case report of 47 adults," *Pain Practice*, vol. 6, no. 4, pp. 278–284, 2006.
- [10] Z. M. Naja, M. El-Rajab, M. A. Al-Tannir, F. M. Ziade, and O. M. Tawfik, "Occipital nerve blockade for cervicogenic headache: a double-blind randomized controlled clinical trial," *Pain Practice*, vol. 6, no. 2, pp. 89–95, 2006.
- [11] M. E. Goldberg, R. J. Schwartzman, R. Domsy, M. Sabia, and M. C. Torjman, "Deep cervical plexus block for the treatment of cervicogenic headache," *Pain Physician*, vol. 11, no. 6, pp. 849–854, 2008.
- [12] International Spine Intervention Society, "Percutaneous radiofrequency cervical medial neurotomy," in *Practice Guidelines for Spinal Diagnostic and Treatment Procedures*, N. Bogduk, Ed., pp. 249–284, International Spine Intervention Society, San Francisco, Calif, USA, 2004.
- [13] W. Halim, N. H. L. Chua, and K. C. Vissers, "Long-term pain relief in patients with cervicogenic headaches after pulsed radiofrequency application into the lateral atlantoaxial (C1-2) joint using an anterolateral approach," *Pain Practice*, vol. 10, no. 4, pp. 267–271, 2010.
- [14] S. R. Haspesslagh, H. A. Van Suijlekom, I. E. Lamé et al., "Randomised controlled trial of cervical radiofrequency lesions as a treatment for cervicogenic headache," *BMC Anesthesiology*, vol. 6, no. 1, article 1, 11 pages, 2006.
- [15] D. Kim, D. Choi, C. Kim, J. Kim, and Y. Choi, "Transverse process and needles of medial branch block to facet joint as landmarks for ultrasound-guided selective nerve root block," *Clinics in Orthopedic Surgery*, vol. 5, no. 1, pp. 44–48, 2013.
- [16] Y. Park, J.-H. Lee, K. D. Park, J. K. Ahn, J. Park, and H. Jee, "Ultrasound-guided vs. fluoroscopy-guided caudal epidural steroid injection for the treatment of unilateral lower lumbar radicular pain: a prospective, randomized, single-blind clinical study," *American Journal of Physical Medicine and Rehabilitation*, vol. 92, no. 7, pp. 575–586, 2013.
- [17] A. Loizides, S. Peer, M. Plaikner et al., "Ultrasound-guided injections in the lumbar spine," *Medical Ultrasonography*, vol. 13, pp. 54–58, 2011.
- [18] A. Blanchais, B. Le Goff, P. Guillot, J.-M. Berthelot, J. Glemarec, and Y. Maugars, "Feasibility and safety of ultrasound-guided caudal epidural glucocorticoid injections," *Joint Bone Spine*, vol. 77, no. 5, pp. 440–444, 2010.
- [19] O. Sjaastad, T. A. Fredriksen, and V. Pfaffenrath, "Cervicogenic headache: diagnostic criteria," *Headache*, vol. 38, no. 6, pp. 442–445, 1998.
- [20] G. Cooper, B. Bailey, and N. Bogduk, "Cervical zygapophysial joint pain maps," *Pain Medicine*, vol. 8, no. 4, pp. 344–353, 2007.
- [21] M. Anthony, "Cervicogenic headache: prevalence and response to local steroid therapy," *Clinical and Experimental Rheumatology*, vol. 18, no. 2, pp. S59–S64, 2000.
- [22] M. J. Cousins and P. O. Bridenbaugh, *Neural Blockade in Clinical Anesthesia and Management of Pain*, Lippincott-Raven, Philadelphia, Pa, USA, 3rd edition, 1998.
- [23] M. Gofeld, S. J. Bristow, and S. Chiu, "Ultrasound-guided injection of lumbar zygapophysial joints: an anatomic study with fluoroscopy validation," *Regional Anesthesia and Pain Medicine*, vol. 37, no. 2, pp. 228–231, 2012.
- [24] M. Gofeld, S. J. Bristow, S. C. Chiu, C. K. McQueen, and L. Bollag, "Ultrasound-guided lumbar transforaminal injections: feasibility and validation study," *Spine*, vol. 37, no. 9, pp. 808–812, 2012.

Research Article

Semiquantitative Evaluation of Extrasynovial Soft Tissue Inflammation in the Shoulders of Patients with Polymyalgia Rheumatica and Elderly-Onset Rheumatoid Arthritis by Power Doppler Ultrasound

Takeshi Suzuki,^{1,2} Ryochi Yoshida,¹ Akiko Okamoto,² and Yu Seri¹

¹Division of Allergy and Rheumatology, Japanese Red Cross Medical Center, Tokyo, Japan

²Division of Rheumatology, Mitsui Memorial Hospital, Tokyo, Japan

Correspondence should be addressed to Takeshi Suzuki; takecsuzu@gmail.com

Received 22 August 2016; Revised 29 December 2016; Accepted 19 January 2017; Published 15 February 2017

Academic Editor: John T. W. Yeow

Copyright © 2017 Takeshi Suzuki et al. This is an open access article distributed under the Creative Commons Attribution License, which permits unrestricted use, distribution, and reproduction in any medium, provided the original work is properly cited.

Objectives. To develop a scoring system for evaluating the extrasynovial soft tissue inflammation of the shoulders in patients with polymyalgia rheumatica (PMR) and elderly-onset rheumatoid arthritis with PMR-like onset (pm-EORA) using ultrasound. **Methods.** We analyzed stored power Doppler (PD) images obtained by the pretreatment examination of 15 PMR patients and 15 pm-EORA patients. A semiquantitative scoring system for evaluating the severity of PD signals adjacent to the anterior aspect of the subscapularis tendon was designed. **Results.** A four-point scale scoring for the hyperemia on the subscapularis tendon was proposed as follows in brief: 0 = absent or minimal flow, 1 = single vessel dots or short linear-shape signals, 2 = long linear-shape signals or short zone-shape signals, or 3 = long zone-shape signals. This scoring system showed good intra- and interobserver reliability and good correlation to quantitative pixel-counting evaluation. By using it, we demonstrated that inflammation in PMR is dominantly localized in extrasynovial soft tissue as compared with pm-EORA. **Conclusions.** We proposed a reliable semiquantitative scoring system using ultrasound for the evaluation of extrasynovial soft tissue inflammation of the shoulders in patients with both PMR and pm-EORA. This system is simple to use and can be utilized in future investigations.

1. Introduction

Polymyalgia rheumatica (PMR), which presents with strong pain and stiffness around the shoulder and hip girdles, is a relatively common disease among adults aged ≥ 50 years [1]. Patients with PMR exhibit a very high inflammatory response and show dramatic improvement following the administration of corticosteroids [2]. Because there is no disease-specific marker, PMR is diagnosed based on its clinical manifestation and course [3]. Elderly-onset RA (EORA) patients often present polymyalgic symptoms that mimic PMR at the onset [4]. In cases in which serological markers are negative and arthritis in the peripheral small joints is lacking, discriminating EORA from PMR is sometimes very difficult, although treatment with antirheumatic drugs is necessary for the effective treatment of EORA.

In 2012, provisional classification criteria for PMR were published [5]. Unfortunately, these criteria were evaluated as useful in general but weak in discriminating between PMR and RA [5]. Two validation studies failed to conclude whether or not the optional use of musculoskeletal ultrasound (US) items in the new criteria improves the differential diagnosis between PMR and EORA [5, 6]. Both studies reported that the optional use of US items did not, however, improve the ability of the criteria to discriminate PMR from EORA with PMR-like onset (pm-EORA). In essence, binary assessment for the presence or absence of shoulder synovitis (tenosynovitis, bursitis, and joint synovitis) and hip synovitis (bursitis and joint synovitis) by US does not provide helpful information for distinguishing between PMR and pm-EORA.

What is the hallmark of the pathology detected by imaging modalities in shoulders with PMR? Studies using

fat-saturated, contrast-enhanced magnetic resonance imaging (MRI) revealed soft tissue inflammation around the shoulder in addition to inflammation in the synovial tissues around the shoulder, such as tenosynovitis of the long head of biceps (LHB), subdeltoid/subacromial bursitis (SDB/SAB), and glenohumeral joint synovitis (GHJ), although no such inflammation in the extrasynovial soft tissues has been mentioned in previous studies employing US [7, 8].

Through clinical experience of the US examination of the shoulder lesions in untreated patients with PMR and pm-EORA, we noted that strong power Doppler (PD) signals indicating hyperemia are detected adjacent to the anterior aspect of the subscapularis tendon (SScT). We assume that this hyperemia on the SScT represents the extrasynovial soft tissue inflammation related to the polymyalgic feature. To clarify the clinical significance of this hyperemia, it is necessary to establish the method for evaluating it. In this study, we proposed and validated a semiquantitative scoring system for evaluating PD signals on the SScT in the shoulders of patients with PMR and pm-EORA. We also used a semiquantitative US scoring system for the three different components of synovitis in the shoulder, namely, tenosynovitis, bursitis, and joint synovitis, for the comprehensive assessment of the shoulder synovitis, in order to compare the severity of inflammation in extrasynovial soft tissue with that in synovial tissues.

2. Methods

2.1. Patients. This study was conducted in accordance with the principles of the Declaration of Helsinki. The medical records of patients who visited the hospital after January 2010 for examination of PMR-like symptoms were retrospectively reviewed to identify patients who fulfilled the following inclusion criteria: (i) musculoskeletal US was performed to evaluate persistent inflammatory pain and stiffness in the neck and shoulder girdle, regardless of pelvic girdle involvement; (ii) musculoskeletal US examination was performed before starting treatment with corticosteroids or antirheumatic drugs; (iii) follow-up clinical information one year after the US examination was available. By reviewing the clinical data during the one-year follow-up, including data on the resistance to corticosteroids alone, the need for and effectiveness of antirheumatic drugs, and the development of proliferative and/or bone-erosive synovitis in the peripheral small joints, the final diagnoses were confirmed by agreement among the attending physician and two rheumatologists (A. O. and Y. S.) certified by the Japan College of Rheumatology. Among patients who were examined between January 2010 and August 2013, 15 consecutive patients who were eventually diagnosed with PMR and 15 consecutive patients who were eventually diagnosed with pm-EORA were enrolled in this study for comparison. The 2012 EULAR/ACR provisional classification criteria for PMR and the 2010 ACR/EULAR classification criteria for RA were also tested to the patients [5, 9].

2.2. Clinical and Serological Data. At the time of US examination, clinical and serological data, including sex, age, disease

duration, rheumatoid factor (RF) titer, anti-citrullinated peptide antibody (ACPA), C-reactive protein (CRP), and erythrocyte sedimentation rate (ESR), were available for all patients. Serum matrix metalloproteinase 3 (MMP-3) was available for 29 patients. CRP, RF, and MMP-3 were measured simultaneously within 10 days prior to US examination. RF was quantified by immunoturbidimetric assay (normal <15 U/ml; N-assay TIA RF; Nittobo Medical, Tokyo, Japan); ACPA was quantified by anti-CCP2 enzyme-linked immunosorbent assay (normal <4.5 U/ml; MESACUP CCP TEST, MBL; Nagoya, Japan); and MMP-3 was quantified by latex turbidimetric immunoassay (normal range, male: 36.9–121 ng/mL, female: 17.3–59.7 ng/mL; Panaclear MMP-3 Late; Daiichi Fine Chemicals, Takaoka, Japan).

2.3. US Image Acquisition for the Evaluation of Hyperemia on the SScT. US examinations were performed using a GE LOGIQ 7 device (GE Medical Systems; Milwaukee, WI) by an experienced examiner (T. S.). A 10 to 14 MHz linear transducer was used at 12.0 MHz for gray scale and 6.7 MHz for color mode. The hyperemia adjacent to the anterior aspect of the SScT was scanned in the horizontal long axis view with a neutral position (Figure 1(a)), because external rotation may lead to a decrease in blood flow possibly due to tension in the soft tissues. PD settings were identical to the preset parameters (pulse repetition frequency 1.0 kHz, Doppler gain 25) for every patient. Images with the most pronounced PD activity were identified from the cine-loop and stored.

2.4. Development and Validation of a Semiquantitative Scoring System. Stored images were used for the semiquantitative and quantitative evaluation. With a focus on the anterior aspect of the SScT, the area (including the anterior soft tissues and the posterior tendon tissues and excluding the intertubercular groove) was assessed for the severity of hyperemia (Figure 1(b), elliptic region). Based on a subjective evaluation, we developed a semiquantitative four-point scale scoring system.

In order to evaluate intra- and interobserver reliability, 40 selected images were randomized and rescored by the sonographer (T. S.) after a one-year interval and by another experienced sonographer/rheumatologist (Y. S.). Unweighted kappa statistics were calculated.

For validating the semiquantitative scoring, the same set of 40 images was used for quantitative evaluation. The images were opened in Adobe Photoshop elements 13, orange color pixels corresponding to the PD signals in the appropriate area were selected using the Magic Wand tool, and the pixel number was counted using the histogram panel. The area of signals was calculated in square millimeters with reference to the scale in the image. The relationship between quantitative measurement and semiquantitative scoring for hyperemia was plotted.

2.5. US Image Acquisition for the Evaluation of Synovial Pathologies. Shoulders were scanned according to a standardized scanning method [10]. With the shoulder in a neutral position, the glenohumeral joint (GHJ) was evaluated

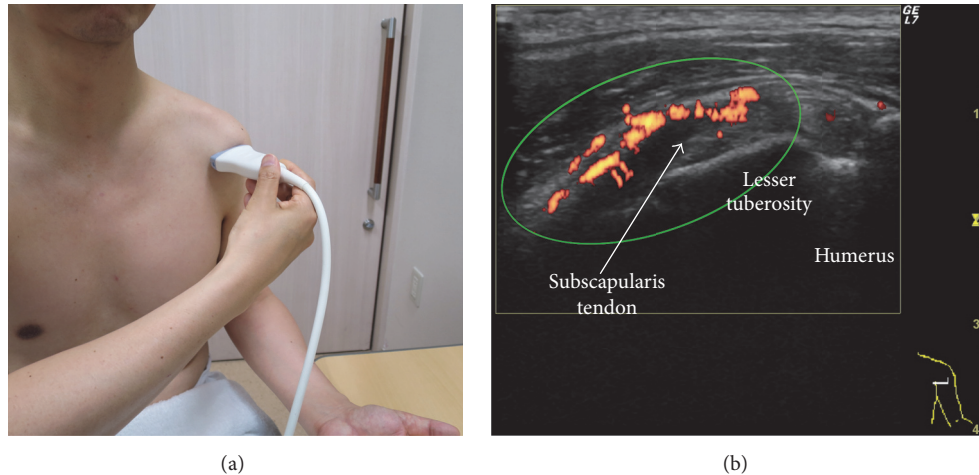


FIGURE 1: Scanning method for the evaluation of hyperemia adjacent to the anterior aspect of the subscapularis tendon. (a) Arm and probe position for the evaluation of the subscapularis tendon in the long axis. The shoulder is in a neutral position, the elbow is fixed to 90° , and the hand is spinated. The probe is placed perpendicular to the shoulder. (b) Long axis ultrasound view of the subscapularis tendon (arrow). The subscapularis tendon is superficial to the lesser tuberosity and medial to the bicipital groove. Note that the hypoechoic appearance of the medial part of the subscapularis tendon is due to the anisotropy. The area indicated by an ellipse, including the anterior soft tissues and the posterior tendon tissues and excluding the bicipital groove, is assessed for the severity of hyperemia.

by transverse scanning of the posterior recess. This was complemented by dynamic observation during internal and external shoulder rotation. Similarly, with the shoulder in a neutral position, the long head of biceps (LHB) tendon sheath was evaluated by transverse and longitudinal scanning in the bicipital groove. The subdeltoid bursa (SDB) and subcoracoid bursa (SCB) were scanned with the shoulder in a neutral position, whereas the subacromial bursa (SAB) was scanned with the shoulder in a modified Crass position.

2.6. Grading and Scoring of Synovial Pathologies. All gray-scale US (GSUS) and power Doppler US (PDUS) findings for each synovial pathology were semiquantitatively graded and scored from 0 to 3 (0 = absent, 1 = mild, 2 = moderate, and 3 = severe) by analyzing the stored images, with the exception that a score of 0 could be given based on the description in a written report. All grading was done by the examiner (T. S.) who performed the US examinations. The GSUS and PDUS grading of GHJ synovitis was based on the SOLAR scoring system [11]. The GSUS and PDUS grading of LHB tenosynovitis was based on the OMERACT definition [12]. The GSUS grading of shoulder bursitis was subjectively determined (0 = absent, 1 = mild, 2 = moderate, and 3 = severe), whereas the PD signal of bursitis was subjectively graded on a semiquantitative scale (0 = absent or minimal flow, 1 = mild or single-vessel signal, 2 = moderate or confluent vessels, and 3 = severe or vessel signals in $>50\%$ of the synovium area). Although the GSUS and PDUS scores were determined for each instance of bursitis of the SDB, SAB, and SCB, those for shoulder bursitis were represented by the largest score among the three lesions. The shoulder synovitis score (SSS) was calculated as the sum of the GSUS and PDUS scores for the three pathologies (total of six scores) in each shoulder. The patient SSS (PSSS) was calculated as the sum of the scores for both shoulders of each patient.

2.7. Statistical Analysis. All statistical analyses were performed with EZR (Saitama Medical Center, Jichi Medical University, Saitama, Japan), which is a graphical user interface for R (The R Foundation for Statistical Computing, Vienna, Austria) [13]. The differences between the two groups were examined using Mann-Whitney U test. A correlation between two variables was examined using Spearman's rank correlation test. Statistical significance was set at a p value of less than 0.05. Intra- and interobserver reliability of the semiquantitative score were estimated using calculations of unweighted kappa statistics.

3. Results

3.1. Patient Demographics. Demographic and clinical data at the time of US examination are shown in Table 1. There were no significant differences in age and sex between the groups. Disease duration was shorter in the PMR group than in the pm-EORA group. Stiffness in the shoulder girdle was present in all patients in both groups. Pain in the bilateral shoulder was present in all patients in the PMR group and in the majority of patients in the pm-EORA group. Peripheral synovitis distal to the shoulder or knee was present in almost all patients in the pm-EORA group and in two patients in the PMR group. One patient in the PMR group tested positive for RF, whereas 60% of the patients in the pm-EORA group were seronegative. Both CRP and ESR were higher in the PMR group than in the pm-EORA group. Serum MMP-3 tended to be higher in the pm-EORA group than in the PMR group. Antirheumatic drugs including methotrexate were administered to all patients in the pm-EORA group, and methotrexate was administered to three patients in the PMR group as a corticosteroid-sparing agent during the one-year follow-up.

TABLE 1: Demographic and clinical characteristics of patients at the time of US examination.

Diagnosis ^a	PMR	pm-EORA
Number of patients	15	15
Age (years) ^b	72.6 ± 7.7	70.7 ± 7.0
Sex (female)	33.3%	46.7%
Disease duration (months) ^b	1.7 ± 0.8	2.7 ± 1.1
Shoulder girdle stiffness	100%	100%
Bilateral shoulder pain	100%	86.7%
Peripheral joint involvement	13.3%	93.3%
Positive RF	6.70%	33.3%
Positive ACPA	0.0%	33.3%
Positive RF and/or ACPA	6.7%	40.0%
CRP (mg/dL) ^b	9.3 ± 5.3	4.2 ± 5.0
ESR (mm/h) ^b	102 ± 27	79 ± 30
MMP-3 (ng/ml) ^b	255 ± 174	333 ± 366 ^c
2012 EULAR/ACR PMR criteria score ≥ 4	100%	60%
2010 ACR/EULAR RA criteria score ≥ 6	0.0%	66.6%
Initiation of antirheumatic drugs during one-year follow-up ^a	20%	100%

a, data after one-year follow-up; b, mean ± standard deviation; c, $n = 14$; ACPA, anti-citrullinated peptide antibody; CRP, C-reactive protein; ESR, erythrocyte sedimentation rate; MMP-3, matrix metalloproteinase 3; pm-EORA, elderly-onset rheumatoid arthritis with PMR-like onset; PMR, polymyalgia rheumatica; RF, rheumatoid factor; US, ultrasound.

TABLE 2: Distribution of the hyperemia on subscapularis tendon scores (HSScTS) in the shoulders among each disease group.

	Score 0	Score 1	Score 2	Score 3
PMR ($n = 30$)	6.7%	36.7%	36.7%	20.0%
pm-EORA ($n = 30$)	26.7%	26.7%	23.3%	23.3%
RA control ($n = 26$)	57.7%	38.5%	3.8%	0.0%
Non-RA control ($n = 22$)	40.9%	59.0%	0.0%	0.0%

PMR, polymyalgia rheumatica; pm-EORA, elderly-onset rheumatoid arthritis with PMR-like onset.

When the clinical data at the time of US examination were evaluated, all patients in the PMR group fulfilled the 2012 EULAR/ACR criteria for PMR. However, one-third of patients in the pm-EORA group did not fulfill the 2010 ACR/EULAR criteria for RA, possibly due to the low prevalence of seropositive patients. In addition, 60% of patients in the pm-EORA group had scores of 4 or higher for the 2012 PMR criteria, possibly because they presented with PMR-like onset. Therefore, it seems that the clinical data at the time of the US examination were not sufficient to predict the final diagnosis confirmed after one year of follow-up.

3.2. Development of a Semiquantitative Four-Point Scale Scoring System. Based on a subjective evaluation, we proposed a semiquantitative four-point scale scoring system for the severity of the hyperemia adjacent to the anterior aspect of the SSCt as follows. Illustrative images are shown in Figure 2. Score 0 = absent or minimal flow (Figure 2(a)); score 1 = single vessel dots (Figure 2(b)) or confluent linear shape signals shorter than half the length of the region to be evaluated (Figure 2(c)); score 2 = confluent linear shape signals longer than half the length of the region to be evaluated (Figure 2(d)) or confluent zone shape signals shorter than half the length of the region to be evaluated (Figure 2(e)); or score 3 = confluent zone shape signals longer than half the length of the region to

be evaluated (Figure 2(f)). The score was denominated as the hyperemia on subscapularis tendon score (HSScTS) and the sum of the scores of bilateral shoulders was denominated as Bil-HSScTS.

3.3. Validation of HSScTS Scoring System. The intraobserver unweighted kappa statistic obtained by rescoring 40 images blindly was 0.852. The interobserver unweighted kappa statistic was 0.745. The relationship between the quantitative measurement of PD-positive pixel areas and the semiquantitative HSScTS was plotted in Figure 3. These data indicated the strong reliability of the semiquantitative four-point scale scoring system for HSScTS.

3.4. Differences in Hyperemia on Subscapularis Tendon between Diseases or Clinical Conditions. The distribution of the HSScTS in the shoulders among each disease group is shown in Table 2. As control groups, 26 shoulders of 15 consecutive new-onset RA patients without a polymyalgic feature and 22 shoulders of 19 consecutive non-RA patients without a polymyalgic feature in whom HSScTS were recorded for symptomatic shoulders by US before starting treatment with corticosteroids or antirheumatic drugs were chosen. The non-RA control group included 5 shoulders with glenohumeral osteoarthritis, 2 shoulders with synovitis, acne, pustulosis,

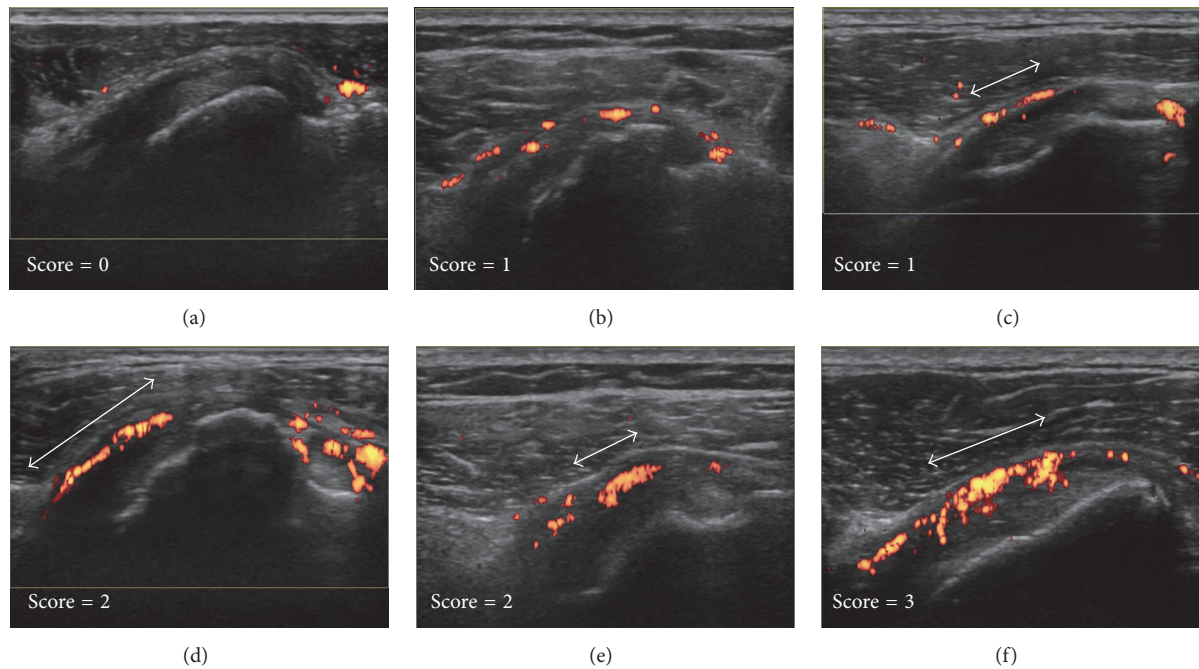


FIGURE 2: Illustrative ultrasound images for the four-point scale scoring of the hyperemia on the subscapularis tendon. Score 0 = absent or minimal flow (a), score 1 = single vessel dots (b), or confluent linear shape signals shorter than half the length of the region to be evaluated (c), score 2 = confluent linear shape signals longer than half the length of the region to be evaluated (d), or confluent zone shape signals shorter than half the length of the region to be evaluated (e), score 3 = confluent zone shape signals longer than half the length of the region to be evaluated (f). Double arrows indicate the length of the linear shape signals (c, d), or the length of the zone shape signals (e, f).

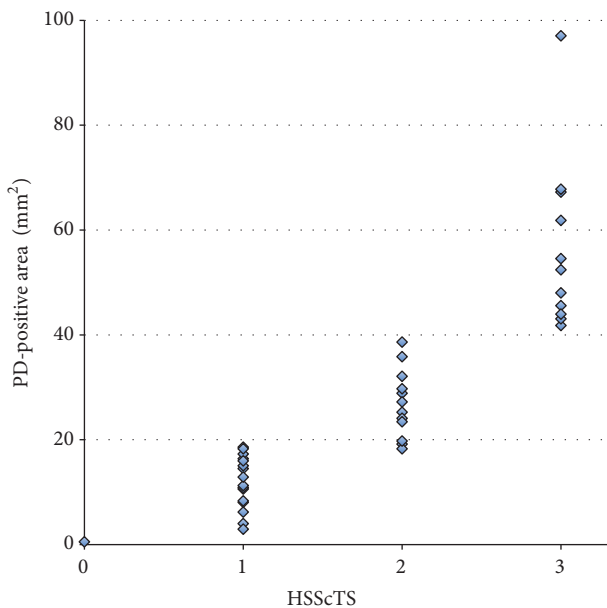


FIGURE 3: Correlations between the hyperemia on the subscapularis tendon score (HSScTS) and the area of power Doppler- (PD-) positive pixels among the 30 patients with polymyalgic symptoms.

hyperostosis, and osteitis (SAPHO) syndrome, 2 shoulders with a rotator cuff tear, and 12 others. A HSScTS of higher than 1 was equally common among the two groups presenting

a polymyalgic feature although it was rare among the control groups.

Next, we compared the Bil-HSScTS, which is the sum of the HSScTS of bilateral shoulders. Bil-HSScTS showed no significant differences between the PMR group (median, 3; min-max [2-5]) and the pm-EORA group (median, 3; min-max [0-6]) (Figure 4). These results suggest that the hyperemia on the SSCT is specific not to PMR but to the polymyalgic conditions.

3.5. Correlation between Severity of the Hyperemia on the SSCT and Serum Markers for Inflammation. Correlations between Bil-HSScTS and serum markers for inflammation were assessed among 30 patients from both the PMR and pm-EORA groups. As shown in Figure 5(a), Bil-HSScTS positively correlated with serum CRP ($R = 0.522, p = 0.00309$). In contrast, as shown in Figure 5(b), Bil-HSScTS did not correlate with serum MMP-3 ($R = 0.121, p = 0.531$). Assuming that the levels of serum CRP are related to the total sum of synovial inflammation and extrasynovial inflammation and that the levels of serum MMP-3 are related to synovial inflammation, we set up a new index, the CRP/MMP-3 ratio, which was defined as serum CRP concentration divided by serum MMP-3 concentration. As shown in Figure 5(c), Bil-HSScTS positively correlated with the CRP/MMP-3 ratio in the patients ($R = 0.425, p = 0.0215$). It is intriguing to speculate that Bil-HSScTS is related to extrasynovial inflammation and that the CRP/MMP-3 ratio can be used as a marker for the extent of extrasynovial

TABLE 3: Intra- and interobserver reliability evaluated by rescoring 184 images blindly shown as unweighted kappa statistics.

Pathology and mode	Number of the images evaluated	Intraobserver	Interobserver
LHB (GS & PD)	72	0.78	0.626
Bursa (GS & PD)	72	0.926	0.72
GHJ (GS & PD)	40	0.753	0.616
GS (all pathologies)	92	0.807	0.657
PD (all pathologies)	92	0.886	0.69
Overall	184	0.844	0.675

LHB, long head of biceps tendon sheath; GHJ, glenohumeral joint; GS, gray scale; PD, power Doppler.

TABLE 4: Distribution of GS and PD grades for three kinds of shoulder synovial pathologies.

Grade (score)	PMR <i>n</i> = 30				pm-EORA <i>n</i> = 30				Fisher's exact test <i>p</i> value
	0	1	2	3	0	1	2	3	
LHB GS (%)	20.0	46.7	30.0	3.3	30.0	26.7	26.7	16.7	0.176
LHB PD (%)	33.3	26.7	36.7	3.3	33.3	13.3	30.0	23.3	0.108
Bursa GS (%)	60.0	30.0	6.7	3.3	40.0	13.3	23.3	23.3	0.0157
Bursa PD (%)	76.7	10.0	13.3	0.0	46.7	16.7	20.0	16.7	0.0424
GHJ GS (%)	80.0	16.7	3.3	0.0	66.7	10.0	16.7	6.7	0.141
GHJ PD (%)	86.7	10.0	3.3	0.0	70.0	20.0	0.0	10.0	0.104

GHJ, glenohumeral joint; GS, gray scale; LHB, long head of biceps tendon sheath; PD, power Doppler; pm-EORA, elderly-onset rheumatoid arthritis with PMR-like onset; PMR, polymyalgia rheumatic.

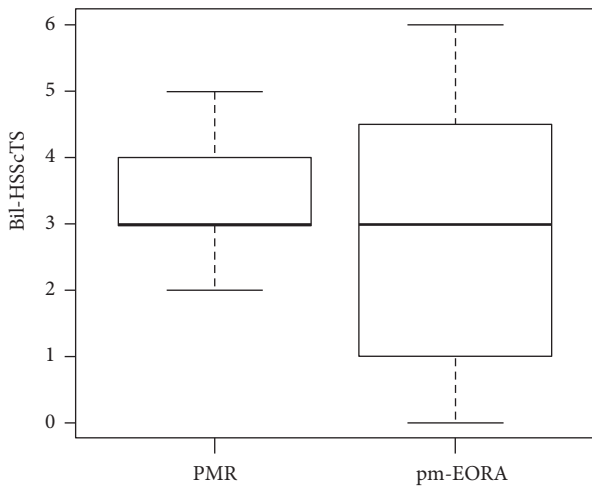


FIGURE 4: Comparison of the sum of the hyperemia on the subscapularis tendon scores of bilateral shoulders (Bil-HSScTS) between patients with PMR and pm-EORA.

inflammation compared to the extent of synovial inflammation.

3.6. *Grading and Scoring of Each Synovial Pathology.* For the quality control of our US scoring of shoulder synovitis, we evaluated the kappa value of intra- and interobserver reliability by blindly rescoring 184 images. The intraobserver agreement was excellent with an unweighted kappa statistic of 0.844. The interobserver agreement was good with an unweighted kappa statistic of 0.675. While reports on the

concordance rate of semiquantitative grading for shoulder bursitis are scarce, intra- and interobserver agreement were higher for shoulder bursitis, as compared with LHB tenosynovitis or GHJ synovitis (Table 3). Representative US images for the grading of the synovial pathology are shown in Figure 6.

The distribution of the GSUS and PDUS grades for the three kinds of synovial pathologies is shown in Table 4. Analysis of the distribution of the grades by Fisher's exact test revealed that the GS- and PD-grades of bursitis in the pm-EORA group were significantly higher than those in the PMR group. Comparison of the scores by Mann-Whitney *U* test showed similar findings. The GS-scores of bursitis in the pm-EORA group (median, 1; min-max [0-3]) were significantly higher than those in the PMR group (median, 0; min-max [0-3]; $p = 0.0167$). The PD-scores of bursitis in the pm-EORA group (median, 1; min-max [0-3]) were significantly higher than those in the PMR group (median, 0; min-max [0-2]; $p = 0.0103$). Whereas shoulder bursitis is generally thought to be a hallmark of PMR, our data obtained by semiquantitative comparison between PMR and pm-EORA revealed that bursitis was less severe in PMR than in pm-EORA.

3.7. *Comprehensive Scoring of Synovial Inflammation for Each Shoulder or Patient.* The SSS was calculated as the sum of the GSUS and PDUS scores for the three pathologies (total of six scores) in each shoulder, and the PSSS was calculated as the sum of the SSS for both shoulders of each patient. As shown in Figure 7, comparison by Mann-Whitney *U* test revealed that the SSS was significantly higher in the pm-EORA group (median, 6; min-max [0-18]) than in the PMR

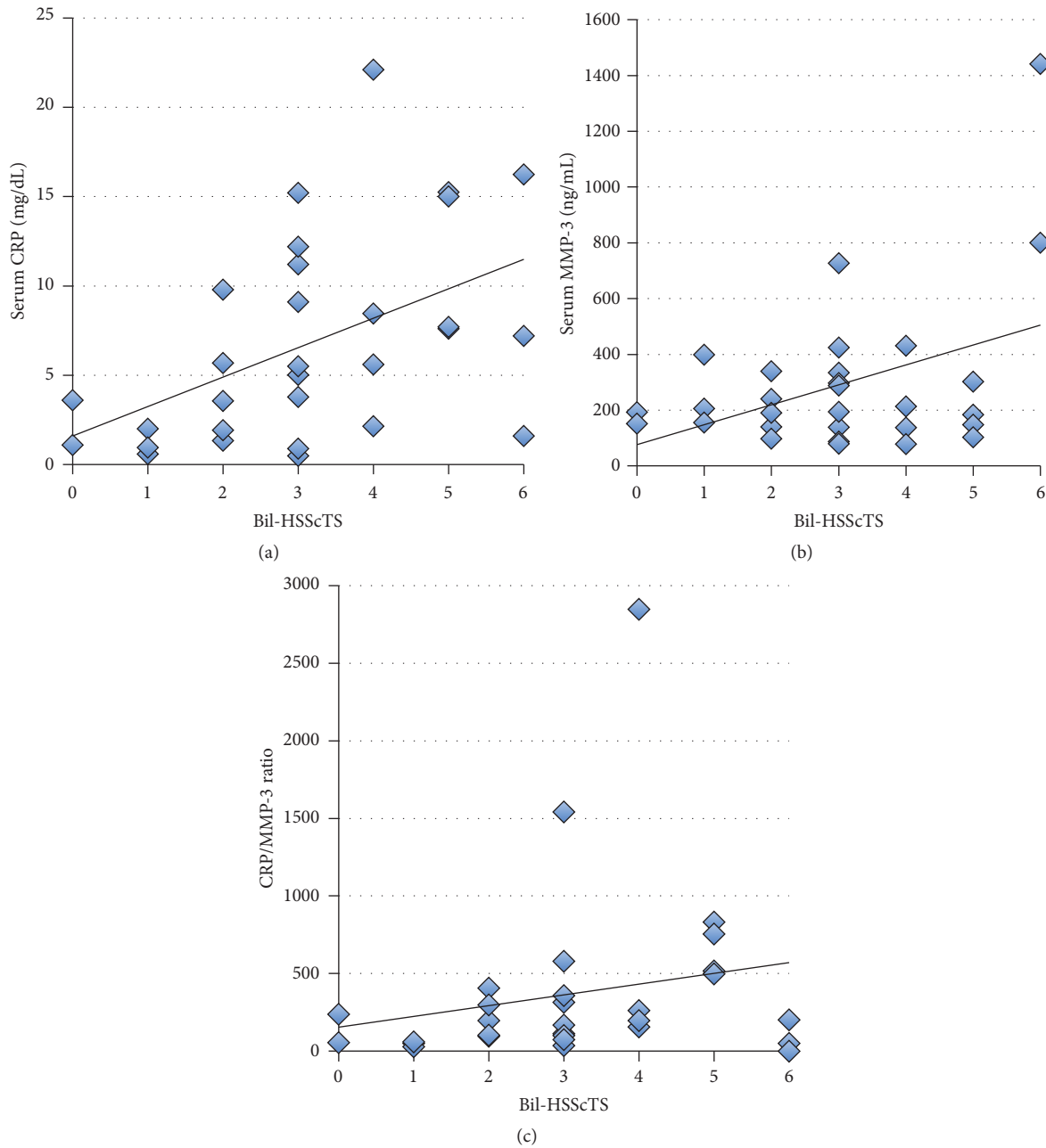


FIGURE 5: Correlations between the sum of the hyperemia on the subscapularis tendon scores of bilateral shoulders (Bil-HSScTS) and serum markers for inflammation. (a) Correlation between Bil-HSScTS and serum CRP. (b) Correlation between Bil-HSScTS and serum matrix metalloproteinase 3 (MMP-3). (c) Correlation between Bil-HSScTS and CRP/MMP-3 ratio. CRP/MMP-3 ratio was calculated by dividing serum CRP concentration by serum MMP-3 concentration.

group (median, 4; min-max [0-8]; $p = 0.0478$). However, the difference in the PSSS between the two groups did not reach the significance level (pm-EORA group median, 10; min-max [2-36] vs PMR group median, 8; min-max [1-15]; $p = 0.0528$). These results suggested that shoulder synovitis in PMR tends to be mild as compared with that observed in pm-EORA, possibly because synovitis in PMR may be characterized as exudative synovitis rather than proliferative synovitis as compared with synovitis in RA.

3.8. The Ratio of Bil-HSScTS to PSSS. We set up another new index, the Bil-HSScTS/PSSS ratio, which was defined as Bil-HSScTS divided by PSSS. As shown in Figure 8, Bil-HSScTS/PSSS ratio was significantly much higher in the PMR group (median, 0.500; min-max [0.250-3.00]) than in the pm-EORA group (median, 0.214; min-max [0-0.400]; $p = 0.000727$). Because we assume that the Bil-HSScTS/PSSS ratio represents the ratio of the severity of the inflammation in extrasynovial soft tissues to the severity of the inflammation

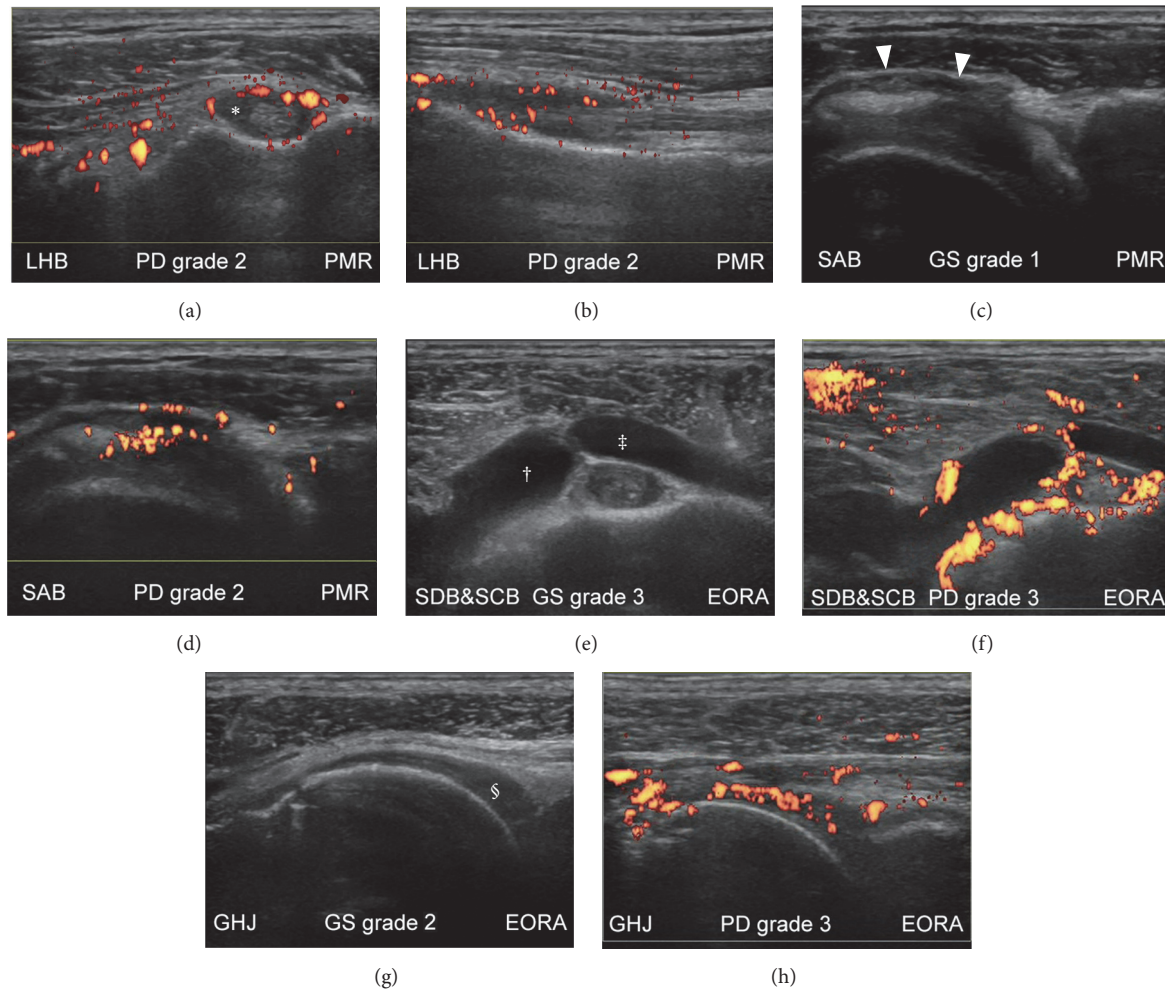


FIGURE 6: Representative ultrasound (US) images for grading of synovial pathology of the shoulder. Images from the shoulders of patients with polymyalgia rheumatica (PMR) (a–d) and elderly-onset rheumatoid arthritis (EORA) with PMR-like onset (e–h) are shown on gray-scale (c, e, and g) and power Doppler (a, b, d, f, and h) ultrasonograms. The shoulder was in a neutral position (a, b, e, f, and h), in a modified Crass position (c, d), or internally rotated (g). Moderate hyperemia was detected in the long head of biceps tendon sheath (*) on transverse (a) and longitudinal (b) scans. Mild synovial effusion (c) and moderate hyperemia (d) were detected in the subacromial bursa (arrowheads). Severe synovial effusion (e) and severe hyperemia (f) were detected in the subcoracoid bursa (†) and subdeltoid bursa (‡). Moderate synovial proliferation (g) and severe hyperemia (h) were detected in the glenohumeral joint (§).

in synovial tissues, it is suggested that the inflammation in PMR is dominantly localized in extrasynovial soft tissues as compared with that in pm-EORA.

3.9. Changes in the Hyperemia on the SSCT after Treatment with Corticosteroids and/or Antirheumatic Drugs. Follow-up data on Bil-HSScTS after starting treatment with corticosteroids and/or antirheumatic drugs were available in only 5 of 30 patients (3 with PMR and 2 with pm-EORA). The intervals between the examinations varied considerably from 0.9 to 8.7 months. In all five cases, Bil-HSScTS decreased after treatment (Figure 9).

4. Discussion

Two groups have employed traditional MRI, fat-saturated MRI, and contrast-enhanced MRI in studying the primary

site of inflammation in PMR since around 2000. Cantini et al. advocated that the primary site in PMR was the extracapsular synovial tissue, that is, the synovial bursa [14–16]. In contrast, McGonagle et al. argued that the primary site of inflammation was detected in nonsynovial soft tissues around the joint capsules and proposed that capsulitis/enthesitis, including inflammation of the functional enthesis, was the primary pathology in PMR and that synovitis occurred secondarily [17–20]. Currently, it remains unknown whether synovitis in the joints and their surroundings (tenosynovitis/bursitis) or capsule-/enthesis-based pathologies are the primary and secondary sites of PMR. Nevertheless, inflammation in PMR appears to be present in nonsynovial soft tissues, and this additional inflammatory element to synovitis likely contributes to the polymyalgic symptoms in PMR. Recent studies from Japan that employed fat-saturated MRI also confirmed

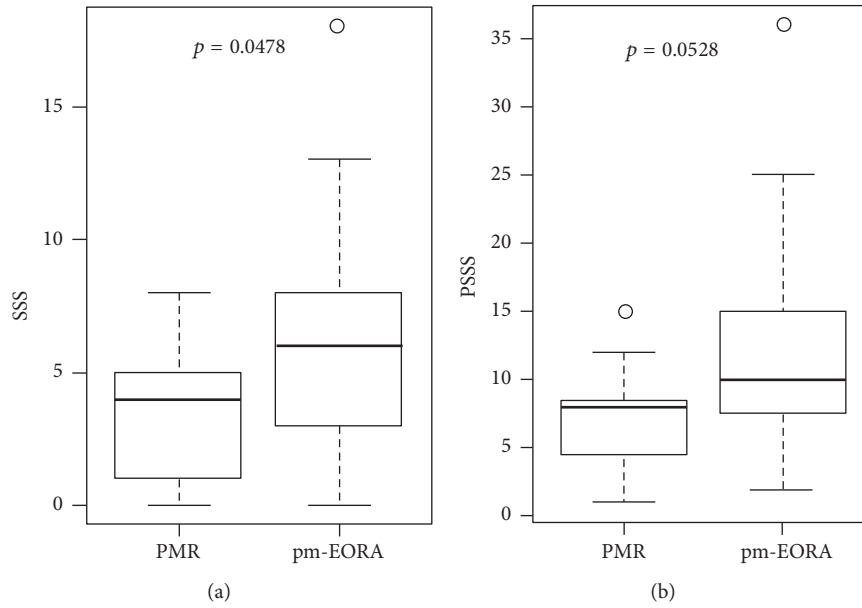


FIGURE 7: Comprehensive score for synovial inflammation for each shoulder or patient. The shoulder synovitis scores (SSS) (a) and patient shoulder synovitis scores (PSSS) (b) were compared between patients with PMR and those with EORA with PMR-like onset (pm-EORA) by Mann–Whitney *U* test.

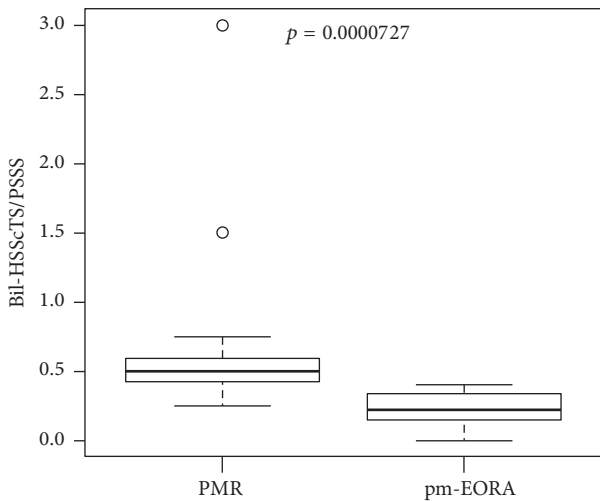


FIGURE 8: The ratio of the sum of the hyperemia on the subscapularis tendon scores of bilateral shoulders (Bil-HSScTS) to patient shoulder synovitis scores (PSSS). The ratio of Bil-HSScTS to PSSS was compared between patients with PMR and those with EORA with PMR-like onset (pm-EORA) by Mann–Whitney *U* test.

that inflammation of both the synovium and extrasynovial soft tissues around the joints were present in PMR [7, 8].

In this study, we indicated that significant hyperemia was often detected adjacent to the anterior aspect of the SSCT in the shoulders with PMR. It is very likely that this hyperemia detected by PDUS corresponds to the extrasynovial soft tissue inflammation depicted by MRI. Moreover, this region on the SSCT may represent the functional enthesis that is possibly affected in PMR. Because the moderate to severe

hyperemia was equally detected in both PMR and pm-EORA, the hyperemia on the SSCT is specific not to PMR but to the polymyalgic features common to both diseases. Presumably, other interfaces between the muscle and the rotator cuff, such as the supraspinatus tendon or the infraspinatus tendon, can be candidate sites for detecting extrasynovial inflammation. However, the anterior aspect of the subscapularis tendon is probably the optimal site because there are “echo windows” that allow good penetration by US.

We proposed the first tool utilizing US for evaluating soft tissue inflammation, which is the key feature of the polymyalgic symptoms around the shoulder. Our semiquantitative four-point scale scoring system for the severity of the hyperemia on the SSCT is not only simple and easy to use, but also well standardized. The system showed good intra- and interobserver reliability and good correlation to quantitative pixel-counting evaluation. Using this scoring system along with the comprehensive scoring system for shoulder synovitis, we demonstrated that Bil-HSScTS/PSSS ratio was significantly higher in the PMR group than in the pm-EORA group. It suggests that the inflammation in PMR is dominantly localized in extrasynovial soft tissue as compared with that in pm-EORA.

This scoring system can be utilized for many investigations, including (i) correlation between the hyperemia on the SSCT and stiffness or range of motion in the shoulders with PMR and (ii) association between the extent of the hyperemia on the SSCT and the necessity for corticosteroid therapy. Unfortunately, we could only show very limited data for the change in hyperemia on the SSCT before and after treatment. Longitudinal studies revealing the characteristics and the significance of the changes in the hyperemia on the SSCT are needed.

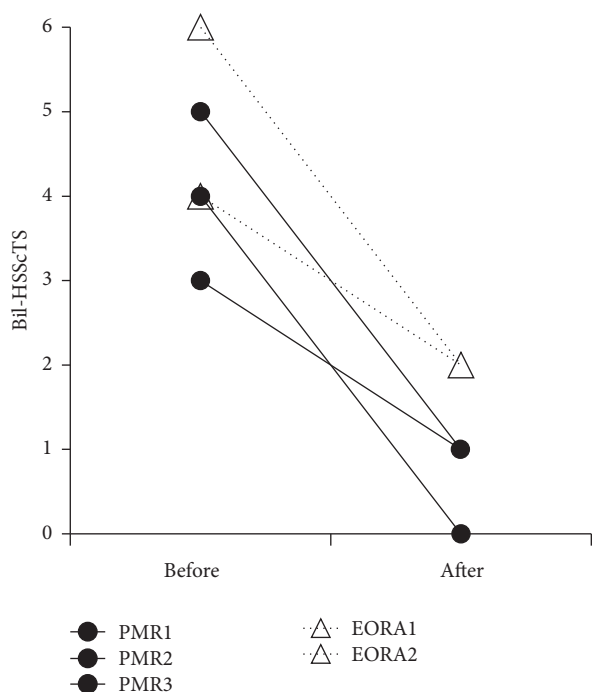


FIGURE 9: Changes in the sum of the hyperemia on subscapularis tendon scores of bilateral shoulders (Bil-HSScTS) after treatment with corticosteroids and/or antirheumatic drugs. Bil-HSScTS decreased after treatment in both PMR patients (circle, solid line) and EORA patients with PMR-like onset (triangle, dashed line).

5. Conclusions

In this study, we proposed the first tool utilizing US for the evaluation of extrasynovial soft tissue inflammation in the shoulders of patients with both PMR and pm-EORA. This semiquantitative four-point scale scoring system with high reliability is simple to use and can be utilized in future investigations.

Competing Interests

The authors declare that they have no competing interests.

Acknowledgments

This work was supported by a Grant-in-Aid from the Ministry of Health, Labour, and Welfare, Japan (H26-meneki-ippan-021).

References

- [1] A. Soriano, R. Landolfi, and R. Manna, "Polymyalgia rheumatica in 2011," *Best Practice & Research: Clinical Rheumatology*, vol. 26, no. 1, pp. 91–104, 2012.
- [2] C. Salvarani, F. Cantini, L. Boiardi, and G. G. Hunder, "Polymyalgia rheumatica," *Best Practice & Research: Clinical Rheumatology*, vol. 18, no. 5, pp. 705–722, 2004.
- [3] T. A. Kermani and K. J. Warrington, "Polymyalgia rheumatica," *The Lancet*, vol. 381, no. 9860, pp. 63–72, 2013.
- [4] G. Bajocchi, R. La Corte, A. Locaputo, M. Govoni, and F. Trotta, "Elderly onset rheumatoid arthritis: clinical aspects," *Clinical and Experimental Rheumatology*, vol. 18, no. 4, supplement 20, pp. S49–S50, 2000.
- [5] B. Dasgupta, M. A. Cimmino, H. Maradit-Kremers et al., "2012 Provisional classification criteria for polymyalgia rheumatica: a European League Against Rheumatism/American College of Rheumatology collaborative initiative," *Annals of the Rheumatic Diseases*, vol. 71, no. 4, pp. 484–492, 2012.
- [6] P. Macchioni, L. Boiardi, M. Catanoso, G. Pazzola, and C. Salvarani, "Performance of the new 2012 EULAR/ACR classification criteria for polymyalgia rheumatica: comparison with the previous criteria in a single-centre study," *Annals of the Rheumatic Diseases*, vol. 73, no. 6, pp. 1190–1193, 2014.
- [7] S. Mori, Y. Koga, and K. Ito, "Clinical characteristics of polymyalgia rheumatica in Japanese patients: evidence of synovitis and extracapsular inflammatory changes by fat suppression magnetic resonance imaging," *Modern Rheumatology*, vol. 17, no. 5, pp. 369–375, 2007.
- [8] J. Ochi, T. Nozaki, M. Okada et al., "MRI findings of the shoulder and hip joint in patients with polymyalgia rheumatica," *Modern Rheumatology*, vol. 25, no. 5, pp. 761–767, 2015.
- [9] D. Aletaha, T. Neogi, A. J. Silman et al., "2010 Rheumatoid arthritis classification criteria: an American College of Rheumatology/European League against Rheumatism collaborative initiative," *Arthritis and Rheumatology*, vol. 62, no. 9, pp. 2569–2581, 2010.
- [10] M. Backhaus, G.-R. Burmester, T. Gerber et al., "Guidelines for musculoskeletal ultrasound in rheumatology," *Annals of the Rheumatic Diseases*, vol. 60, no. 7, pp. 641–649, 2001.
- [11] W. Hartung, H. Kellner, J. Strunk et al., "Development and evaluation of a novel ultrasound score for large joints in rheumatoid arthritis: one year of experience in daily clinical practice," *Arthritis Care & Research*, vol. 64, no. 5, pp. 675–682, 2012.
- [12] E. Naredo, M. A. D'Agostino, R. J. Wakefield et al., "Reliability of a consensus-based ultrasound score for tenosynovitis in rheumatoid arthritis," *Annals of the Rheumatic Diseases*, vol. 72, no. 8, pp. 1328–1334, 2013.
- [13] Y. Kanda, "Investigation of the freely available easy-to-use software 'EZ' for medical statistics," *Bone Marrow Transplantation*, vol. 48, no. 3, pp. 452–458, 2013.
- [14] C. Salvarani, F. Cantini, I. Olivieri et al., "Proximal bursitis in active polymyalgia rheumatica," *Annals of Internal Medicine*, vol. 127, no. 1, pp. 27–31, 1997.
- [15] F. Cantini, C. Salvarani, I. Olivieri et al., "Shoulder ultrasonography in the diagnosis of polymyalgia rheumatica: a case-control study," *Journal of Rheumatology*, vol. 28, no. 5, pp. 1049–1055, 2001.
- [16] F. Cantini, C. Salvarani, L. Niccoli et al., "Fat suppression magnetic resonance imaging in shoulders of patients with polymyalgia rheumatica," *Journal of Rheumatology*, vol. 31, no. 1, pp. 120–124, 2004.
- [17] D. McGonagle, C. Pease, H. Marzo-Ortega, P. O'Connor, and P. Emery, "The case for classification of polymyalgia rheumatica and remitting seronegative symmetrical synovitis with pitting edema as primarily capsular/enthesal based pathologies," *Journal of Rheumatology*, vol. 27, no. 4, pp. 837–840, 2000.
- [18] D. McGonagle, C. Pease, H. Marzo-Ortega, P. O'Connor, W. Gibbon, and P. Emery, "Comparison of extracapsular changes by magnetic resonance imaging in patients with rheumatoid

arthritis and polymyalgia rheumatica,” *Journal of Rheumatology*, vol. 28, no. 8, pp. 1837–1841, 2001.

- [19] H. Marzo-Ortega, L. A. Rhodes, L. T. Ai et al., “Evidence for a different anatomic basis for joint disease localization in polymyalgia rheumatica in comparison with rheumatoid arthritis,” *Arthritis and Rheumatism*, vol. 56, no. 10, pp. 3496–3501, 2007.
- [20] S. L. Mackie, C. T. Pease, E. Fukuba et al., “Whole-body MRI of patients with polymyalgia rheumatica identifies a distinct subset with complete patient-reported response to glucocorticoids,” *Annals of the Rheumatic Diseases*, vol. 74, no. 12, pp. 2188–2192, 2015.

Research Article

Ultrasonographic Validation of Anatomical Landmarks for Localization of the Tendon of the Long Head of Biceps Brachii

Saiyun Hou,¹ John Harrell,¹ and Sheng Li²

¹Department of Physical Medicine and Rehabilitation, Baylor College of Medicine, Houston, TX, USA

²Department of Physical Medicine and Rehabilitation, University of Texas Health Science Center-Houston, Houston, TX, USA

Correspondence should be addressed to Sheng Li; sheng.li@uth.tmc.edu

Received 15 October 2016; Accepted 19 January 2017; Published 12 February 2017

Academic Editor: John T. W. Yeow

Copyright © 2017 Saiyun Hou et al. This is an open access article distributed under the Creative Commons Attribution License, which permits unrestricted use, distribution, and reproduction in any medium, provided the original work is properly cited.

Objectives. To establish anatomical landmarks for biceps tendon groove localization based on intrinsic anatomical relations and to validate the localization with ultrasonographic measurement. **Design.** Perspective, observational, single-blinded pilot study. **Participants.** 25 healthy male and female volunteers ages 24–50 years. **Methods.** We used two anatomical landmarks, the medial epicondyle vertical line related landmark and the coracoid process landmark. The distance from the groove skin mark to the medial epicondyle vertical line and the coracoid process was measured horizontally and was measured at 0° and 45° of shoulder external rotation, respectively. **Results.** Medial epicondyle vertical lines were 9.3 mm/21.5 mm medial to the groove at 0°/45° of shoulder external rotation, respectively. Correlation coefficients were 0.04/0.10, 0.32/0.42, and 0.26/0.37 for weight, height, and BMI in 0°/45° of shoulder external rotation, respectively. The distance between the coracoid process and the groove was 44.0 mm/62.2 mm in 0°/45° of shoulder external rotation, respectively. Correlation coefficients were 0.36/0.41, 0.36/0.54, and 0.18/0.12 for weight, height, and BMI in 0°/45° of shoulder external rotation, respectively. **Conclusions.** The medial epicondyle vertical line and the coracoid process landmark are both useful anatomical landmarks to localize the biceps groove. The anatomical landmark based localization is essentially not correlated with subject's weight, height, or BMI.

1. Introduction

The long biceps tendon arises mainly from the supraglenoid tubercle and partly from the superior glenoid labrum, passes through the glenohumeral joint, and enters the intertubercular groove. Its intra-articular and extra-articular portions are stabilized by a series of soft-tissue restraints arising from the coracohumeral ligament, superior glenohumeral ligament, and supraspinatus and subscapularis tendons [1]. Pathologies of the long head of the biceps tendon (LHBT) present an important source of shoulder pain, often causing significant losses in this joint flexion. Isolated disorders of LHBT include tendinopathy, dislocation, and partial or complete tears. LHBT tendinopathy is generally due to inflammatory, traumatic, and degenerative causes related to overuse, becoming chronic in most cases [2]. Also it is commonly accompanied by shoulder pathology such as rotator cuff dysfunction, scapular dyskinesis, adhesive capsulitis, glenohumeral joint arthritis, SLAP (superior labrum anterior to posterior)

lesions, or supraspinatus tendinosis [3–5]. A few studies [6–9] have found a close relationship between rotator cuff tears and associated injuries produced in LHBT. Disorders of the LHBT are associated with rotator cuff tear in up to 90% of cases [6, 8]. Physical examination is unreliable in the diagnosis of LHBT pathology. Local anesthetic or steroid injection into the biceps long head tendon sheath is commonly used for diagnosis and treatment. Ultrasonography is preferred for visualizing the LHBT. However, it has a disadvantage of machine use and being time consuming. Long head of biceps palpation at the level of the intertubercular groove not only plays a central role in the physical examination of patients who present with anterior shoulder pain but is also the primary means of localization for biceps tendon sheath injections. Unfortunately, only approximately 5.3% overall accurate rate of long head of biceps groove palpation was reported in 25 examiners including attending physicians, fellows, and residents [10]. In this study we developed two anatomical landmarks, medial related vertical line, and

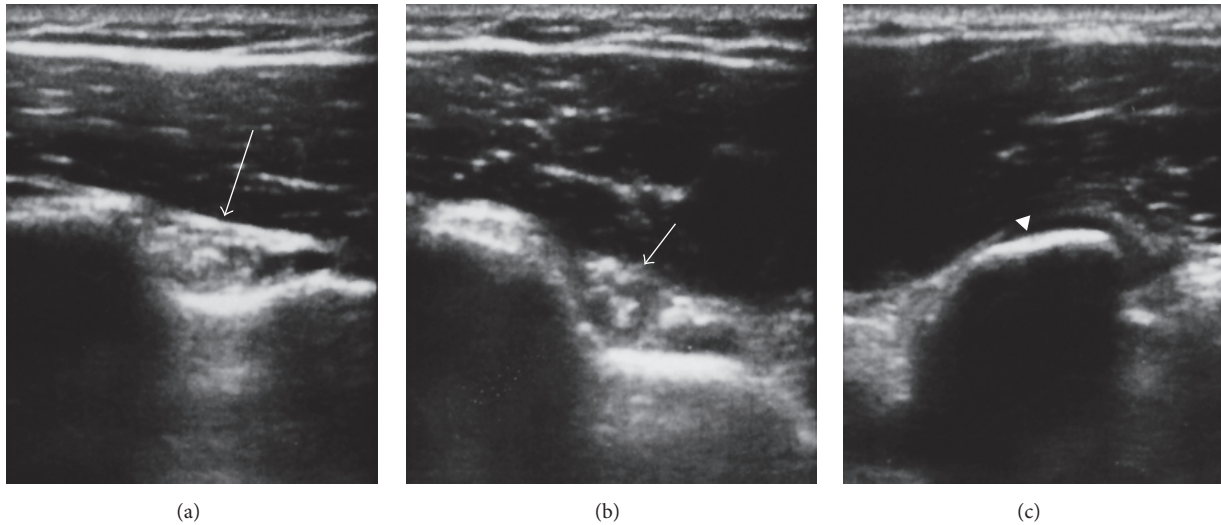


FIGURE 1: Biceps long head tendon groove (arrow) in the neutral position (a) and 45° of shoulder external rotation (b) was marked under ultrasound guidance. Coracoid process (arrowhead) was marked under ultrasound guidance (c).

coracoid related landmarks which are based on intrinsic anatomical relations. The relationship between those two landmarks and LHBT is consistent and reliable. The purpose of the present study was to introduce these two anatomical landmarks for localization of biceps tendon groove and to validate the localization with ultrasonographic measurement.

2. Methods

2.1. Design. The perspective, observational study was completed in a tertiary care center at an academic institution. All of participants were blinded to study. Two anatomical landmarks were developed to localize LHBT groove and localization was validated with ultrasonographic measurement.

2.2. Participants. Participants were recruited on a volunteer basis through word of mouth and posters. Participants were included if they are healthy adults between 18 and 64 years old. Exclusion criteria were those who (1) had a history of shoulder pain or injury and those of shoulder surgical intervention; of biceps tendinitis or injury; or of shoulder joint chronic pathology, including but not limited to such issues as osteoarthritis, Rheumatologic, or autoimmune disorders and (2) were pregnant or lactating. Each participant's height, weight, and calculated BMI were recorded.

2.3. Ethic Statement. The study protocol (H36580) was approved by the local Institutional Review Board and was conducted at a single-site rehabilitation center in an urban tertiary academic medical center. Written informed consent was obtained from all patients before enrollment into the study.

2.4. Equipment. All ultrasound scans were performed on a Philips iU22 ultrasound machine with a 12–5 MHz linear

array transducer (Philips Ultrasound Systems, Bothell, WA). The measurement was performed with an electronic digital caliper (NEIKO TOOLS, Gardena, CA). A 90° angle rule was used to mark the site of medial epicondyle vertical line at intertubercular groove for each participant.

2.5. Procedures. Left shoulder was used to complete the study to standardize the procedure. After obtaining informed consent, age, weight, and height of the subject were recorded by a study coinvestigator. Two anatomical landmarks were used to localize the LHBT.

(1) Medial Epicondyle Vertical Line Related Landmark. Participants stood upright with the shoulder in the neutral position (0°), the elbow at 90° of flexion, and the forearm in the neutral position between pronation and supination. Firstly the biceps long head tendon groove was marked under ultrasound guidance (Figure 1(a)). Then a vertical line was drawn to pass through medial epicondyle of humerus and perpendicular to the ground with a 90° angle rule (Figure 2). The line to where the vertical line passed through anterior shoulder at the biceps groove level was marked. The distance from biceps long head tendon groove to the vertical line was measured horizontally with a digital caliper. Then participants changed their shoulder position to 45° of shoulder external rotation. The above procedure was repeated and the distance from biceps long head groove to the vertical line was measured again horizontally with a digital caliper (Figure 1(b)).

(2) Coracoid Process Landmark. Participants stood upright with the shoulder in the neutral position (0°), the elbow at 90° of flexion, and the forearm in the neutral position between pronation and supination. The coracoid process and biceps long head tendon groove were marked under ultrasound guidance (Figure 1(c)). The distance of the coracoid process

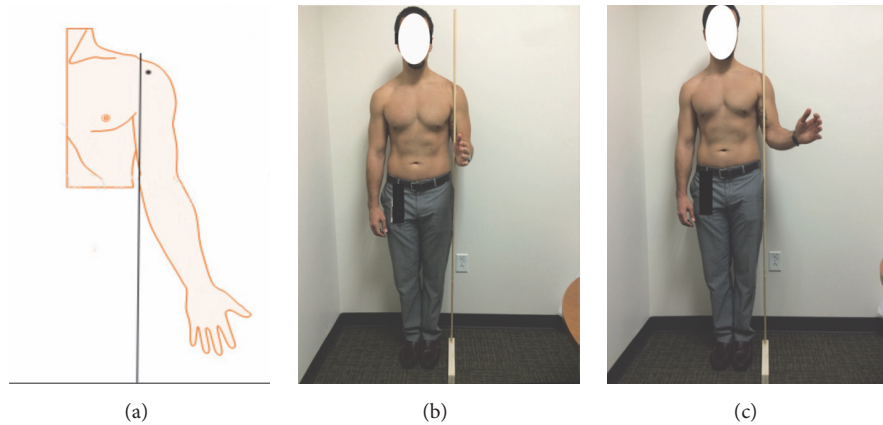


FIGURE 2: (a) Black line represents a vertical line passing through the medial epicondyle of humerus and perpendicular to ground. Black dot represents the intertubercular groove. Medial epicondyle related landmark was marked with a 90° angle ruler in the neutral position (b) and 45° of shoulder external rotation (c).

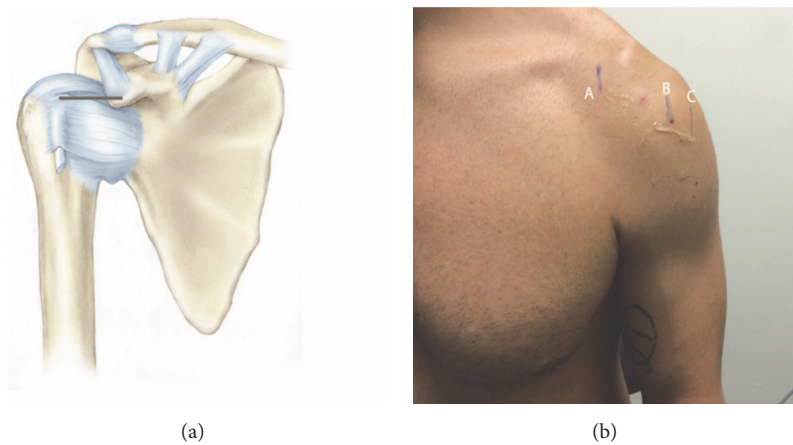


FIGURE 3: (a) Black line represents the distance between the coracoid process and the intertubercular groove. (b) Coracoid process (A), intertubercular groove in 0° (B), and 45° (C) of shoulder external rotation were marked with ultrasound. The distance of the coracoid process and the biceps long head tendon groove was measured horizontally between A and B or C at the coracoid level.

and the biceps long head tendon groove was measured horizontally with a digital caliper at the coracoid level (Figure 3). The above procedure was repeated when participant's arm was kept at 45° of shoulder external rotation. The distance of the coracoid process and the biceps long head tendon groove was measured with a digital caliper at 45° of shoulder external rotation.

2.6. Data Analysis. Mean and 95% confidence interval (CI) of the distance measured at 0° and 45° of shoulder external rotation were calculated for those two anatomical landmarks, respectively. Also correlation coefficients between height, weight, and body mass index (BMI) and those two anatomical landmarks related measurement were calculated.

3. Results

25 healthy volunteers (16 female and 9 male; 24–50 years of age; mean, 29.5 ± 5.4 years) had body mass index (BMI) of

17.7–35.8 (mean, 23.2 ± 3.7). According to American CDC BMI classification criteria, this sample included 19 normal weight subjects (BMI 18.5–24.9), 1 underweight subjects (BMI < 18.5), and 5 overweight subjects (BMI 25–29.9).

All anatomic landmarks were identified under ultrasound guidance in all subjects. All medial epicondyle vertical lines were medial to the biceps groove at both 0° and 45° of shoulder external rotation. The horizontal distance between the biceps groove and medial epicondyle vertical line was found to be 9.3 mm (95% CI, 6.8 to 11.8) and 21.5 mm (95% CI, 18.9 to 24.1) in 0° and 45° of shoulder external rotation, respectively. Correlation coefficients were 0.04/0.10, 0.32/0.42, and 0.26/0.37 for weight, height, and BMI in 0°/45° of shoulder external rotation, respectively (Table 1).

The horizontal distance between the coracoid process and the biceps tendon groove was found to be 44.0 mm (95% CI, 41.5 to 46.5) and 62.2 mm (95% CI, 59.2 to 65.2) in 0° and 45° of shoulder external rotation, respectively. Correlation coefficients were 0.36, 0.36, and 0.18 for weight, height, and

TABLE 1: Medial epicondyle vertical line related landmark: average distance between the biceps groove and medial epicondyle vertical line were measured at 0° and 45° external rotation. Correlation coefficients between the distance and weight, height, and BMI were calculated at 0° and 45° of shoulder external rotation. CC: correlation coefficients. BMI: body mass index.

	Average distance (95% CI)	CC between the distance and weight	CC between the distance and height	CC between the distance and BMI
0° neural position	9.3 mm (6.8–11.8)	0.04	0.32	0.26
45° external rotation	21.5 mm (18.9–24.1)	0.10	0.42	0.37

TABLE 2: Coracoid process landmark: average distance between biceps groove and coracoid process were measured at 0° and 45° external rotation. Correlation coefficients between the distance and weight, height, and BMI were calculated at 0° and 45° external rotation. CC: correlation coefficients. BMI: body mass index.

	Average distance (95% CI)	CC between the distance and weight	CC between the distance and height	CC between the distance and BMI
0° neural position	44.0 mm (41.5–46.5)	0.36	0.36	0.18
45° external rotation	62.2 mm (59.2–65.2)	0.41	0.54	0.13

BMI in 0° neutral position, respectively. At 45° of shoulder external rotation, correlation coefficients were 0.41, 0.54, and 0.12 for weight, height, and BMI, respectively (Table 2). Collectively, the results support the intrinsic anatomical relations between these landmarks and the LHBT groove.

4. Discussion

The long head of the biceps tendon (LHBT) can be a source of pain or shoulder dysfunction [11]. Local anesthetic or steroid injection into the biceps long head tendon sheath is commonly used for diagnosis and treatment. Identifying the biceps tendon as a pain generator in patients presenting with shoulder pain syndromes has significant and diagnostic and therapeutic implications. An accurate and complete diagnosis facilitates optimal treatment [12].

In the study described herein, two anatomic landmarks for biceps tendon identification were used and their relationships to LHBT within the intertubercular groove were evaluated. The medial epicondyle vertical line lies approximately 1 centimeter medial to the biceps groove when the shoulder is in the neutral position and about 2 centimeters when shoulder is at 45° of external rotation. The coracoid process landmark lies approximately 4.4 centimeters when the shoulder is in the neutral position, about 6.2 centimeters when the shoulder is at 45° of external rotation. Therefore, these two anatomical landmarks are effective for LHBT identification and can be performed easily in an outpatient setting.

The relationship between the observed landmarks and the LHBT is rooted in intrinsic anatomical relations among them. The medial epicondyle of the humerus is a bony protrusion located on the medial side of distal humerus (Figure 2). The relationship among them is consistent and reliable. Given this intrinsic relation, this anatomical landmark based localization is not correlated with subject's weight, height, or BMI. The coracoid process is a small hook-like structure on the lateral edge of the superior anterior portion of the

scapula. It is localized in the deltopectoral groove between the deltoid and pectoralis major muscles. There is certain intrinsic relation between coracoid process and intertubercular groove. Glenohumeral joint subluxation, dislocation, or effusion may change this relationship. Physician should be aware of it when patient has the comorbidity of GH joint pathology. Given this intrinsic relation, coracoid related landmark is not correlated with subject's weight or BMI. The height has the moderate correlation to the distance measured in 45° of shoulder external rotation, but no correlation in 0° of shoulder external rotation. Therefore we recommend that physicians localize the LHBT in the neutral position of shoulder when measuring with coracoid process related landmark.

The two anatomical landmarks introduced in this study were developed to identify the localization of LHBT within the intertubercular groove. The localization was validated with ultrasonographic measurement. Correlation between the distance and weight, height, and BMI increased when shoulder externally rotated to 45 degree compared with the neutral position for these two landmarks. We recommend that the neutral position of shoulder is a better way to localize the LHBT.

5. Limitations

Firstly, although 25 subjects were conducted for this pilot study, further study including increased sample size could help improve the accuracy of the measurements and increase its generalisability. Secondly, this measurement is reliable only if the coracoid process, LHBT, and medial epicondyle of humerus and LHBT are intact as was the case in our subjects. If the coracoid process and medial epicondyle of humerus are fractured or the LHBT is dislocated, these measurements cannot provide guidance about where the LHBT may be found. Thirdly, intraobserver and interobserver error were not included because all measurements were made by one author.

6. Conclusion

We used two new anatomical landmarks for biceps tendon groove localization. The medial epicondyle vertical line is a useful anatomical landmark to localize the biceps groove. It lies approximately 1 centimeter medial to the biceps groove when the shoulder is in the neutral position and about 2 centimeters when shoulder is at 45 degrees of external rotation. This anatomical landmark based localization is not correlated with subject's weight, height, or BMI. The coracoid process landmark is also a useful anatomical landmark to localize the biceps groove. It lies approximately 4.4 centimeters when the shoulder is in the neutral position, about 6.2 centimeters when the shoulder is at 45 degree of external rotation. No correlation exists between the distance to the biceps groove and weight, height, or BMI in 0° of shoulder external rotation, whereas a moderate correlation with height exists in 45° of shoulder external rotation. Those two anatomical landmarks allow for efficient and safe identification of the tendon of the long head of biceps brachii when examining or injection.

Abbreviations

BMI: Bone mass index
 CI: Confidence interval
 LHBT: Long head of the biceps tendon
 GH: Glenohumeral joint
 SLAP: Superior labrum anterior to posterior.

Competing Interests

The authors declare that they have no competing interests.

Acknowledgments

This study was supported in part by NIH NICHD/NCMRR IR21HD087128-01.

References

- [1] P. Habermeyer, P. Magosch, M. Pritsch, M. T. Scheibel, and S. Lichtenberg, "Anterosuperior impingement of the shoulder as a result of pulley lesions: A Prospective Arthroscopic Study," *Journal of Shoulder and Elbow Surgery*, vol. 13, no. 1, pp. 5–12, 2004.
- [2] U. G. Longo, M. Loppini, G. Marineo, W. S. Khan, N. Maffulli, and V. Denaro, "Tendinopathy of the tendon of the long head of the biceps," *Sports Medicine and Arthroscopy Review*, vol. 19, no. 4, pp. 321–332, 2011.
- [3] M. Khazzam, M. S. George, R. S. Churchill, and J. E. Kuhn, "Disorders of the long head of biceps tendon," *Journal of Shoulder and Elbow Surgery*, vol. 21, no. 1, pp. 136–145, 2012.
- [4] M. I. Harwood and C. T. Smith, "Superior labrum, anterior-posterior lesions and biceps injuries: diagnostic and treatment considerations," *Primary Care: Clinics in Office Practice*, vol. 31, no. 4, pp. 831–855, 2004.
- [5] C. D. Peltz, S. M. Perry, C. L. Getz, and L. J. Soslowsky, "Mechanical properties of the long-head of the biceps tendon are altered in the presence of rotator cuff tears in a rat model," *Journal of Orthopaedic Research*, vol. 27, no. 3, pp. 416–420, 2009.
- [6] D. P. Beall, E. E. Williamson, J. Q. Ly et al., "Association of biceps tendon tears with rotator cuff abnormalities: degree of correlation with tears of the anterior and superior portions of the rotator cuff," *American Journal of Roentgenology*, vol. 180, no. 3, pp. 633–639, 2003.
- [7] C.-H. Chen, K.-Y. Hsu, W.-J. Chen, and C.-H. Shih, "Incidence and severity of biceps long head tendon lesion in patients with complete rotator cuff tears," *Journal of Trauma—Injury, Infection and Critical Care*, vol. 58, no. 6, pp. 1189–1193, 2005.
- [8] A. M. Murthi, C. L. Vosburgh, and T. J. Neviasser, "The incidence of pathologic changes of the long head of the biceps tendon," *Journal of Shoulder and Elbow Surgery*, vol. 9, no. 5, pp. 382–385, 2000.
- [9] C. D. Peltz, J. E. Hsu, M. H. Zgonis, N. A. Trasolini, D. L. Glaser, and L. J. Soslowsky, "The effect of altered loading following rotator cuff tears in a rat model on the regional mechanical properties of the long head of the biceps tendon," *Journal of Biomechanics*, vol. 43, no. 15, pp. 2904–2907, 2010.
- [10] G. P. Gazzillo, J. T. Finnoff, M. M. Hall, Y. A. Sayeed, and J. Smith, "Accuracy of palpating the long head of the biceps tendon: an ultrasonographic study," *PM&R*, vol. 3, no. 11, pp. 1035–1040, 2011.
- [11] F. Elser, S. Braun, C. B. Dewing, J. E. Giphart, and P. J. Millett, "Anatomy, function, injuries, and treatment of the long head of the biceps brachii tendon," *Arthroscopy—Journal of Arthroscopic and Related Surgery*, vol. 27, no. 4, pp. 581–592, 2011.
- [12] M. Zanetti, D. Weishaupt, C. Gerber, and J. Hodler, "Tendinopathy and rupture of the tendon of the long head of the biceps brachii muscle: evaluation with MR arthrography," *American Journal of Roentgenology*, vol. 170, no. 6, pp. 1557–1561, 1998.

Research Article

Ultrasonic Measurement of Dynamic Muscle Behavior for Poststroke Hemiparetic Gait

Xin Chen,^{1,2,3} Xudong Zhang,^{1,2,3} Wenxiu Shi,^{1,2,3} Jun Wang,⁴ Yun Xiang,⁴
Yongjin Zhou,^{1,2,3} and Wan-Zhang Yang⁵

¹School of Biomedical Engineering, Shenzhen University, Shenzhen, China

²National-Regional Key Technology Engineering Laboratory for Medical Ultrasound, Shenzhen, China

³Guangdong Key Laboratory for Biomedical Measurements and Ultrasound Imaging, Shenzhen, China

⁴Shenzhen Sixth People's Hospital, Shenzhen, China

⁵Shenzhen Hospital of Southern Medical University, Shenzhen, China

Correspondence should be addressed to Yongjin Zhou; yjzhou@szu.edu.cn and Wan-Zhang Yang; ywz565@sina.com

Received 5 August 2016; Revised 10 November 2016; Accepted 21 December 2016; Published 23 January 2017

Academic Editor: Qing-Hua Huang

Copyright © 2017 Xin Chen et al. This is an open access article distributed under the Creative Commons Attribution License, which permits unrestricted use, distribution, and reproduction in any medium, provided the original work is properly cited.

Quantitative evaluation of the hemiparesis status for a poststroke patient is still challenging. This study aims to measure and investigate the dynamic muscle behavior in poststroke hemiparetic gait using ultrasonography. Twelve hemiparetic patients walked on a treadmill, and EMG, joint angle, and ultrasonography were simultaneously recorded for the gastrocnemius medialis muscle. Pennation angle was automatically extracted from ultrasonography using a tracking algorithm reported previously. The characteristics of EMG, joint angle, and pennation angle in gait cycle were calculated for both (affected and unaffected) sides of lower limbs. The results suggest that pennation angle could work as an important morphological index to continuous muscle contraction. The change pattern of pennation angle between the affected and unaffected sides is different from that of EMG. These findings indicate that morphological parameter extracted from ultrasonography can provide different information from that provided by EMG for hemiparetic gait.

1. Introduction

Hemiparesis refers to the sensorimotor impairments on only one side of the body commonly observed in poststroke patients [1]. Gait recovery is a major objective in the rehabilitation of hemiparesis patients. Quantitative gait analysis is the best way to evaluate the complex gait dysfunctions that are related to inappropriate control of the central nervous system or changes in the mechanical properties of the muscle [2]. Diverse gait analysis techniques, of which the most commonly used include measurement of temporospatial gait parameters [3, 4], electromyography (EMG) [5], kinematics [6, 7], and kinetics [8], have been developed. In addition, some brain imaging techniques, such as functional magnetic resonance imaging (fMRI) [9] and positron emission tomography (PET) [10], have provided an approach to studying the neural circuitry involved in poststroke motor control.

Several articles have reviewed how these techniques have been used to quantify the abnormal patterns in hemiparetic gait [2, 11, 12].

The architecture of skeletal muscle, defined as the geometric arrangement of muscle fibers, is a primary determinant of muscle function. Therefore, assessing the morphological changes in muscle provides an alternative measurement of muscle activity [13]. Since ultrasonography (US) offers the unique advantages of being noninvasive, real-time, and easily accessible, it has been widely applied to measure in vivo changes in muscle during static and dynamic contractions [14–16]. US has been showed to reliably measure changes in muscle thickness [17, 18], fiber length [19, 20], pennation angle [21–23], fascicle curvature [24], and cross-sectional area [16]. Several studies investigated the effect of poststroke impairments on muscle architecture as measured by ultrasound during static contraction [25, 26]. The results

TABLE 1: Patient characteristics.

Subject	Age (year)	Gender	Time poststroke (day)	Affected side	Brunnstrom motor stage
1	45	Male	50	Left	3
2	60	Male	130	Right	4
3	45	Male	25	Left	4
4	46	Male	211	Right	4
5	44	Female	197	Left	3
6	62	Female	64	Left	4
7	47	Male	119	Left	3
8	69	Male	731	Right	5
9	77	Male	53	Right	4
10	55	Male	76	Right	4
11	70	Female	30	Right	5
12	39	Male	18	Right	3

showed significant architectural changes in the affected side due to weakness in the muscle after stroke. However, all the previous ultrasonography studies measured the static architectural values under different contraction conditions, and the continuous muscle behavior during hemiparetic gait has not previously been clarified. Although some studies have applied US to investigate the dynamic muscle behavior during human running and walking [27, 28], it has seldom been used in a hemiparetic gait study.

In this study, an experimental and data analysis platform was employed to dynamically capture EMG, joint angle, and ultrasonography signals. The gaits of twelve hemiparetic patients were measured and the characteristics of their muscle behaviors were analyzed. The goal of this study is to investigate the dynamic muscle behavior for poststroke hemiparetic gait using ultrasonography.

2. Patients and Methods

2.1. Patients. Both chronic and subacute stroke patients were included in this study. A total of twelve patients (9 male and 3 female) participated. Their mean age was 54.9 years (SD = 12.4 years), and the mean poststroke time was 142 days (SD = 196.2 days). The characteristics of the patients are shown in Table 1. The study was approved by the local ethics committee, and all participants gave their written informed consent.

2.2. Experimental Procedure. All patients walked on a treadmill at a self-selected speed for 60 s. The walking speed is between 1.0 km/h and 1.5 km/h. In some cases, in order to ensure security, the patients were allowed to hold onto a rail to maintain their balance. For each patient, the experimental procedure was performed twice for test on each of the lower limbs (the affected and unaffected sides). The subjects rested for several minutes after each test.

2.3. Data Acquisition and Synchronization. The EMG, joint angle, and US were simultaneously recorded from the gastrocnemius medialis (GM) muscle during walking. A real-time B-mode ultrasonic scanner (Sonostar Technologies Co., Guangzhou, Guangdong, China) with an electronic linear array probe was used to obtain longitudinal ultrasound images of the GM muscle. As shown in Figure 1, the ultrasound probe was secured steadfastly by a custom-designed adjustable bracket on the mid-belly of GM muscle. The long axis of the probe was carefully arranged aligning with the middle line of the GM muscle. Ultrasound gel was applied to secure acoustic coupling between the probe and the skin. The B-mode images outputted from the scanner were digitized by a video capture card (Weishi Digital Image Technology Co., Xian, Shanxi, China) with a frame rate of 25 Hz. Surface bipolar Ag-AgCl EMG electrodes (Tianrun Sunshine Medical Supplies Co., Beijing, China) with a diameter of 2 cm were used to capture the EMG signal. Two electrodes were placed on one side of the probe. The line between the centers of the electrodes was parallel to the long axis of the probe. A reference EMG electrode was placed near the kneecap. The joint angle of the ankle was measured by an electronic goniometer (model XM110; Penny & Giles Biometrics, Ltd.; Gwent, United Kingdom) attached in the sagittal plane between the anterior tibia and the dorsum of foot. The surface EMG signal was amplified by an amplifier with a gain of 2,000, filtered by a 10–400 Hz band-pass analog filter (EMG100C, BIOPAC Systems Inc., Goleta, CA, USA). The angle signal was amplified by an amplifier with a gain of 2,000, filtered by a 5–100 Hz band-pass analog filter (DA100C, BIOPAC Systems Inc., Goleta, CA, USA). Both signals were digitized by a 12-bit data acquisition card (DAQ USB-6216, National Instruments Corporation, Austin, TX, USA) with a sampling rate of 1 KHz. The ultrasound images, EMG, and joint angle signals were simultaneously collected and stored for offline analysis using custom-developed software under the LabVIEW environment.

2.4. Image Processing. The pennation angle of the GM muscle was extracted from the ultrasound image sequence using an automatic tracking algorithm. Specifically, we enhanced the ultrasound image using Gabor filtering and then used revoting Hough transform (RVHT) to obtain the orientations of the major fascicles and took their mean as the final pennation angle. The details of the algorithm were described elsewhere [21, 23].

2.5. EMG and Angle Signals Processing. The EMG signal was segmented into 256 ms epochs. The center of each epoch was aligned in time with the corresponding ultrasound image according to the timestamp, so that the epochs were synchronized with the image sequence in the time domain. The root mean square (RMS) values of the EMG were calculated for each epoch. The angle signal was synchronized with the ultrasound images in the same way.

2.6. Statistical Analysis. For each patient, the minimum and maximum values of the joint angle and pennation angle

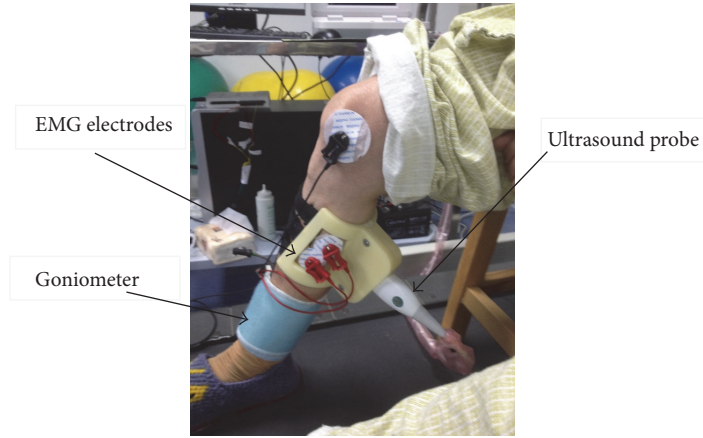


FIGURE 1: Experimental setup.

were extracted for each trial. The group means of joint angle and pennation angle were calculated for the trials of both the affected and the unaffected sides. A Kolmogorov-Smirnov (K-S) test was performed to compare the joint angle, EMG, and pennation angle between the affected side and unaffected side. To demonstrate the spatial patterning of the muscle activity, a 2-dimensional histogram based on the distributions of the joint angle and pennation angle was calculated.

For each patient, the EMG, joint angle, and pennation angle signals were manually checked by an experienced operator. The joint angle signal was used as a reference to segment the gait cycles. Eight gait cycles, in which all the three signals have no breaks, were manually selected. For each signal, the time curves in the eight gait cycles were averaged to obtain the mean time curve for each patient. Then the interindividual mean curve among the twelve patients was computed for each signal.

3. Results

Figure 2 shows the EMG and angle signals from one representative trial on the affected side. The RMS_{EMG} curve is also overlapped in the figure. One set of typical US images from the same trial is shown in Figure 3. The corresponding time course of the pennation angle, which was automatically extracted from the ultrasound image sequence, is shown in Figure 4. Figure 5 shows the scatter plots of the joint angle versus the pennation angle for a typical trial. The interindividual mean curves of gait cycle for the three signals for both affected and unaffected sides are displayed in Figure 6. For visual clarity, the standard deviation (SD) is not displayed in this figure. Instead, the average SD over each curve was calculated. For the unaffected side, the mean SD values are 5.2 degrees for joint angle, $34.4 \mu V$ for EMG, and 4.0 degrees for pennation angle. For the affected side, the mean SD values are 7.7 degrees for joint angle, $6.2 \mu V$ for EMG, and 1.8 degrees for pennation angle. The comparisons of the joint angle, pennation angle, and EMG between the affected side and the unaffected side are shown in Figure 7. For the comparisons for the minimum

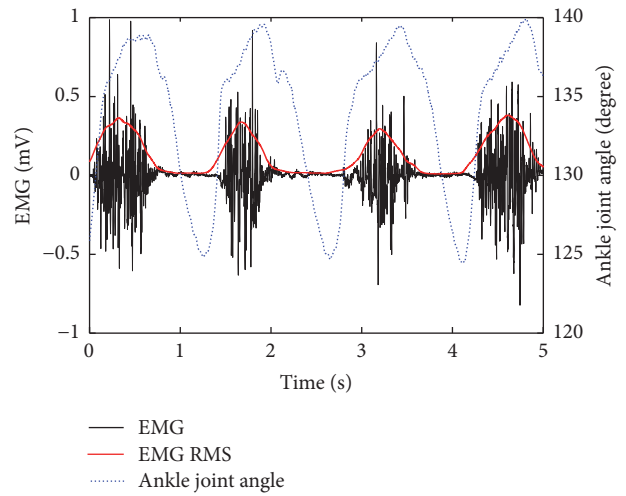


FIGURE 2: Time curves of the EMG and joint angle during a representative trial on the affected side. The RMS_{EMG} curve is overlapped onto the raw EMG curve.

values, the p values are 0.01, 0.04, and 0.63 for joint angle, EMG, and pennation angle, respectively. For the comparisons for the maximum values, the p values are 0.01, 0.03, and 0.62 for joint angle, EMG, and pennation angle, respectively.

4. Discussion

In this study, we simultaneously collected US, EMG, and joint angle signals from the GM muscle during hemiparetic gait. The purpose was to examine the contraction patterns of the lower extremity muscle activity and to compare these between the affected and unaffected sides. To the best of our knowledge, this is the first attempt to investigate continuous muscle behavior during hemiparetic gait using ultrasonography.

The conventional techniques for gait analysis are measurement of temporospatial parameters, EMG, kinematics, and kinetics. Of these techniques, kinetic variables refer

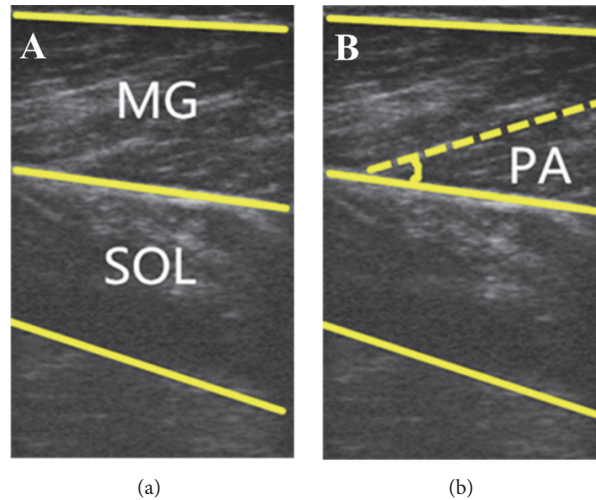


FIGURE 3: Typical ultrasound images of the medial gastrocnemius muscle during walking.

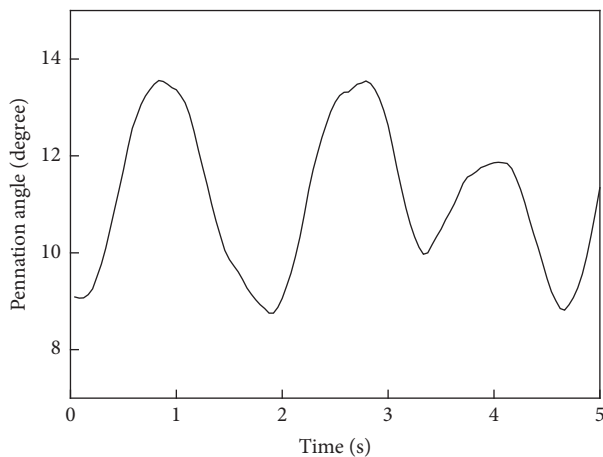


FIGURE 4: Dimensional change in the pennation angle in a typical trial on the affected side.

to moments resulting from forces generated at the joints. This information is particularly helpful in understanding and interpreting the characteristics of stroke gait because kinetic variables are the results of the kinematic and temporospatial outcomes of walking [11]. However, kinetic variables cannot be measured directly but rather are computed by inverse dynamics. In contrast, muscle functions, such as the amplitude of force production, are closely related to architectural characteristics [13]. Therefore, dynamic muscle architectural changes assessed by ultrasonography are more direct measurements than kinetic variables and have the potential to provide more information about stroke gait. Some previous studies have demonstrated that ultrasonography is helpful in measuring the effect of poststroke impairments [25, 26]. However, all the previous ultrasonography studies measured static architectural values at discrete times during contraction. Therefore, continuous muscle behavior

during hemiparetic gait has remained unclear. In this study, we developed an image tracking algorithm to automatically extract continuous changes in the pennation angle of the GM muscle, making it possible to identify muscle morphology at a higher temporal resolution.

As shown in Figure 5, the dynamic ranges of the joint angle and the pennation angle were more diffuse for the affected side than for the unaffected side. However, as shown in Figure 7 for the composite mean level, the maximum and minimum values of the pennation angle do not differ between the two sides, but those of the joint angle do. This finding was different from the previous study [29] which reported decreased pennation angle of medial gastrocnemius muscle at separate ankle joint angles. One possible reason for the difference is that our study and that study were conducted under different conditions (dynamic gait and controlled manner, respectively). Although a reasonable explanation for the relationship between the pennation angle and joint angle may involve additional neuromuscular investigations and is beyond the scope of this report which is presented from more of an engineering perspective, it is encouraging to see that the proposed method has made it possible to reveal such findings. Another advantage of the proposed method is that US signal can reveal more information about the hemiparetic pattern than the conventional EMG signal. As shown in Figure 6, the EMG curves for affected and unaffected sides have similar waveforms with significant amplitude difference. The pennation angle curves for affected and unaffected sides have relatively small amplitude difference. Instead, the two curves have significantly different timing. These findings indicate that morphological parameter extracted from ultrasonography can provide different information than that provided by EMG.

The experiment setup in this study has several shortcomings. First, though we tried to keep the probe in the same imaging plane via visual feedback from one sampling time to the next, the imaged section of the 3D muscle structure

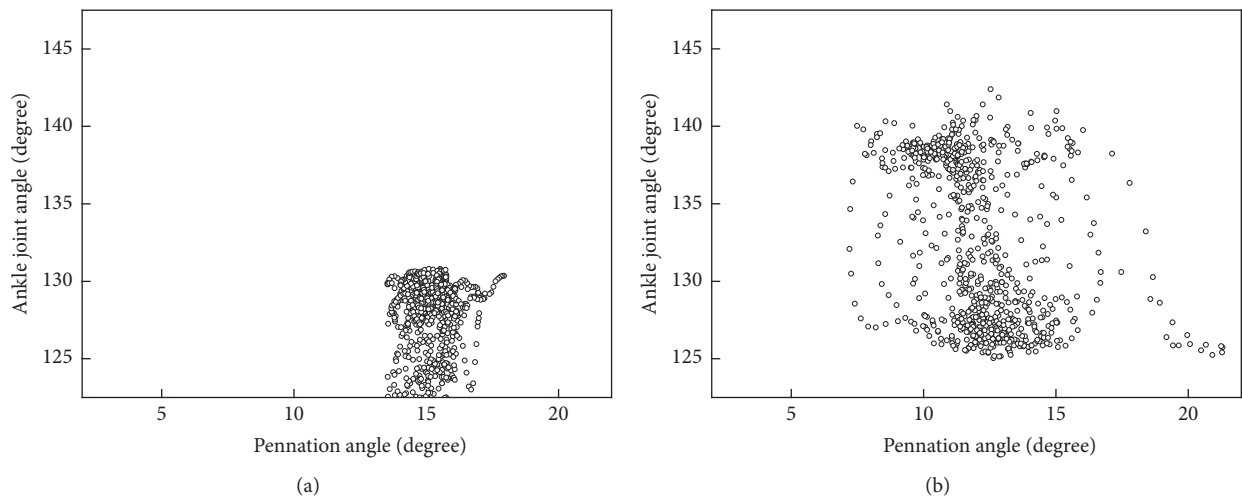


FIGURE 5: Correlations between the pennation angle and joint angle for (a) the unaffected side and (b) the affected side in a typical trial.

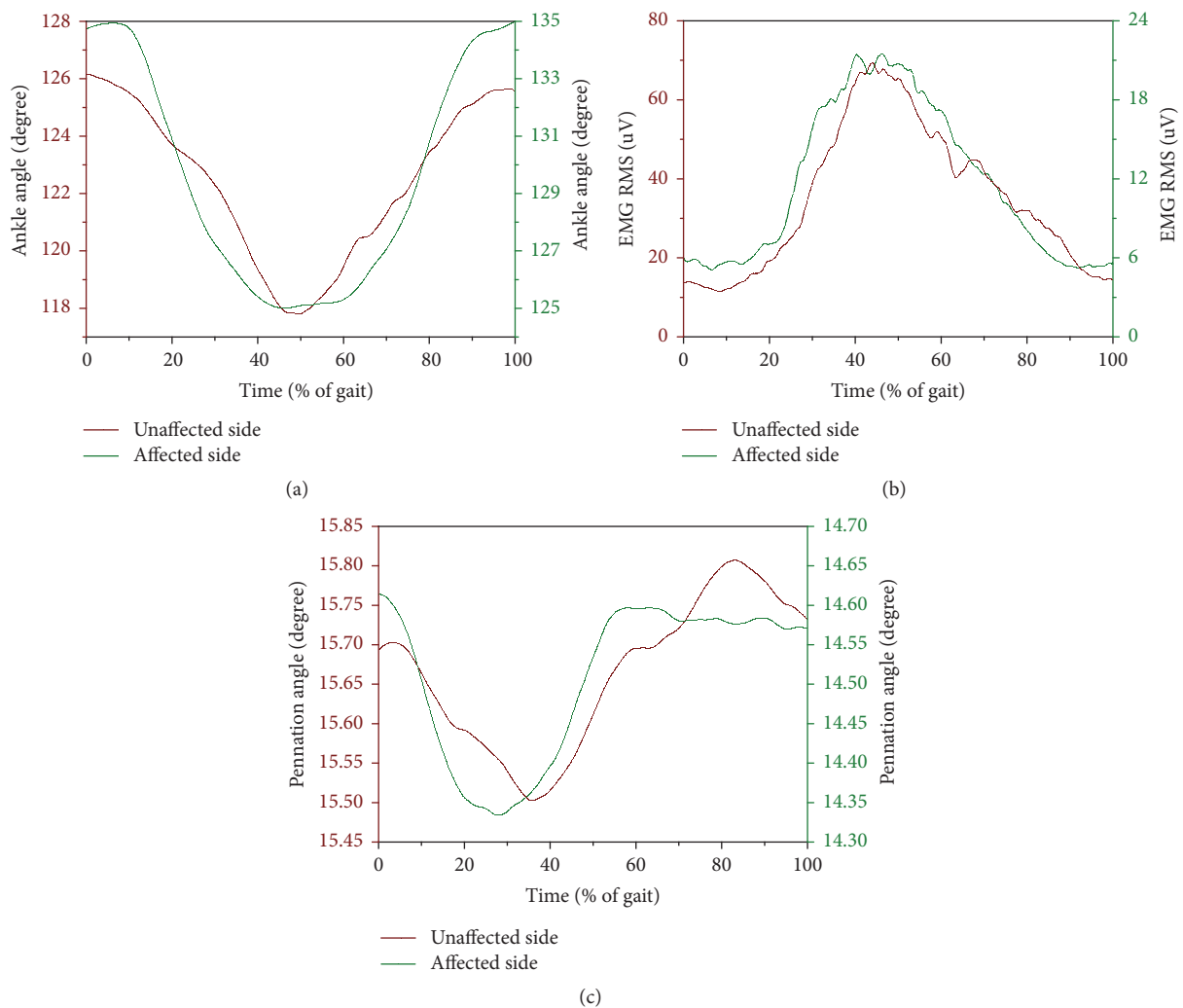


FIGURE 6: The interindividual mean curve of gait cycle among the twelve patients for (a) joint angle, (b) EMG RMS, and (c) pennation angle for both affected and unaffected sides. For visual clarity, the standard deviation (SD) is not displayed in this figure.

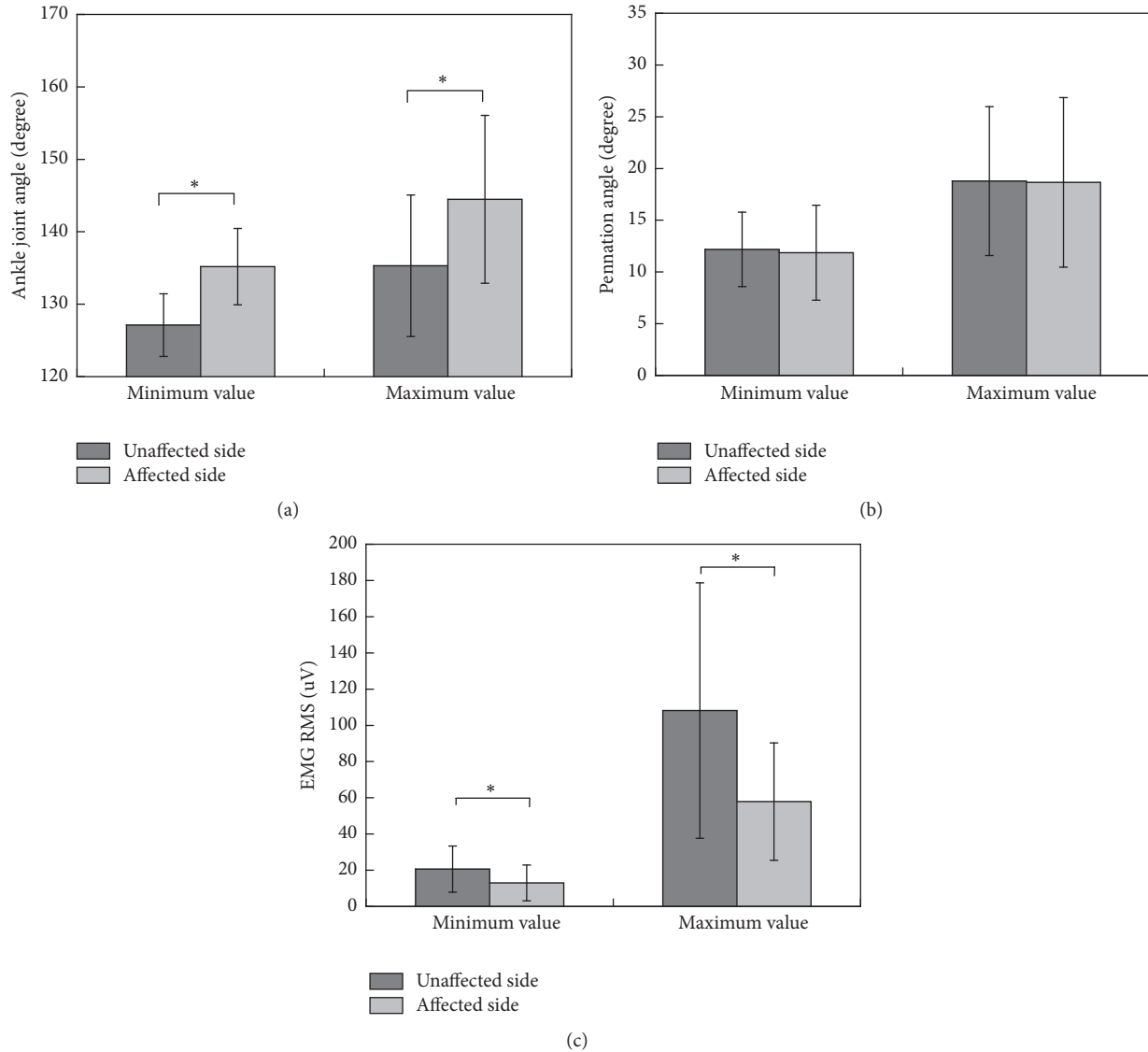


FIGURE 7: Minimum and maximum joint angle and pennation angle values for both sides during walking. An asterisk indicates that the two groups are significantly different.

was not completely consistent. Consequently, the pennation angle estimations could have included inaccurate values. In other words, it is impossible for longitudinal imaging of a muscle to adequately reflect the 3D motion of the muscle. Better imaging facilities and setup, as well as more comprehensive modeling, can help to disclose the pennation angle dynamics in ultrasound images in future studies. This problem is actually common to all current 2D US methods. Second, we did not use a fixed walking speed for all the patients. It is well known that speed has strong influences in the gait pattern, in respect to both kinematics and kinetics. However, each patient has his own adapted speed and he may not be used to another speed without training. Therefore patients walked at a self-selected speed in this study. At last, the ankle angle is conventionally defined as positive values for dorsiflexion and negative values for plantar flexion.

However, this angle is difficult to measure because it requires attachment of goniometer sensor to bottom of foot. In this study, we measured the angle between the anterior tibia and the dorsum of foot as alternative for ankle angle. The two angles are directly related and both of them can be used as reference for gait cycle.

5. Conclusion

In this study, the gaits of twelve hemiparetic patients were measured and the characteristics of their muscle behaviors were analyzed. The results suggested that morphological parameter extracted from ultrasonography can provide different information from that provided by EMG. Thus, ultrasonography can be a useful additional tool for the assessment of hemiparesis patients in clinical applications.

Competing Interests

The authors declare that they have no competing interests.

Acknowledgments

This work was supported by the National Natural Science Foundation of China (Grant nos. 81000637, 81471735, 81572233, and 61640018) and National Science & Technology Pillar Program (2015BAI01B02). The authors thank Rhoda E. and Edmund F. Perozzi for assistance with English and content editing.

References

- [1] M. Rijntjes, "Mechanisms of recovery in stroke patients with hemiparesis or aphasia: new insights, old questions and the meaning of therapies," *Current Opinion in Neurology*, vol. 19, no. 1, pp. 76–83, 2006.
- [2] A. Lamontagne, J. L. Stephenson, and J. Fung, "Physiological evaluation of gait disturbances post stroke," *Clinical Neurophysiology*, vol. 118, no. 4, pp. 717–729, 2007.
- [3] P. A. Goldie, T. A. Matyas, and O. M. Evans, "Gait after stroke: initial deficit and changes in temporal patterns for each gait phase," *Archives of Physical Medicine and Rehabilitation*, vol. 82, no. 8, pp. 1057–1065, 2001.
- [4] C. K. Balasubramanian, M. G. Bowden, R. R. Neptune, and S. A. Kautz, "Relationship between step length asymmetry and walking performance in subjects with chronic hemiparesis," *Archives of Physical Medicine and Rehabilitation*, vol. 88, no. 1, pp. 43–49, 2007.
- [5] C. Frigo and P. Crenna, "Multichannel SEMG in clinical gait analysis: a review and state-of-the-art," *Clinical Biomechanics*, vol. 24, no. 3, pp. 236–245, 2009.
- [6] C. M. Kim and J. J. Eng, "Magnitude and pattern of 3D kinematic and kinetic gait profiles in persons with stroke: relationship to walking speed," *Gait & Posture*, vol. 20, no. 2, pp. 140–146, 2004.
- [7] L. Bensoussan, S. Mesure, J.-M. Viton, and A. Delarque, "Kinematic and kinetic asymmetries in hemiplegic patients' gait initiation patterns," *Journal of Rehabilitation Medicine*, vol. 38, no. 5, pp. 287–294, 2006.
- [8] D. C. Kerrigan, M. E. Karvosky, and P. O. Riley, "Spastic paretic stiff-legged gait: joint kinetics," *American Journal of Physical Medicine & Rehabilitation*, vol. 80, no. 4, pp. 244–249, 2001.
- [9] N. S. Ward, M. M. Brown, A. J. Thompson, and R. S. J. Frackowiak, "Neural correlates of motor recovery after stroke: a longitudinal fMRI study," *Brain*, vol. 126, no. 11, pp. 2476–2496, 2003.
- [10] F. Chollet, V. Dipiero, R. J. S. Wise, D. J. Brooks, R. J. Dolan, and R. S. J. Frackowiak, "The functional anatomy of motor recovery after stroke in humans: a study with positron emission tomography," *Annals of Neurology*, vol. 29, no. 1, pp. 63–71, 1991.
- [11] S. J. Olney and C. Richards, "Hemiparetic gait following stroke. Part I: characteristics," *Gait & Posture*, vol. 4, no. 2, pp. 136–148, 1996.
- [12] B. Balaban and F. Tok, "Gait disturbances in patients with stroke," *PM&R*, vol. 6, no. 7, pp. 635–642, 2014.
- [13] R. L. Lieber and J. Fridén, "Functional and clinical significance of skeletal muscle architecture," *Muscle and Nerve*, vol. 23, no. 11, pp. 1647–1666, 2000.
- [14] J. Shi, Y.-P. Zheng, Q.-H. Huang, and X. Chen, "Continuous monitoring of sonomyography, electromyography and torque generated by normal upper arm muscles during isometric contraction: sonomyography assessment for arm muscles," *IEEE Transactions on Biomedical Engineering*, vol. 55, no. 3, pp. 1191–1198, 2008.
- [15] S. Delaney, P. Worsley, M. Warner, M. Taylor, and M. Stokes, "Assessing contractile ability of the quadriceps muscle using ultrasound imaging," *Muscle & Nerve*, vol. 42, no. 4, pp. 530–538, 2010.
- [16] X. Chen, Y.-P. Zheng, J.-Y. Guo, Z. Zhu, S.-C. Chan, and Z. Zhang, "Sonomyographic responses during voluntary isometric ramp contraction of the human rectus femoris muscle," *European Journal of Applied Physiology*, vol. 112, no. 7, pp. 2603–2614, 2012.
- [17] C. K. English, K. A. Thoirs, L. Fisher, H. McLennan, and J. Bernhardt, "Ultrasound is a reliable measure of muscle thickness in acute stroke patients, for some, but not all anatomical sites: a study of the intra-rater reliability of muscle thickness measures in acute stroke patients," *Ultrasound in Medicine and Biology*, vol. 38, no. 3, pp. 368–376, 2012.
- [18] J. Li, Y. Zhou, Y. Lu, G. Zhou, L. Wang, and Y.-P. Zheng, "The sensitive and efficient detection of quadriceps muscle thickness changes in cross-sectional plane using ultrasonography: a feasibility investigation," *IEEE Journal of Biomedical and Health Informatics*, vol. 18, no. 2, pp. 628–635, 2014.
- [19] N. J. Cronin, C. P. Carty, R. S. Barrett, and G. Lichtwark, "Automatic tracking of medial gastrocnemius fascicle length during human locomotion," *Journal of Applied Physiology*, vol. 111, no. 5, pp. 1491–1496, 2011.
- [20] L. K. Kwah, R. Z. Pinto, J. Diong, and R. D. Herbert, "Reliability and validity of ultrasound measurements of muscle fascicle length and pennation in humans: a systematic review," *Journal of Applied Physiology*, vol. 114, no. 6, pp. 761–769, 2013.
- [21] Y. Zhou and Y.-P. Zheng, "Estimation of muscle fiber orientation in ultrasound images using revolving Hough transform (RVHT)," *Ultrasound in Medicine and Biology*, vol. 34, no. 9, pp. 1474–1481, 2008.
- [22] H. Zhao and L.-Q. Zhang, "Automatic tracking of muscle fascicles in ultrasound images using localized radon transform," *IEEE Transactions on Biomedical Engineering*, vol. 58, no. 7, pp. 2094–2101, 2011.
- [23] Y. Zhou and Y.-P. Zheng, "Longitudinal enhancement of the hyperechoic regions in ultrasonography of muscles using a gabor filter bank approach: a preparation for semi-automatic muscle fiber orientation estimation," *Ultrasound in Medicine and Biology*, vol. 37, no. 4, pp. 665–673, 2011.
- [24] J. Darby, B. Li, N. Costen, I. Loram, and E. Hodson-Tole, "Estimating skeletal muscle fascicle curvature from B-mode ultrasound image sequences," *IEEE Transactions on Biomedical Engineering*, vol. 60, no. 7, pp. 1935–1945, 2013.
- [25] F. Gao and L.-Q. Zhang, "Altered contractile properties of the gastrocnemius muscle poststroke," *Journal of Applied Physiology*, vol. 105, no. 6, pp. 1802–1808, 2008.
- [26] L. Li, K. Y. Tong, and X. Hu, "The effect of poststroke impairments on brachialis muscle architecture as measured by ultrasound," *Archives of Physical Medicine and Rehabilitation*, vol. 88, no. 2, pp. 243–250, 2007.
- [27] M. Ishikawa, P. V. Komi, M. J. Grey, V. Lepola, and G.-P. Bruggemann, "Muscle-tendon interaction and elastic energy usage in human walking," *Journal of Applied Physiology*, vol. 99, no. 2, pp. 603–608, 2005.

- [28] M. Ishikawa, J. Pakaslahti, and P. V. Komi, "Medial gastrocnemius muscle behavior during human running and walking," *Gait & Posture*, vol. 25, no. 3, pp. 380–384, 2007.
- [29] F. Gao, T. H. Grant, E. J. Roth, and L.-Q. Zhang, "Changes in passive mechanical properties of the gastrocnemius muscle at the muscle fascicle and joint levels in stroke survivors," *Archives of Physical Medicine and Rehabilitation*, vol. 90, no. 5, pp. 819–826, 2009.

Research Article

Early Detection of Tibial Cartilage Degradation and Cancellous Bone Loss in an Ovariectomized Rat Model

Yinong Wang,¹ Zhiwei Liu,¹ Qing Wang,^{1,2} Qianjin Feng,^{1,2} and Wufan Chen^{1,2}

¹*Institute of Medical Information, School of Biomedical Engineering, Southern Medical University, Guangzhou 510515, China*

²*Guangdong Provincial Key Laboratory of Medical Image Processing, Southern Medical University, Guangzhou 510515, China*

Correspondence should be addressed to Qing Wang; wq8740@smu.edu.cn

Received 17 August 2016; Accepted 18 December 2016; Published 15 January 2017

Academic Editor: Magali Cucchiarini

Copyright © 2017 Yinong Wang et al. This is an open access article distributed under the Creative Commons Attribution License, which permits unrestricted use, distribution, and reproduction in any medium, provided the original work is properly cited.

This study aimed to investigate degradation of the articular cartilage and loss of the cancellous bone in an ovariectomized (OVX) rat model simulating early human menopausal stage. Fourteen health female Sprague-Dawley rats were randomly divided into two groups ($n = 7$ per group): an OVX group that underwent bilateral ovariectomy to create an OVX model with low estrogen levels and a sham group in which only the periovarian fatty tissue was exteriorized. All the animals were sacrificed at 3 weeks after ovariectomy. The left tibiae were harvested. The articular cartilage at medial tibial plateau (MTP) and lateral tibial plateau (LTP) was assessed with quantitative high-frequency ultrasound. The cancellous bone was evaluated with micro-CT. The results indicated that, in comparison with the sham rats, the OVX rats exhibited significant alterations in acoustic parameters of the articular cartilage but insignificant changes in microarchitectural parameters of the cancellous bone in early stage of low estrogen levels. The results of this study suggest that cartilage degradation induced by estrogen reduction was detected earlier with quantitative ultrasound than that of the cancellous bone loss in 3 wk OVX rats.

1. Introduction

Osteoporosis (OP) and osteoarthritis (OA) are severe progressive diseases with high prevalence in the elderly and affect both men and women. However, the incidence of OP and OA increases in menopausal women. Main consequence of OP is the increased risk of bone fractures due to abnormalities in amount and microarchitectural arrangement of bone tissue. OA, on the other hand, causes pain and disability of one or many synovial joints resulted from progressive degradation of the articular cartilage with alterations in the bone and surrounding structures. These two diseases play a negative role in the longevity and health of menopausal women.

Both the bone and articular cartilage are the target tissues of estrogens. It has been found that estrogen receptors (ER) such as ER α and ER β exist in osteoclasts, osteoblasts, and articular chondrocytes [1–3]. Estrogen deficiency exacerbates bone resorption exceeding bone formation resulting in menopausal OP [4–6]. The low estrogen level induces a faster loss of knee joint cartilage in menopausal women than in men

of the same age [7]. The degradation of articular cartilage is one of indications of the early OA and can trigger the occurrence of menopausal OA [8].

Therefore, the menopause-related changes in estrogen levels affect generation of both bone and articular cartilage and thus induce the pathogenesis of OP and OA. Due to their high prevalence in elderly women, it could be anticipated that OP and OA coexist frequently. However, a defined relationship between OP and OA has not yet clearly delineated. There are conflicting findings. Some studies reported that OA was associated with higher bone mineral density (BMD), that is, an inverse relationship between OA and OP [9–11]. Some studies suggested a positive association between OP and OA that bone loss occurred with cartilage loss in OA patients [12, 13]. One study interestingly found that both high and low BMD conditions could induce OA [14]. Others did not find a relation between cartilage degradation and bone loss [15].

Furthermore, the occurrence of OA and OP is found to be of site-relevance [9]. However, the clearly defined site-relationship between OA and OP is still debatable. Okano

et al. found that end-stage hip OA induced lower BMD in the calcaneus but higher BMD in the spine and radius [16]. Lethbridge-Çejku et al. reported that knee OA patients had higher BMD in spine but not in hip [17], while Multanen et al. suggested that knee OA menopausal women had higher hip bone strength [11]. Therefore, more investigations are needed to delineate associations between cartilage degradation and bone loss at different anatomic locations.

To effectively evaluate BMD, dual-energy X-ray absorptiometry (DXA) has been widely used [10, 11, 16]. DXA, however, provides little information of bone structure. Micro-computed tomography (micro-CT), a high resolution imaging tool, is used in quantitative assessments of osteoporotic alterations and therapeutic improvements in microarchitectural characteristics of the trabecular and cortical bone in the OP animal model [18–20]. Quantitative ultrasound, on the other hand, is used to characterize the degeneration of articular cartilage [21–23].

Therefore, the present study focused on menopausal alterations in the bone and articular cartilage in the tibia. We applied bilateral ovariectomy to create an OVX rat model with low estrogen levels and then assessed early-stage alterations in the bone and articular cartilage with micro-CT and quantitative ultrasound.

2. Materials and Methods

2.1. Animal Care and Experimental Protocol. Fourteen female Sprague-Dawley rats, aged 10 months old and weighting 299.1 to 383.8 g, were used in this study. They were purchased from Guangdong Medical Laboratory Animal Center, China, and individually kept in metal cages under 12-hour light-dark cycle with standard rat diet and water ad libitum. The animals were randomly divided into two groups ($n = 7$ per group): an OVX group that underwent bilateral ovariectomy to create an OVX model with low estrogen levels and a sham group in which only the periovarian fatty tissue was exteriorized. After ovariectomy, the animals were returned to their cages and fed according to the aforementioned feeding protocol. Before conducting the experiments, ethical approval of this study (SYXK[Yue]2008-0002) was obtained from the Animal Experimental Ethical Inspection Committee of Guangdong Medical Laboratory Animal Center, China. Experiments on rats were performed in accordance with the Guidelines for the Care of Laboratory Animals of the National Institutes of Health.

All animals, weighting 309.9 to 423.3 g, were euthanized with an overdose of sodium pentobarbital (P3761, Sigma, USA) 3 weeks after ovariectomy. The left tibias were excised, harvested, and stored at -20°C until the ultrasound examination.

2.2. Ultrasound Examinations. Before ultrasound scanning, the tibial sample to be measured was thawed in a saline solution for 2 hours. Then, the specimen was vertically fixed with a clamp and immersed in saline in the container. A square region of $0.3\text{ mm} \times 0.3\text{ mm}$ on the top surface of

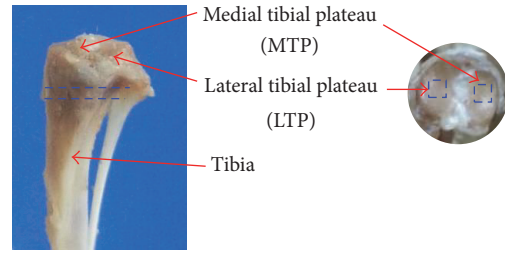


FIGURE 1: Schematic of the areas scanned by ultrasound biomicroscopy (two blue dotted squares $0.3\text{ mm} \times 0.3\text{ mm}$ on the medial and lateral tibial plateaus) and micro-CT (two blue dotted lines presenting the volume of interest of the tibial metaphysis, approximately 0.1 mm in thickness).

cartilage tissue from the medial tibial plateau (MTP) and lateral tibial plateau (LTP) was, respectively, selected as region of interest (ROI) (Figure 1) and perpendicularly placed to the ultrasound beam.

The ultrasound system was comprised of an ultrasound pulser/receiver (Olympus 5900 PR, Panametrics-NDT, Waltham, MA, USA), a 50 MHz transducer (Olympus, PI50-2-R0.75, Panametrics-NDT), and a computer with a 12-bit A/D acquisition card (CompuScope 12400, Gage, ON, Canada). The ultrasound scanning over ROI was controlled by custom-developed software to move the transducer with a 3D translating stage (ETSN400, Tian-Rui-Zhong-Hai Instrument, Beijing, China). After the transducer was properly positioned approximately 1 cm above the cartilage tissue, the ultrasound examination started. The ultrasound radiofrequency (RF) signals were saved for offline parameter extraction.

Four parameters were then automatically extracted from ultrasound RF signals processed using a self-developed MATLAB program (The MathWorks, Natick, MA, USA): ultrasound roughness index (URI) of the cartilage surface, reflection coefficient of the cartilage surface (RC_1), reflection coefficient of the cartilage-subchondral bone interface (RC_2), and the thickness (h) of the cartilage tissue. These parameters were defined by (1)–(4), respectively.

$$URI = \sqrt{\frac{1}{m} \sum_{i=1}^m (d_i - \bar{d})^2} \quad (1)$$

$$RC_1 = \frac{1}{m} \sum_{i=1}^m \frac{A_i}{A_{\text{ref}}} \times 100\% \quad (2)$$

$$RC_2 = \frac{1}{m} \sum_{j=1}^m \frac{A_j}{A_{\text{ref}}} \times 100\% \quad (3)$$

$$h = \frac{1}{m} \sum_{i=1}^m \left(C_{\text{cartilage}} \times \frac{\text{TOF}_i}{2} \right). \quad (4)$$

In these equations, m is the total number of the sampling lines that is equal to 100 in this study. In (1), d_i represents the distance from the transducer surface to the cartilage surface in the sampling line i and \bar{d} is the mean of d_i . In (2) and (3), A_i , A_j , and A_{ref} , respectively, represent the peak-to-peak amplitude of the echoes from the cartilage surface in the sampling line i , from the cartilage-bone interface in sampling line j , and from a perfect reflector. In (4), TOF_i is the time-of-flight from the cartilage surface to the cartilage-bone interface in the sampling line i , and $C_{cartilage}$ is the average sound speed (equal to 1675 m/s) in the cartilage.

2.3. Micro-CT Measurements. After ultrasound examinations, the tibial samples were fixed in 4% paraformaldehyde solution for more than 72 hours. Then, 3D microarchitecture of the cancellous bone was assessed using a micro-CT system (μ CT80, Scanco Medical, AG, Switzerland) with energy settings of 55 kV and 145 μ A. The proximal tibial metaphysis was scanned starting at approximately 1 mm distal to the growth plate (Figure 1). A total of 100 consecutive tomographic CT slices were taken from proximal to distal with thickness of 0.01 mm per slice.

In order to analyze the cancellous part of the tibial metaphysis, the trabecular area was contoured manually slice by slice. Then, the trabecular volume of interest (VOI) of the tibial metaphysis was reconstructed by a reconstruction software (Scanco Medical, AG, Switzerland). The micro-CT analysis was performed, giving an isotropic voxel size of 12 μ m. Trabecular number (Tb.N), trabecular thickness (Tb.Th), trabecular separation/spacing (Tb.Sp), connectivity density (Conn.D.), and structure model index (SMI) were extracted to characterize the trabecular microarchitecture of the cancellous bone in menopausal rats. Moreover, BV/TV, which stands for mineralized bone volume over total volume of the given VOI, was used to evaluate relative changes in bone volume density.

2.4. Statistical Analysis. Statistical analyses were performed with SPSS Statistics (Version 20, IBM, Armonk, NY, USA). All values in the text were presented as mean \pm standard deviation (SD). The statistical differences in the acoustic parameters and the micro-CT parameters between the OVX and sham groups were analyzed using Mann-Whitney U test. Significant differences were accepted with $p \leq 0.05$.

3. Results

3.1. Results of Ultrasound Examinations. From the results of ultrasound examination of the articular cartilage at MTP (Figure 2), we found significant alterations in the surface cartilage tissue in the OVX group. In comparison with the sham group, RC_1 of the OVX group significantly decreased ($p < 0.01$). URI of the OVX group significantly increased ($p < 0.05$) indicating that the surface of articular cartilage became rougher in the early-stage of low estrogen levels. Furthermore, the cartilage thickness in the OVX rats significantly decreased ($p < 0.05$). However, no significant alteration ($p >$

0.05) was found in RC_2 , which is related to the property of the cartilage-subchondral bone interface.

Similar to the findings of MTP, significant alterations in the surface cartilage tissue at LTP were observed in the OVX group compared with the sham group (Figure 3). The significant changes in URI ($p = 0.05$) and cartilage thickness ($p < 0.01$) were observed in the OVX group. However, no significant changes ($p > 0.05$) in RC_1 and RC_2 were found in the OVX group compared with the sham group.

3.2. Results of Micro-CT Scanning. The 3D reconstruction of the trabecular bone structures in the proximal tibial metaphysis by micro-CT is shown in Figures 4(a) and 4(b). The remarkable change of cancellous bone was not observed between the sham and OVX rats, although some of the connecting rods were missed in the OVX group.

The results of quantitative micro-CT assessment indicate no statistical difference ($p > 0.05$) in bone microarchitectural parameters between the OVX and sham groups (Figures 4(c)–4(h)).

4. Discussion

This study focused on the knee joint, especially the tibia, and applied micro-CT and quantitative ultrasound to evaluate alterations in the bone and articular cartilage in an OVX rat model. The primary finding of this study was that significant changes in acoustic parameters of articular cartilage were detected in the rats with ovariectomy, whereas there were insignificant changes in microarchitecture of the cancellous bone. These results indicated that although both articular cartilage and bone are target tissues of estrogens, the degradation of the articular cartilage induced by estrogen deficiency occurred earlier and its characterizations could be detected by quantitative ultrasound. This study provides evidence to previous study suggesting that cartilage degradation might occur in an early stage of low estrogen levels [24].

The cartilage results of this study are similar to those of previous study showing that disuse-induced significant changes in the cartilage tissue [25]. However, disuse simultaneously induced cartilage degradation and bone loss [26]. This may be due to the fact that the articular cartilage and bone are subjected to high loads under gravitation force during daily walking, running, and jumping. Loading is important for keeping knees healthy. Therefore, the two tissues are sensitive to disuse or unloading. Although previous studies reported that estrogens affect the synthesis of both articular cartilage and cancellous bone through the receptor activator nuclear factor-kappa B ligand (RANKL) signaling pathway [27, 28], the present study suggested a rapid response of the articular cartilage to estrogen deficiency.

The definite relationship between OP and OA still expected more efforts. Herrero-Beaumont et al. reported that both high and low BMD conditions might initiate cartilage degradation in OA [14]. In this study, no significant alterations in the cancellous bone in the 3 wk OVX rats were found, whereas cartilage degradation was shown. Furthermore, a tendency of deterioration in the trabecular

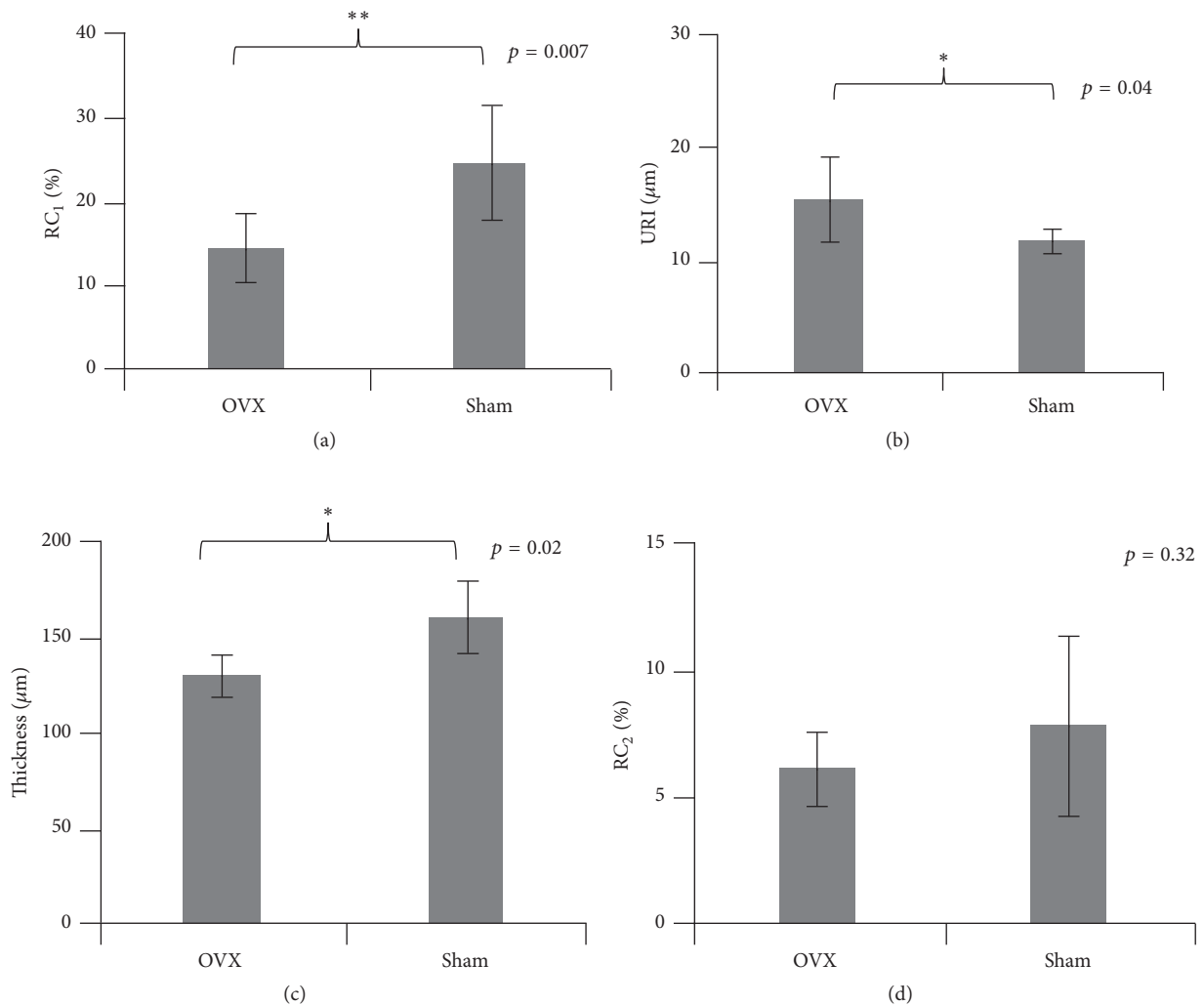


FIGURE 2: Comparisons of ultrasound results measured at medial tibial plateau (MTP) between the OVX and sham groups. (a) Reflection coefficient (RC₁) of the cartilage surface; (b) ultrasound roughness index (URI); (c) cartilage thickness (h); and (d) reflection coefficient (RC₂) of the cartilage-bone interface. *Statistically significant difference at level $p < 0.05$ exists between OVX group and sham group. **Statistically significant difference at level $p < 0.01$ exists between OVX group and sham group.

bone was shown in Figure 4, which is consistent with the findings (a decrease in BV/TV and Tb.N with an increase in Tb.Sp and SMI) of previous studies discovered in the 4 wk OVX rats [29], 6 wk OVX rats [30], and 12 wk OVX rats [19]. Brouwers et al. [31], however, showed significant deterioration in BV/TV, Tb.N, and Tb.Th in the 1 wk OVX rats. One possible cause of this divergence might be different ages, weight, and species of the investigated animals. 10-month-old Sprague-Dawley rats used in this study were in an old stage similar to the 50–60-year-old women, whereas 5.5-month rats were young adult rats. The findings of previous studies and this study implicate that the sudden estrogen deficiency after ovariectomy may have dissimilar significant effect on bone structure in the elderly rats to that in adult rats.

The present study has some limitations. Firstly, this study was limited in the detection of OP and OA occurred at the proximal tibia. Because OP and OA may occur at different joints and mechanisms of OP and OA are complex, the findings of previous studies are debatable, indicating that a defined relationship between OP and OA has not yet clearly delineated so far. Therefore, this study preliminarily focused on the tibia in the knee joint finding that the early effect of estrogen deficiency on the articular cartilage was faster detected using quantitative ultrasound than that on the cancellous bone detected using micro-CT. Secondly, in consideration of the relatively small sample size of each experimental group, nonparametric analyses were used in this study to reduce some impacts on the statistical results. In future, further studies with more samples are expected on the basis

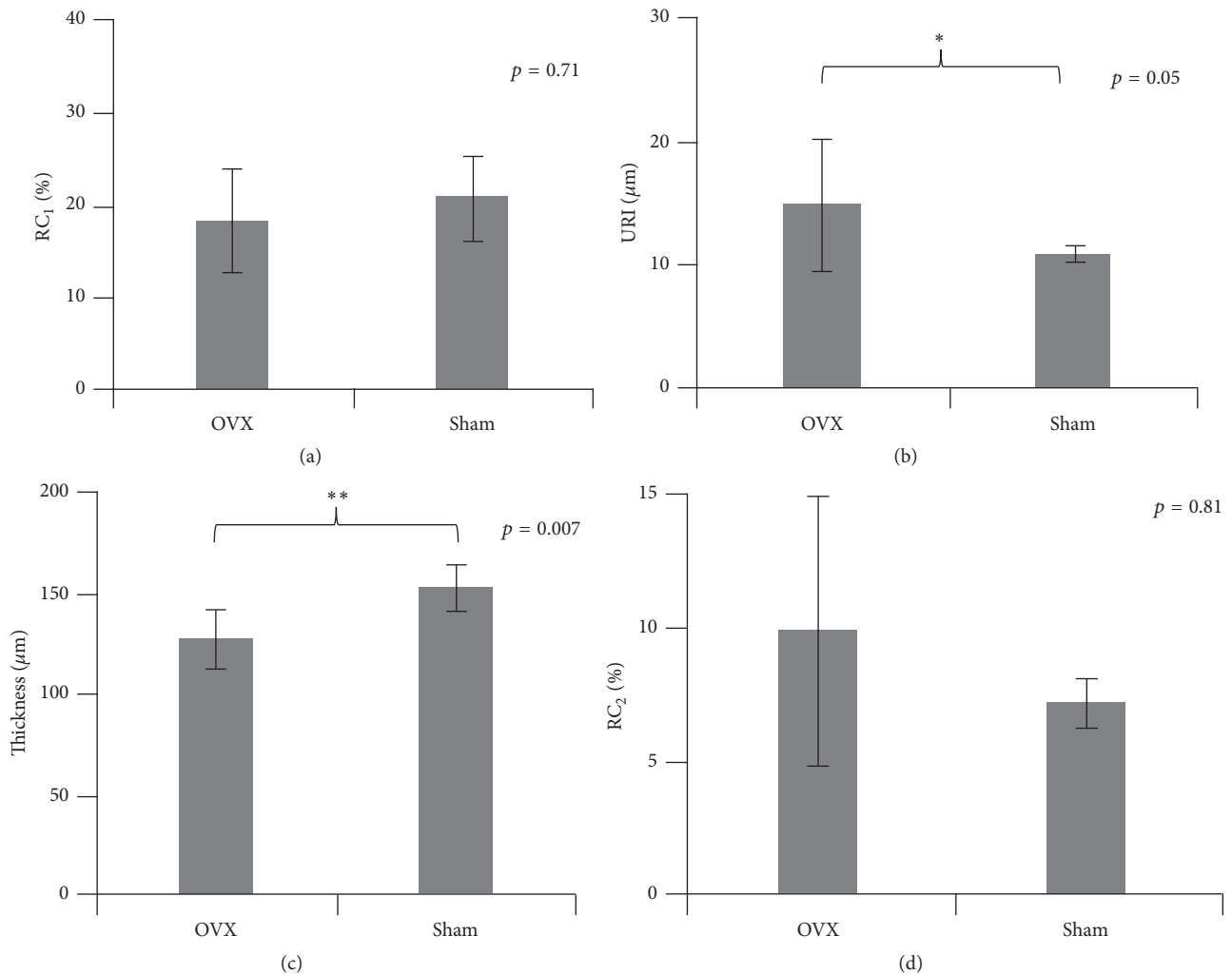


FIGURE 3: Comparisons of ultrasound results measured at lateral tibial plateau (LTP) between the OVX and sham groups. (a) Reflection coefficient (RC_1) of the cartilage surface; (b) ultrasound roughness index (URI); (c) cartilage thickness (h); and (d) reflection coefficient (RC_2) of the cartilage-bone interface. *Statistically significant difference at level $p < 0.05$ exists between OVX group and sham group. **Statistically significant difference at level $p < 0.01$ exists between OVX group and sham group.

of the preliminary result of this study. The other limitation of this study is one time point. In the light of previous studies showing that the bone loss occurred in a relative late-stage (4 weeks after the ovariectomy operation) [19, 29, 30], this study aimed to detect the early alterations in tibial cartilage and cancellous bone 3 weeks after ovariectomy operation. However, according to our results, changes in the cartilage tissue at more time points such as 1 week or 2 weeks after ovariectomy are needed to be determined in future by quantitative ultrasound during the progression of menopause.

In conclusion, this study demonstrated that degradation of articular cartilage was detected earlier with quantitative ultrasound than that of the cancellous bone in 3 wk OVX rats. These results have implications that deterioration of the cartilage tissue after estrogen deficiency developed faster than cancellous bone. However, due to inconsistent findings of OP and OA, further studies are expected.

Competing Interests

The authors have declared that no competing interests exist.

Authors' Contributions

Qing Wang and Wufan Chen conceived and designed the experiments. Yinong Wang and Zhiwei Liu performed the experiments. Yinong Wang, Zhiwei Liu, and Qing Wang analyzed the data. Qing Wang, Qianjin Feng, and Wufan Chen contributed reagents/materials/analysis tools. Yinong Wang and Qing Wang Contributed to the writing of the manuscript.

Acknowledgments

This work was supported by National Natural Science Funds of China (no. 81371560), Special Fund for Talent Introduction

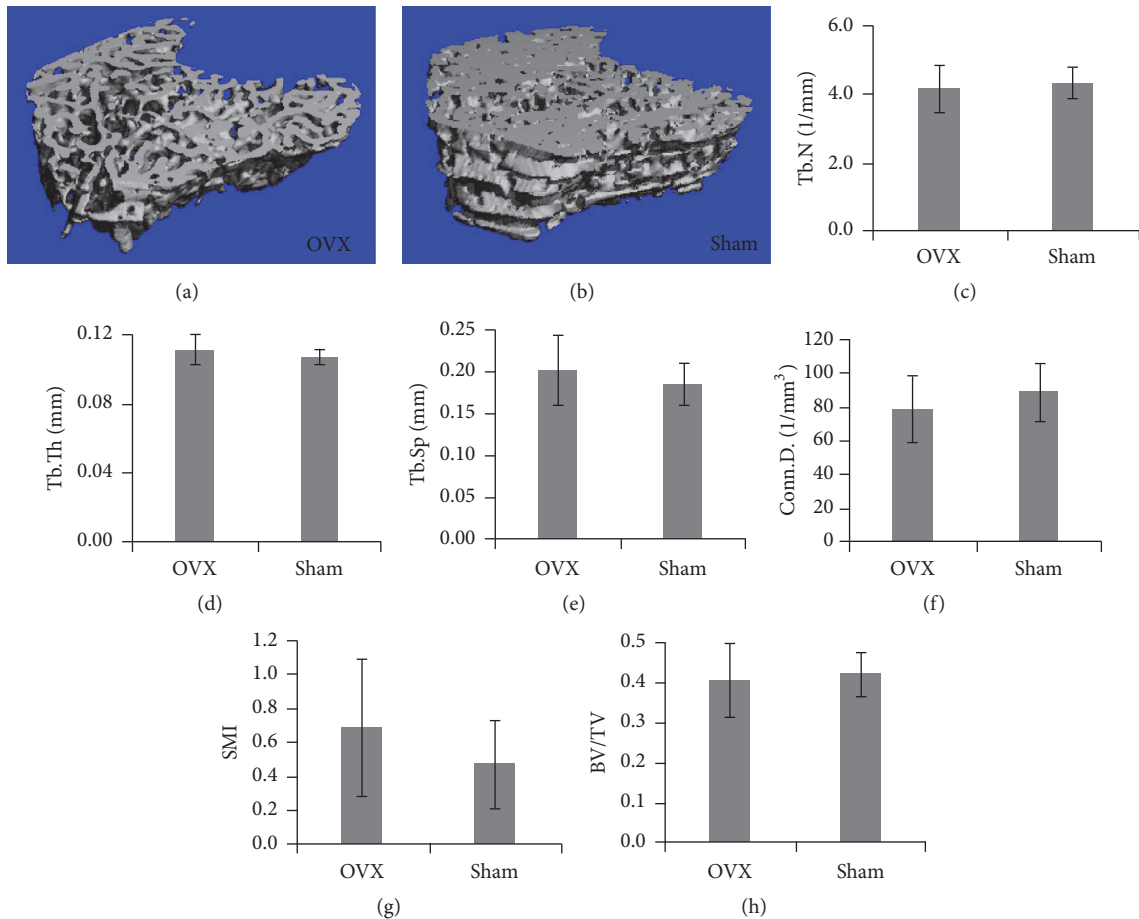


FIGURE 4: Comparisons of micro-CT results measured at the cancellous bone between the OVX and sham groups. (a) 3D reconstruction of the trabecular bone of the OVX group; (b) 3D reconstruction of the trabecular bone of the sham group; (c) Tb.N; (d) Tb.Th; (e) Tb.Sp; (f) Conn.D.; (g) SMI; (h) BV/TV.

in Guangdong Universities (no. 2050205), Guangdong Provincial Natural Science Funds (no. 2014A030313329), and Guangdong Provincial Technological Funds (no. 2013B021800039).

References

- [1] I. P. Braidman, L. Hainey, G. Batra, P. L. Selby, P. T. K. Saunders, and J. A. Hoyland, "Localization of estrogen receptor β protein expression in adult human bone," *Journal of Bone and Mineral Research*, vol. 16, no. 2, pp. 214–220, 2001.
- [2] S. H. Windahl, M. K. Lagerquist, N. Andersson et al., "Identification of target cells for the genomic effects of estrogens in bone," *Endocrinology*, vol. 148, no. 12, pp. 5688–5695, 2007.
- [3] T. Ushiyama, H. Ueyama, K. Inoue, I. Ohkubo, and S. Hukuda, "Expression of genes for estrogen receptors α and β in human articular chondrocytes," *Osteoarthritis and Cartilage*, vol. 7, no. 6, pp. 560–566, 1999.
- [4] M. Martin-Millan, M. Almeida, E. Ambrogini et al., "The estrogen receptor-alpha in osteoclasts mediates the protective effects of estrogens on cancellous but not cortical bone," *Molecular Endocrinology*, vol. 24, no. 2, pp. 323–334, 2010.
- [5] K. M. Melville, N. H. Kelly, S. A. Khan et al., "Female mice lacking estrogen receptor-alpha in osteoblasts have compromised bone mass and strength," *Journal of Bone and Mineral Research*, vol. 29, no. 2, pp. 370–379, 2014.
- [6] S. Khosla, M. J. Oursler, and D. G. Monroe, "Estrogen and the skeleton," *Trends in Endocrinology and Metabolism*, vol. 23, no. 11, pp. 576–581, 2012.
- [7] F. S. Hanna, A. J. Teichtahl, A. E. Wluka et al., "Women have increased rates of cartilage loss and progression of cartilage defects at the knee than men: a gender study of adults without clinical knee osteoarthritis," *Menopause*, vol. 16, no. 4, pp. 666–670, 2009.
- [8] P. Høegh-Andersen, L. B. Tankó, T. L. Andersen et al., "Ovariectomized rats as a model of postmenopausal osteoarthritis: validation and application," *Arthritis research & therapy*, vol. 6, no. 2, pp. R169–R180, 2004.
- [9] D. Avci and G. A. Bachmann, "Osteoarthritis and osteoporosis in postmenopausal women: clinical similarities and differences," *Menopause*, vol. 11, no. 6, part 1, pp. 615–621, 2004.
- [10] L. Ichchou, F. Allali, S. Rostom et al., "Relationship between spine osteoarthritis, bone mineral density and bone turn over markers in post menopausal women," *BMC Women's Health*, vol. 10, article no. 25, 2010.

- [11] J. Multanen, A. Heinonen, A. Häkkinen et al., "Bone and cartilage characteristics in postmenopausal women with mild knee radiographic osteoarthritis and those without radiographic osteoarthritis," *Journal of Musculoskeletal Neuronal Interactions*, vol. 15, no. 1, pp. 69–77, 2015.
- [12] E. Calvo, S. Castañeda, R. Largo, M. E. Fernández-Valle, F. Rodríguez-Salvanés, and G. Herrero-Beaumont, "Osteoporosis increases the severity of cartilage damage in an experimental model of osteoarthritis in rabbits," *Osteoarthritis and Cartilage*, vol. 15, no. 1, pp. 69–77, 2007.
- [13] J. Y. Lee, W. F. Harvey, L. L. Price, J. K. Paulus, B. Dawson-Hughes, and T. E. McAlindon, "Relationship of bone mineral density to progression of knee osteoarthritis," *Arthritis and Rheumatism*, vol. 65, no. 6, pp. 1541–1546, 2013.
- [14] G. Herrero-Beaumont, J. A. Roman-Blas, R. Largo, F. Berenbaum, and S. Castañeda, "Bone mineral density and joint cartilage: four clinical settings of a complex relationship in osteoarthritis," *Annals of the Rheumatic Diseases*, vol. 70, no. 9, pp. 1523–1525, 2011.
- [15] M. C. Nevitt, N. E. Lane, J. C. Scott et al., "Radiographic osteoarthritis of the hip and bone mineral density," *Arthritis & Rheumatism*, vol. 38, no. 7, pp. 907–916, 1995.
- [16] K. Okano, M. Ito, K. Aoyagi, M. Osaki, H. Enomoto, and K. Yamaguchi, "Discrepancy in bone mineral densities at different skeletal sites in hip osteoarthritis patients," *Modern Rheumatology*, vol. 24, no. 2, pp. 340–342, 2014.
- [17] M. Lethbridge-Çejku, J. D. Tobin, W. W. Scott Jr. et al., "Axial and hip bone mineral density and radiographic changes of osteoarthritis of the knee: data from the Baltimore Longitudinal Study of Aging," *Journal of Rheumatology*, vol. 23, no. 11, pp. 1943–1947, 1996.
- [18] D. Lim, C.-Y. Ko, D. H. Seo et al., "Low-intensity ultrasound stimulation prevents osteoporotic bone loss in young adult ovariectomized mice," *Journal of Orthopaedic Research*, vol. 29, no. 1, pp. 116–125, 2011.
- [19] F. Li, X. Yang, Y. Yang et al., "Antiosteoporotic activity of echinacoside in ovariectomized rats," *Phytomedicine*, vol. 20, no. 6, pp. 549–557, 2013.
- [20] N. Ibrahim, M. F. Khamis, M. F. M. Yunoh, S. Abdullah, N. Mohamed, and A. N. Shuid, "Targeted delivery of lovastatin and tocotrienol to fracture site promotes fracture healing in osteoporosis model: micro-computed tomography and biomechanical evaluation," *PLoS ONE*, vol. 9, no. 12, Article ID e115595, 2014.
- [21] Q. Wang, Z. Liu, Y. Wang et al., "Quantitative ultrasound assessment of cartilage degeneration in ovariectomized rats with low estrogen levels," *Ultrasound in Medicine and Biology*, vol. 42, no. 1, pp. 290–298, 2016.
- [22] S.-Z. Wang, Y.-P. Huang, S. Saarakkala, and Y.-P. Zheng, "Quantitative assessment of articular cartilage with morphologic, acoustic and mechanical properties obtained using high-frequency ultrasound," *Ultrasound in Medicine and Biology*, vol. 36, no. 3, pp. 512–527, 2010.
- [23] S. Saarakkala, M. S. Laasanen, J. S. Jurvelin, and J. Töyräs, "Quantitative ultrasound imaging detects degenerative changes in articular cartilage surface and subchondral bone," *Physics in Medicine and Biology*, vol. 51, no. 20, article 017, pp. 5333–5346, 2006.
- [24] U. Mouritzen, S. Christgau, H.-J. Lehmann, L. B. Tankó, and C. Christiansen, "Cartilage turnover assessed with a newly developed assay measuring collagen type II degradation products: influence of age, sex, menopause, hormone replacement therapy, and body mass index," *Annals of the Rheumatic Diseases*, vol. 62, no. 4, pp. 332–336, 2003.
- [25] Q. Wang, X. Guo, M.-Q. Liu, X.-Y. Wang, and Y.-P. Zheng, "Effect of laser acupuncture on disuse osteoarthritis: an ultrasound biomicroscopic study of patellar articular cartilage in rats," *Evidence-based Complementary and Alternative Medicine*, vol. 2012, Article ID 838420, 8 pages, 2012.
- [26] Q. Wang, X. Guo, X. Y. Wang et al., "Effect of laser acupuncture therapy on bone and articular cartilage under simulated microgravity," in *6th World Congress of Biomechanics (WCB 2010). August 1–6, 2010 Singapore: In Conjunction with 14th International Conference on Biomedical Engineering (ICBME) and 5th Asia Pacific Conference on Biomechanics (APBiomech)*, vol. 31 of *IFMBE Proceedings*, pp. 852–855, Springer, Berlin, Germany, 2010.
- [27] J. Kular, J. Tickner, S. M. Chim, and J. Xu, "An overview of the regulation of bone remodelling at the cellular level," *Clinical Biochemistry*, vol. 45, no. 12, pp. 863–873, 2012.
- [28] J. Xu, H. F. Wu, E. S. M. Ang et al., "NF- κ B modulators in osteolytic bone diseases," *Cytokine and Growth Factor Reviews*, vol. 20, no. 1, pp. 7–17, 2009.
- [29] M. Ito, A. Nishida, T. Nakamura, M. Uetani, and K. Hayashi, "Differences of three-dimensional trabecular microstructure in osteopenic rat models caused by ovariectomy and neurectomy," *Bone*, vol. 30, no. 4, pp. 594–598, 2002.
- [30] J. Yang, S. M. Pham, and D. L. Crabbe, "High-resolution Micro-CT evaluation of mid- to long-term effects of estrogen deficiency on rat trabecular bone," *Academic Radiology*, vol. 10, no. 10, pp. 1153–1158, 2003.
- [31] J. E. M. Brouwers, F. M. Lambers, B. Van Rietbergen, K. Ito, and R. Huiskes, "Comparison of bone loss induced by ovariectomy and neurectomy in rats analyzed by in vivo micro-CT," *Journal of Orthopaedic Research*, vol. 27, no. 11, pp. 1521–1527, 2009.

Research Article

Transverse and Oblique Long Bone Fracture Evaluation by Low Order Ultrasonic Guided Waves: A Simulation Study

Ying Li,¹ Dan Liu,¹ Kailiang Xu,^{1,2} Dean Ta,^{1,3,4} Lawrence H. Le,⁵ and Weiqi Wang¹

¹Department of Electronic Engineering, Fudan University, Shanghai 200433, China

²Laboratoire d'Imagerie Biomédicale, UPMC Univ Paris 06, INSERM UMR-S 1146, CNRS UMR 7371, Sorbonne Université, 75006 Paris, France

³State Key Laboratory of ASIC and System, Fudan University, Shanghai 200433, China

⁴Key Laboratory of Medical Imaging Computing and Computer Assisted Intervention (MICCAI) of Shanghai, Shanghai 200032, China

⁵Department of Radiology and Diagnostic Imaging, University of Alberta, Edmonton, AB, Canada

Correspondence should be addressed to Dean Ta; tda@fudan.edu.cn

Received 4 October 2016; Accepted 28 November 2016; Published 15 January 2017

Academic Editor: Qing-Hua Huang

Copyright © 2017 Ying Li et al. This is an open access article distributed under the Creative Commons Attribution License, which permits unrestricted use, distribution, and reproduction in any medium, provided the original work is properly cited.

Ultrasonic guided waves have recently been used in fracture evaluation and fracture healing monitoring. An axial transmission technique has been used to quantify the impact of the gap breakage width and fracture angle on the amplitudes of low order guided wave modes S_0 and A_0 under a 100 kHz narrowband excitation. In our two dimensional finite-difference time-domain (2D-FDTD) simulation, the long bones are modeled as three layers with a soft tissue overlay and marrow underlay. The simulations of the transversely and obliquely fractured long bones show that the amplitudes of both S_0 and A_0 decrease as the gap breakage widens. Fixing the crack width, the increase of the fracture angle relative to the cross section perpendicular to the long axis enhances the amplitude of A_0 , while the amplitude of S_0 shows a nonmonotonic trend with the decrease of the fracture angle. The amplitude ratio between the S_0 and A_0 modes is used to quantitatively evaluate the fracture width and angles. The study suggests that the low order guided wave modes S_0 and A_0 have potentials for transverse and oblique bone fracture evaluation and fracture healing monitoring.

1. Introduction

Long bone fractures are typically classified by their shape complexity, locations, such as transverse, oblique, spiral, comminuted, compression, and greenstick fractures, and so forth [1]. Approximately 7.9 million patients sustain fractures in the United States annually, and up to 10% go on to have impaired bone healing, resulting in a delayed union or a nonunion [2]. More than 3 million incident fractures at a cost of \$35 billion are predicted for 2025 [3]. Long bone fractures represent one of the most commonly sustained injuries following trauma and account for nearly 4% of emergency department visits in the United States each year [4]. Therefore, fracture diagnosis and subsequent healing

monitoring are vital [5–7]. Although conventional X-ray radiographies are still the most common methods to evaluate fractures and monitor the subsequent healing process, ultrasonic measurement is emerging as an alternative owing to its advantages of being quick, portable, noninvasive, and inexpensive [4, 8–14]. Especially for pediatric long bone fractures, ultrasound does not necessitate exposing children to ionizing radiation, which has been linked with cancer [4, 15].

Pulse echo ultrasonic imaging showed its advantage in pediatric fracture assessment owing to children's relative thinner soft tissue compared with that of adults [10]. Li et al. proposed a split-step Fourier echo imaging method to process the signals measured by axial scanning and image the oblique

cracks in the cervine long bone plate, which illustrates the potential of better resolution for ultrasound imaging [16]. However, ultrasonography still cannot detect fractures with a width less than 1 mm [9].

Axial transmission ultrasound has drawn more and more attention recently [17–20]. Two techniques have already been proposed, first arriving signal (FAS) [17, 20–23] and guided wave [19, 24–27]. 2D-FDTD simulations and in vitro experiments on the bovine tibia have been performed, and the results illustrated that both transverse and oblique cracks resulted in the amplitude loss and velocity decrease of FAS [20]. The increase of the fracture angle would impair the sensitivity of the crack width assessment. Further simulation and experimental measurements of bovine femur samples in vitro were performed [21, 28], and the influence of bone mineralization was analyzed. The results showed that the speed of the FAS could reflect the long bone fracture healing stages. An in vitro experiment on the sheep tibia confirmed that the speed of FAS had the capability to detect the long bone fracture healing stages [29]. FAS is found to be relatively low magnitude compared with the subsequently arriving guided waves and is only sensitive to changes in the periosteal regions along the propagating path of the long cortical bone [21].

Ultrasonic guided waves propagate throughout the whole waveguide with great sensitivity to the boundary conditions, such as the endosteal and periosteal regions of the long cortical bone. Previous numerical and experimental studies mainly focus on relatively high frequency [19, 26, 32]. The propagation of guided waves in long bones with different healing stages was analyzed using finite element simulation, and it was found that the cortical fracture significantly affected the propagation of guided waves [19, 26]. However, the serious mode overlap and conversion prevent accurate quantification. Many mode recognition and separation algorithms have been proposed, such as the Radon transform [33, 34], wideband dispersion reversal method [35], sparse SVD based mode extraction [36], time-frequency ridge extraction [25], and joint spectrum separation ridge extraction [37]. However, limited by the complexity of clinical measurement, the severe multimode overlap still highly complicates the ultrasonic guided wave based long cortical bone fracture evaluation.

Recently, a narrowband frequency excitation of the low order guided modes was applied to evaluate the fracture of the long cortical bone, which significantly simplifies the mode identification and signal processing [27, 38, 39]. Simulation studies and in vitro experiments demonstrated that only two fundamental modes, S0 and A0, can be excited, and the mode conversion between S0 and A0 is capable of indicating the depth of the diaphyseal cracks [27]. However, in the previous study, only transverse cracks are analyzed in the results. Actually bone fractures are often in irregular shapes and with oblique angles to the axial direction of the long bone. Aiming to investigating the impact of irregularities of cortical fractures, a 2D-FDTD simulation was carried out in this paper. We attempt to quantitatively illustrate the possibilities of using low order guided waves to evaluate the oblique fractures in long bones.

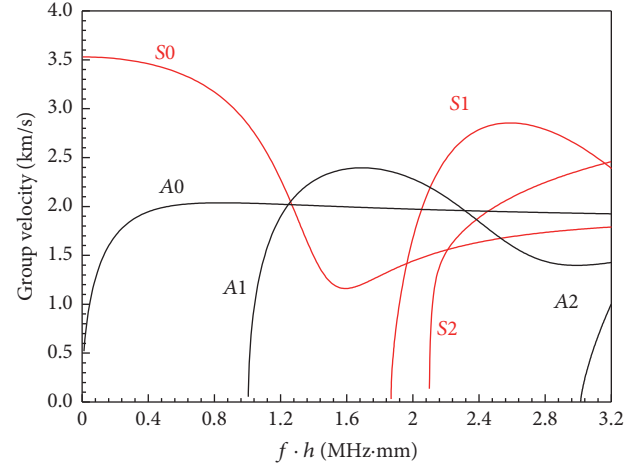


FIGURE 1: Group velocity dispersion curves of a free bovine tibia cortical bone plate. The red and black lines are the symmetric and asymmetric Lamb modes, respectively.

2. Methods

2.1. Guided Mode Excitation. Ultrasound propagation through a waveguide is always accompanied with the mode conversion between shear and longitudinal waves. After multiple refractions and reflections, wave packets with a similar phase will propagate together as a stable guided mode. Guided waves in the plates, also named Lamb waves, can be general grouped as symmetric and antisymmetric modes according to their different vibration features. In a plate, the vibration is constrained to the Rayleigh-Lamb equations [40]:

$$\frac{\tan(ph/2)}{\tan(qh/2)} + \frac{(k^2 - q^2)^2}{4pqk^2} = 0 \quad \text{symmetric}$$

$$\frac{\tan(ph/2)}{\tan(qh/2)} + \frac{4pqk^2}{(k^2 - q^2)^2} = 0 \quad \text{anti-symmetric} \quad (1)$$

$$k^2 = \frac{\omega^2}{V_p^2}, \quad p^2 = \frac{\omega^2}{V_L^2}, \quad q^2 = \frac{\omega^2}{V_T^2},$$

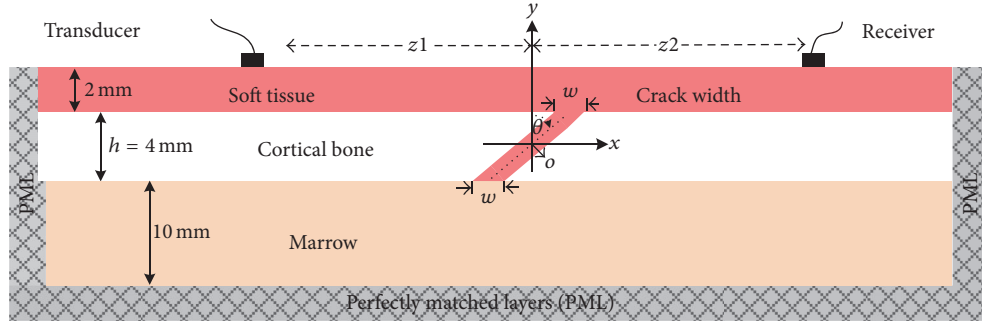
where h is the plate thickness and the angular wave number k is the ratio between the phase velocity V_p and angular frequency ω . V_L and V_T are the bulk longitudinal and shear wave velocities, respectively. The numerical solutions of (1) constitute the dispersion curves which can be expressed as functions of the frequency thickness product $f \cdot h$.

Group velocity dispersion curves of a free cortical bone plate are shown in Figure 1, where the red and black lines are the symmetric and antisymmetric Lamb modes, respectively. The material parameters of cortical bone are given in Table 1.

As shown in Figure 1, only two Lamb modes exist at the low frequency thickness ($f \cdot h$) range (<1 MHz·mm). On the contrary, at the high $f \cdot h$ range (>1 MHz·mm), there exist many high order modes which brings the challenges of mode separation. Thus, simulations are performed on

TABLE 1: Parameters of cortical bone and soft tissue.

Tissue	ρ (g/m ³)	V_L (km/s)	V_T (km/s)	Attenuation (dB·cm ⁻¹ ·MHz ⁻¹)
Cortical bone [20]	2.00	4.20	2.00	5.09
Soft tissue [30]	0.92	1.47	0.10	1.20
Marrow [31]	0.10	1.40	0.07	0.80

FIGURE 2: Simulation model of obliquely fractured long bone ($h = 4$ mm) with overlying 2 mm thick soft tissue and underlying 10 mm thick marrow.

the low $f \cdot h$ range. Narrowband low frequency sinusoids (5-cycle Gaussian-modulated pulse with a 100 kHz central frequency) are employed in our simulation to merely excite two fundamental guided waves, symmetric mode S_0 and asymmetric mode A_0 .

2.2. Numerical Simulation and Models. The numerical simulation of the axial transmission ultrasound in the long bone is performed using a self-developed two-dimension (2D) finite-difference time-domain (FDTD) software that can numerically solve the wave field in the time and space domains [20, 23]. As shown in Figure 2, a model with dimension of 300 mm \times 16 mm is used to model the obliquely fractured long bone.

The long bones are built as three layers, 2 mm thick overlying soft tissue, 4 mm thick cortical bone, and 10 mm thick marrow. The perfectly matched layers (PML) were arranged at the two ends of the model and the beneath the marrow layer to avoid the reflection. A free boundary condition is applied on upper layer of soft tissue. In the middle of the cortical bone layer, a crack is set with a width w and fracture angle θ relative to the y -axis. The crack width w changes from 0 mm (intact) to 1 mm with an interval of 0.125 mm. The fracture angle θ changes from 0° (vertical) to 83° . Constrained by the model's resolution of 0.025 mm, the fracture angle cannot be set continuously. Consequently, the fracture angles are modeled with 0° , 14° , 18° , 26° , 37° , 45° , 53° , 63° , 76° , and 83° . A pair of transducers are kept in contact with the soft tissue with the incident angle of 0° . The radius of the transducer is 5 mm. The distance from the transmitter to the central y -axis z_1 is 60 mm, and the distance from the receiver to the central y -axis z_2 is changeable from 30 mm to 90 mm with an interval of 2.5 mm. The material properties used in the simulation are given in Table 1, and the simulation temporal discretization is 0.015 μ s.

2.3. Data Processing. In this study, a low frequency narrow-band Gaussian-modulated pulse is used to avoid multimode overlapping. Thus, only two fundamental guided modes, S_0 and A_0 , are excited in the received guide waves, so that the mode packets can be identified and separated by simple temporal windows [38, 41].

The peak amplitude of the A_0 and S_0 wave packets is obtained to calculate the amplitude ratio between the two modes. The energy characteristics of the A_0 mode and S_0 mode are investigated with fracture angles and widths variation.

The propagation delays of these two converted modes can be calculated by (2a) and (2b) [27]. If z_1 equals z_2 , the wave packets of the two converted modes merge into a mixed wave packet propagating between the original S_0 and A_0 modes

$$T(A_0_{S_0}) = \frac{z_1}{V_{S_0}} + \frac{z_2}{V_{A_0}}, \quad (2a)$$

$$T(S_0_{A_0}) = \frac{z_1}{V_{A_0}} + \frac{z_2}{V_{S_0}}. \quad (2b)$$

At 100 kHz, the duration of the 5 cycle excitation Gaussian-modulated pulse is 50 μ s, and the group velocities of S_0 and A_0 are 3.95 km/s and 1.51 km/s, respectively. We measure the peaks of the two wave packets in time domain, which are the maximum amplitudes of the two original modes S_0 and A_0 and calculate the amplitude ratio between them for use in evaluating the long bone crack width with different fracture angles.

3. Results

Figure 3 shows the envelope curves extracted from fractured long bones with different fracture degrees and fracture oblique angles. The envelope amplitude is depicted in different colors with maxima in red and 0 in gray. The propagation

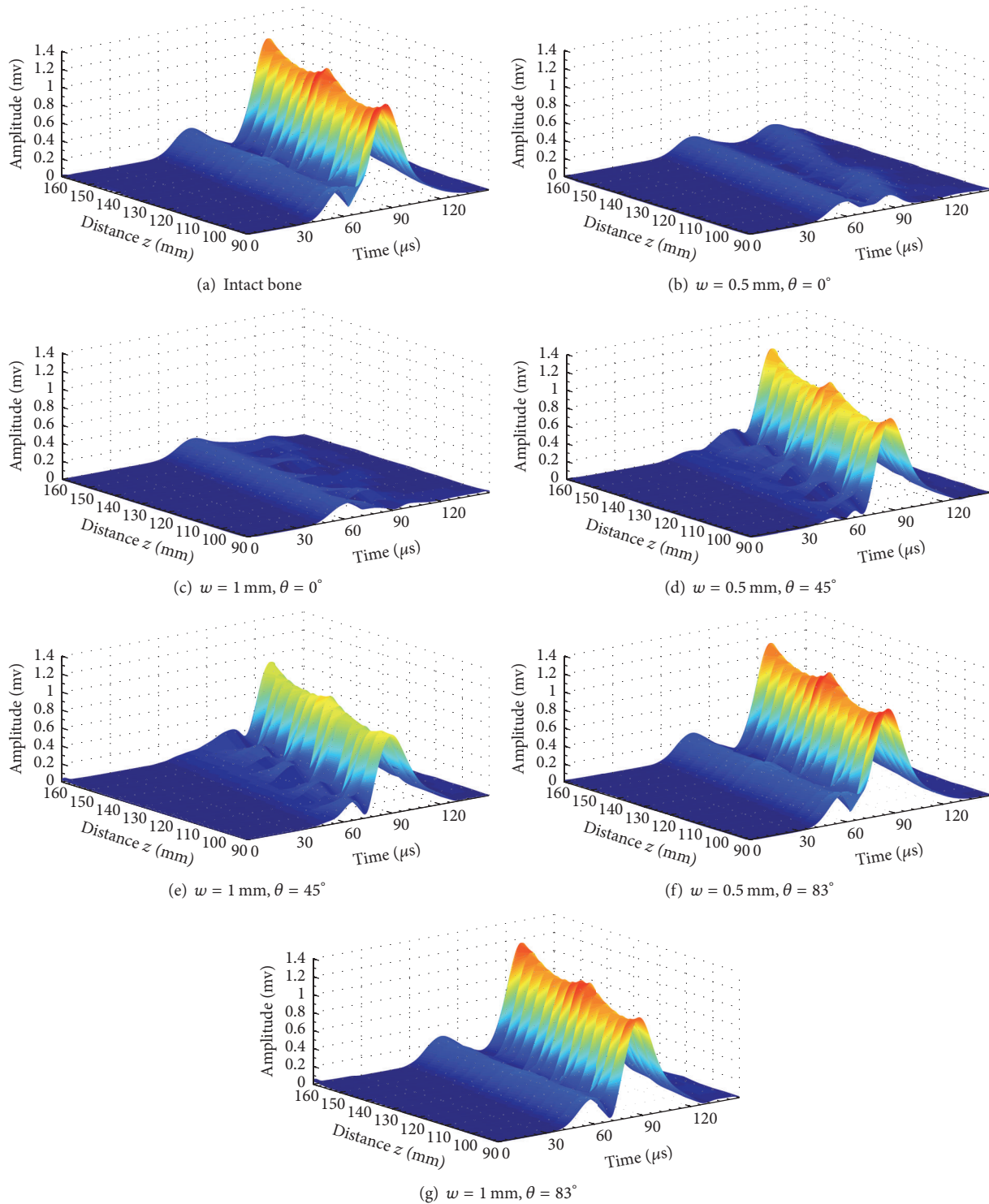


FIGURE 3: The envelope diagrams of the received signals ($90 \text{ mm} < z < 150 \text{ mm}$) with different fracture degree and oblique angles, (a) intact model, (b) transverse fracture model with 0.5 mm wide crack, (c) transverse fracture model with 1.0 mm wide crack, (d) 45° oblique fracture model with 0.5 mm wide crack, (e) 45° oblique fracture model with 1.0 mm wide crack, (f) 83° oblique fractured model with 0.5 mm wide crack, and (g) 83° oblique fracture model with 1.0 mm wide crack.

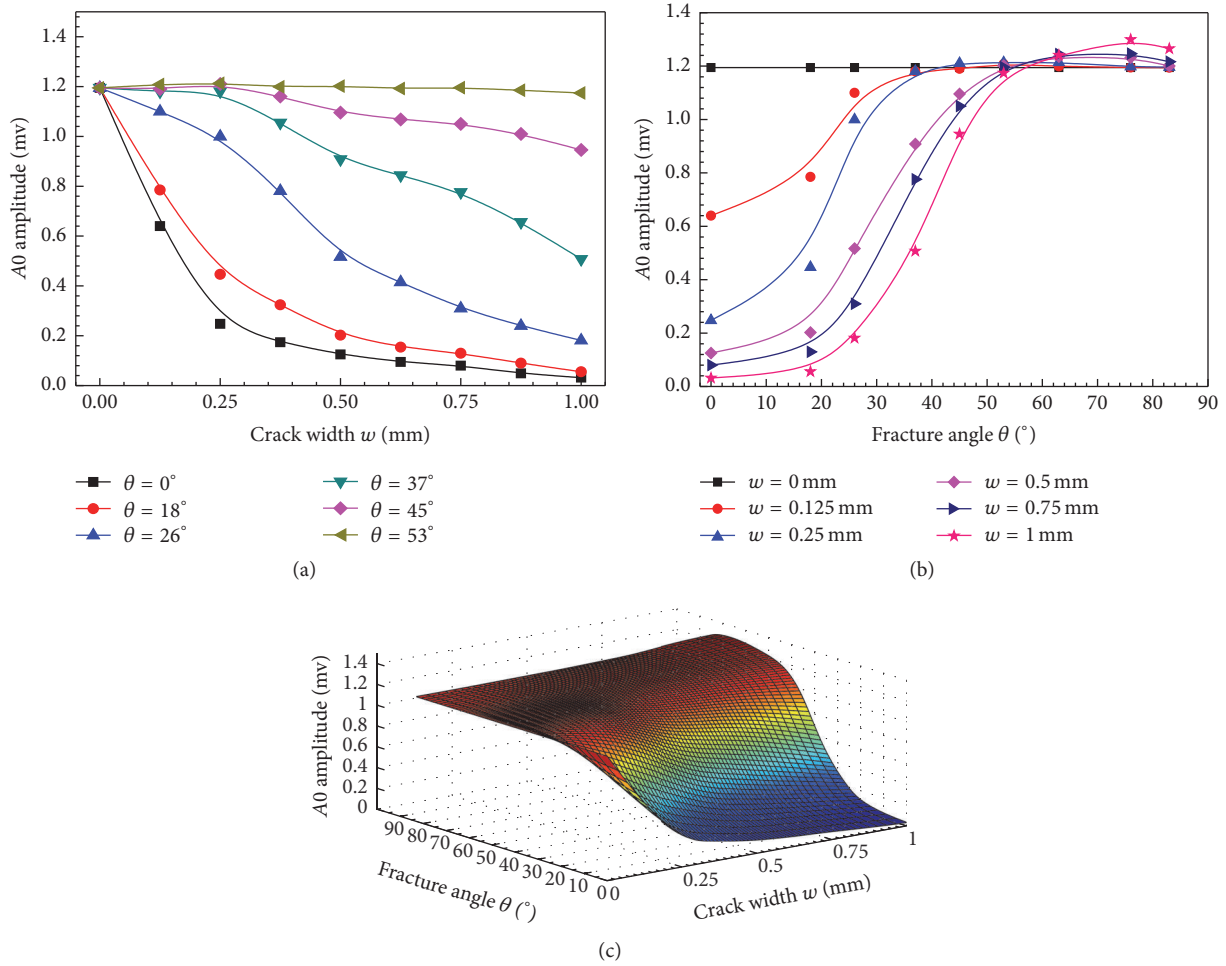


FIGURE 4: Amplitudes of A0 change as functions of the crack width w and the fracture angle θ ; (a) with a fixed θ , the A0 amplitude curves with w variation; (b) with a fixed w , the A0 amplitude curves with θ variation; and (c) the B-spline fitting results of A0 amplitude to θ and w .

distance z varies from 90 mm to 150 mm with an interval of 2.5 mm.

Figure 3(a) shows the envelopes of the received waveforms with two Lamb modes S0 and A0 in the intact bone. The amplitude of antisymmetric mode A0 is much higher than that of S0, because of the perpendicular incidence and reception angles. No converted modes are observed in this model. However, in Figures 3(b) and 3(c) for transverse fracture with 0.5 mm and 1 mm wide cracks, both the S0 and A0 amplitudes attenuate significantly. As shown in Figures 3(d) and 3(e), the converted modes can be observed from the results of the 45° oblique fracture. According to the velocity analysis, the converted modes usually exist between the two original modes S0 and A0. Furthermore, the peak amplitudes of the conversion modes and original mode are difficult to be extracted due to mode overlapping. For larger fracture angle models in Figures 3(f) and 3(g), it seems that the original mode energy still can transmit through the cracks without obvious appearance of the converted modes. With a fixed fracture angle, the increasing of the crack width may lead to the amplitude reduction of both S0 and A0, such as in Figures 3(a), 3(b), and 3(c). In Figures 3(b), 3(d), and 3(f), with a

fixed crack width, the increasing fracture angle may lead to the amplitude increasing of transmitted energy of the A0 mode, but the change of the S0 amplitude is nonmonotonic. To quantitatively illustrate the mode conversion, we further investigate different models with crack and fracture angle variation.

3.1. A0 Mode Amplitude Analysis. Figure 4(a) presents the A0 amplitude changes as functions of the crack width and fracture angles. The propagation distance z is fixed at 120 mm. With the crack width increasing, a decrease trend of the A0 amplitude can be observed, which is sensitive to the small crack ($w < 0.25$ mm).

The A0 amplitudes decrease more than 95% in the 0° and 18° fractures, but they are almost constant as w increases to large angles ($\theta > 53^\circ$). Figure 4(b) shows the variation of the A0 amplitude with the fracture angle. The A0 amplitude obtained from the intact model is set as a benchmark. The A0 amplitude shows three stages in the increase of the fracture angle: a slow increase for small angles ($\theta < 20^\circ$), a rapid increase for the range of $20^\circ \sim 50^\circ$, and a final slow increase for large angles ($\theta > 50^\circ$). Figure 4(c) shows the A0 amplitude

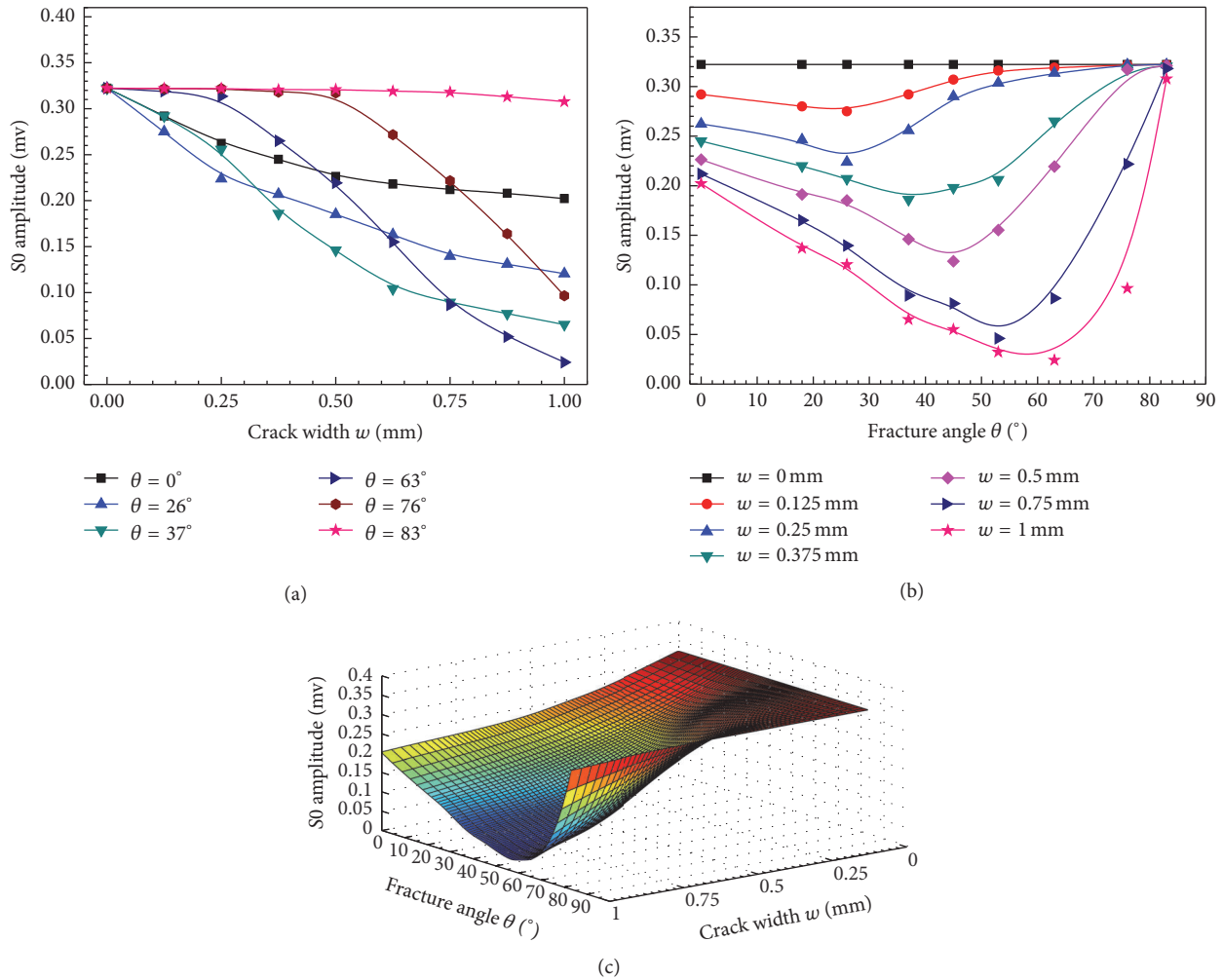


FIGURE 5: Amplitudes of S0 change as functions of crack width w and fracture angle θ ; (a) with a fixed θ , the S0 amplitude curves with w variation; (b) with a fixed w , the S0 amplitudes curves with θ variation; and (c) the B-spline fitting results of S0 amplitude to θ and w .

changes with the crack width and fracture angle in three dimensions. A B-spline fitting is performed to obtain the smooth amplitude functions. It shows that, comparing with the wide cracks and transverse fractures, the narrow cracks or the large angle oblique cracks can enhance the A0 mode transmission with larger A0 amplitude. The sensitivity of the A0 amplitude to the crack width and fracture angle shows potentials for fracture evaluation.

3.2. S0 Mode Amplitude Analysis. Figure 5(a) presents the S0 amplitude changes as functions of the crack width with different fracture angles. The propagation distance z is fixed at 120 mm. The S0 amplitude obtained in an intact model is used as a benchmark. With a fixed fracture angle, the S0 amplitude decreases with the crack widening. As shown in Figure 5(b), with a fixed crack width, the S0 amplitude shows a nonmonotonic trend with the fracture angle variation, and the minimal S0 amplitude is obtained at the range of 30° to 60° , which is smaller than the amplitude obtained in the model with a transverse fracture. The S0 amplitude decreases

as the fracture angle increases, and then it increases as the fracture angle further increases, ultimately coming close to the value of the intact model at 83° . Figure 5(c) shows the B-spline fitting results of the S0 amplitude variation with the crack width and fracture angle in three-dimensional form. It can be found that the S0 amplitude generally decreases as the crack width increases, but it also shows a nonmonotonic trend to the fracture angle.

3.3. Impact of Crack Width and Fracture Angle on S0/A0. The above results indicate that the S0 and A0 amplitudes can reflect the w change of fractured long bones with different angles. However, in actual clinical use, the magnitudes of the guided modes are easily affected by many factors such as the coupling conditions and excitation energy. Thus, the amplitude ratio between S0 and A0 can be adopted as a more robust parameter.

To investigate the impact of the propagation distance, the average amplitude ratios are computed from the multichannel signals ($90 < z < 150$ mm with an interval of 2.5 mm). Figures

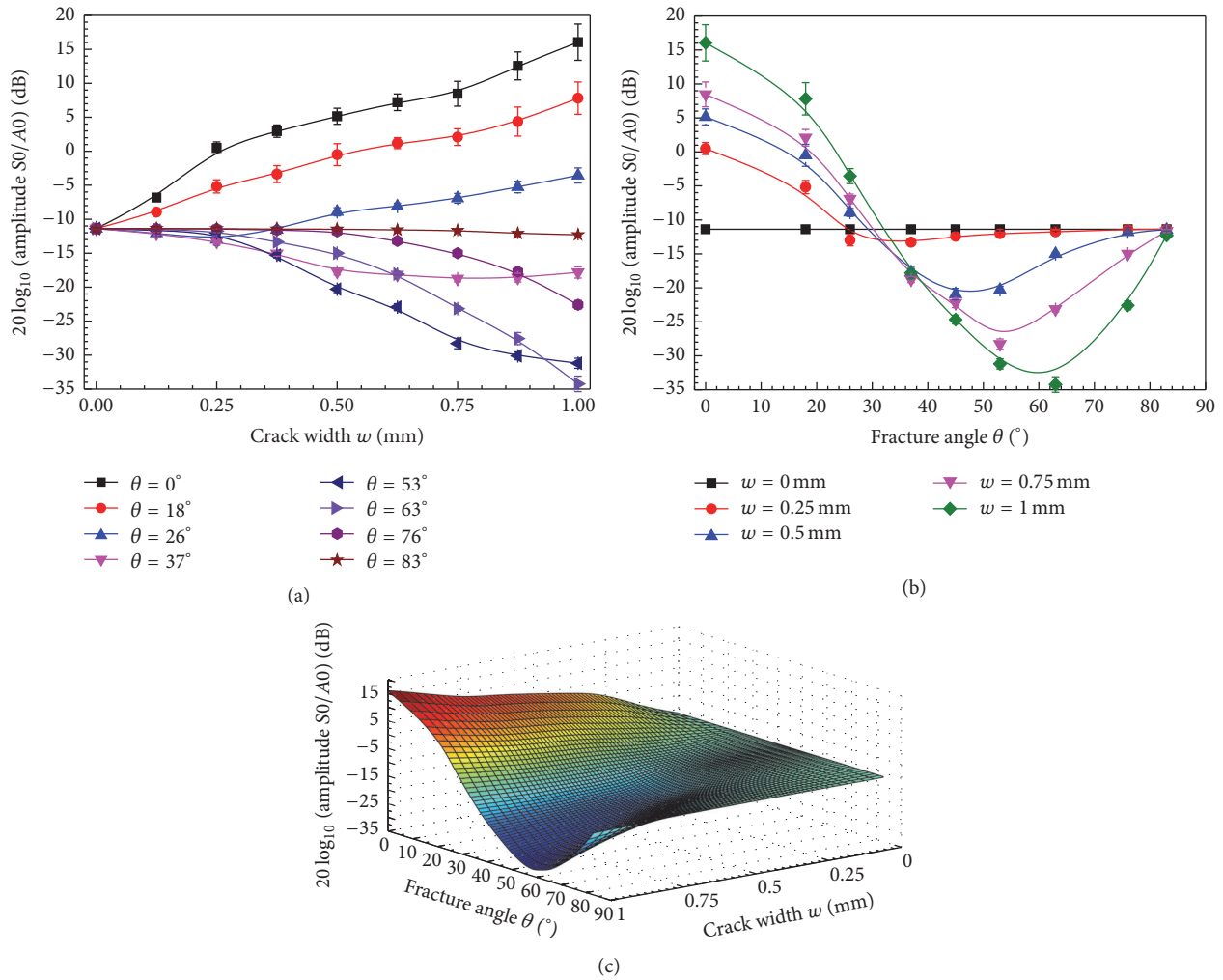


FIGURE 6: Amplitude ratios (dB) between S0 and A0 varying as functions of crack width w and fracture angle θ ; (a) with a fixed θ , the amplitude ratio (dB) changes with w , where the error bars denote the standard errors for results obtained at different propagation distances z ($90 < z < 150$ mm); (b) with a fixed crack width w , the amplitude ratio (dB) changes with θ , where the error bars denote the standard errors for results obtained at different propagation distances z ($90 < z < 150$ mm); and (c) distance $z = 120$ mm, the B-spline fitting results of the amplitude ratios (dB) varying with fracture angle θ and crack width w .

6(a) and 6(b) present the amplitude ratio changes with the variance of w and θ , respectively, where the error bar denotes the root mean square errors (RMSE) of the ratios obtained at different propagation distances for each fractured model.

As shown in Figure 6(a), for small angles ($\theta < 26^\circ$), the amplitude ratio increases with w . Comparing with the intact model, the amplitude ratios between the S0 and A0 modes in the fracture bone increase by values of 27.4 dB and 7.8 dB for 0° and 26° , respectively. However, for large angles ($\theta > 26^\circ$), the amplitude ratio decreases with the crack width by an average of 12.4 dB. Comparing to the intact model, with the oblique fracture angles of 53° and 63° , amplitude ratios between the S0 and A0 modes decrease by 19.8 dB and 22.9 dB, respectively.

Figure 6(b) presents the amplitude ratio of S0 and A0 varying with the fracture angle. It can be seen that the amplitude ratio curves first decrease as the fracture angle increases and then increase with angle increases. For 0.25 mm

and 1 mm wide cracks, the turning points are approximately 35° and 60° . It can be found that, with a wide crack, the turn points of the amplitude ratio curves appear out with large angle.

The results reveal that the propagation distance has a small impact on the amplitude ratio with an average RSME of 0.78 dB. Furthermore, it is notable in Figures 6(a) and 6(b) that the largest RMSE of the amplitude ratio between the S0 and A0 modes can be obtained in the fractured bones with a small oblique angles (0° , 26° , and 37°) and large crack widths ($w > 0.5$ mm). For other fracture angles ($\theta > 26^\circ$), the average RSME of the amplitude ratio between the S0 and A0 modes is 0.46 dB. The small RSME reveals that the propagation distance variation between 60 mm and 150 mm has a small impact on the amplitude ratio parameter.

Figure 6(c) is the B-spline fitting result of the amplitude ratio parameter varying with the fracture angle θ and crack width w at a 120 mm distance. As shown in Figure 5(a), the

line cross actually indicates that, in the oblique fractured bone model, with the crack widening the decline slopes of the S_0 amplitude curves are different. The decline slope corresponding to the 63° fracture is more negative than those of other angles. Such a phenomenon also can be learned from the amplitude ratios curves between the S_0 and A_0 modes in Figure 6(c). It can be seen that the amplitude ratio may be able to indicate the oblique angle and the crack width of the bone fractures.

4. Discussion

This study presents a quantitative investigation of using low order guided wave modes to evaluate long bone fractures with oblique fracture angles. A 2D-FDTD simulation is performed in a three-layer model. Using a 100 kHz narrowband excitation, only two guided wave modes, S_0 and A_0 , are excited. The impact of the crack width and fracture angle on the S_0 and A_0 amplitudes is thoroughly studied. The crack width increase leads to amplitude decreases for both the A_0 and S_0 modes (Figures 4(a) and 5(a)). The A_0 amplitude shows a monotonic relationship with the fracture angle (Figure 4(b)), while the S_0 amplitude shows a nonmonotonic relationship (Figure 5(b)). Although only simulation is performed in this study, the simulation results yielded interesting findings, including the use of the amplitude ratio to evaluate the crack width and fracture angle (Figures 6(a) and 6(b)). These findings illustrate the potential of guided mode conversion for the quantitative prediction of the cortical bone fracture degree and healing status.

To reduce the influence of the coupling and excitation, the amplitude ratio between S_0 and A_0 is adopted to evaluate the long bone fracture degree. The amplitude ratio shows a two-stage change with the fracture angle (Figure 6(b)). In the first stage, the amplitude ratio decreases as the angle increases, and the average decrease at different widths is $6.1 \text{ dB}/10^\circ$. In the second stage, the amplitude ratio increases with the further increase in the angle, and the average increase at different widths is $4.9 \text{ dB}/10^\circ$. The increase of crack width raises the amplitude ratio for small angles ($\theta < 26^\circ$) (Figure 6(a)), while it decreases the amplitude ratio for large angles ($\theta > 26^\circ$). The amplitude ratio between S_0 and A_0 shows a great capacity for fracture width detection with different fracture angles, even for very small crack widths ($w < 1 \text{ mm}$): $27.4 \text{ dB}/\text{mm}$ for a transverse fracture, $19.2 \text{ dB}/\text{mm}$ for a 18° oblique fracture, $-19.8 \text{ dB}/\text{mm}$ for a 53° oblique fracture, and $-22.9 \text{ dB}/\text{mm}$ for a 63° oblique fracture (Figure 6(a)).

It has been demonstrated that when the cortical bone thickness (h) is much larger than the longitudinal wave length (λ), the speed of FAS is larger than that of the S_0 mode, but for very thin plate, the speed of the FAS signal approaches the velocity of S_0 mode [17]. Numerical and experimental results showed that the detection accuracy of the amplitude of FAS for the transverse and oblique crack widths was approximately $2 \text{ dB}/\text{mm}$ in a 6 mm thick long bone plate at an excitation of 200 kHz ($h \approx 0.3\lambda$) [20]. In the performed study, as the excitation frequency is 100 kHz and the cortical bone plate thickness is 4 mm ($\lambda \approx 40 \text{ mm}$, $h \approx 0.1\lambda$), the FAS can be regarded as the ultrasonic Lamb

mode S_0 . Compared with high frequency excitation, these simulation results show that the amplitude ratio between S_0 and A_0 may also be used to detect the crack width. In addition, for the oblique fracture model with a $37\text{--}63^\circ$ fracture, the S_0 amplitude significantly decreases as the crack width increases, so it is relatively hard to measure mode S_0 . Therefore, the incident angle should be optimized to increase the excitation of S_0 . The different distance signal results reveal that the propagation distance has a small impact on the amplitude ratio, with an average RSME of 0.78 dB. These results indicate the theoretical feasibility for the clinical application.

In the performed simulation, we consider that the crack surface is uniform, but it is actually irregular, which will affect the propagations of S_0 and A_0 . Moreover, the crack region is filled with soft tissue in our simulation, while actually the tissue in the crack site will gradually recover, with a callus appearing and changing during the healing [26, 42–44]. Further experiments are needed to validate our hypothesis that the amplitude ratio between the S_0 and A_0 modes can indeed facilitate long bone fracture and healing process evaluation.

5. Conclusions

The impacts of the crack width and fracture angle on the low order guided wave S_0 and A_0 amplitudes were studied in a three-layer model (soft tissue, cortical bone, and marrow) using the 2D-FDTD simulation. The results show that the S_0 and A_0 amplitudes decrease as the crack width increases. The A_0 amplitude increases as the fracture angle increases, while the S_0 amplitude firstly decreases and then increases. To avoid the influence of coupling conditions and excitation signals, the use of the amplitude ratio between S_0 and A_0 is proposed to evaluate crack width changes at different fracture angles. The results indicate that the amplitude ratio between S_0 and A_0 is sensitive to the crack width in fractures with different oblique angles. The amplitude ratio shows good capability for crack width evaluation, with sensitivities of $25.1 \text{ dB}/\text{mm}$ for a transverse fracture, $18.7 \text{ dB}/\text{mm}$ for an 18° oblique fracture, and $-23.3 \text{ dB}/\text{mm}$ for 53° oblique fracture. The average RSME of 0.78 dB for different propagation distances indicates the small distance impact on the amplitude ratio. Thus, the amplitude ratio between S_0 and A_0 has the capability of reflecting the long bone fracture status, including the crack width and angle. The variation of the amplitude ratio with the crack width and fracture angle was further discussed, which shows its good potential for monitoring the fracture angle and crack width in fractured long cortical bone.

Competing Interests

The authors state that they have no conflict of interests.

Acknowledgments

This work was supported by the National Natural Science Foundation of China (11327405, 11304043, and 11525416) and

the Ph.D. Programs Foundation of the Ministry of Education of China (20130071110020).

References

- [1] K. M. Iyer, "Anatomy of Bone, Fracture, and Fracture Healing," pp. 1–11, 2013.
- [2] N. Wu, Y.-C. Lee, D. Segina et al., "Economic burden of illness among US patients experiencing fracture nonunion," *Orthopedic Research and Reviews*, vol. 5, pp. 21–33, 2013.
- [3] R. Burge, B. Dawson-Hughes, D. H. Solomon, J. B. Wong, A. King, and A. Tosteson, "Incidence and economic burden of osteoporosis-related fractures in the United States, 2005–2025," *Journal of Bone and Mineral Research*, vol. 22, no. 3, pp. 465–475, 2007.
- [4] I. Barata, R. Spencer, C. Raio, M. Ward, and A. Sama, "15 ultrasound detection of long bone fractures in pediatric emergency department patients," *Annals of Emergency Medicine*, vol. 58, no. 4, pp. S182–S183, 2011.
- [5] R. Burge, B. Dawson-Hughes, D. H. Solomon, J. B. Wong, A. King, and A. Tosteson, "Incidence and economic burden of osteoporosis-related fractures in the United States, 2005–2025," *Journal of Bone and Mineral Research*, vol. 22, no. 3, pp. 465–475, 2007.
- [6] D. W. Dempster, "Osteoporosis and the burden of osteoporosis-related fractures," *The American Journal of Managed Care*, vol. 17, supplement 6, pp. S164–S169, 2011.
- [7] P. Corso, E. Finkelstein, T. Miller, I. Fiebelkorn, and E. Zaloshnja, "Incidence and lifetime costs of injuries in the United States," *Injury Prevention*, vol. 12, no. 4, pp. 212–218, 2006.
- [8] L. C. Y. Wong, W. K. Chiu, M. Russ, and S. Liew, "Review of techniques for monitoring the healing fracture of bones for implementation in an internally fixated pelvis," *Medical Engineering & Physics*, vol. 34, no. 2, pp. 140–152, 2012.
- [9] J. E. Rabiner, H. Khine, J. R. Avner, L. M. Friedman, and J. W. Tsung, "Accuracy of point-of-care ultrasonography for diagnosis of elbow fractures in children," *Annals of Emergency Medicine*, vol. 61, no. 1, pp. 9–17, 2013.
- [10] K. P. Cross, "Bedside ultrasound for pediatric long bone fractures," *Clinical Pediatric Emergency Medicine*, vol. 12, no. 1, pp. 27–36, 2011.
- [11] Q. Huang, B. Xie, P. Ye, and Z. Chen, "3-D ultrasonic strain imaging based on a linear scanning system," *IEEE Transactions on Ultrasonics, Ferroelectrics, and Frequency Control*, vol. 62, no. 2, pp. 392–400, 2015.
- [12] Q. Huang, Y. Huang, W. Hu, and X. Li, "Bezier interpolation for 3-D freehand ultrasound," *IEEE Transactions on Human-Machine Systems*, vol. 45, no. 3, pp. 385–392, 2015.
- [13] C. Liu, F. Xu, D. Ta et al., "Measurement of the human calcaneus in vivo using ultrasonic backscatter spectral centroid shift," *Journal of Ultrasound in Medicine*, vol. 35, no. 10, pp. 2197–2208, 2016.
- [14] Z. Chen, Y. Chen, and Q. Huang, "Development of a wireless and near real-time 3D ultrasound strain imaging system," *IEEE Transactions on Biomedical Circuits and Systems*, vol. 10, no. 2, pp. 394–403, 2016.
- [15] K. Eckert, O. Ackermann, B. Schweiger, E. Radloff, and P. Liedgens, "Ultrasound evaluation of elbow fractures in children," *Journal of Medical Ultrasonics*, vol. 40, no. 4, pp. 443–451, 2013.
- [16] H. Li, L. H. Le, M. D. Sacchi, and E. H. M. Lou, "Ultrasound imaging of long bone fractures and healing with the split-step fourier imaging method," *Ultrasound in Medicine & Biology*, vol. 39, no. 8, pp. 1482–1490, 2013.
- [17] E. Bossy, M. Talmant, and P. Laugier, "Effect of bone cortical thickness on velocity measurements using ultrasonic axial transmission: a 2D simulation study," *Journal of the Acoustical Society of America*, vol. 112, no. 1, pp. 297–307, 2002.
- [18] P. Laugier, "Instrumentation for in vivo ultrasonic characterization of bone strength," *IEEE Transactions on Ultrasonics, Ferroelectrics, and Frequency Control*, vol. 55, no. 6, pp. 1179–1196, 2008.
- [19] V. Protopappas, M. Vavva, D. Fotiadis, and K. Malizos, "Ultrasonic monitoring of bone fracture healing," *IEEE Transactions on Ultrasonics, Ferroelectrics, and Frequency Control*, vol. 55, no. 6, pp. 1243–1255, 2008.
- [20] S. P. Dodd, J. L. Cunningham, A. W. Miles, S. Gheduzzi, and V. F. Humphrey, "Ultrasound transmission loss across transverse and oblique bone fractures: an in vitro study," *Ultrasound in Medicine & Biology*, vol. 34, no. 3, pp. 454–462, 2008.
- [21] C. B. Machado, W. C. de Albuquerque Pereira, M. Talmant, F. Padilla, and P. Laugier, "Computational evaluation of the compositional factors in fracture healing affecting ultrasound axial transmission measurements," *Ultrasound in Medicine & Biology*, vol. 36, no. 8, pp. 1314–1326, 2010.
- [22] I. M. Siegel, G. T. Anast, and T. Fields, "The determination of fracture healing by measurement of sound velocity across the fracture site," *Surgery, Gynecology & Obstetrics*, vol. 107, no. 3, pp. 327, 1958.
- [23] S. Gheduzzi, S. P. Dodd, A. W. Miles, V. F. Humphrey, and J. L. Cunningham, "Numerical and experimental simulation of the effect of long bone fracture healing stages on ultrasound transmission across an idealized fracture," *The Journal of the Acoustical Society of America*, vol. 126, no. 2, pp. 887–894, 2009.
- [24] P. Moilanen, "Ultrasonic guided waves in bone," *IEEE Transactions on Ultrasonics, Ferroelectrics, and Frequency Control*, vol. 55, no. 6, pp. 1277–1286, 2008.
- [25] K. Xu, D. Ta, and W. Wang, "Multiridge-based analysis for separating individual modes from multimodal guided wave signals in long bones," *IEEE Transactions on Ultrasonics, Ferroelectrics, and Frequency Control*, vol. 57, no. 11, pp. 2480–2490, 2010.
- [26] V. T. Potsika, K. N. Grivas, V. C. Protopappas et al., "Application of an effective medium theory for modeling ultrasound wave propagation in healing long bones," *Ultrasonics*, vol. 54, no. 5, pp. 1219–1230, 2014.
- [27] K. Xu, D. Ta, R. He, Y.-X. Qin, and W. Wang, "Axial transmission method for long bone fracture evaluation by ultrasonic guided waves: simulation, phantom and in vitro experiments," *Ultrasound in Medicine & Biology*, vol. 40, no. 4, pp. 817–827, 2014.
- [28] C. B. Machado, W. C. D. A. Pereira, M. Granke, M. Talmant, F. Padilla, and P. Laugier, "Experimental and simulation results on the effect of cortical bone mineralization in ultrasound axial transmission measurements: a model for fracture healing ultrasound monitoring," *Bone*, vol. 48, no. 5, pp. 1202–1209, 2011.
- [29] G. Barbieri, C. H. Barbieri, N. Mazzer, and C. A. Pelá, "Ultrasound propagation velocity and broadband attenuation can help evaluate the healing process of an experimental fracture," *Journal of Orthopaedic Research*, vol. 29, no. 3, pp. 444–451, 2011.
- [30] P. Laugier, "Quantitative ultrasound instrumentation for bone in vivo characterization," *Bone Quantitative Ultrasound*, pp. 47–71, 2010.
- [31] M. G. Vavva, V. C. Protopappas, L. N. Gergidis, A. Charalambopoulos, D. I. Fotiadis, and D. Polyzos, "The effect of boundary

- conditions on guided wave propagation in two-dimensional models of healing bone,” *Ultrasonics*, vol. 48, no. 6-7, pp. 598–606, 2008.
- [32] K. Xu, D. Ta, P. Moilanen, and W. Wang, “Mode separation of Lamb waves based on dispersion compensation method,” *Journal of the Acoustical Society of America*, vol. 131, no. 4, pp. 2714–2722, 2012.
- [33] T. N. H. T. Tran, K.-C. T. Nguyen, M. D. Sacchi, and L. H. Le, “Imaging ultrasonic dispersive guided wave energy in long bones using linear radon transform,” *Ultrasound in Medicine and Biology*, vol. 40, no. 11, pp. 2715–2727, 2014.
- [34] K. Xu, D. Ta, D. Cassereau et al., “Multichannel processing for dispersion curves extraction of ultrasonic axial-transmission signals: comparisons and case studies,” *The Journal of the Acoustical Society of America*, vol. 140, no. 3, pp. 1758–1770, 2016.
- [35] K. Xu, D. Ta, B. Hu, P. Laugier, and W. Wang, “Wideband dispersion reversal of lamb waves,” *IEEE Transactions on Ultrasonics, Ferroelectrics, and Frequency Control*, vol. 61, no. 6, pp. 997–1005, 2014.
- [36] K. Xu, J. Minonzio, D. Ta, B. Hu, W. Wang, and P. Laugier, “Sparse SVD method for high-resolution extraction of the dispersion curves of ultrasonic guided waves,” *IEEE Transactions on Ultrasonics, Ferroelectrics, and Frequency Control*, vol. 63, no. 10, pp. 1514–1524, 2016.
- [37] Z. Zhang, K. Xu, D. Ta, and W. Wang, “Joint spectrogram segmentation and ridge-extraction method for separating multimodal guided waves in long bones,” *Science China: Physics, Mechanics and Astronomy*, vol. 56, no. 7, pp. 1317–1323, 2013.
- [38] K. Xu, D. Ta, Z. Su, and W. Wang, “Transmission analysis of ultrasonic Lamb mode conversion in a plate with partial-thickness notch,” *Ultrasonics*, vol. 54, no. 1, pp. 395–401, 2014.
- [39] K. Xu, D. Liu, D. Ta, B. Hu, and W. Wang, “Quantification of guided mode propagation in fractured long bones,” *Ultrasonics*, vol. 54, no. 5, pp. 1210–1218, 2014.
- [40] J. L. Rose, “Ultrasonic waves in solid media,” 2004.
- [41] E. Bossy, M. Talmant, M. Defontaine, F. Patat, and P. Laugier, “Bidirectional axial transmission can improve accuracy and precision of ultrasonic velocity measurement in cortical bone: a validation on test materials,” *IEEE Transactions on Ultrasonics, Ferroelectrics, and Frequency Control*, vol. 51, no. 1, pp. 71–79, 2004.
- [42] I. Dudkiewicz, M. Heim, M. Salai, and A. Blankstein, “The biology of fracture healing in long bones,” *Journal of Musculoskeletal Research*, vol. 12, no. 2, pp. 105–112, 2009.
- [43] D. Comiskey, B. J. MacDonald, W. T. McCartney, K. Synnott, and J. O’Byrne, “Predicting the external formation of callus tissues in oblique bone fractures: idealised and clinical case studies,” *Biomechanics and Modeling in Mechanobiology*, vol. 12, no. 6, pp. 1277–1282, 2013.
- [44] V. C. Protopappas, D. I. Fotiadis, and K. N. Malizos, “Guided ultrasound wave propagation in intact and healing long bones,” *Ultrasound in Medicine & Biology*, vol. 32, no. 5, pp. 693–708, 2006.

Research Article

Combined Ultrasound Imaging and Biomechanical Modeling to Estimate Triceps Brachii Musculotendon Changes in Stroke Survivors

Le Li^{1,2} and Raymond Kai-yu Tong³

¹Department of Rehabilitation Medicine, The First Affiliated Hospital, Sun Yat-sen University, Guangzhou, China

²Department of Physical Medicine and Rehabilitation, University of Texas Health Science Center at Houston and Research Center at TIRR Memorial Hermann Hospital, Houston, TX, USA

³Biomedical Engineering Division, Department of Electronic Engineering, The Chinese University of Hong Kong, Sha Tin, Hong Kong

Correspondence should be addressed to Le Li; lile5@mail.sysu.edu.cn

Received 30 August 2016; Revised 26 October 2016; Accepted 7 November 2016

Academic Editor: Qing Wang

Copyright © 2016 L. Li and R. K.-y. Tong. This is an open access article distributed under the Creative Commons Attribution License, which permits unrestricted use, distribution, and reproduction in any medium, provided the original work is properly cited.

The aim of this study was to investigate the changes of musculotendon parameters of triceps brachii in persons after stroke based on subject-specific biomechanical modeling technique combined with in vivo ultrasound measurement. Five chronic stroke survivors and five normal control subjects were recruited. B-mode ultrasound was applied to measure muscle pennation angle and the optimal length of three heads of triceps' brachii at different joint angle positions in resting and isometric contraction. Measured ultrasound data were used to reduce the unknown parameters during the modeling optimization process. The results showed that pennation angles varied with joint angles, and the longhead TRI pennation from stroke group was smaller than the literature value. The maximum isometric muscle stress from persons after stroke was significantly smaller than that found in the unimpaired subjects. The prediction of joint torque fits well with the measured data from the control group, whereas the prediction error is larger in results from persons after stroke. In vivo parameters from ultrasound data could help to build a subject-specific biomechanical model of elbow extensor for both unimpaired and hemiplegic subjects, and then the results driven from the model could enhance the understanding of motor function changes for persons after stroke.

1. Introduction

The movement disorders presented in persons after stroke include weakness, spasticity, and muscle cocontraction, which causes difficulties for achieving critical activities in daily life [1–3]. Coordinated human movement is a complex behavior, even for a seemingly simple one-degree-of-freedom task. For example, elbow extension movement is modulated by the coordinated action of at least three extensor muscles [4]. Forces generated by these muscles are transferred to the bones via the tendons and affect motion of the joint [5]. Since in vivo muscle forces cannot be measured directly, computer modeling is a useful tool for enhancing our understanding of muscle force change related to aging [6] and pathological disease [7, 8]. The modeling approach can describe the kinetic

response of activated muscle at different angle contractions, represent the force producing characteristics of the muscle, and compute the individual muscle force and moment during motor tasks. The modeling technique has been successfully applied to many human joints of the upper arm, such as the hand [9], wrist [10, 11], and elbow [7, 12–14].

However, one of the major challenges in musculoskeletal modeling is to accurately estimate the musculotendon parameters on a subject-specific basis. Sensitivity analysis has shown that musculoskeletal model behavior tends to be very sensitive to the values of musculotendon parameters [11, 15]. For example, when a muscle is constantly activated, its moment arm, physiological cross section area (PCSA), and its operating range (what portion of the isometric force-length relationship curve the muscles use during joint rotation)

are the key factors that characterize maximum moment-generating capacity as a function of joint position [16].

Ultrasound imaging techniques have been used to obtain the parameters of musculotendon in vivo and noninvasively [17]. Accuracy of the ultrasound method in measuring muscle architecture features has also been demonstrated to show good agreement with direct anatomical measurement on a cadaver [18]. The pennation angle and muscle fascicle length are two architectural variables readily measured by using ultrasound imaging previously [19, 20]. Our previous ultrasound study on brachialis of persons after stroke showed there were significant muscle changes of affected side compared to those from the unaffected side [21]. Stroke survivors often present a flexed elbow [22]. The literature has shown that elbow extension impairment after stroke is sometimes even worse than flexion. For example, Zackowski and colleagues investigated reaching movement from hemiparetic subjects and found reaching out movement which involved more elbow extension was worse versus the reaching up condition [3]. In addition, in a review of clinical studies of upper movement in hemiplegic cerebral palsy, the results had shown that elbow extension is reduced and compensated by increased trunk flexion to reach an object [23]. However, there is limited knowledge about the architectural changes of triceps brachii after stroke as well as how these muscle structural alterations contribute to the changes of force generation in stroke survivors. Therefore, the investigation of the mechanisms underlying changes in elbow extension after neurological insult is warranted, and biological modeling could provide important insights into it. Due to the variation of the impairments on persons after stroke, it may be better to obtain the parameters in vivo to acquire more precise information for the modeling on the specific subjects.

This study extended our previous efforts on elbow flexor modeling to design a subject-specific method of musculoskeletal model using in vivo ultrasound data on the elbow extensors and aimed to investigate the feasibility of estimating the musculotendon parameters during elbow extensions of both unimpaired subjects and persons after stroke. Our hypothesis is that the maximal isometric muscle stress, one of the modeling outputs, would be less on the affected side of stroke group compared to that from control group. In addition, different contributions of three heads of triceps (long, lateral, and medial) to elbow extension could also be evaluated and compared between stroke and control subjects. It is hoped that, through this ultrasound-combined subject-specific technique, we can enhance our understanding of the muscle parameters and force generating capacity changes of individual stroke survivors on elbow extension and help to design suitable rehabilitation intervention for them.

2. Materials and Methods

2.1. Subject Recruitment. Five persons after stroke and five normal subjects were recruited for this study. Clinical characteristics of the persons after stroke were summarized in Table 1. The selection criteria were (1) a single unilateral lesion of the brain with the duration of stroke more than 1 year; (2) having spasticity with Modified Ashworth Score

TABLE 1: Clinical characteristics of the 5 hemiparetic subjects including Modified Ashworth Scale [24].

Subject	Age (y) and sex	Years after injury	Arm affected	Modified Ashworth Score [24]
LI	63 (F)	3	L	3
CO	52 (M)	4	L	2
CH	61 (M)	2	R	1
ZH	52 (F)	4	L	1+
WO	44 (M)	4	L	1

F, female; M, male; R, right; L, left.

(MAS) larger than 1 and sufficient passive range of motion (flexion is up to 105°) at the elbow joint; (3) adequate mental ability to understand the experimental tasks as instructed; (4) no surgical procedure on the affected side of the upper limb; (5) absence of significant medical complications. The participants gave informed consent following the ethical procedures and this study was approved by the human subject ethics subcommittee of local university.

2.2. Model Consideration. In this study, cylinder and sphere shape of wrapping objects have been applied to simulate the humerus head and capitulum on the muscle path in the geometry model. Via points were determined to allow the muscle to move around the bone surface during joint movement. The whole wrapping muscle path was then defined by connecting the origin, via points, and insertion point of that particular muscle [25]. The musculotendon length (l_{mt}) from muscle origin to muscle insertion points was estimated through summing each line segment on the whole muscle path in SIMM (Software for Interactive Musculoskeletal Modeling, MusculoGraphics, Inc., USA) and then scaled on subject-specific bases based on the segment ratio from anthropometric measurements. Then, l_{mt} was determined as follows:

$$l_{mt} = \sum_{i=1}^{n-1} |P_{i+1} - P_i|, \quad (1)$$

where P_1, P_2, \dots, P_n are muscle via and attachment points on the path of each muscle and we allowed the joint angle range of 0° – 130° with an increment of 1° .

l_{mt} is then used to estimate moment arm (MA) as the following partial derivative of joint angle (θ) with the following equation:

$$MA = \frac{\partial l_{mt}}{\partial \theta}. \quad (2)$$

The biomechanical characteristics of musculotendon dynamics could be evaluated by a modified Hill-type model that describes force-length and force-velocity relationships of the muscle at active and passive contraction conditions and the elastic properties of the tendon [26]. The force generated

by each musculotendon complex can be calculated as in the following equations:

$$F_t = F_m \cdot \cos \alpha = F_z \left[f_a(l) f(v) a(t) + f_p(l) \right] \cos \alpha, \quad (3)$$

$$F_z = PCSA \cdot \sigma_m, \quad (4)$$

where F_z is the maximum isometric muscle force, σ_m is the maximum isometric muscle stress, $a(t)$ is the activation level, and α is the pennation angle. During maximum isometric voluntary elbow extension, it is assumed that all the elbow extensors are fully activated (i.e., $a(t) = 1$). $f_a(l)$ is the force-length relationship of contractile element and $f_p(l)$ is the parallel muscle force of passive elastic element [27]:

$$f_p(l) = A_P \cdot \left[e^{k_{pe}(l-l_{mo})/l_{mo}} - 1 \right],$$

$$f_a(l) = \sin \left[b_1 \cdot \left(\frac{l}{l_{mo}} \right)^2 + b_2 \cdot \frac{l}{l_{mo}} + b_3 \right]. \quad (5)$$

Herein, the coefficients $A_P = 0.129$, $k_{pe} = 4.525$, $b_1 = -1.317$, $b_2 = -0.403$, and $b_3 = 2.454$.

Tendon is taken as a nonlinear spring for which the nominal force-strain relationship is composed of two regions (i.e., an initial exponential relationship and a linear relationship for larger deformations) which satisfied the following relationship:

$$F_t(\varepsilon_t) = \begin{cases} F_z \cdot A \cdot (e^{k_1 \varepsilon_t} - 1) & 0 \leq \varepsilon_t < \varepsilon_c \\ k_2 \cdot F_z \cdot (\varepsilon_t - \varepsilon_c) + F_c & \varepsilon_t \geq \varepsilon_c, \end{cases} \quad (6)$$

where ε_t is tendon strain at tendon length l_t (i.e., $\varepsilon_t = (l_t - l_{to})/l_{to}$), ε_c is the tendon strain at tendon length l_{tc} (i.e., $\varepsilon_c = (l_{tc} - l_{to})/l_{to}$), l_{to} is the tendon slack length, and l_{tc} is the tendon length at which tendon force shifts from nonlinear to linear region. Based on the experimental results from other studies, Zajac [26] constructed a generic nominal force-strain curve of tendon and estimated the dimensionless coefficients for the tendon force-strain relationship: $A = 0.1238$; $k_1 = 81.1438$; $k_2 = 37.5$; and $F_c/F_z = 0.5$. In addition, Zajac [26] found the linear region that begins after tendon is stretched by 2% (i.e., $\varepsilon_c = 0.02$) and the corresponding stress is 16 MPa; the strain of the tendon at which the tendon force equals maximum isometric muscle force F_z is tendon independent and equals 3.3% and the corresponding stress is also tendon independent and equals 32 MPa [26].

Equation (6) is used to calculate tendon force, and together with (3)~(5) on estimating muscle force, all the equations are substituted into (3).

Tendon length (l_t) was estimated from the whole musculotendon length (l_{mt}), muscle fascicle length (l_m), and pennation angle (α):

$$l_t = l_{mt} - l_m \cos \alpha. \quad (7)$$

The torque generated by the elbow extensors during maximum voluntary contraction (MVC) could be calculated from the summation of each muscle's contribution, considering the moment arm of each muscle:

$$T(\theta) = \sum_{i=1}^3 F_i(\theta) \times MA_i(\theta), \quad (8)$$

where $F_i(\theta)$ is the tendon force and $MA_i(\theta)$ is the moment arm of each prime elbow extensor i (i.e., 1: the medial head of triceps brachii (MHT), 2: the lateral head of triceps brachii (LatHT), and 3: long head of triceps brachii (LngHT) at joint position θ).

2.3. Ultrasound Measurement. B-mode ultrasound machine with a 7.5-MHz, 38 mm probe (resolution of 0.3 mm) (Sonosite 180 Plux, Sonosite Inc., USA) was applied to measure elbow extensor's pennation angle and optimal length at the optimal angle when the muscle is fully activated [28]. Based on (7) and the definitions of muscle optimal length and tendon slack length, the following equation was applied for the calculation of the tendon slack length (l_{to}):

$$l_{to} = l_{mt}^o - l_m \cdot \cos \alpha_o, \quad (9)$$

where l_{mt}^o , l_m , and α_o are the musculotendon length, muscle optimal length, and pennation angle at the optimal angle of the elbow joint, respectively.

The optimal angle, which is the joint angle that corresponds to the muscle optimal length, determines the operating range in a length-tension relationship by the joint movement and tendon excursion. Previous studies reported the optimal joint angle of elbow extension is 90° [29] and since the triceps brachii contribute nearly 80% of the moment to the joint, it is reasonable to assume that the 90° was set as optimal angle of triceps in this study. Similar angle was applied in a study in literature recently [16].

During the experiment, the subject was seated in a height-adjustable chair, with the arm to be tested put on the arm holder of a custom-made dynamometer (motor: Dynaserv, Yokogawa, Japan; torque sensor: AKC-205A, China Academy of Aerospace Aerodynamics, accuracy of 0.03 Nm, China). The motor can drive the arm holder to exact testing position and the torque sensor could measure the generated elbow extension torque from the subject during isometric contraction. The testing plane of the arm is parallel to the floor at the same height as the shoulder, with the shoulder abducted 90° and flexed 0° .

For each elbow joint position from 0° to 105° with 15° increment, the probe was put in the posterior part of the upper arm and the position of the probe was on the muscle belly which is just in the middle of the upper arm, for measuring MHT and LngHT. The probe was then parallelly moved 2 cm to the lateral direction to measure LatHT. Coupling gel (Parker Aquasonic 100 Gel, USA) was applied to enhance ultrasound conduction between the ultrasound probe and the skin surface. Typical ultrasound images taken of the prime elbow extensors and the demonstration of calculating the muscle architectural parameters are shown in Figure 1. The ultrasound images were stored in the computer and analyzed offline (UTHSCSA imaging tool, USA) to estimate the muscle architecture parameters.

2.4. Torque and EMG Data Recording. The setup of experiment in second stage of EMG and torque data collection was shown in Figure 2. The testing position of torque and EMG is similar to ultrasound measurement. Briefly, each

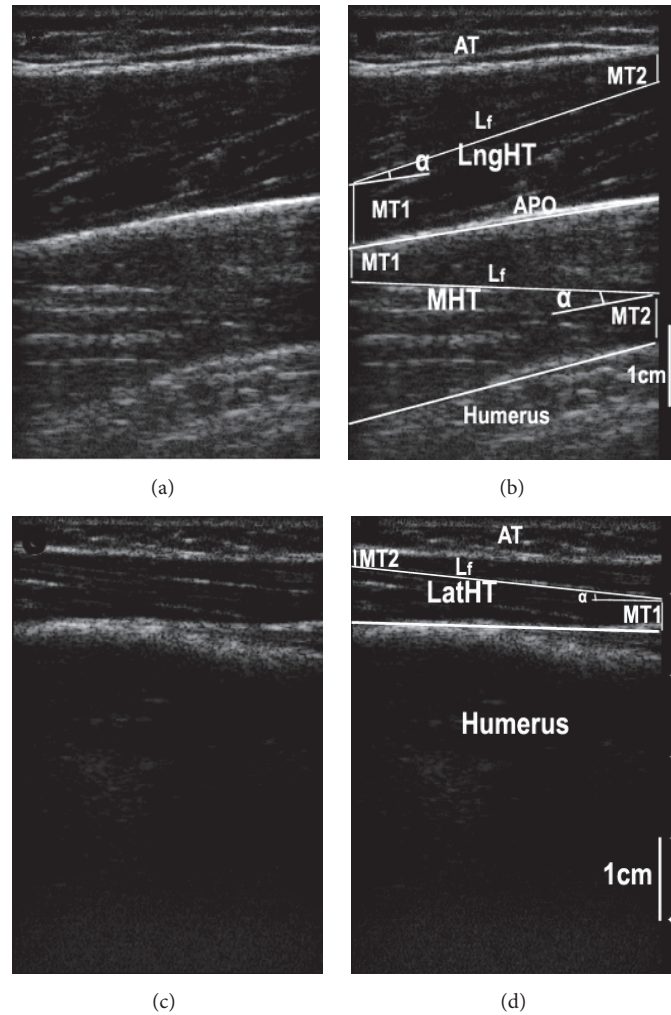


FIGURE 1: Typical ultrasonography imaging of the prime elbow extensors: long head of triceps brachii (LngHT), medial head of triceps brachii (MHT), and lateral head of triceps brachii muscle. (a) Original ultrasound image of MHT and LngHT; (b) MHT and LngHT image with labels; (c) original ultrasound image of LatHT; and (d) LatHT image with labels. In (a) and (b), the APO (bright fringe in the middle region) shows the boundary between MHT and LngHT. The white fringe in the lower range is the muscle-bone boundary (MHT-humerus). In (c) and (d), the bright fringe shows the muscle-bone boundary (LatHT-humerus). In (b) and (d), L_f is the visualized part of the entire muscle fascicle length; MT_1 and MT_2 are the distance of the fiber proximal end to the bone and the distance of the fiber distal end point to the superficial aponeurosis, respectively; AT is adipose tissue; α is the pennation angle.

subject sat on the assessment chair and the forearm was attached to the arm holder, which was connected to the end of the torque sensor. An orthosis with semicircular cross section was attached to the arm holder. The subject's forearm was placed inside the orthosis and straps were used to fasten the forearm. The upper arm was also fastened by a strap to a supporter mounted on the upper aluminum plate. The orthosis and arm holder could guide the forearm to rotate with an axis of rotation in line with the motor and the torque sensor. The subject was asked to grasp the handle of the arm holder and could voluntarily perform elbow extension in the horizontal plane. A screen with visual feedback was placed in front of the subject to provide guidance (Figure 2). There were three trials of extension at each testing position and each contraction lasted for around 5

seconds. A two-minute recovery period was allowed between contractions to minimize muscle fatigue.

In this study, surface electrodes were applied to record the myoelectric activities of the target muscles to record the activities of many motor units within a muscle [30]. Bipolar pregelled Ag/AgCl surface electrodes (Noraxon dual electrode, Noraxon Inc., USA), placed 3 cm apart, were used to record EMG of the three elbow extensors. An additional reference electrode was placed distant lateral of the elbow, over the skin surface of olecranon. Electrode placement was verified by functional muscle testing. Torque and EMG signals were recorded with a sampling frequency of 2000 Hz and stored on a PC computer via the data acquisition (DAQ) card (PCI 6036E, National Instrument, Texas, USA). The amplifier gain for surface EMG signal is 1000.

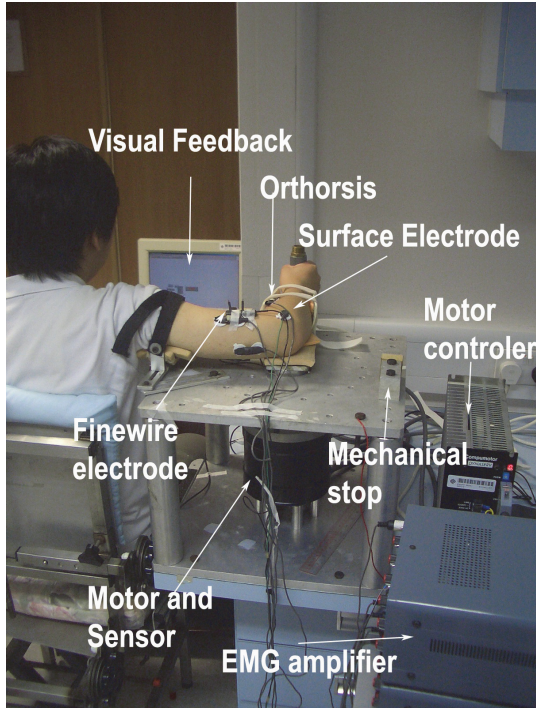


FIGURE 2: Experiment setup of EMG and torque data collection in MVC. Surface EMG electrodes were attached on long, medial, and lateral head of triceps brachii. In this photo, the elbow was positioned at the 90° flexed position.

2.5. EMG and Torque Data Processing. The digitized EMG and elbow torque signals were processed offline. A detailed analysis on MVC torques and the associated EMG of prime elbow extensors was performed. The torque signals were low-pass filtered (fourth-order Butterworth filter) at 5 Hz. The torque data measured at different elbow angles were curved-fitted to the lowest-order polynomial equation with an R^2 value greater than 0.9. This torque-angle relationship would be incorporated into the model to calculate the musculo-tendon parameters of each target muscle. The raw surface EMG were band-pass filtered (fourth-order Butterworth filter 10 Hz–500 Hz) and then rectified and further processed with a 100 ms moving average window. The filtered EMG signals were normalized by peak value of EMG amplitude measured during the MVC test.

2.6. Optimization Process. The optimization program calculated the individual maximum muscle force for each prime elbow extensor individually. The optimization algorithm tried to minimize the root mean square difference between the polynomial fitted with a third-order function and torque-sensor measured maximal isometric extension torques with the range from 10° to 100° at elbow joint, with increments of 2° [31]:

$$\text{minimize } F = \sqrt{\frac{\sum_{i=1}^{46} (T_i^m - T_i^p)^2}{46}}, \quad (10)$$

where T^m is the measured elbow extension torque and T^p is the predicted elbow extension torque. As mentioned before, the input parameters of the model included the muscle optimal length and pennation angle from the ultrasound measurements and the musculotendon length and moment arm from the geometric model after subject-specific scaling based on segment length from upper arm and forearm. The optimization of maximum isometric muscle force was conducted in two steps. In the first step, the optimization scheme would produce the value of maximum isometric muscle stress in order to obtain a suitable initial value and proper searching boundary for the main process of the optimization in the second step. In step 1, the same maximum isometric muscle stress value was assumed for all prime elbow extensors [13]. The value of PCSA for each muscle was scaled using literature data [32], based on the ratio of the upper arm circumference of cadaver and our subjects. The search process was one full dimensional Nelder-based simplex call [33] and it continued until the root mean square difference between the measured torque and the estimated torque was minimized. The results from the first step provided the value of maximum isometric muscle stress of the prime elbow extensors which was multiplied by PCSA of each muscle to obtain the initial value of maximum isometric muscle force to be used in the second step of optimization. In step 2, plus and minus 15% percent of the initial value were used as the upper and lower boundaries (for the stroke simulation, the initial boundary was set to 30% considering the lower activation level of the affected muscle due to the stroke). The three muscles' maximum isometric muscle forces became variables and the same optimization scheme and constraints as the first step were applied in the second step. The optimization scheme was to stop when the root mean square difference of the measured torque and calculated torque was minimized. After obtaining the maximum isometric muscle force, the maximum isometric muscle stress was calculated by dividing the force by the corresponding PCSA of each muscle [32].

2.7. Statistical Analysis. One-way repeated measures analysis of variance (ANOVA) was applied to evaluate if there are significant differences of the pennation angle of each muscle in different elbow joint positions. Linear regression was used to describe the relationship with ultrasound-measured muscle pennation angle and the joint angle. One-way ANOVA with post hoc Bonferroni test was also used to evaluate optimal muscle length, tendon slack length, and maximum isometric muscle stress (σ_m) from different elbow extensor muscles in each subject group. If there is no significance, data from three muscles would be combined together and t -tests were used to compare the group difference between persons after stroke and health control. p values less than 0.05 were regarded as statistical significance.

3. Results

Figure 3(a) shows the musculotendon length of each prime elbow extensor in this study from a typical subject (CO, male in Table 1) and musculotendon length of triceps brachii muscle as a whole from literature [34]. l_{mt} from our estimation

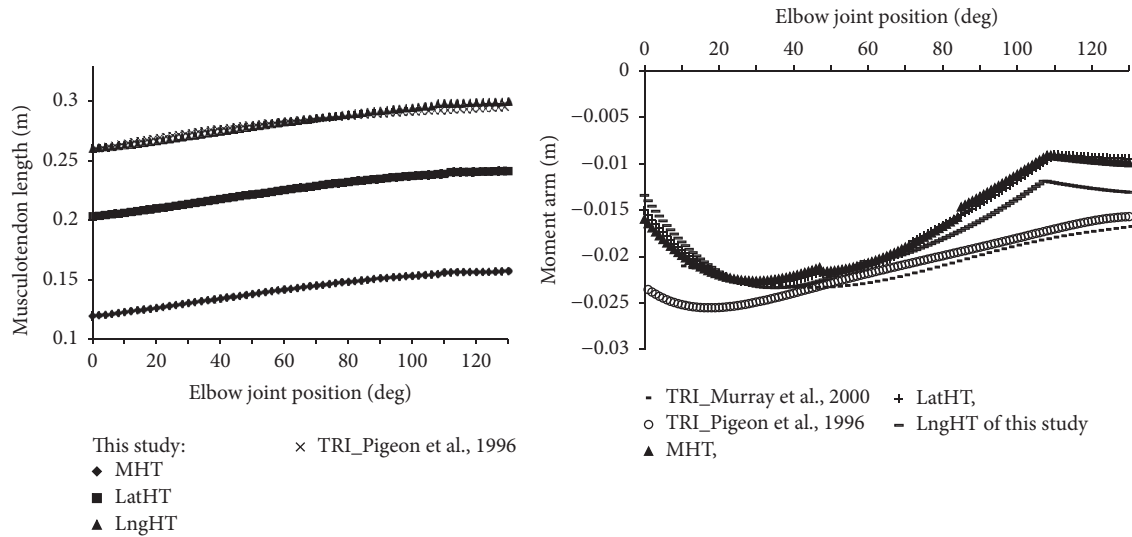


FIGURE 3: Musculotendon length (a) and moment arm (b) of elbow prime extensors of this study, that is, medial head of triceps (MHT), lateral head of triceps (LatHT), and long head of triceps (LngHT) of this study, compared with corresponding literature results from Pigeon et al. [34] and Murray et al. [32]. Pigeon et al. [34] derived data in other studies to obtain a relationship between joint angles and upper limb muscle parameters by curve fitting. MA data from Murray et al.'s study was based on the polynomial equations and the linear regression equations between anthropometric variables and peak moment arm derived by Murray et al. [32].

had similar trend to that of the literature that l_{mt} of elbow extensor increased about 21% as the joint angle flexed from extended position (0°) to flexed position (130°). The moment arm of three prime elbow extensors estimated from geometric model was shown in Figure 3(b). The moment arm-angle results for the range of 0° – 130° with an increment of 1° were compared with literature cadaver data [34, 35]. The average moment arm of each muscle over the range of 0° – 130° was as follows: MHT = 1.70 cm; LatHT = 1.71 cm; LngHT = 1.81 cm.

Figure 4 shows the ultrasound-measured pennation angles (mean values) of MHT, LatHT, and LngHT of unimpaired group (Figure 4(a)) and hemiparetic group (Figure 4(b)), as well as pennation angles adopted in literature [36]. The results revealed that the in vivo pennation angle of elbow extensor was angle-dependent with difference of measure joint position (one-way ANOVA, $p < 0.05$) in both unimpaired and hemiparetic group. For unimpaired group, the pennation angles decreased from 11.7° to 7.1° , 7.6° to 6.3° , and 12.8° to 8.1° for MHT, LatHT, and LngHT, respectively, as the joint position changed from 15° to 105° . The linear regression results from unimpaired group showed MHT ($\alpha = -0.05\theta + 11.43$; $R^2 = 0.843$) and LngHT ($\alpha = -0.051\theta + 12.99$; $R^2 = 0.913$) have similar slope and initial value which, both of them, were larger than those from LatHT ($\alpha = 0.019\theta + 8.14$; $R^2 = 0.648$). Similar pennation angle from hemiparetic group was observed when compared with unimpaired group.

Figure 5 shows the typical result of the measured and predicted maximum isometric extension torque versus elbow joint angle for a subject in unimpaired group (a) and for one hemiparetic subject (b). In general, the predicted torque-angle fits the measured one well except at the more extended positions ($<50^\circ$). The RMS differences ranged from 1.43 to 6.78 Nm (mean = 3.64, SD = 2.25, $n = 5$). The predicted

torque-angle profile follows the similar trend as the measured one with the RMS differences ranging from 1.76 to 4.33 Nm (mean = 3.01, SD = 0.95, $n = 5$) for extension in hemiplegic group.

Muscle optimal lengths of the three heads of triceps (MHT, LatHT, and LngHT) in the unimpaired group were found to have no significant difference ($p = 0.34$) among them and with a mean and SD of 8.8 ± 2.2 , 11.0 ± 2.8 , and 9.2 ± 2.3 cm, respectively (Table 2). The mean and SD of tendon slack lengths were 5.7 ± 1.3 , 11.4 ± 1.9 , and 18.7 ± 1.2 cm, respectively, and were found to be significantly different ($p < 0.001$) in the unimpaired group. Post hoc results showed l_{to} from MHT was significantly smaller ($p < 0.001$) than that from LatHT and also significantly smaller ($p < 0.001$) than that from LngHT. Similarly, the mean muscle optimal lengths of the three heads of triceps (MHT, LatHT, and LngHT) in hemiplegic group were found to be not significantly different ($p = 0.241$) with a mean and SD of 10.9 ± 2.1 , 12.8 ± 1.9 , and 10.5 ± 2.4 cm, respectively. The mean and SD of tendon slack lengths were 3.2 ± 1.6 , 9.3 ± 2.7 , and 17.0 ± 2.3 cm, respectively, and were found to be significantly different among them ($p < 0.001$). Post hoc results showed l_{to} from MHT was significantly smaller ($p = 0.003$) than that from LatHT and also significantly smaller ($p < 0.001$) than that from LngHT in hemiparetic group.

Figure 6 shows there was no significant difference in σ_m (maximum isometric muscle stress) of LatHT, LngHT, and MHT in hemiparetic group and unimpaired group, respectively. Therefore, the mean value (σ_e) of these three prime elbow extensors was used in comparisons below. The value of maximum isometric muscle stress for extensor of unimpaired group was found to range from 60.9 to 115.4 N/cm². In hemiparetic group, the maximum muscle stress of extensor

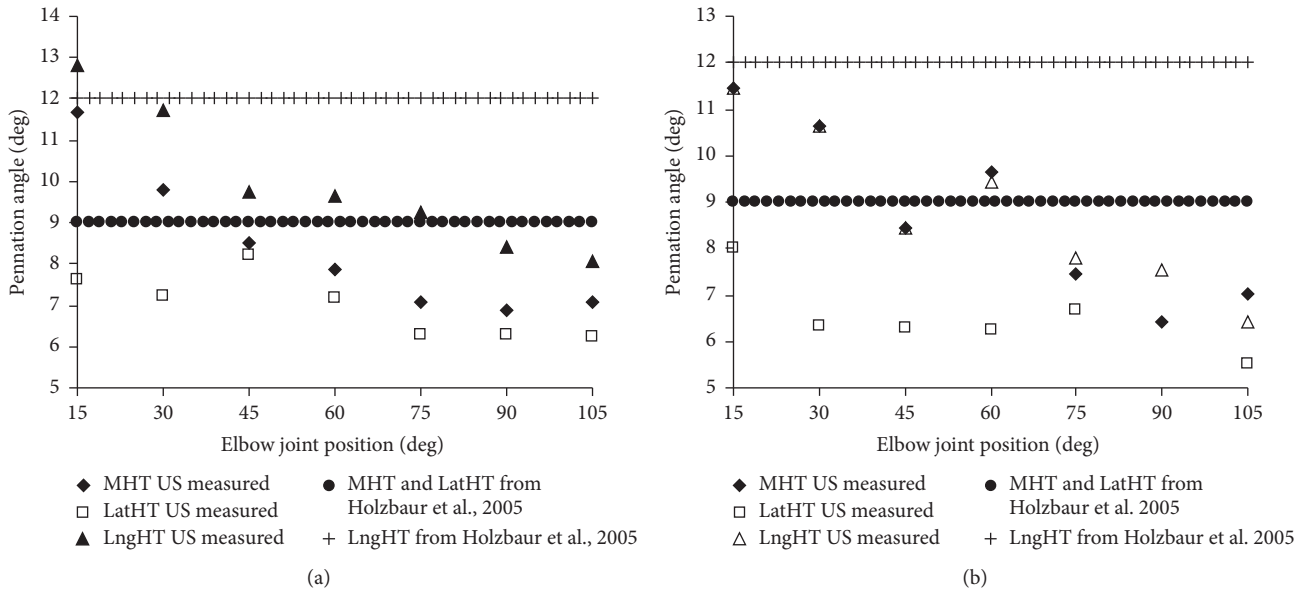


FIGURE 4: In vivo measurement of pennation angles of elbow extensors to the joint angle in the MVC condition for unimpaired group (a) and hemiparetic group (b) as well as pennation angle from literature [36].

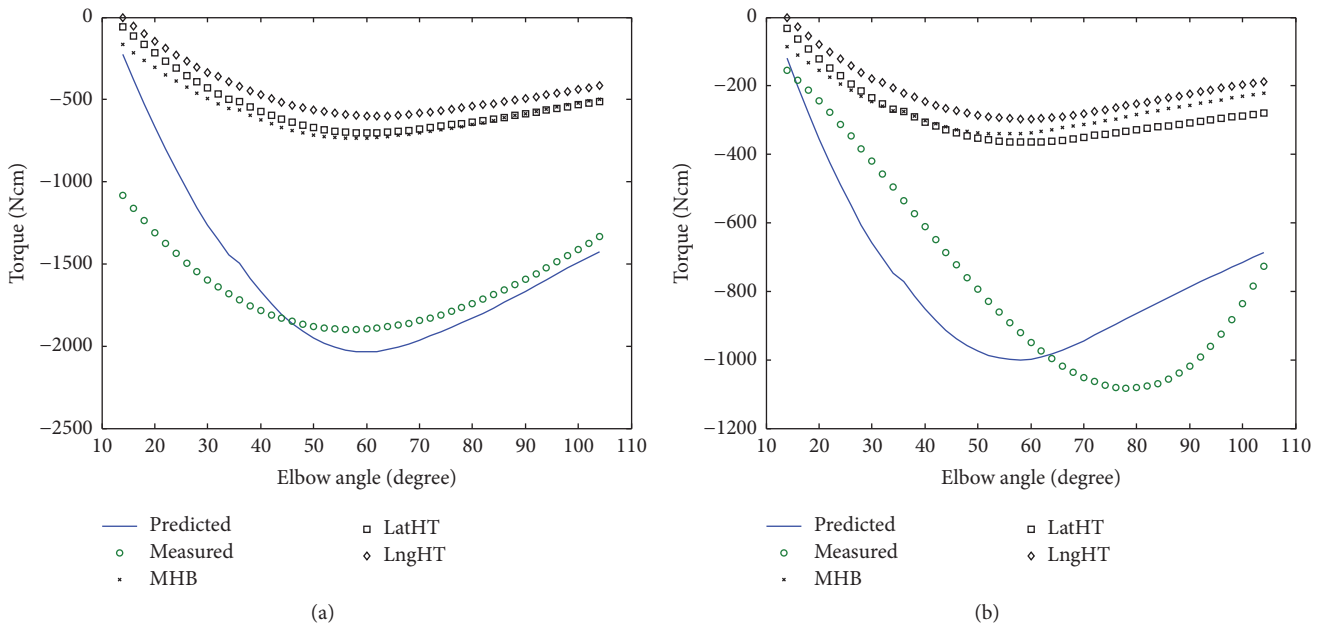


FIGURE 5: Modeling results: comparison of typical predicted profiles with measured extension torque-angle results for (a) one unimpaired subject and (b) one person after stroke. Individual elbow extensor generated torque-angle profiles were also plotted.

group was found to range from 18.5 N/cm² to 66.1 N/cm². The mean \pm SD for the unimpaired and hemiparetic group was 89.3 \pm 21.8 and 50.8 \pm 18.6 N/cm², respectively, and the value from hemiparetic group was found to be significantly smaller than that of the unimpaired group ($p = 0.023$).

4. Discussion

In this study, a biomechanical model of elbow extensors was built for both unimpaired subjects and persons after

stroke based on subject-specific ultrasound-measured and experimentally optimized parameters.

4.1. Muscle Path and Moment Arm. The results showed that l_{mt} in this study of LngHT is almost the same as literature l_{mt} of triceps brachii [18]. In general, the modeled moment arms matched well with the data from the literature in terms of the trend and amplitude. Similar moment arms were noted among the three heads of triceps and discontinuities in the

TABLE 2: Comparison of muscle optimal lengths and tendon slack lengths of prime elbow extensors of healthy group found in the study (mean value, $n = 5$) and those reported in other literature.

	Muscle	Holzbaur et al., 2005	Langenderfer et al., 2004	Murray et al., 2000	Winters and Stark, 1988	Garner and Pandey, 2003	Current study
Muscle optimal length (cm)	MHT	11.4	14.5	NR	6	8.77*	8.8
	LatHT	11.4	10.3	6.6–13.9	7	8.77	11.0
	LngHT	13.4	17.6	9.5–16.5	9	8.77	9.2
Tendon slack length (cm)	MHT	9.1	NR	NR	17	19.05*	5.7
	LatHT	9.8	NR	18.7	19	19.05	11.4
	LngHT	14.3	NR	21.7	22	19.05	18.7

NR: not reported. *Combination of MHT, LatHT, and LngHT as triceps brachii in Garner and Pandey, 2003.

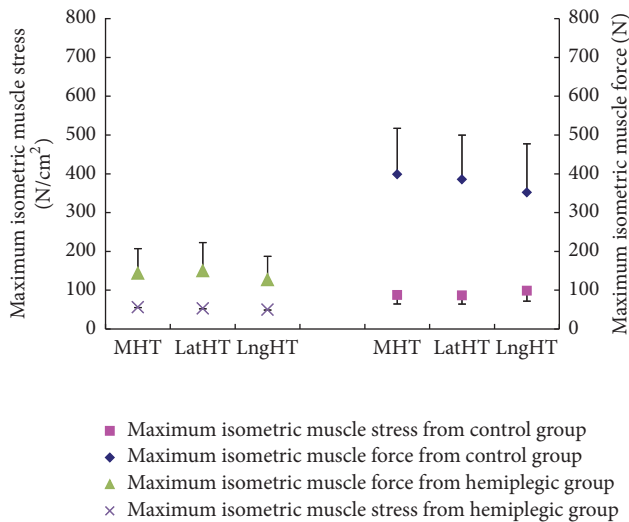


FIGURE 6: Maximum isometric muscle force and maximum muscle stress (mean value, $n = 5$) for each prime elbow extensor for unimpaired group and hemiparetic group. The error bar indicates one-standard-deviation length.

moment arm were noted in flexed position about 110° where the additional via points become active.

Previous literature outlined methods of calculating muscle moment arm based on consideration of the line of action or tendon excursion [35, 37]. Furthermore, in other studies, muscle length was defined as linear functions [38] or nonlinear functions of joint angles [34] or a straight line from origin to insertion, which might not represent accurately the real complex morphology of passive structures such as joint articulating surfaces and ligaments. Another study used the constraint points of the muscle path and defined them using interpolation point technology [13]. However, doing this probably resulted in the muscle “punching through” the bone when the joint angle was changed to an extreme position. This is unreasonable and may lead to the calculated moment arm being disconnected. In addition, the constraint points needed to be defined individually on each degree of freedom (DOF), which becomes a very complex task when multi-DOF movement is to be modeled. In one of the modeling studies, the investigators used geometric-shaped

objects to make the muscle wrap its path smoothly over bony landmarks or other constraints [39]. The wrapping objects could constrain via points of the muscles moving on the bone contours. In our study, cylindrical and spherical shapes for wrapping objects have been applied to simulate the humerus head and capitulum on the muscle path and then have effects on the moment arm. The general profile of the moment arm across the joint positions was similar to the literature but our calculated moment arm was continuous, making the later calculating of joint moment more reliable. It is difficult to access the accuracy of moment arm directly. It was believed that the discrepancy might be due to the underestimation of the triceps moment arms at the more extended positions. Another reason for the discrepancy may be the optimal angle selection since this value was observed from the active contraction. The accuracy of musculotendon length and moment arm is important to the later estimation of muscle force and joint trajectory [40]. The results of the geometric model, such as musculotendon length and moment arm, could be used further for 3D motion analysis or force prediction in dynamic conditions [30].

4.2. Musculotendon Parameters and Ultrasound Measurement. Appropriate musculoskeletal modeling can provide both qualitative and quantitative information into the neuromusculoskeletal system and its motion dynamics to analyze human movement [4]. The modeling parameters are important to the success of the model. Manal and Buchanan (2004) used a numerical method based on Hill-type model to estimate the elbow muscle architecture parameters and they found that the 5% change of the tendon slack length resulted in upwards 30% difference on the estimated output fiber force [5]. Especially in poststroke survivors, the muscle parameters have changed after the insult [14]. In this current study, the pennation of lateral head of triceps of this study was smaller (about 9°) than that from the literature [36]. The results also showed that the in vivo pennation angle of long head of triceps in hemiparetic group was smaller (around 12°) than the literature value. In literature, it is suggested better to obtain subject-specific modeling parameters to tailored individual biomechanical modeling. For example, Hasson and Caldwell found subject-specific models in aging study gave good predictions of experimental concentric torque-time curve with 10–14% error; well the prediction errors would

go twice as large with generic muscle properties parameters [6]. In our previous study of elbow flexor modeling in the hemiparetic subjects, we also revealed significantly smaller RMS errors between the predicted and measured movement trajectories when using subject-specific dataset than that from applying cadaveric data from the literature [41].

Previous models using pure mathematical optimization or using outcome torque or force to inversely obtain musculotendon parameters have the limitations such as the following: only partial insight into relating the optimization outcome with explicit physically and biologically meaningful principles were provided; curve-fitting technique always used before the experimental torque-joint angle data to proceed and the fitting results might affect the effectiveness of the modeling to “unknown and unpredictable” values [42].

The optimal fascicle length is the muscle fascicle length at which a muscle can generate its maximum isometric force and it is generally assumed to be the fascicle length at which a muscle begins to develop passive force [27]. This parameter was found to be related to the amount of excursion of the muscle fiber over the force-length relationship [13, 30]. In this study, optimal fascicle length of each elbow extensor was obtained based on ultrasound measurement on muscle optimal angle. Our results showed the modeling data and ultrasound data were in the similar range which could be a cross-validation for the ultrasound measurement and the modeling calculation [28, 32, 36, 43, 44] (Table 2). In addition, the fascicle length from hemiparetic muscle seemed to have a larger deviation between ultrasound-measured data and modeling results in elbow extensors (Figure 5(b)), which might indicate the variation of the affected extensor properties in the isometric contraction. As seen in Figure 5, the estimation error may be due to the bad motor control ability (i.e., coactivation from elbow flexors) or the lower activation level since the estimation simply assumed the muscle was in fully activation ($a(t) = 1$). The extension simulation RMS increased at the extended joint positions ($>80^\circ$) which may be caused by the underestimation of the moment arm at those positions.

4.3. Maximum Isometric Muscle Stress: A Modeling Output. Our results showed that there is no significant difference of maximum isometric muscle stress among the three elbow extensors in both healthy and stroke group which could be explained that the three-head-of-triceps brachii has similar force generation potential. As our expectation, we found that the maximum isometric muscle stress value from the hemiparetic group was significantly smaller than that found in the unimpaired group in extensor (Figure 6). This finding is in line with the study by Feng and coworkers [7]. The difference of the muscles stress between persons after stroke and healthy people could be explained in biomechanical and/or neurological factor. Previously, other investigators found that differences in muscle stress between muscle groups might be due to differences in specific tension of different muscle fiber or motor unit populations [45]. That is, the fast twitch fibers may have higher muscle stress than those of the slow twitch fibers. Fiber composition could be very different between subjects and/or between muscles. Moreover, it has been found by Robinson and coworkers that immobilization would result

in significant increase in the proportion of no-force units and a trend toward preferential reduction in type FF units [46]. Furthermore, there is evidence on fiber measurements in biopsied muscle that supports the idea that the type FF or FR motor units are atrophied in patients with hemiparesis [47]. This implies reduction in number of fast twitch fibers after stroke. On the other hand, hypertrophy of type S motor units has also been reported, which reflects increase in the number of slow twitch fibers. Moreover, Young and Mayer (1982) had found a unique class of motor units in long-term hemiparetic muscle-slow-contracting and fatigable, which is not present in normal muscle [48]. These all substantiate that the muscle stress can be very different between subjects and/or between muscles, and then they form the rationales to optimize muscle stress in the current study.

Another factor to explain the lower muscle stress from persons after stroke was that some hemiparetic subjects might not be able to fully activate their muscles when instructed. There is evidence that this deficit in muscle activation is mostly due to reduced neural drive from higher centers (i.e., motor cortex) secondary to the lesion [49, 50]. The results suggested that the hemiparetic subjects could suffer from muscle weakness, which might be biomechanical or/and neurological in nature. In addition, there is a limitation in the current study that the calculation of PCSA is from the scaling of literature data which results in underestimation of the muscle stress from stroke group. The physiologic cross-sectional area of a muscle or, in essence, the number of sarcomeres in parallel is related directly to the amount of tension that the muscle can produce and the paretic arm may have significantly greater intramuscular fat and connective tissue than the unaffected or control arm. Further dedicated ultrasound study should combine measurements on transverse direction for cross section area with longitudinal direction on fascicle length and pennation angle to improve the accuracy.

In summary, this study considered and measured elbow extensor architectural changes after the onset of stroke and these in vivo parameters were used to build subject-specific biomechanical model. The maximum isometric muscle stress of elbow extensors from persons after stroke was found to be lower than that from control subjects, which indicated the weakness of muscle force generation potential after stroke. The technique and results in this study may help to evaluate the functional improvement of the affected muscle after an intervention program and to enhance the understanding of the effects on the muscle architecture and model during rehabilitation treatment.

Competing Interests

No commercial party having a direct financial interest in the results of the research supporting this paper has or will confer a benefit upon the authors or upon any organization with which the authors are associated.

Acknowledgments

This study is supported by the Natural Science Foundation of Guangdong Province, China (no. 2015A030313139),

Science and Technology Planning Project of Guangdong Province, China (nos. 2015A05050202, 2015B020214003, 2014B090901056, and 2013b090500099), and the Research Grants Council of Hong Kong (GRF PolyU 527511).

References

- [1] L. Ada, C. G. Canning, and S.-L. Low, "Stroke patients have selective muscle weakness in shortened range," *Brain*, vol. 126, no. 3, pp. 724–731, 2003.
- [2] J. P. A. Dewald, P. S. Pope, J. D. Given, T. S. Buchanan, and W. Z. Rymer, "Abnormal muscle coactivation patterns during isometric torque generation at the elbow and shoulder in hemiparetic subjects," *Brain*, vol. 118, no. 2, pp. 495–510, 1995.
- [3] K. M. Zackowski, A. W. Dromerick, S. A. Sahrman, W. T. Thach, and A. J. Bastian, "How do strength, sensation, spasticity and joint individuation relate to the reaching deficits of people with chronic hemiparesis?" *Brain*, vol. 127, no. 5, pp. 1035–1046, 2004.
- [4] T. K. K. Koo and A. F. T. Mak, "Feasibility of using EMG driven neuromusculoskeletal model for prediction of dynamic movement of the elbow," *Journal of Electromyography and Kinesiology*, vol. 15, no. 1, pp. 12–26, 2005.
- [5] K. Manal and T. S. Buchanan, "Subject-specific estimates of tendon slack length: a numerical method," *Journal of Applied Biomechanics*, vol. 20, no. 2, pp. 195–203, 2004.
- [6] C. J. Hasson and G. E. Caldwell, "Effects of age on mechanical properties of dorsiflexor and plantarflexor muscles," *Annals of Biomedical Engineering*, vol. 40, no. 5, pp. 1088–1101, 2012.
- [7] C. J. Feng, A. F. T. Mak, and T. K. K. Koo, "A surface EMG driven musculoskeletal model of the elbow flexion-extension movement in normal subjects and in subjects with spasticity," *Journal of Musculoskeletal Research*, vol. 3, no. 2, pp. 109–123, 1999.
- [8] M. G. Pandy, "Computer modeling and simulation of human movement," *Annual Review of Biomedical Engineering*, vol. 3, pp. 245–273, 2001.
- [9] B. W. Infantolino and J. H. Challis, "Measuring subject specific muscle model parameters of the first dorsal interosseous in vivo," *Annals of Biomedical Engineering*, vol. 42, no. 6, pp. 1331–1339, 2014.
- [10] T. S. Buchanan, M. J. Moniz, J. P. A. Dewald, and W. Z. Rymer, "Estimation of muscle forces about the wrist joint during isometric tasks using an EMG coefficient method," *Journal of Biomechanics*, vol. 26, no. 4–5, pp. 547–560, 1993.
- [11] R. V. Gonzalez, T. S. Buchanan, and S. L. Delp, "How muscle architecture and moment arms affect wrist flexion-extension moments," *Journal of Biomechanics*, vol. 30, no. 7, pp. 705–712, 1997.
- [12] R. V. Gonzalez, E. L. Hutchins, R. E. Barr, and L. D. Abraham, "Development and evaluation of a musculoskeletal model of the elbow joint complex," *Journal of Biomechanical Engineering*, vol. 118, no. 1, pp. 32–40, 1996.
- [13] T. K. K. Koo, A. F. T. Mak, and L. K. Hung, "In vivo determination of subject-specific musculotendon parameters: applications to the prime elbow flexors in normal and hemiparetic subjects," *Clinical Biomechanics*, vol. 17, no. 5, pp. 390–399, 2002.
- [14] L. Li, K. Tong, R. Song, and T. K. K. Koo, "Is maximum isometric muscle stress the same among prime elbow flexors?" *Clinical Biomechanics*, vol. 22, no. 8, pp. 874–883, 2007.
- [15] M. A. Lemay and P. E. Crago, "A dynamic model for simulating movements of the elbow, forearm, and wrist," *Journal of Biomechanics*, vol. 29, no. 10, pp. 1319–1330, 1996.
- [16] P. A. Huijing and G. C. Baan, "Stimulation level-dependent length-force and architectural characteristics of rat gastrocnemius muscle," *Journal of Electromyography and Kinesiology*, vol. 2, no. 2, pp. 112–120, 1992.
- [17] P. W. Hodges, L. H. M. Pengel, R. D. Herbert, and S. C. Gandevia, "Measurement of muscle contraction with ultrasound imaging," *Muscle and Nerve*, vol. 27, no. 6, pp. 682–692, 2003.
- [18] M. V. Narici, T. Binzoni, E. Hiltbrand, J. Fasel, F. Terrier, and P. Cerretelli, "In vivo human gastrocnemius architecture with changing joint angle at rest and during graded isometric contraction," *The Journal of Physiology*, vol. 496, no. 1, pp. 287–297, 1996.
- [19] G. S. Chleboun, A. R. France, M. T. Crill, H. K. Braddock, and J. N. Howell, "In vivo measurement of fascicle length and pennation angle of the human biceps femoris muscle," *Cells Tissues Organs*, vol. 169, no. 4, pp. 401–409, 2001.
- [20] Y. Kawakami, T. Abe, and T. Fukunaga, "Muscle-fiber pennation angles are greater in hypertrophied than in normal muscles," *Journal of Applied Physiology*, vol. 74, no. 6, pp. 2740–2744, 1993.
- [21] L. Li, K. Y. Tong, and X. Hu, "The effect of poststroke impairments on brachialis muscle architecture as measured by ultrasound," *Archives of Physical Medicine and Rehabilitation*, vol. 88, no. 2, pp. 243–250, 2007.
- [22] T. E. Hewett, K. R. Ford, P. Levine, and S. J. Page, "Reaching kinematics to measure motor changes after mental practice in stroke," *Topics in Stroke Rehabilitation*, vol. 14, no. 4, pp. 23–29, 2007.
- [23] E. Jaspers, K. Desloovere, H. Bruyninckx et al., "Three-dimensional upper limb movement characteristics in children with hemiplegic cerebral palsy and typically developing children," *Research in Developmental Disabilities*, vol. 32, no. 6, pp. 2283–2294, 2011.
- [24] R. W. Bohannon and M. B. Smith, "Interrater reliability of a modified Ashworth scale of muscle spasticity," *Physical Therapy*, vol. 67, no. 2, pp. 206–207, 1987.
- [25] S. L. Delp and J. P. Loan, "A graphics-based software system to develop and analyze models of musculoskeletal structures," *Computers in Biology and Medicine*, vol. 25, no. 1, pp. 21–34, 1995.
- [26] F. E. Zajac, "Muscle and tendon: properties, models, scaling, and application to biomechanics and motor control," *Critical Reviews in Biomedical Engineering*, vol. 17, no. 4, pp. 359–411, 1989.
- [27] Y. Giat, J. Mizrahi, W. S. Levine, and J. Chen, "Simulation of distal tendon transfer of the biceps brachii and the brachialis muscles," *Journal of Biomechanics*, vol. 27, no. 8, pp. 1005–1014, 1994.
- [28] B. A. Garner and M. G. Pandy, "Estimation of musculotendon properties in the human upper limb," *Annals of Biomedical Engineering*, vol. 31, no. 2, pp. 207–220, 2003.
- [29] K. Kulig, J. G. Andrews, and J. G. Hay, "Human strength curves," *Exercise & Sport Sciences Reviews*, vol. 12, no. 1, pp. 417–466, 1984.
- [30] R. V. Gonzalez, L. D. Abraham, R. E. Barr, and T. S. Buchanan, "Muscle activity in rapid multi-degree-of-freedom elbow movements: solutions from a musculoskeletal model," *Biological Cybernetics*, vol. 80, no. 5, pp. 357–367, 1999.

- [31] J. D. Given, J. P. A. Dewald, and W. Z. Rymer, "Joint dependent passive stiffness in paretic and contralateral limbs of spastic patients with hemiparetic stroke," *Journal of Neurology, Neurosurgery and Psychiatry*, vol. 59, no. 3, pp. 271–279, 1995.
- [32] W. M. Murray, T. S. Buchanan, and S. L. Delp, "The isometric functional capacity of muscles that cross the elbow," *Journal of Biomechanics*, vol. 33, no. 8, pp. 943–952, 2000.
- [33] J. A. Nelder and R. Mead, "A simplex method for function minimization," *The Computer Journal*, vol. 7, no. 4, pp. 308–313, 1965.
- [34] P. Pigeon, L. H. Yahia, and A. G. Feldman, "Moment arms and lengths of human upper limb muscles as functions of joint angles," *Journal of Biomechanics*, vol. 29, no. 10, pp. 1365–1370, 1996.
- [35] W. M. Murray, S. L. Delp, and T. S. Buchanan, "Variation of muscle moment arms with elbow and forearm position," *Journal of Biomechanics*, vol. 28, no. 5, pp. 513–525, 1995.
- [36] K. R. S. Holzbaur, W. M. Murray, and S. L. Delp, "A model of the upper extremity for simulating musculoskeletal surgery and analyzing neuromuscular control," *Annals of Biomedical Engineering*, vol. 33, no. 6, pp. 829–840, 2005.
- [37] K. N. An, K. R. Kaufman, and E. Y. S. Chao, "Physiological considerations of muscle force through the elbow joint," *Journal of Biomechanics*, vol. 22, no. 11–12, pp. 1249–1256, 1989.
- [38] J. R. Flanagan, D. J. Ostry, and A. G. Feldman, "Control of trajectory modifications in target-directed reaching," *Journal of Motor Behavior*, vol. 25, no. 3, pp. 140–152, 1993.
- [39] I. W. Charlton and G. R. Johnson, "Application of spherical and cylindrical wrapping algorithms in a musculoskeletal model of the upper limb," *Journal of Biomechanics*, vol. 34, no. 9, pp. 1209–1216, 2001.
- [40] T. S. Buchanan, D. G. Lloyd, K. Manal, and T. F. Besier, "Neuromusculoskeletal modeling: estimation of muscle forces and joint moments and movements from measurements of neural command," *Journal of Applied Biomechanics*, vol. 20, no. 4, pp. 367–395, 2004.
- [41] L. Li, K. Y. Tong, X. L. Hu, L. K. Hung, and T. K. K. Koo, "Incorporating ultrasound-measured musculotendon parameters to subject-specific EMG-driven model to simulate voluntary elbow flexion for persons after stroke," *Clinical Biomechanics*, vol. 24, no. 1, pp. 101–109, 2009.
- [42] N. Zheng, G. S. Fleisig, R. F. Escamilla, and S. W. Barrentine, "An analytical model of the knee for estimation of internal forces during exercise," *Journal of Biomechanics*, vol. 31, no. 10, pp. 963–967, 1998.
- [43] J. Langenderfer, S. A. Jerabek, V. B. Thangamani, J. E. Kuhn, and R. E. Hughes, "Musculoskeletal parameters of muscles crossing the shoulder and elbow and the effect of sarcomere length sample size on estimation of optimal muscle length," *Clinical Biomechanics*, vol. 19, no. 7, pp. 664–670, 2004.
- [44] J. M. Winters and L. Stark, "Estimated mechanical properties of synergistic muscles involved in movements of a variety of human joints," *Journal of Biomechanics*, vol. 21, no. 12, pp. 1027–1041, 1988.
- [45] R. E. Burke and P. Tsairis, "Anatomy and innervation ratios in motor units of cat gastrocnemius," *The Journal of Physiology*, vol. 234, no. 3, pp. 749–765, 1973.
- [46] G. A. Robinson, R. M. Enoka, and D. G. Stuart, "Immobilization-induced changes in motor unit force and fatigability in the cat," *Muscle and Nerve*, vol. 14, no. 6, pp. 563–573, 1991.
- [47] M. Lukács, L. Vécsei, and S. Beniczky, "Large motor units are selectively affected following a stroke," *Clinical Neurophysiology*, vol. 119, no. 11, pp. 2555–2558, 2008.
- [48] J. L. Young and R. F. Mayer, "Physiological alterations of motor units in hemiplegia," *Journal of the Neurological Sciences*, vol. 54, no. 3, pp. 401–412, 1982.
- [49] D. J. Newham and S.-F. Hsiao, "Knee muscle isometric strength, voluntary activation and antagonist co-contraction in the first six months after stroke," *Disability and Rehabilitation*, vol. 23, no. 9, pp. 379–386, 2001.
- [50] C. S. Klein, D. Brooks, D. Richardson, W. E. McIlroy, and M. T. Bayley, "Voluntary activation failure contributes more to plantar flexor weakness than antagonist coactivation and muscle atrophy in chronic stroke survivors," *Journal of Applied Physiology*, vol. 109, no. 5, pp. 1337–1346, 2010.